JOHANNES GUTENBERG UNIVERSITY MAINZ

DOCTORAL THESIS

Structure, Dynamics and Vibrational Spectroscopy of Interfacial Alkali Nitrate and Alkali Halide Aqueous Solutions from *ab initio* Molecular Dynamics

Author:
Gang HUANG

Supervisor:
Apl. Prof. Dr. Marialore SULPIZI
Second reviewer:
J-Prof. Dr. Jamir MARINO

A thesis submitted for the award of the title "Doctor of Natural Sciences"

to the Faculty of

Physics, Mathematics and Computer Science of
Johannes Gutenberg University Mainz

2021

Declaration of Authorship

I, Gang HUANG, declare that this thesis titled, "Structure, Dynamics and Vibrational Spectroscopy of Interfacial Alkali Nitrate and Alkali Halide Aqueous Solutions from *ab initio* Molecular Dynamics" and the work presented in it are my own. I confirm that:

- This work was done wholly or mainly while in candidature for a research degree at this University.
- Where any part of this thesis has previously been submitted for a degree or any other qualification at this University or any other institution, this has been clearly stated.
- Where I have consulted the published work of others, this is always clearly attributed.
- Where I have quoted from the work of others, the source is always given. With the exception of such quotations, this thesis is entirely my own work.
- I have acknowledged all main sources of help.
- Where the thesis is based on work done by myself jointly with others, I have made clear exactly what was done by others and what I have contributed myself.

Signed:

Date:

"*If a problem is worth looking at at all, then no mathematical technique is to be judged too sophisticated.*"

David Ruelle

Abstract

The interfacial structure and dynamics of solutions containing alkali nitrates and alkali halides have been studied by density functional theory-based molecular dynamics (DFTMD) simulations. We have presented a detailed analysis of the hydrogen bond (HB) structure at the interface and have calculated the interface vibrational sum-frequency generation (VSFG) spectra to provide a molecular interpretation of available experimental data.

Both the measured and calculated VSFG spectra of alkali nitrate solution show a reduced intensity in the lower frequency portion of the stretching band, when compared to the water/vapor interface. This reduction is attributed to the hydrogen (H-) bonds established between nitrate and the surrounding water molecules at the interface. This spectral feature is only related to the presence of nitrate at the water surface and is not influenced by the alkali metal ions. We have also shown that, to provide a microscopic interpretation of the spectra, realistic models of the interface are required beyond the simple cluster models.

Heavier halide anions, such as iodine, have an effect similar to that of nitrate on the structure and dynamics of the water/vapor interface. From the results of the simulations and from the calculation of the nonlinear susceptibilities, we conclude that water molecules at the interfaces of LiI, NaI, and KI solutions are participating in weaker H-bonds, compared with those at the water/vapor interface. This feature originates from the unique distribution of I^- ions and alkali metal cations, which form a double layer over a thickness of about 5–10 Å.

The second aspect which we have investigated is the HB dynamics. To analyze HB dynamics at interfaces, we determined the instantaneous interface based on spatial density, and proposed a statistical scheme based on the interfacial HB (IHB) population for identifying the instantaneous interface. Combining the IHB method with interfacial molecule sampling (IMS), we have obtained a method to determine the thickness of the water/vapor interface. The IHB method has been also extended to the solvation shells of ions in aqueous solutions.

Zusammenfassung

Die Grenzflächenstruktur und -dynamik von Lösungen, die Alkalinitrate und Alkalihalogenide enthalten, wurden mit Hilfe von auf Dichtefunktionaltheorie basierenden Molekulardynamik-Simulationen (DFTMD) untersucht. Wir haben eine detaillierte Analyse der Wasserstoffbrückenbindungsstruktur (HB) an der Grenzfläche vorgelegt und haben die Spektren der Schwingungssummen-Frequenz-Generierung (VSFG) an der Grenzfläche berechnet, um eine molekulare Interpretation der verfügbaren experimentellen Daten zu ermöglichen.

Sowohl die gemessenen als auch die berechneten VSFG-Spektren der Alkalinitratlösung zeigen eine verringerte Intensität im unteren Frequenzbereich der Streckbande, im Vergleich zur Wasser/Dampf-Grenzfläche. Diese Verringerung wird auf die Wasserstoffbrückenbindungen (H-) zurückgeführt, die zwischen dem Nitrat und den umgebenden Wassermolekülen an der Grenzfläche entstehen. Dieses spektrale Merkmal hängt nur mit dem Vorhandensein des Nitrats an der Wasseroberfläche zusammen und wird nicht von den Alkalimetallionen beeinflusst. Wir haben auch gezeigt, dass für eine mikroskopische Interpretation der Spektren realistische Modelle der Grenzfläche erforderlich sind, die über die einfachen Clustermodelle hinausgehen.

Schwerere Halogenidanionen, wie z. B. Jod, haben eine ähnliche Wirkung auf die Struktur und Dynamik der Wasser-Dampf-Grenzfläche wie Nitrationen. Aus den Ergebnissen der Simulationen und der Berechnung der nichtlinearen Suszeptibilitäten, schließen wir, dass die Wassermoleküle an den Grenzflächen von LiI-, NaI- und KI-Lösungen an schwächeren H-Bindungen beteiligt sind als an der Wasser/Dampf-Grenzfläche. Dieses Merkmal ist auf die einzigartige Verteilung von I-Ionen und Alkalimetallkationen zurückzuführen, die eine Doppelschicht mit einer Dicke von etwa 5-10 Angström bilden.

Der zweite Aspekt, den wir untersucht haben, ist die HB-Dynamik. Um die HB-Dynamik an Grenzflächen zu analysieren, haben wir die momentane Grenzfläche anhand der räumlichen Dichte bestimmt, und schlugen ein statistisches Schema vor, das auf der HB-Population an den Grenzflächen (IHB) basiert, um die momentane Grenzfläche zu identifizieren. Durch die Kombination der IHB-Methode mit dem Interfacial Molecule Sampling (IMS) haben wir eine Methode zur Bestimmung der Dicke der Wasser/Dampf-Grenzfläche entwickelt. Die IHB-Methode wurde auch auf die Solvatationsschalen von Ionen in wässrigen Lösungen ausgedehnt.

Acknowledgements

I wish to express my sincere gratitude to my supervisor, Prof. Dr. Marialore Sulpizi for her excellent guidance during my doctoral studies, and her detailed and valuable advice for my writing. I thank her for bringing me into interesting and novel areas of density functional theory-based molecular dynamics simulation and interface physics and chemistry. By communicating with her, I was implicitly and positively affected. She is rigorous in academic studies, optimistic and active, and has a wide range of interests. All these have kept in my heart and gave me greater confidence in my future work.

I am grateful to Prof. Dr. Friederike Schmid and Prof. Dr. Kurt Binder for their talks and guidance. I wish to thank Prof. Dr. Thomas Kühne, Dr. Giovanni Settanni, PD Dr. Peter Virnau, Dr. Hans Behringer and Prof. Dr. Thomas Speck at the institute for physics for leading me to the fundamental statistical physics and excellent lectures and discussions.

I thank Prof. Dr. Harvey Meyer at the institute for nuclear physics. I feel very honored to be a teaching assistant in his quantum field theory course. I thank Prof. Marie-Pierre Gaigeot at Université d'Evry val d'Essonne for useful discussions.

I am grateful to Dr. Rémi Khatib for helpful guidance on the programs for calculating the VSFG spectra. I thank Dr. Qi Shuanhu, Dr. Zhou Jiajia and Dr.Yu Fei for useful discussions. I would like to thank Leila Salimi, Isidro Lorenzo Geada, Santosh Kumar Meena and Anusha Lalitha, at the Institute for Physics, for their assistance. I thank Astrid Chase, Andreas Nussbaumer and Daniela Reibel for their enthusiastic and patient help.

The financial supports of the China Scholarship Council and TRR146 are gratefully acknowledged.

I thank Prof. Luo Honggang, Prof. Fang Haiping and Prof. Zhou Haijun for their great help in my study during my doctoral studies. The cooperation and discussions with Dr. Shi Guosheng, Dr. Shao Junming, Dr. Zhou Bo and Dr. Wang Chunlei have benefited me a lot.

I thank Prof. Jin Yuliang for his support, trust and teachings over the past two years.

I would like to thank the following teachers who have benefited me for life: Mr. Lu Yongliang, Mr. Li Yiyou, Mr. Yang Bing, Mr. Chen Jiexian, Mr. Chen Jiangen, Mr. Li Yiji, Mr. Wu Xiukui, Mr. Chen Wenfeng, Mr. Liao Changchun, Mr. Zhou Wende, Mr. Yan Zhengzhou, Prof. Huang Ruibin, Prof. Ran Qiyin, Prof. Huang Yong, Prof. Luo Zhiquan, Prof. Fan Silin, Prof. Tao Caide, Prof. Ren Weiyi, Prof. Tan Lei and Prof. Liu Yuxiao.

I am grateful to my parents Diao Yuhua and Huang Dehuai, and my brother Jialiang, for their care, understanding and support for me for decades. This thesis is dedicated to my grandparents Zhong Yuhtsing, Diao Sherngwern, Ma Suhfang, and Huang Zongyirn. I will always remember the kindness, open-mindedness, diligence and perseverance.

Contents

Declaration of Authorship **iii**

Abstract **vii**

Zusammenfassung **ix**

Acknowledgements **xi**

1 Introduction **1**

2 Methods **7**
- 2.1 Modeling interfaces with *ab initio* molecular dynamics 7
- 2.2 Density functional theory 8
- 2.3 Born-Oppenheimer and Car-Parrinello molecular dynamics 13
- 2.4 Vibrational density of states 15
- 2.5 Calculation of VSFG spectra from molecular dynamics simulations . . 16
  - 2.5.1 Nonlinear susceptibility of solution/vapor interfaces 16
  - 2.5.2 VSFG spectra from velocity auto-correlation functions 18
- 2.6 Definitions of HB population and correlation functions 21

3 Alkali nitrate clusters **27**
- 3.1 Cluster of nitrate and water molecules 27
- 3.2 Cluster of alkali metal cation and water molecules 28
- 3.3 Clusters of alkali nitrate and water molecules 29

4 VSFG spectroscopy of the water/vapor and solution/vapor interfaces **33**
- 4.1 VSFG spectra of the $LiNO_3$ solution/vapor interface 34
- 4.2 VSFG spectra of the alkali iodide solution/vapor interfaces 38

5 Hydrogen bond dynamics at the water/vapor interface **45**
- 5.1 Dynamical properties of H-bonds in bulk water and at the water/vapor interface 45
- 5.2 Instantaneous interfacial HB dynamics 49
- 5.3 Summary 54

6 Hydrogen bond dynamics in electrolyte solutions **57**
- 6.1 Ion-water HB dynamics at electrolyte/vapor interface 57
  - 6.1.1 Lithium nitrate solutions 57
  - 6.1.2 Alkaline iodide solutions 59
  - 6.1.3 Ion-water bond dynamics: breaking and reforming 61
- 6.2 Water-water HB dynamics within ions' solvation shells 63
- 6.3 Rotational anisotropy decay of water molecules at the water/vapor interface 66

6.4 Rotational anisotropy decay of water molecules in ions' solvation shells 71
6.5 Summary 73

7 Conclusions and Perspectives 75

A Calculation of nonlinear optical susceptibilities 79

B Computational details of the DFTMD simulations 85

C HB dynamics and instantaneous interfaces 87
C.1 Relations between HB lifetime distributions 87
C.2 Hydrogen bond population operator 90
C.3 Reorientation dynamics of water molecules at solution/vapor interfaces 91

D Structural characterization of water clusters and solutions 93
D.1 Water clusters 93
D.2 Solution/vapor interfaces 95
D.3 Free energy of the water separated and the contact ion pair 98
D.4 Classification of water molecules based on H-bonds 98

E Thickness of the interface of aqueous solutions 103
E.1 Interfacial HB dynamics 103
E.2 Thickness of the solution/vapor interfaces 104

Bibliography 107

List of Figures

2.1 The schematic diagram of the VSFG process which involves IR and Raman transitions. The $\nu = 0$, $\nu = 1$ levels denote the ground and the first excited state of the oscillator[207], respectively. The dashed line denotes a virtual electronic state in the Raman transition. 16
2.2 The representation of the bond (a) and the molecular (b) frameworks[114]. 20
2.3 Dynamics of $r_{\mathrm{OO}}(t)$ (top panel), cos$\phi(t)$ (middle panel), and $h(t)$ (bottom panel) for a typical HB in a water cluster. The dashed lines show the inter-oxygen distance boundary $r^{\mathrm{c}}_{\mathrm{OO}}$=3.5 Å (top panel) and criterion of cosine of H−O$\cdots$O angle cosϕ^{c} with ϕ^{c}=30° (middle panel), respectively. 22
2.4 The $c(t)$ for bulk water, as computed from the ADH (solid line) and AHD (dashed line) criterion of H-bonds. (a) the interchange processes are included; (b) The interchange processes are neglected. 22
2.5 Time dependence of $s(t)$ for bulk water. 24

3.1 Geometry optimized structure of clusters: (a) $[\mathrm{NO_3{\cdot}(H_2O)_3}]^-$; (b) $\mathrm{RNO_3(H_2O)_3}$; (c) $\mathrm{RNO_3(H_2O)_4}$; (d) $\mathrm{RNO_3(H_2O)_5}$ (R=Li, Na, K). More structural properties are given in Appendix D. 27
3.2 VDOS for the two OH bonds in w1 (Fig. 3.1 a) of $[\mathrm{NO_3{\cdot}(H_2O)_3}]^-$. . . 28
3.3 The cluster $[\mathrm{Li{\cdot}(H_2O)_4}]^+$. 28
3.4 RDFs $g_{\text{Li-O}}$ and $g_{\text{Li-H}}$ for the cluster $[\mathrm{Li{\cdot}(H_2O)_4}]^+$. 28
3.5 (A) The VDOS for the four water molecules (all water molecules) in the cluster $[\mathrm{Li{\cdot}(H_2O)_4}]^+$. (B) The VDOS for water molecules (three water molecules) bound to Li in the cluster $[\mathrm{Li{\cdot}(H_2O)_4}]^+$. 29
3.6 (a) RDF $g_{\text{R-O}}$ for clusters $\mathrm{RNO_3(H_2O)_3}$ (R=Li, Na, K); (b) RDF $g_{\text{O-H}}$ for clusters $\mathrm{RNO_3(H_2O)_3}$ and $[\mathrm{NO_3{\cdot}(H_2O)_3}]^-$ (no alkali metal cation, denoted as "R=-"). 30
3.7 VDOS for $\mathrm{H_2O}$ in clusters: (a) $\mathrm{LiNO_3(H_2O)_3}$, (b) $\mathrm{NaNO_3(H_2O)_3}$ and (c) $\mathrm{KNO_3(H_2O)_3}$. w1: $\mathrm{H_2O}$ bound to R and $\mathrm{H_2O}$; w2: $\mathrm{H_2O}$ bound to nitrate and $\mathrm{H_2O}$; w3: $\mathrm{H_2O}$ bound to R and nitrate. 30
3.8 VDOS for $\mathrm{H_2O}$ in clusters $\mathrm{LiNO_3(H_2O)}_n$: (a) $n = 3$; (b) $n = 4$; (c) $n = 5$. w1: $\mathrm{H_2O}$ bound to Li and $\mathrm{H_2O}$; w2: $\mathrm{H_2O}$ bound to nitrate and $\mathrm{H_2O}$; w3: $\mathrm{H_2O}$ bound to Li and nitrate; w4: $\mathrm{H_2O}$ bound to $\mathrm{H_2O}$; w5: $\mathrm{H_2O}$ only bound to Li. 31

4.1 The salty water interface of $\mathrm{LiNO_3}$ solution (left, top) and the water/vapor interface (left, bottom). The right panel shows that the Li^+ and the $\mathrm{NO_3^-}$ ions are separated by a water molecule at the salty interface. 33
4.2 Probability distributions of ions and water molecules for $\mathrm{LiNO_3}$ water interface along the normal direction. 34
4.3 (a) The $\Im\chi^{(2),\mathrm{R}}_{SSP}$ and (b) $|\chi^{(2),\mathrm{R}}_{SSP}|^2$ for water molecules at the interface of $\mathrm{LiNO_3}$ solution. 35

4.4 Experimental VSFG intensity of $LiNO_3$ solutions, compared with that of neat water[134]. 35

4.5 VDOS $g_z(\nu)$ for water molecules at the interface of $LiNO_3$ solution (solid line) and at the water/vapor interface (dashed line). (a): $d = 1$ Å; (b): $d = 2$ Å; (c): $d = 5$ Å. 36

4.6 VDOS for the six water molecules bound to NO_3^- at the $LiNO_3$ solution/vapor ($LiNO_3$/vapor) interface (salty water) and that for 15 water molecules at the top layer (d=1 Å) of the neat water. 36

4.7 Free energy profile with respect to the distance r between Li^+ and the nitrogen in NO_3^- in the cluster $LiNO_3(H_2O)_{30}$. A: configuration A where r is equal to 2.9 Å; B: configuration B where r is equal to 4.3 Å; C: the transition states. 37

4.8 Probability distribution $P(z)$, along the normal direction (z-axis), of Li^+, I^- and O in LiI solution/vapor interface. 39

4.9 RDFs for the LiI solution/vapor interface: (a) $g_{\text{Li-O}}$ and $g_{\text{Li-H}}$. The first two peaks of $g_{\text{Li-O}}$ and $g_{\text{Li-H}}$: 1.97 and 4.12 Å, and, 2.61 and 4.73 Å, respectively. (b) $g_{\text{I-O}}$ and $g_{\text{I-H}}$. The first two peaks of $g_{\text{I-O}}$ and $g_{\text{I-H}}$: 3.62 and 5.28 Å; and, 2.69 and 4.11 Å, respectively. 40

4.10 RDFs for the NaI solution/vapor interface: (a) $g_{\text{Na-O}}$ and $g_{\text{Na-H}}$. The first two peaks of $g_{\text{Na-O}}$ and $g_{\text{Na-H}}$: 2.41 and 4.55 Å, and, 3.02 and 4.96 Å, respectively. (b) $g_{\text{I-O}}$ and $g_{\text{I-H}}$. The first two peaks of $g_{\text{I-O}}$ and $g_{\text{I-H}}$: 3.59 and 5.04 Å; and, 2.63 and 4.15 Å, respectively. 40

4.11 RDFs for the KI solution/vapor interface: (a) $g_{\text{K-O}}$ and $g_{\text{K-H}}$. The first two peaks of $g_{\text{K-O}}$ and $g_{\text{K-H}}$: 2.84 and 4.71 Å, and, 3.40 and 5.51 Å, respectively. (b) $g_{\text{I-O}}$ and $g_{\text{I-H}}$. The first two peaks of $g_{\text{I-O}}$ and $g_{\text{I-H}}$: 3.59 and 5.43 Å; and, 2.65 and 4.10 Å, respectively. 41

4.12 (a) $\Im\chi_{SSP}^{(2),\text{R}}$ and (b) $|\chi_{SSP}^{(2),\text{R}}|^2$ of the LiI solution/vapor (solid line) and the water/vapor (dashed line) interface. The data for the water/vapor interface is calculated from the DFTMD simulation for the water interface with the same thickness (5 Å) (the same for Fig.s 4.13 and 4.14). 41

4.13 (a) $\Im\chi_{SSP}^{(2),\text{R}}$ and (b) $|\chi_{SSP}^{(2),\text{R}}|^2$ of the NaI solution/vapor (solid line) and the water/vapor (dashed line) interface. 41

4.14 (a) $\Im\chi_{SSP}^{(2),\text{R}}$ and (b) $|\chi_{SSP}^{(2),\text{R}}|^2$ of the KI solution/vapor (solid line) and the water/vapor (dashed line) interface. 42

4.15 $\Im\chi_{XXZ}^{(2),R}$ and $\Im\chi_{YYZ}^{(2),R}$ spectra for the KNO_3 solution/vapor interface. . . 43

5.1 Partial RDFs of the simulated bulk water. 46

5.2 Time dependence of (a) $n(t)$, $c(t)$ and (b) $k(t)$ for *bulk* water. 46

5.3 Time dependence of (a) $n(t)$, $c(t)$ and (b) $k(t)$ for the water/vapor *interface*. 46

5.4 Time dependence of $k(t)$ for (a) bulk water and (b) the water/vapor interface. 47

5.5 Time dependence of $k(t)$ for the water/vapor interface, according to Eq. 2.61. 47

5.6 Time dependence of $n(t)$ for bulk water and the water/vapor interface from the (a) ADH and (b) AHD criteria. 48

5.7 A slab of water (128 water molecules are included) with the instantaneous interface represented as a blue mesh on the upper and lower phase boundary. The normal is along the z-axis and the parameter d is the thickness of the interfacial layer. The grey surfaces are obtained by translating the interfaces to the interior of the slab along the z-axis (or the opposite direction) by d. 50

5.8 The $c^{(\mathrm{s})}(t)$ for the instantaneous interfacial H-bonds with different thicknesses, as computed from the (a) ADH and (b) AHD criteria through the IHB method. 51

5.9 The $c(t)$ for the instantaneous interfacial H-bonds with different thicknesses, as computed from the (a) ADH and (b) AHD criteria. The IMS method is used, and the sampling rate is 1/4 per ps. 52

5.10 Dependence of (a) the reaction rate constants k and k' and (b) the HB lifetime τ_{HB} on the interface thickness d, obtained by the IHB and the IMS method, respectively. The corresponding k, k' and τ_{HB} in bulk water are drawn with dashed lines as references. In panel a, the k of bulk water is represented by a *black dashed* line, and the k' of bulk water by a *blue dashed* line; in panel b, the τ_{HB} of bulk water by a *black dashed* line. The ADH criterion of H-bonds is used and the least square fits are carried on the time region 0.2 ps $< t <$ 12 ps. 52

6.1 Distribution of ions at the $\mathrm{LiNO_3}$/vapor interface. (A) Distances between ions and one of the instantaneous surfaces (blue meshes) for a slab of aqueous $\mathrm{LiNO_3}$ solution. (B) Density distribution of the $\mathrm{Li^+}$–surface and $\mathrm{NO_3^-}$–surface distances at the $\mathrm{LiNO_3}$/vapor interface. The horizontal axis represents the distance between the ion and the instantaneous surface, which is defined in Eq. 6.1. The *distance* refers specifically to $d_{\mathrm{X},1}$, the distance between the ion X and one of the instantaneous surfaces. Zero distance denotes the instantaneous surface of the interfacial system of $\mathrm{LiNO_3}$ solution. 58

6.2 Time dependence of (a) $c(t)$ and (b) $\ln s(t)$ of all W–W and N–W bonds for the slab of $\mathrm{LiNO_3}$ solution, as computed from the ADH (solid line) and AHD (dashed line) criteria of H-bonds. The W–W bonds represents H-bonds between all pairs of water molecules in the entire slab. 58

6.3 Density distribution of ions at the LiI/vapor and NaI/vapor interfaces. (A) The $\mathrm{Li^+}$–surface and $\mathrm{I^-}$–surface distances. (B) The $\mathrm{Na^+}$–surface and $\mathrm{I^-}$–surface distances. 59

6.4 (A) Distances between ions and one of the instantaneous surfaces (grey meshes) for a slab of the KI solution. (B) Density distribution of the $\mathrm{K^+}$–surface and $\mathrm{I^-}$–surface distances at the KI/vapor interface, respectively. 60

6.5 Time dependence of $s(t)$: (a) the LiI/vapor interface; (b) the NaI/vapor interface. The insets show the plots of $\ln s(t)$. 61

6.6 The $s(t)$ of W–W and N–W bonds at the $\mathrm{LiNO_3}$/vapor interface. The inset is the plot of $\ln s(t)$. The results are calculated for the temporal resolution $t_{\mathrm{t}} = 1$ fs. For the definition of t_{t} see Appendix E. 62

6.7 Time dependence of $c(t)$ of $\mathrm{I^-}$–water ($\mathrm{I^-}$–W) and W–W bonds: (a) ADH; (b) ADH. A base-10 log scale is used for the x-axis. 62

6.8 Time dependence of $s(t)$ of $\mathrm{I^-}$–water ($\mathrm{I^-}$–W) and W–W bonds. 63

6.9 RDFs for the alkali nitrate solutions. 64

6.10 The $c^{(k)}(t)$ for the second solvation shell H-bonds as computed from different HB definitions: (a) ADH; (b) AHD. The r_{shell} is set to be 5.0 and 4.0 Å for Li^+ an Nitrate O, respectively. The $c(t)$ (dashed line) for bulk water is also plotted in panel a and b, respectively. 65
6.11 The $c^{(k)}(t)$ for the second solvation shell H-bonds as computed from different HB definitions: (a) ADH; (b) AHD. The r_{shell} is set to be 5.0 and 6.5 Å for Li^+ an I^-, respectively. The $c(t)$ (dashed line) for bulk water is also plotted in panel a and b, respectively. 66
6.12 (A) Time dependence of $C_2(t)$ for water molecules at the water/vapor interface with different thickness in the range of 1 Å to 6 Å. (B) The dependence of decay time τ_2 on the thickness d in the exponential fitting of $C_2(t)$ for water molecules at the water/vapor interface. . . . 67
6.13 Anisotropy decay of OH bonds in water molecules at the $LiNO_3$/vapor interface. The water molecules considered are in an instantaneous layer with $d = 2$ Å. 68
6.14 Distribution $P(n)$ of the number of H-bonds per OH group at instantaneous layers with thickness d. The red (black) line is for the $LiNO_3$/vapor (water/vapor) interface. 69
6.15 Distribution $P(n)$ of the number of H-bonds per OH group at instantaneous layers with thickness d ($d = 1, \cdots, 6$ Å). The red (black) line is for the interfaces (bulk) phase. 69
6.16 Time dependence of $C_2(t)$ for OH bonds at the LiI/vapor (solid line) and the water/vapor (dashed line) interface. The water molecules considered are in instantaneous layer with $d = 2$ Å. 70
6.17 Distribution $P(n)$ of the number of H-bonds per OH group at instantaneous layers with thickness d. The red (black) line is for the LiI/vapor (water/vapor) interface. 70
6.18 Distribution $P(n)$ of the number of H-bonds per OH group at instantaneous layers with thickness d ($d = 1, \cdots, 6$ Å). The red (black) line is for the interfaces (bulk) phase. 71
6.19 The $C_2(t)$ for water molecules in the solvation shell of Li^+, Na^+, K^+, I^- and NO_3^- ions at alkali nitrate (alkali iodide) solution/vapor interfaces. For comparison, the $C_2(t)$ for bulk water (black line) is shown. 72
6.20 Dependence of τ_2 on the radius of the first solvation shell of molecules and ions (H_2O, Li^+, Na^+, K^+, I^- and NO_3^- ions) in the slab of alkali nitrate (iodide) solutions. 73

C.1 The H-bonds with lifetime τ in a certain configuration. At time t, we assume that there are totally n_{tot} H-bonds can be detected, and n_τ H-bonds are of lifetime τ, therefore, the fraction of H-bonds that have the lifetime τ in the configuration at time t is $P_{\text{tc}}(\tau) = n_\tau / n_{\text{tot}}$. Let τ take all the values in the interval $[0, \infty]$, we can get the HB lifetime distribution $P_{\text{tc}}(t)$. 88

D.1 The nitrate O (ON)–water O (OW) and nitrate O–water H (HW) RDFs for $[NO_3{\cdot}(H_2O)_3]^-$. Peaks for the former are 1.93, 2.95 and 3.95 Å, and for the later are 2.95 and 4.80 Å. 95
D.2 The VDOS $g(\nu)$ for water molecules in the cluster $[NO_3{\cdot}(H_2O)_3]^-$ at 100 K. 95
D.3 The dipole orientation distribution of water molecules at the water/-vapor and the $LiNO_3$ solution/vapor interfaces. 96

D.4 The $c^{(k)}(t)$ of W–W bonds in the solvation shell of (a) cations and (b) I^- at the interfaces of 0.9 M LiI, NaI and KI solutions, respectively. As a reference, the $c(t)$ for the 1-Å water/vapor interface (Paragraph 5.2 in Chapter 5) and bulk water are also shown. 96

D.5 RDFs $g_{\text{Li-OW}}(r)$, $g_{\text{Li-HW}}(r)$, $g_{\text{ON-OW}}(r)$ and $g_{\text{ON-HW}}(r)$ in bulk $LiNO_3$ solution. 97

D.6 RDFs $g_{\text{Li-OW}}(r)$, $g_{\text{Li-HW}}(r)$, $g_{\text{I-OW}}(r)$ and $g_{\text{I-HW}}(r)$ for the LiI/vapor interface. 97

D.7 (a) RDFs $g_{\text{X-O}}(r)$($X=Li^+$, Na^+, K^+) and (b) the coordination number of Li^+ (Na^+, K^+) ions at the interfaces of LiI (NaI, KI) solution. The coordination numbers are n_{Li^+}=4, n_{Na^+}=5 and n_{K^+}=6. 98

D.8 Four types of water molecules at the LiI/vapor interface, regarding the HB environments: (a) DDAA; (b) DDA; (c) D′AA; (d) D′AA. The cyan balls denote I^- ions. 99

D.9 Time dependence of $C_2(t)$ for DD′A, DD′AA, and D′AA water molecules at the LiI/vapor interface. 100

E.1 The calculated $|\chi^{(2),\text{R}}_{SSP}|^2$, of water molecules at the $LiNO_3$ solution/vapor interfaces with different thickness. 105

E.2 The calculated $|\chi^{(2),R}_{SSP}|^2$, of water molecules at the LiI solution/vapor interface with different thickness. 105

E.3 The function $s(t)$ and its logarithm for water-water H-bonds at interfaces with different thickness in the LiI solution. 105

E.4 The resolution dependence of the continuum lifetime τ_{HB} of water–water H-bonds at interfaces of different alkali-iodine solutions at 330 K, calculated for six temporal resolutions (t_{t})[335–337]. 106

List of Tables

3.1 The average length r_a of H-bonds (Li-O bonds) in the cluster $LiNO_3(H_2O)_3$. 30

4.1 Peaks of $g_{\text{Li-O}}$ and $g_{\text{Li-H}}$ for the LiI solution. (unit: Å, the same for Tables 4.2 and 4.3) 39
4.2 Peaks of $g_{\text{Na-O}}$ and $g_{\text{Na-H}}$ for the NaI solution. 40
4.3 Peaks of $g_{\text{K-O}}$ and $g_{\text{K-H}}$ for the KI solution. 40

5.1 The forward and backward rate constants, k and k', for bulk water (bulk) and the water/vapor interface (w/v). We carried on the short time region 0.2 ps $< t <$ 2 ps. The unit for k (k') is ps^{-1}, and that for τ_{HB} $(= 1/k)$ is ps. (Same for Table 5.2.) 48
5.2 The forward and backward rate constants, k and k', for bulk water (bulk) and the water/vapor interface (w/v). We carried on the long time region 2 ps $< t <$ 12 ps. 49
5.3 The k and k' for the interfacial HB dynamics of the water/vapor interface, through the IHB method, with the ADH criteria. We carried on the longer time region 0.2 ps $< t <$ 12 ps (same below). 53
5.4 The k and k' for the interfacial HB dynamics of the water/vapor interface through the IHB method, with the AHD criteria. 54
5.5 The k and k' for the interfacial HB dynamics of the water/vapor interface through the IMS method, with the ADH criteria. 54
5.6 The k and k' for the interfacial HB dynamics of the water/vapor interface through the IMS method, with the AHD criteria. 54

6.1 The average of the continuum HB lifetimes $\langle \tau_{\text{a}} \rangle = \int_0^\infty s(t)dt$ (unit: ps) in the first solvation shell of I^- ion and of alkali metal ion at the interface of three 0.9 M alkali iodide solutions. 60
6.2 The relaxation time τ_{R} (unit: ps) of the $c(t)$ for the interface of the LiI (NaI) solutions. 61
6.3 Dynamical properties of I^-–water and N–W bonds within the ADH (AHD) criterion. 63
6.4 The radius r of the first solvation shells and corresponding relaxation times τ_2 at the interface of alkali nitrate (alkali iodide) solutions. For NO_3^-, we use the O–OW distance, instead of the N–OW distance to define the radius of the ion's solvation shell. 72
6.5 The peaks' position (unit: Å) of RDFs for the LiI/vapor, the $LiNO_3$/vapor and the water/vapor interfaces (see Table D.5 and D.6). 73

C.1 The k and k' for bulk water. We carried on the short time region 0.2 ps $< t <$ 2 ps. The unit for k (k') is ps^{-1}, and that for τ_{HB} $(= 1/k)$ is ps. The $h(t)$ is bond-based. 90

C.2 The k and k' for bulk water. We carried on the long time region 2 ps $< t <$ 12 ps. The unit for k (k') is ps^{-1}, and that for τ_{HB} ($= 1/k$) is ps. The $h(t)$ is bond-based. 91
C.3 The fitted parameters of anisotropy decay of water molecules at the LiI (NaI, KI) solution/vapor interface according to Eq. C.17 for the time range [0,10] ps. The standard errors: $\delta A_i \sim 0.01$, $\delta\tau_{2,i} \sim 0.1$ ps ($i = 1, 2$). 91
C.4 The fitted (single exponential) parameters of anisotropy decay of water molecules at the LiI (NaI, KI) solution/vapor interface according to Eq. C.17 for the time range [0,10] ps. The standard errors: $\delta A \sim 0.01$, $\delta\tau_2 \sim 0.1$ ps. 92

D.1 Hydrogen bond lengths r_a in $[NO_3{\cdot}(H_2O)_3]^-$. 93
D.2 Parameters of water molecules and H-bonds in $[NO_3{\cdot}(H_2O)_3]^-$. 93
D.3 Structural parameters of $RNO_3(H_2O)_3$ from geometry optimization. . 93
D.5 Lengths of H-bonds in $[NO_3{\cdot}(H_2O)_3]^-$. Indices of H atoms: H6, H7 in w1; H9, H10 in w2; and H12, H13 in w3. 94
D.4 Parameters of $RNO_3(H_2O)_3$ at 300 K, obtained from the averaging during a DFTMD trajectory. For $RNO_3(H_2O)_3$, R_{OH} and R'_{OH} denote the lengths of O-H bonds in which H atoms is H-bonded and is free, respectively. 94
D.6 Biexponential fitting of $C_2(t)$ for water molecules in the LiI solution. The relative standard errors: $\Delta A/A \leq 10^{-2}$, $\Delta\tau_2/\tau_2 \leq 3 \times 10^{-2}$. . . . 101

List of Abbreviations

AIMD	*ab initio* **M**olecular **D**ynamics
BLYP	**B**eck-**L**ee-**Y**ang-**P**arr
BOMD	**B**orn-**O**ppenheimer **M**olecular **D**ynamics
CPMD	**C**ar-**P**arrinello **M**olecular **D**ynamics
DFT	**D**ensity **F**unctional **T**heory
DFTMD	**D**ensity **F**unctional **T**heory-based **M**olecular **D**ynamics
EDA	**E**lectric **D**ipole **A**pproximation
GGA	**G**eneralised **G**radient **A**pproximation
GPW	**G**aussian and **P**lane **W**aves
H-	**H**ydrogen
HB	**H**ydrogen **B**ond
HD	**H**eterodyne **D**etected
HK	**H**ohenberg-**K**ohn
IHB	**I**nterfacial **H**ydrogen **B**ond
IMS	**I**nterfacial **M**olecule **S**ampling
KS	**K**ohn-**S**ham
LDA	**L**ocal **D**ensity **A**pproximation
MD	**M**olecular **D**ynamics
MLWF	**M**aximally-**L**ocalized **W**annier **F**unctions
MP2	**M**oller-**P**lesset **P**erturbation
PBE	**P**erdew-**B**urke-**E**rnzherhof
PS	**P**hase-**S**ensitive
RDF	**R**adial **D**istribution **F**unction
SHB	**S**olvation shell **H**ydrogen **B**ond
SCF	**S**elf **C**onsistent **F**ield
VACF	**V**elocity **A**uto-**C**orrelation **F**unction
VDOS	**V**ibrational **D**ensity **O**f **S**tates
VSFG	**V**ibrational **S**um-**F**requency **G**eneration
XC	e**X**change and **C**orrelation

Physical Constants

Avogadro constant	$N_\mathrm{A} = 6.022\ 140\ 76\ \times 10^{23}$ /mol (exact)
Boltzmann constant	$k_\mathrm{B} = 1.380\ 649\ \times 10^{23}\ \mathrm{J\,K^{-1}}$ (exact)
elementary charge	$e = 1.602\ 176\ 634\ \times 10^{-19}$ C (exact)
electron mass	$m_\mathrm{e} = 9.109\ 381\ 887\ \times 10^{-31}$ kg
molar gas constant	$R = 8.314\ 459\ 8\ \mathrm{J\ mol^{-1}\ K^{-1}}$,
proton mass	$m_\mathrm{p} = 1.672\ 621\ 581\ \times 10^{-27}$ kg
Planck constant	$h = 6.626\ 070\ 15\ \times 10^{-34}$ J s (exact)
reduced Planck constant	$\hbar = 1.054\ 571\ 817\ \times 10^{-34}$ J s
speed of light in vacuum	$c = 299\,792\,458\,\mathrm{m\,s^{-1}}$ (exact)

List of Symbols

Z_X	atomic number of atom X
$\mathbf{R}$	atomic coordinates
τ_a	average lifetime of H-bonds: $\langle\tau_\mathrm{a}\rangle = \int_0^\infty tP_\mathrm{a}(t)dt$
μ_i	chemical potential of component i
κ_i	decay rate of $C_2(t)$
n_X	coordination number for ion X
δ_1	difference between the first peaks' positions of the RDFs g_{X-O} and g_{X-H}
$\mathbf{M}$	dipole moment
$\mu^{i,l,\epsilon}$	dipole moment of the bond ϵ of the i-th water molecule in the lab frame
A	dipole polarizability (tensor)
D	direction cosine matrix
r	distance
μ	electric dipole vector
ϕ	electric potential
$\mathbf{E}$	electric field strength
$n(\mathbf{r})$	electron density
H_e	electronic many-body Hamiltonian
$E_\mathrm{I}(\mathbf{R})$	energy of the nuclei
$V(\mathbf{r})$	external potential
V_ee	electron-electron repulsion energy
$T[n]$	electronic kinetic energy
$E^{(2)}_\mathrm{disp}$	empirical two-body dispersion correction of energy
$E^{(3)}_\mathrm{disp}$	empirical three-body nonadditivity dispersion correction of energy
$E^\mathrm{XC}[n]$	Exchange correlation energy functional
ΔF_{AB}	free energy difference between configuration A and B
F_A	free energy of configuration A
$L_{\eta\kappa}$	Fresnel coefficients
ω_SFG	frequency of the sum-frequency generation beam
ω_vis	frequency of the incident visible beam
ω_IR	frequency of the incident infrared beam
V_H	Hartree potential of electrons
$h(t)$	HB population operator
$h^{(d)}(t)$	HB population operator (it is 1 if the tagged pair are closer than r^c_OO)
$H(t)$	HB population operator (continuously)
$C_\mathrm{HB}(t)$ (or $c(t)$)	HB population auto-correlation function
ω_I	highest nuclear phonon frequency
θ	H-O-H angle in a water molecule, or polar angle of a molecule
β	hyperpolarizability, or reciprocal temperature
$h^{(s)}(t)$	interfacial HB population operator
$j(t)$	integrated flux departing the HB configuration space at time t
I_SFG	intensity of the sum-frequency generation beam
I_vis	intensity of the incident visible beam

I_{IR}	intensity of the incident infrared beam
r_{OO}	interoxygen distance
δt	inverse sampling frequency
$E^{\mathrm{KS}}[n]$	Kohn-Sham energy functional
ω_{e}	the lowest electronic frequency
$r^{\mathrm{c}}_{\mathrm{OO}}$	the maximum value of the interoxygen distance (in the definition of HB)
ϕ^{c}	the maximum value of the angle between the O–O axis and one of the O–H bonds (in the definition of HB)
N	number of water molecules
n	number of H-bonds per OH group
R_{OH}	O-H length in water molecule
$C_2(t)$	orientational anisotropy decay
Z	partition function
α	polarizability tensor
$\alpha^{i,l,\epsilon}$	polarizability of the bond ϵ of the i-th water molecule in the lab frame
$P_a(t)$	probability distribution of the first HB breaking in time t
$C_z(t)$	projected velocity auto-correlation function along z-axis
$x^{\mathrm{l}}, y^{\mathrm{l}}, z^{\mathrm{l}}$	position coordinates in the lab frame
$x^{\mathrm{m}}, y^{\mathrm{m}}, z^{\mathrm{m}}$	position coordinates in the molecular frame
$x^{\mathrm{b}}, y^{\mathrm{b}}, z^{\mathrm{b}}$	position coordinates in the bond frame
$g_z(\nu)$	projected VDOS for selected atoms along z-axis
$g_{\mathrm{A–B}}$	radial distribution function
k	rate constant of breaking a HB
k'	rate constant of reforming a HB
r_{X}	ratio of number of X to that of H_2O among neighbors of a water molecule
θ_{SFG}	reflected angle of SFG beam w.r.t. the normal direction in the medium
$k(t)$	reactive flux
τ_{R}	relaxation time of HB population operator correlation function
$P_2(x)$	the second Legendre polynomial
$\chi^{(2),\mathrm{R}}$	second-order resonant susceptibility
$\chi^{(2),\mathrm{NR}}$	second-order nonresonant susceptibility
E_{KSDFT}	self consistent KS energy
$\Delta\nu'$	shift of vibrational frequency
$h^{\mathrm{k,X}}(t)$	solvation shell HB population operator
ν_i	stoichiometry of ion i
Γ_i	surface excess of component i
$K_{\mathrm{p,X}}$	surface/bulk molar concentration ratio of ion X
γ	surface tension
$S_{\mathrm{HB}}(t)$ (or $s(t)$)	survival probability of HB
t_{t}	temporal resolutions for calculating HB dynamics
d	thickness of layer of interface (model)
τ	time for switching allegiance of a HB
$\hat{\mu}(t)$	unit vector of the transition dipole
$g(\nu)$	VDOS for selected atoms
z_i	valence of species i
$\mathbf{v}$	velocity of an atom
$C(t)$	velocity auto-correlation function
ν	vibrational frequency, or vibrational quantum number

To my parents.

Chapter 1

Introduction

Interfaces of aqueous electrolyte solutions are ubiquitous in biology, atmosphere, chemistry, man-made systems and industrial processes[1–14]. The aqueous interface appears in different forms, such as sprays, aerosols, nanoscopic and microscopic water droplets, water/vapor interfaces. Many phenomena, such as solvation[15], adsorption[16], bubble formation[17–21], occur at aqueous interfaces[22, 23].

Compared to bulk atoms or molecules, interfacial atomic or molecular layers generally have very different properties. At the water/vapor interface, the hydrogen bond (HB) network is sharply terminated, which makes the interface more heterogeneous than bulk water[24]. The statistical distribution of the orientation of water molecules at the interface is different from that of bulk water, and thus the local structure, light absorption, molecular rotations and diffusion are different at the interface[25]. Experiments also demonstrate that there exists an on-water catalysis effect, which means that some chemical reactions take place much faster on water surface with respect to those in bulk phase[26–28]. Molecular simulations also show that the effective dielectric constant of interfacial water is significantly lower than its bulk value, and it also depends on the curvature of the interface[29]. Overall, aqueous/vapor interfaces provide a unique environment for many physical, chemical and biological processes.

Ions at interfaces Due to the presence of ions, many properties of the interface are significantly affected. For example, the stability of cell membranes is affected by the distribution of counter-ions[30]; the free energies of ions across liquid surfaces are essential to solvent extraction processes and phase transfer catalysis[31]; the uptake of pollutants by water droplets in cloud depends on the ion distribution at the aqueous liquid/vapor interfaces. The surface tension of the water/vapor interface changes with the addition of electrolytes in water[32]. In most alkali and inorganic salt solutions, the surface tension increases as the concentration of the electrolyte increases; however, in most acid solutions, the surface tension decreases as the concentration of the acid increases. It was also observed that there exists specific ion effect. The most typical example is that the solvation structure surrounding the more polarizable I^- anion at the interface is more anisotropic than the solvation structure around the less polarizable Cl^-.

Ions also modify HB dynamics at the interface[22, 33, 34]. The microscopic structure of water is determined by O-H$\cdots$O bonds between the hydroxyl group and O atoms of neighboring molecules. Because of the hydrogen (H-) bonding, electrostatic force and dispersion forces, at aqueous interfaces there exists an interface-specific bonding network[35–41], which is different from H-bonding network in corresponding bulk liquid[42, 43]. Experiments have shown that, the presence of ions in aqueous electrolyte solutions may significantly change the property of the H-bonding network.

The formation of H-bonding network indicates a reduction in the orientational degree of freedom, an enhancement in the local structure of water around the solute, or change of entropy[44–46].

A clear microscopic understanding of interfaces of aqueous salt solutions is also essential to further energy and human development. For example, the chemical potential difference of the interface between two seawaters with different salt concentrations can provide new energy for mankind[47, 48]. Many ocean and atmospheric reaction processes, including many key climate properties such as surface activity, solubility and interfacial molecular structure, influence climate[49, 50].

Therefore, understanding the equilibrium properties and dynamics of the electrolyte solution interfaces is important in designing and controlling the chemical reactions at liquid interfaces.

Methods to selectively probe the interface For obtaining the information on the specific mechanism underlying the interfacial phenomena, and gaining molecular-level understanding of the interfacial water organization and ions distribution at interfaces, we need detection methods with interface selectivity.

Experimentally, the vibrational sum-frequency generation (VSFG) spectroscopy is the most frequently used and powerful interface analytical tool[51–53]. It is based on a simple idea that optical responses of a surface and bulk of a medium follow different selection rules. The VSFG spectroscopy uses a second-order nonlinear optical process and the resulting signal is very sensitive to surface ions and molecules of a sub-monolayer level[54–58]. For any material exhibiting inversion symmetry, the experimentally recorded signal, namely nonlinear susceptibility $\chi^{(2)}$ is identically 0, and VSFG is precluded[59]. This result implies that, the VSFG process is forbidden in any centrosymmetric bulk medium[60], such as isotropic liquids and glasses, but it is allowed at interfaces because of the broken inversion symmetry[61]. The advantage of VSFG is its wide applicability to almost every interface which lack a center of inversion, as long as light can reach them. Conventional VSFG spectroscopy detect the intensity of VSFG light, i.e., it gives only the absolute square $|\chi^{(2)}|^2$ of the nonlinear susceptibility[53, 62, 63]. The phase sensitive (PS-)VSFG[64] and heterodyne detected (HD-)VSFG technology[65] permit to overcome this shortcoming. The most important feature is that they can measure complex $\chi^{(2)}$ spectra. In other words, they can provide $\Re\chi^{(2)}$ and $\Im\chi^{(2)}$, or the amplitude and phase of the components of $\chi^{(2)}$. Since $\Im\chi^{(2)}$ spectra shows an absorptive line shape that directly represents a vibrational resonance, it can be interpreted more straightforwardly[66]. The sign of $\Im\chi^{(2)}$ is also closely related to the orientation of molecules at the interface[67–69]. Recently, broadband HD-VSFG spectroscopy with a high phase stability has been developed and has been used to study the polar orientation and HB structure of interfacial water[70, 71].

Therefore, VSFG spectroscopy can be used to probe many types of interfaces, namely, liquid-liquid and solid-liquid interfaces[6, 54, 72–77], metal and semiconductor surfaces[78, 79], and to determine the molecular orientation at the aqueous solution/vapor interfaces. It allows to detect intramolecular vibrational modes, and molecular orientation by detecting polarization dependence of the VSFG signals[80]. The VSFG spectra suggest that the interfacial H-bonding between water molecules is changed by the presence of salt, especially the anions[33]. Molecular-level properties of interfacial materials arising from interactions between water and minerals, such as swelling, wetting, hydrodynamics can also be studied by the VSFG spectroscopy[81].

On the comuputational side, molecular dynamics (MD) simulations are also powerful tools in the microscopic study of interfaces, allowing a straightforward investigation of structure and dynamics of molecules at interfaces[54]. They gives insights into direct interactions between ions and water, and have been used for calculating properties, such as the depth profile of ion concentrations of interfaces[82, 83], and the VSFG spectra of electrolyte solution surfaces[57, 76, 84, 85]. Polarizable force field have been widely used to calculate VSFG spectra[86–89], however, they lack of transferability when complex interfaces are considered. To overcome this problem, *ab initio* MD (AIMD) simulations[90–92] can be used. In particular density functional theory-based molecular dynamics (DFTMD) simulations[90, 93] can provide the dynamic trajectory of the liquid interface, from which macroscopic properties, such as distribution and orientation of ions, as well as the VSFG spectra can be calculated. The advantage of AIMD is that it does not require a priori parameterization and it is capable to include polarization effects[94], also including electronic polarization. AIMD at the gradient corrected level, and also including dispersion corrections[95–99] has been shown to provide an accurate description of vibrational properties at interface[100–112]. Recently, progresses in the calculations of VSFG spectra have permitted to reduce their computational cost and to investigate more complex systems[113, 114].

Selected experimental data and simulation works The ions propensity for the liquid/vapor interface, as well as their influence on water's HB network are of special interest to the atmospheric chemistry community.Various ions play critical roles in the kinetics and mechanisms of heterogeneous chemical reactions at the water/vapor interface of atmospheric aerosols. A first question which has been subject of intensive investigation regards the ions distribution in the proximity of an interface for the different ionic species.

As early as the beginning of the last century, Heydweiller discovered that anions affected the surface tension significantly and the magnitude of the variation of the surface tension follows the same sequence discovered by Hofmeister earlier[115], i.e., namely $CO_3^{2-} > SO_4^{2-} > F^- > Cl^- > Br^- > NO_3^- > I^- > ClO_4^- > SCN^-$[116–121]. Langmuir[122] was the first to attempt a theoretical explanation of the physical mechanism for the increase of the surface tension by added electrolytes. The adsorption, or surface excess per unit area, of electrolytes can be described by the well-known Gibbs adsorption equation, which relate surface tension, surface excesses and chemical potentials for a system of any number of components. Using the Gibbs adsorption equation, Langmuir concluded that this phenomenon was a consequence of ion depletion near the water/vapor interface, i.e., the *increase* in surface tension implies a *deficiency* of solute in the surface layer[123], and estimated the thickness of the depleted layer in the range 3.3 to 4.2 Å. Later, MD simulations have shown that more polarizable anions (e.g., larger halide anions) can be present in the surface region[82, 83]. Tian and coworkers[69] have also predicted that some ions, such as I^- and Br^-, could accumulate at the interface. These seemingly contradictory conclusions with the Gibbs adsorption equation mean that our understanding of the interface is still incomplete.

The use of surface specific vibrational spectroscopy techniques has permitted to elucidate some aspects of surface HB structure for water in the presence of ions[124, 125]. Raymond and Richmond[33] have shown, using VSFG, that anions are present at the surface of alkali halide salt solutions, such as NaF, NaCl, NaBr and NaI. Their experiments showed that the changes of the interfacial H-bonding depend on the anion's species, indicating the presence of anions in the interfacial region. The frequency shifts in the peaks of the VSFG spectra display the structure-breaking characteristics of larger halogen ions.

The influence of molecular ions such as nitrate (NO_3^-), sulfate and carbonate ions has also been analyzed, but proved more elusive than that for halide solution[126, 127]. Recently considerable attention has been given to nitrate in aqueous phase for their ubiquitous and diverse role in atmospheric aerosols, polluted water, and the remote troposphere[50, 124, 128–133]. Hua *et al.*[134] have recently measured the VSFG spectra of water/vapor interface of $LiNO_3$ salt solutions in the OH stretching region using HD-VSFG spectroscopy[135–137]. It has been suggested that the depletion, and in some cases the enhancement of peaks in the spectra of $LiNO_3$ solutions are caused by the presence of ions at the interface. A similar behaviour had been observed for the interface of $NaNO_3$ and $Mg(NO_3)_2$ solutions[124, 134]. On the other hand the small cations should have little surface propensity. It has also been argued that the positive electric field found at the interface of NaCl, NaI and $NaNO_3$ salt solutions is due to the formation of an ionic double layer between anions located near the surface and their counter-cations (e.g. Na^+) located further below. In PS-VSFG experiments the magnitude of the induced change in the $\Im\chi^{(2)}$ spectra comparatively to that of the neat water suggested that NO_3^- has a surface propensity just in between I^- and Cl^-[138, 139].

This thesis DFTMD simulations can provide detailed information on the structure and dynamics of water in these simple but non-the-less still puzzling systems: alkali metal nitrate and alkali metal halide solutions[140].

As first we provide a molecular interpretation of the main characteristics of the VSFG spectra of the electrolytic solution/vapor interfaces. We focus on nitrate solutions and alkali halide solutions because these anions have a significant impact on the structure and dynamics of the interface. We have used AIMD to provide a realistic description of the electrolytic solution/vapor interface and calculated the VSFG spectra. The nonlinear susceptibility of solution/vapor interfaces is obtained by the Fourier transform (FT) of the time correlation function of the dipole moment and the polarization tensor. This requires, for each step of DFTMD, the calculation of the dipole moment and polarization tensor of molecules in the interface. To simplify the calculation, we express the correlation function as the autocorrelation function of the velocity of atoms. Accordingly, we calculated the VSFG spectrum of the interface for $LiNO_3$ solution, which resulted to be consistent with the experiment. In addition to the spectra interpretation, we also provide the distribution of anions and cations relative to the interface: nitrate ions are located in the uppermost layer of the interface, and alkali metal ions are located in the layer below and form with the anion a water separated ion pair. Using free energy calculations, we also proved that this water-separated ion configuration is more stable than the contact ion pair.

The adsorption of halide anions, in both surface tension experiments and MD simulations, follows the Hofmeister series. These results suggest that heavier halide anions have a similar effect to nitrate ions on the structure and dynamics of the water/vapor interface. To verify the experimental suggestion, we also simulated the interface of lithium iodide, sodium iodide and potassium iodide solutions using the DFTMD simulation, and we calculated the corresponding VSFG spectra. The results show some common characteristics: in all the cases, the H-bonded OH-stretching peak of $|\chi^{(2),R}|^2$ is blue-shifted, indicating that the water molecules at the interfaces are forming weaker H-bonding. In addition, we also confirmed that the vibrational properties of interfaces of water and aqueous electrolyte solutions cannot be obtained from small water cluster containing the same ion pair.

A second aspect which we have investigated in the thesis is the HB dynamics. HB dynamics of aqueous solution/vapor interface is different from bulk as suggested by vibrational two-dimensional sum-frequency generation (2DSFG) spectroscopy[141–147] and force-field MD simulations[148–150]. Using polarizable water models, Liu *et al.*[150] showed that the dynamics of breaking and forming H-bonds at the water/vapor interface is faster than that in bulk water. Benjamin[151] showed that, for some water/organic liquid interfaces, the dynamics are slower at the interface than in the bulk and are sensitive to the location of the water molecules along the interface normal. However, all these simulation results depend on the force-field. Here we have investigated HB dynamics of the interface using DFTMD simulations, which do not require an apriori parameterization. For example, Usui and coworkers[152] had shown that the long-lived $\text{O-D}\cdots\text{O}_{\text{TMAO}}$ H-bonds between Trimethylamine N-oxide (TMAO) and water (D_2O) in aqueous TMAO solutions can be only reproduced with AIMD instead of force field-based MD simulations. Recent works based on novel *ab initio* computational methods[153–156] also show that AIMD can provide unprecedented insights into the nature of H-bonding between water molecules. In the analysis of DFTMD simulations, to selectively address the interface, we have used the concept of instantaneous interface. The traditional method to describe the interface layer makes use of the Gibbs dividing surface, and therefore regard its boundary as a plane. We consider here the spatial fluctuations of the aqueous interface into the definition of the interface layer. Specifically, we choose the interface layer using the instantaneous Willard-Chandler surface. Within the instantaneous interfacial layer, the characteristic time of HB breaking and forming, and the characteristic time of the orientation relaxation of water molecules have been calculated. The dependence of the average number of H-bonds possessed by water molecules on the thickness of the interface has also been studied.

As the interface thickness cannot be directly inferred from the VSFG experiments, MD simulations are a precious tool to understand how far is the interface extending. Due to molecular motions, the identity of molecules at the interface also changes over time[157], and the fixed interface will no longer apply. Therefore, the instantaneous interfaces are calculated for the aqueous electrolyte solutions, and are used in the analysis of interfacial HB dynamics and reorientation relaxation rate of water molecules. Combining two different sampling methods, the analysis of interfacial HB dynamics allows us to calculate the interface thickness.

Finally, the concept of instantaneous interface has been extended to analyze the first solvation shell around the ions. Furthermore, properties such as solvation shell HB (SHB) dynamics have also been obtained.

The thesis is organized as follows. In Chapter 2, we present the foundations of AIMD and the method to calculate the VSFG spectra. In Chapter 3, we present the results of the vibrational properties of water *clusters* including alkali nitrates, which are calculated for interpreting the vibrational characteristics of water molecules in water clusters. The theoretical results of VSFG spectra of solution/vapor interfaces of alkali metal nitrate solutions are included in Chapter 4. Chapter 5 focuses on the HB dynamics of the water/vapor interface, and introduce the method for studying the HB dynamics of the instantaneous interface layer of the water/vapor interface. In addition to the alkali nitrate solutions, in Chapter 6, we simulated and analyzed the alkali iodide solutions and their interfaces, which have similar properties in terms of ions' surface propensities and HB dynamics to those of the alkali nitrate solutions. The conclusions are summarized in Chapter 7.

Chapter 2

Methods

In this chapter, we describe the methods to study the structure and dynamics of water and aqueous electrolyte solutions. DFTMD simulations are performed to calculate the VSFG spectra. Our motivations for adopting DFTMD simulations are manifold. In general, DFTMD simulations have the following advantages: (1) structure and reactivity can be treated in a consistent way; (2) efficient treatments of basis sets and long range interactions in DFT do extend the simulation capabilities to thousands of atoms, i.e., it allows realistic models for interfaces; (3) they provide information on the structural organization of the solvent at the interfaces. In particular, the interface of solutions contains a large number of H-bonded water molecules. As Stillinger said, since H-bonding is the most important interaction in liquid water and since these interactions are cooperative, it is insufficient for the purposes of computer simulation to use the potential energy function for dimers alone[158].

The organization of this chapter is the following. Paragraphs 2.1 to 2.3 give an introduction to the basic ideas of DFTMD as well as Born-Oppenheimer MD (BOMD) we adopted. Paragraphs 2.4 and 2.5 introduce the analysis methods used in this thesis, including the method of calculating vibrational properties from velocity autocorrelation and the method of calculating the VSFG spectra from velocity autocorrelation function (ACF). Paragraph 2.6 reviews the Luzar-Chandler HB population operator and associated correlation functions, which are the basis for studying the instantaneous interfacial HB dynamics.

2.1 Modeling interfaces with *ab initio* molecular dynamics

Modern theoretical methodology, aided by the advent of high speed computing, has advanced to a level where the microscopic details of dynamical processes in condensed phases can be treated on a relatively routine basis. One common theoretical approach for obtaining these microscopic details of the system is the MD simulations In the MD simulations, classical Newton equations of motion for a system are solved numerically starting from a pre-specified initial state, and subject to a set of boundary conditions appropriate to the problem. The MD methodology allows both equilibrium thermodynamic and dynamical properties of a system at finite temperature to be computed, while simultaneously providing a view of the microscopic motion of individual atoms in the system[159].

Despite the success of classical MD simulations, they have some limitations. First, charges are treated as static parameters, therefore electronic polarization effects are not included. The so-called polarizable models[160–162], in which charges and induced dipoles are allowed to fluctuate in a changing environment, have been proposed to overcome this problem. While having considerable success, they also have serious limitations, including a lack of transferability and standardization[163]. Second, force fields assume a pre-specified connectivity among the atoms, therefore, they suffer from an inability to describe chemical bond-forming and -breaking. This problem can be treated using techniques such as the empirical valence bond method[164] or other semi-empirical approaches. Unfortunately, these methods are also not transferable and, therefore, need to be reparametrized for each type of reaction and may end up biasing the reaction path in undesirable ways.

To overcome these limitations of force field based approaches, AIMD simulation techniques[165–171] can be used. The AIMD method combines finite temperature dynamics with forces obtained from electronic structure calculations performed 'on the fly' as the MD simulation proceeds[170]. Because the electronic structure is treated explicitly in AIMD calculations, many-body forces, electronic polarization and bond-forming and -breaking events are described with the accuracy of the electronic structure representation. Moreover, the AIMD method can be easily extended to incorporate nuclear quantum effects via the Feynman path integral approach[172, 173], leading to the *ab initio* path integral technique[174–176].

The AIMD method have been used to study a wide variety of chemically interesting problems in areas such as chemical reactivity, H-bonds for the interfacial structure, pKa, and vibrational spectroscopy. The AIMD applications include calculations of the structure and dynamics of water and other H-bonded liquids, proton transport in aqueous and condensed phase environments, structure, proton order/disorder and dynamical properties of ice, structure of liquid silicates and glasses, mechanisms of polymer knotting, Ziegler-Natta industrial catalysis and other surface catalytic processes. More recently, the AIMD method has started to impact the biological sciences and has been applied in calculations of nuclear magnetic resonance chemical shifts in drug-enzyme complexes, structure of nucleic acids, exploration of the design of possible biomimetics and structure, dynamics and binding mechanisms in myoglobin. In many of these applications, new physical phenomena have been revealed, which could not have been uncovered using empirical models, often leading to new interpretations of experimental data and even suggesting new experiments to perform[163].

To study the heterogeneous environment at water interface, the AIMD method is particularly suitable for the following reasons: (1) The AIMD method is only relying on the atomic coordinates of the model system $\mathbf{R}$, and not on any adjustable parameter, i.e., the inter-atomic forces $\mathbf{F}_\mathrm{I} = -\nabla_{\mathbf{R}_\mathrm{I}} V(\mathbf{R})$, where $V(\mathbf{R})$ is the potential energy[177], are determined using the first principle electronic structure methods on the fly; (2) New phenomena that are not foreseen before starting the simulation can simply happen if necessary. Therefore, the AIMD method is also a good predictive tool. However, as a drawback, the AIMD simulations are expensive and can nowadays be performed on size-limited system of 100–1000 atoms for up to a few hundred picoseconds (ps).

2.2 Density functional theory

In most currently performed AIMD simulations, the dynamics is performed within the so-called Born-Oppenheimer (BO) approximation[178]. The mass of an electron is much smaller than that of any nuclei. This means that electrons respond much more rapidly to changes in their environment than nuclei can. As a result, there is a strong separation of timescales between the electronic and nuclear motion, i.e., the kinetic energy of the nuclei can be ignored. First, we solve the question that describe the electron motion, for fixed positions of the nuclei. In other words, for a set of electrons moving in the field of a set of fixed nuclei, we find the lowest energy configuration (or *ground state*) of the electrons. Then we can express the ground state energy as a function of the positions of the nuclei (*adiabatic potential energy surface* of atoms). In this approximation, the electrons are treated independently at constant nuclear coordinates $\mathbf{R}$. This is BO approximation, or adiabatic approximation. Applying BO approximation, the potential energy $V(\mathbf{R})$ is written as

$$V(\mathbf{R}) = \langle \Psi_0 | H_\mathrm{e} | \Psi_0 \rangle + E_I(\mathbf{R}), \tag{2.1}$$

where $|\Psi_0\rangle$ is the ground state, $E_I(\mathbf{R})$ is the energy of the nuclei, and H_e is the electronic many-body Hamiltonian, which depends on the electronic coordinates but parametrically on the nuclear degrees of freedom,

After using BO approximation, a formidable task is to solve the electronic, non-relativistic, time independent many-body Schödinger equation

$$H_\mathrm{e}|\Psi_0\rangle = \epsilon_0(\mathbf{R})|\Psi_0\rangle. \tag{2.2}$$

This is a high-dimensional eigenvalue problem, and it is still time consuming. One great solution to the electronic structure problem is density functional theory (DFT)[179, 180].

DFT can be used to map the problem of an interacting electron gas onto that of a non-interacting particles in an effective non-local potential[166].

DFT fundamental theorems Hohenberg and Kohn (HK) proved that the total energy of a many-electron system is a unique functional of the electron density $n(\mathbf{r})$. The first HK theorem proves that there exists a one-to-one correspondence between the ground state electronic density $n_0(\mathbf{r})$ and an external potential $v(\mathbf{r})$, i.e., the electron density n determines all properties of a non-degenerate ground state of an atom or molecule (for a degenerate ground state the density n determines the energy). (If we want to solve variationally for the ground state energy of a system with $H = T + V_{ee} + \sum_{i=1}^{N} v(i)$) the HK theorem says that there exists a valid functional $Q[n]$ that delivers the sum of the electronic kinetic energy $T[n]$ and electron-electron repulsion energy $V_{ee}[n]$ of each trial electron density n[181].

The electronic density $n(\mathbf{r})$, which depends on just 3 electronic degrees of freedom, become the central quantity in DFT in place of the complex $3N_\mathrm{e}$-dimensional many-body wave-function.

The second HK theorem states that the total energy in the electronic density space satisfies

$$E^{\mathrm{DFT}}[n_0] = \psi_0 H_\mathrm{e} \psi_0 \leq \psi' H_\mathrm{e} \psi' = E^{\mathrm{DFT}}[n'], \tag{2.3}$$

for which the equality holds if and only if $n_0 = n'$ (variational principle). One try to choose different n to optimize $E^{\mathrm{DFT}}[n]$, the quantum expectation value of $H_\mathrm{e}[n]$, thus to determine $E^{\mathrm{DFT}}[n_0]$, i.e.

$$E^{\mathrm{DFT}}[n_0] = \min_{\psi} \psi H_\mathrm{e} \psi = \min_{n} \psi[n] H_\mathrm{e}[n] \psi[n] = \min_{n} E^{\mathrm{DFT}}[n], \tag{2.4}$$

Eq. (2.2) can be solved by iteratively diagonalizing $H_\mathrm{e}[n]$ within a self consistent field (SCF) procedure.

Assuming atomic units and considering the physical relevant Coulomb interaction, the total Hamiltonian is

$$\begin{aligned} H_\mathrm{e} =& \frac{1}{2}\sum_{i=1}^{N_\mathrm{e}} \nabla_i^2 + \sum_{i<j}^{N_\mathrm{e}} \frac{1}{|\mathbf{r}_i - \mathbf{r}_j|} + \sum_{I,i}^{N,N_\mathrm{e}} \frac{Z_I}{|\mathbf{R}_I - \mathbf{r}_i|} \\ =& \hat{T} + \hat{U} + \hat{V}, \end{aligned} \tag{2.5}$$

where Z_I is the atomic number of the I-th atom, $\hat{T}$ is the operator of kinetic energy of electrons, $\hat{U}$ is the electron-electron interaction and $\hat{V} = \sum_i v(\mathbf{r}_i)$ is the electron-nuclei operator.

In DFT, we obtain the ground state energy of a many-electron system as minimum of an energy functional

$$E^{\mathrm{DFT}}[n(\mathbf{r})] = T[n(\mathbf{r})] + U[n(\mathbf{r})] + V[n(\mathbf{r})]. \tag{2.6}$$

The next problem is how to provide an explicit form for the three terms appearing in Eq. (2.6). The solution is the Kohn-Sham approach to DFT. A reference system with the same electron density as the density for the full interacting system and without electron electron repulsion is introduced. For such reference system, the kinetic energy functional is

$$T_\mathrm{s}[n(\mathbf{r})] = -\frac{1}{2}\sum_{i=1}^{N_\mathrm{e}} \int d\mathbf{r}\psi_i^*(\mathbf{r}) \nabla^2 \psi_i(\mathbf{r}) = T_\mathrm{s}[\{\psi_i[n(\mathbf{r})]\}], \tag{2.7}$$

and the electronic density can be written as

$$n(\mathbf{r}) = \sum_{i=1}^{N_\mathrm{occ}} f_i \psi_i(\mathbf{r})\psi_i^*(\mathbf{r}), \tag{2.8}$$

in which N_occ is the number of occupied orbitals and f_i the occupation number of the ith state, so that

$$\sum_{i=1}^{N_\mathrm{occ}} f_i = N_\mathrm{e}, \tag{2.9}$$

and $\psi_i(\mathbf{r})$ is the wave-function of the i-th state.

The total energy functional of the Kohn-Sham (KS) system is

$$\begin{aligned} E^{\mathrm{KS}}[n(\mathbf{r})] =& E^{\mathrm{KS}}[\{\psi_i[n(\mathbf{r})]\}] \\ =& T_\mathrm{s}[\{\psi_i[n(\mathbf{r})]\}] + U_H[n(\mathbf{r})] + V[n(\mathbf{r})] + E_\mathrm{XC}[n(\mathbf{r})] \qquad (2.10) \\ =& -\frac{1}{2}\sum_{i=1}^{N} f_i \int d\mathbf{r}\psi_i^*(\mathbf{r}) \nabla^2 \psi_i(\mathbf{r}) + \frac{1}{2}\int d\mathbf{r} \int d\mathbf{r}' \frac{n(\mathbf{r})n(\mathbf{r}')}{\mathbf{r} - \mathbf{r}'} \\ &+ \int d\mathbf{r} v_\mathrm{ext}(\mathbf{r}) n(\mathbf{r}) + E_\mathrm{XC}[n(\mathbf{r})], \qquad (2.11) \end{aligned}$$

where $E_\mathrm{XC}[n(\mathbf{r})] \equiv (T[n(\mathbf{r})] - T_\mathrm{s}[\{\psi_i[n(\mathbf{r})]\}]) + (U[n(\mathbf{r})] - U_H[n(\mathbf{r})])$ is the exchange and correlation (XC) energy functional and $v_\mathrm{ext} = \delta V[n(\mathbf{r})]/\delta n(\mathbf{r})$ is the external potential. The energy functional $E_\mathrm{XC}[n(\mathbf{r})]$ is the only unknown part of the total energy functional. This definition of XC energy functional shows that a significant of part E_XC is due to correlation effects of the kinetic energy, that is expressed explicitly only with the reduced 2-particle density matrix.

Directly minimizing Eq. (2.10) is not straightforward because $T_\mathrm{s}[\{\psi_i[n(\mathbf{r})]\}]$ is an explicit orbital functional. However, it is more appropriate to make $E_{\mathrm{KS}}[\{\psi_i[n(\mathbf{r})]\}]$ stationary by the following Euler-Lagrange equation. It is possible to use the variational principle to derive the corresponding Euler-Lagrange equation of the non-interacting system within the potential v_{ext}. The KS scheme permits to map the full interacting many-body problem, with the electron-electron interaction $\hat{U}$ onto an equivalent fictitious single-body problem, with an effective potential operator $\hat{V}_{\mathrm{KS}} = \hat{U}_s + \hat{V}_{\mathrm{H}} + \hat{V}_{\mathrm{XC}}$.

If we figure out a way to approximate V_{XC} accurately, we will have a much less demanding set of equations to solve than those of the true system[182]. Using variational principle is possible to derive corresponding Euler-Lagrange equation of the reference system (non-interaction system) within the potential v. To determine the set of wave-functions ψ_i which minimize the KS energy functional , we can iteratively solve the equation

$$[T_{\mathrm{s}}[n(\mathbf{r})] + V_{\mathrm{H}}[n(\mathbf{r})] + V[n(\mathbf{r})] + E_{\mathrm{XC}}[n(\mathbf{r})]]\,\psi_i(\mathbf{r}) = \varepsilon_i \psi_i(\mathbf{r}), \tag{2.12}$$

where ε_i is the eigenvalue of each equation, V_{H} is the Hartree potential of electrons:

$$V_{\mathrm{H}} = e^2 \int \frac{n(\mathbf{r})n(\mathbf{r}')}{|\mathbf{r}-\mathbf{r}'|} d\mathbf{r}', \tag{2.13}$$

and the exchange and correlation potential is

$$V_{\mathrm{XC}} = \frac{\delta E_{\mathrm{XC}}[n(\mathbf{r})]}{\delta n(\mathbf{r})}. \tag{2.14}$$

Given the explicit form of the exchange and correlation functional E_{XC}, the exchange and correlation potential V_{XC} can be determined, and thus electron density $n(\mathbf{r})$. Thus the KS equation must be solved self-consistently.

Exchange and correlation: LDA and GGA functionals The simplest density functional approximation is local density approximation (LDA). In LDA, the exchange and correlation energy of an electronic system is

$$E_{\mathrm{XC}}[n(\mathbf{r})] = \int \varepsilon_{\mathrm{XC}}(\mathbf{r}) n(\mathbf{r}) d\mathbf{r}, \tag{2.15}$$

and

$$\frac{\delta E_{\mathrm{XC}}[n(\mathbf{r})]}{\delta n(\mathbf{r})} = \frac{\partial n(\mathbf{r})\varepsilon_{\mathrm{XC}}(\mathbf{r})}{\partial n(\mathbf{r})}, \tag{2.16}$$

where

$$\varepsilon_{\mathrm{XC}}(\mathbf{r}) = \varepsilon_{\mathrm{XC}}^{\mathrm{hom}}[n(\mathbf{r})]. \tag{2.17}$$

Local density approximation is accurate for systems with slowly varying charge densities. It has a tendency to favor more homogeneous systems and over-binds solids and molecules. The dielectric and piezoelectric constant calculated from LDA are approximately 10% over estimated. The limitations of LDA suggest that care must be taken into its applications. For example, the independent particle picture breaks down in strongly correlated systems, where LDA is very inaccurate. Furthermore, LDA does not take into account variation of electronic density and van der Waals interactions[182], so it does not give a very accurate description of H-bonding. H-bonding is essential for a correct description of water and interfaces with water, therefore, a functional beyond LDA is needed in the description of hydrogen-bonded systems, including water.

For any density that varies sufficiently slowly, an expansion of a functional f in gradients should have increasing accuracy:

$$f[n] = \int d^3r[an(\mathbf{r}) + bn(\mathbf{r})|\nabla n(\mathbf{r})|^2 + \cdots]. \tag{2.18}$$

But the gradient expansion of the exchange-correlation energy does not always improve results, sometimes it leads to divergences. Therefore, a more general approach which is called generalised gradient approximation (GGA) is considered. An approach to improve LDA is to include gradient corrections , in which E_{XC} is a functional of density and its gradient:

$$E_{\mathrm{XC}}^{\mathrm{GGA}}[n(\mathbf{r})] = \int \varepsilon_{\mathrm{XC}}(n(\mathbf{r}))n(F_{\mathrm{XC}}[n(\mathbf{r}), |\nabla n(\mathbf{r})|])d\mathbf{r}, \tag{2.19}$$

where $F_{\mathrm{XC}}[n(\mathbf{r})]$ is a correction chosen to satisfy conditions for E_{XC}. Exchange and correlation energy depends locally on the gradient of the density ∇n as well as the density n. There are several forms of GGA.

GGA is usually the best compromise between speed and accuracy in large systems. For solids, the most commonly used functional with GGA is the one proposed by Perdew, Burke and Ernzherhof (PBE)[183]. Another popular GGA functional is the BLYP functional[184, 185]. Electron densities of electric dipole and quadruple moments are not uniform in space. Physically, GGAs include information on the spatial variation in the electron densities, and thus they can create functionals with better flexibility to describe dipole and quadruple moments. Therefore, GGAs generally describe the dipole and quadruple moments of the monomer quite well. However, they somewhat overestimate polarizabilities, the predicted dipolar polarizability (also called dipole polarizability) being typically 10% too large.

Dispersion corrections Dispersion is a general term referring to weak, long-range correlations in electronic structure. It includes van der Waals interactions, which originates from the coupling of the electric field generated by fluctuations in the electronic density at position $\mathbf{r}$ in the system with the density at another point $\mathbf{r}'$[186, 187]. These interactions are not well modeled by any mean-field level of theory, the *ab initio* wave-function theory such as second-order Moller-Plesset perturbation theory (MP2), or standard DFT functionals, eg. LDA, GGAs, etc. The mean-field theory does not include the electron correlation effect, MP2 theory usually overestimate the binding energies and underestimates inter-molecular equilibrium distances, and all the gradient corrected DFT are unable to describe dispersion interactions,because they can not describe the long-range electron correlation. In the last two decades, a series of empirical corrections have been proposed which can improve the structural properties without more computational cost[95–98, 188–190]. Among such empirical approaches we choose DFT-D3 correction which can be used in our application to interfaces with water[98, 191].

In DFT-D3 correction, also used in this thesis, the input parameters are cutoff radii and dispersion coefficients, and they can be calculated by KS-DFT methods using extended atomic orbital basis sets. The use of structure dependent dispersion coefficients, i.e., functional coordination number, to interpolate between dispersion coefficients of atoms in different chemical environments, increases the accuracy. Moreover, no atom connectivity information is required and all the properties are calculated only from Cartesian coordinates and atomic numbers[98].

If the three-body nonadditivity terms are considered, as well as the pairwise terms, the total energy is given by

$$E_{\text{DFT}} = E_{\text{KS-DFT}} + E^{(2)}_{\text{disp}} + E^{(3)}_{\text{disp}}, \tag{2.20}$$

where $E_{\text{KS-DFT}}$ is the usual self-consistent KS energy obtained from the chosen density functional, $E^{(2)}_{\text{disp}}$ is the empirical two-body dispersion correction term and $E^{(3)}_{\text{disp}}$ is the three-body nonadditivity term. $E^{(2)}_{\text{disp}}$ is given by

$$E^{(2)}_{\text{disp}} = \sum_{\text{AB}} \sum_{n=6,8,10,\cdots} s_n \frac{C_n^{\text{AB}}}{R^n_{\text{AB}}} f_{\text{dmp},n}(r_{\text{AB}}), \tag{2.21}$$

where $\sum\limits_{\text{AB}}$ denotes the sum over all atom pairs in the system[186], C_n^{AB} is the averaged n-order dispersion coefficients ($n = 6,8,10,\cdots$) for atom pair AB, r_{AB} is the internuclear distance of atom pair AB, and $f_{\text{dmp},n}(r_{\text{AB}})$ is the damping function used to avoid near-singularities for small distance R between nuclei. The damping function in Eq. (2.21) is given by

$$f_{\text{dmp},n}(r_{\text{AB}}) = \frac{1}{1 + 6(r_{\text{AB}}/(s_{r,n} R_0^{\text{AB}}))^{-\alpha_n}}, \tag{2.22}$$

where $s_{r,n}$ is the order-dependent scaling factor of the cutoff radii R_0^{AB}, which is the most important parameter that has to be adjusted for each density functional and α_n is a parameter which can be adjusted manually such that the dispersion correction is smaller than 1% of max($|E_{\text{disp}}|$) for typical covalent bond distances. In Ref.[98] $s_{r,6}$ is optimized by a least-squares fitting procedure and $s_{r,8}$ is fixed to 1 for all density functionals.

The leading non-additive dispersion term for three atoms A, B and C is

$$E^{(3)}_{\text{disp}} = \frac{C_9^{\text{ABC}}(3\cos\theta_a\cos\theta_b\cos\theta_c + 1)}{(r_{\text{AB}} r_{\text{BC}} r_{\text{CA}})^2}, \tag{2.23}$$

where θ_a, θ_b and θ_c are the internal angles of the ΔABC, and C_9^{ABC} is the triple-dipole constant defined by

$$C^{\text{ABC}} = \frac{3}{\pi} \int_0^\infty \alpha^{\text{A}}(i\omega)\alpha^{\text{B}}(i\omega)\alpha^{\text{C}}(i\omega), \tag{2.24}$$

which can be approximated by a geometric mean

$$C^{\text{ABC}} \approx -\sqrt{C_6^{\text{AB}} C_6^{\text{AC}} C_6^{\text{BC}}}, \tag{2.25}$$

since the total three-body contribution is typically 5–10% of $E_{\text{disp}} = E^{(2)}_{\text{disp}} + E^{(3)}_{\text{disp}}$.

2.3 Born-Oppenheimer and Car-Parrinello molecular dynamics

In computational material science, the most popular AIMD simulation methods are the BOMD and Car-Parrinello MD (CPMD) methods. In BOMD, the potential energy $E[\{\psi_i\}; \mathbf{R}]$ is minimized at each MD step with respect to $\{\psi_i(\mathbf{r})\}$ under the orthonormality condition

$$\langle\psi_i(\mathbf{r})|\psi_j(\mathbf{r})\rangle = \delta_{ij}. \tag{2.26}$$

Thus the Lagrangian density is

$$\begin{aligned} L_{\mathrm{BO}}(\{\psi_i\};\mathbf{R}_I) =& \frac{1}{2}\sum_{I=1}^{N} M_I\dot{\mathbf{R}}_I^2 - \min_{\{\psi_i\}}E[\{\psi_i\};\mathbf{R}_I] \\ &+\sum_{i,j}\Lambda_{ij}(\langle\psi_i|\psi_j\rangle - \delta_{ij}), \end{aligned} \tag{2.27}$$

in which Λ is the Hermitian Lagrangian multiplier matrix. By Euler-Lagrange equations one obtains the equations of motion

$$\begin{aligned} M_I\ddot{\mathbf{R}}_I =& -\nabla_{R_I}[\min_{\{\psi_i\}}E[\{\psi_i\};\mathbf{R}_I]|_{\langle\psi_i|\psi_j\rangle=\delta_{ij}}] \\ =& -\frac{\partial E}{\partial\mathbf{R}_I} + \sum_{i,j}\Lambda_{ij}\frac{\partial}{\partial\mathbf{R}_I}\langle\psi_i|\psi_j\rangle \\ &-2\sum_i\frac{\partial\langle\psi_i|}{\partial\mathbf{R}_I}\left(\frac{\delta E}{\delta\langle\psi_i|} - \sum_j\Lambda_{ij}|\psi_j\rangle\right). \end{aligned} \tag{2.28}$$

The term $-\frac{\partial E}{\partial\mathbf{R}_\mathrm{I}}$ is the Hellmann-Feynman force, and the term $\sum_{i,j}\Lambda_{ij}\frac{\partial}{\partial\mathbf{R}_\mathrm{I}}\langle\psi_i|\psi_j\rangle$, i.e., the wave-function force F_{WF}[192], is a constraint force due to the orthonormality constraint. The last term comes from the fact that there is always an implicit dependence on the atomic positions through the expansion coefficient $c_{ij}(\mathbf{r})$ that is defined by

$$\psi_i(\mathbf{r}) = \sum_j c_{ij}(\mathbf{r})\phi_i(\mathbf{r}), \tag{2.29}$$

where the KS orbitals are assumed to be real.

CPMD is an alternative method to BOMD, which includes electrons in a single state[90]. In CPMD, a coupled electron-ion dynamics is performed. The CP Lagrangian is

$$\begin{aligned} L_{\mathrm{CP}}(\{\psi_i\};\mathbf{R},\dot{\mathbf{R}}) =& \frac{\mu}{2}\sum_i\langle\dot{\psi}_i|\dot{\psi}_i\rangle + \frac{1}{2}\sum_{I=1}^{N}M_\mathrm{I}\dot{\mathbf{R}}_\mathrm{I}^2 - E[\{\psi_i\};\mathbf{R}] \\ &+\sum_{i,j}\Lambda_{ij}(\langle\psi_i|\psi_j\rangle - \delta_{ij}), \end{aligned} \tag{2.30}$$

where the electronic degrees of freedom carries a fictitious mass parameter μ, and are characterized by orbital velocities $\{\dot{\psi}_i\}$. Applying Euler-Lagrangian equations leads equations of motion:

$$\begin{aligned} M_\mathrm{I}\ddot{\mathbf{R}}_\mathrm{I} =& -\nabla_{R_\mathrm{I}}[E[\{\psi_i\};\mathbf{R}]|_{\langle\psi_i|\psi_j\rangle=\delta_{ij}}] \\ =& -\frac{\partial E}{\partial\mathbf{R}_\mathrm{I}} + \sum_{i,j}\Lambda_{ij}\frac{\partial}{\partial\mathbf{R}_\mathrm{I}}\langle\psi_i|\psi_j,\rangle \end{aligned} \tag{2.31}$$

$$\begin{aligned} \mu\ddot{\psi}_i(\mathbf{r},t) =& -\frac{\partial\langle\psi_i|}{\partial\mathbf{R}_\mathrm{I}}\left(\frac{\delta E}{\delta\langle\psi_i|} + \sum_j\Lambda_{ij}|\psi_j\rangle\right) \\ =& -\hat{H}_\mathrm{e}\langle\psi_i| + \sum_j\Lambda_{ij}|\psi_j\rangle, \end{aligned} \tag{2.32}$$

where $-\delta E/\delta\psi_i$ are the electronic forces to propagate the electronic degrees of freedom in time within a fictitious Newtonian dynamics. No SCF cycle is required to quench the electrons to the BO surface and to force them to evolve adiabatically with respect to the nuclei.

To ensure the adiabatic energy-scale separation of the nuclear and the electronic degrees of freedom, i.e. to prevent energy transfer between them, the highest nuclear phonon frequency ω_{I} must be much smaller than the lowest electronic phonon frequency ω_{e}. The condition $\omega_{\mathrm{I}} \ll \omega_{\mathrm{e}}$ is ensured by a proper choice of the fictitious mass μ. The fictitious mass determines the computational accuracy.

Which method is to favor depends largely on the definition of accuracy, as well as on the particular application. In this thesis, we use the BOMD method, as implemented in CP2K package[93, 177]. In BOMD, (1) the nuclear positions are propagated in time followed Newton's equations of motion with the electronic ground state energy as the potential energy surface; (2) the time evolution of the atomic coordinates is performed with the velocity-Verlet algorithm[193].

Since there is no explicit electron dynamics, the maximum integration time step is simply given by the one intrinsic to nuclear motion, i.e., $\tau_e^{\mathrm{BO}} \approx \tau_{\mathrm{n}}$. In BOMD, the time step can be even larger if the nuclear dynamics becomes fairly slow[194]. But in order to resolve vibrations in molecular systems, the time step is decreased to less than 1 fs in this thesis[170].

2.4 Vibrational density of states

To obtain vibrational properties of a molecular system, it is possible to use the velocity ACF, as calculated from AIMD trajectories. The obtained vibrational density of states (VDOS) can provide information on the local environment of the water molecules' OH-stretching mode. For a system comprised of N atoms, the velocity ACF $C(t)$ for a molecule is[195–197]

$$C(t) = \frac{\langle \sum_{i=1}^{N} \mathbf{v}_i(t) \cdot \mathbf{v}_i(0) \rangle}{\langle \sum_{i=1}^{N} \mathbf{v}_i(0) \cdot \mathbf{v}_i(0) \rangle}, \tag{2.33}$$

where $\langle \dots \rangle$ denotes the average over starting times, t is the time interval, and $\mathbf{v}_i$ denotes the velocity of the i-th atom. The VDOS $g(\nu)$ for selected atoms, which is a function of the vibrational frequency ν of atoms, is expressed in terms of the FT of the velocity ACF of the atoms[198]. In equilibrium, $C(-t) = C(t)$, and $g(\nu)$ is a real function, i.e.,

$$g(\nu) = \sqrt{\frac{2}{\pi}} \int_0^{\infty} \mathrm{d}t \cos(2\pi\nu t) C(t). \tag{2.34}$$

In the case of an interface it may be of interest to look at z-component (where z is the direction perpendicular to the Gibbs interface), we can calculate the FT $g_z(\nu)$ of the auto-correlation function of the vertical component of atomic velocity. $g_z(\nu)$ can be calculated by Eq. (2.34) if we replace $C(t)$ by

$$C_z(t) = \frac{\langle \sum_{i=1}^{N} v_{i,z}(t) v_{i,z}(0) \rangle}{\langle \sum_{i=1}^{N} \mathbf{v}_i(0) \cdot \mathbf{v}_i(0) \rangle}, \tag{2.35}$$

where $v_{i,z}$ is the vertical component of the velocity of the i-th atom. Vibrational density of state $g_z(\nu)$ for water molecules is used to extract the O-H stretch along the vertical direction to the interface.

2.5 Calculation of VSFG spectra from molecular dynamics simulations

As introduced in Chapter 1, the VSFG spectroscopy is a powerful tool for extracting structural and dynamical information on surfaces and interfaces. It can be applied to any interface as long as light can reach it, also including liquid/metal interfaces[199–203] and buried interfaces[204, 205]; it can probe liquid interface with molecular sensitivity[106, 113, 114]. Therefore, the VSFG spectroscopy can yield structural information about solution/vapor interfaces which could not be obtained with other techniques.

2.5.1 Nonlinear susceptibility of solution/vapor interfaces

VSFG VSFG is a coherent nonlinear optical process in which incident laser beams with frequency and wave vector $(\omega_1, \mathbf{k}_1)$ and $(\omega_2, \mathbf{k}_2)$ produce a signal with frequency and wave vector $(\omega_1+\omega_2, \mathbf{k}_1+\mathbf{k}_2\ )$ (Fig. 2.1). In this process, the fields arise from the polarization induced over a macroscopically large volume superposition coherently. The VSFG signal intensity is proportional to the square of the resonant and non-resonant terms:

$$\begin{aligned} I_{\mathrm{SFG}}(\omega) &\propto |\chi^{(2)}(\omega)|^2 \\ &= |\chi^{(2),\mathrm{R}}(\omega) + \chi^{(2),\mathrm{NR}}(\omega)|^2, \end{aligned} \tag{2.36}$$

where $\chi^{(2)}$ is a third-rank tensor called second-order nonlinear susceptibility, or hyperpolarizability for a molecule[206], and it is responsible to the VSFG process. $\chi^{(2),\mathrm{R}}$ is the vibrationally resonant term, while $\chi^{(2),\mathrm{NR}}$ is the nonresonant term. Because experiments usually employed visible and the VSFG frequencies are far from resonant conditions, $\chi^{(2),\mathrm{NR}}$ can be considered totally off-resonant and therefore insensitive to the laser beams' frequencies involved. Therefore, we can neglect the frequency dependence of the non-resonant term. The molecular information is contained in the

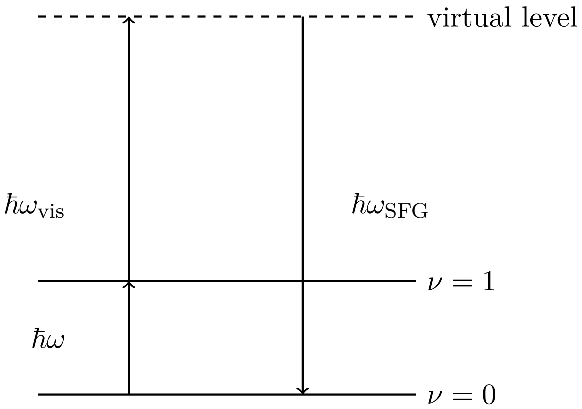

FIGURE 2.1: The schematic diagram of the VSFG process which involves IR and Raman transitions. The $\nu = 0$, $\nu = 1$ levels denote the ground and the first excited state of the oscillator[207], respectively. The dashed line denotes a virtual electronic state in the Raman transition.

resonant signal. The resonant susceptibility $\chi^{(2),\mathrm{R}}(\omega)$ is given by

$$\chi^{(2),\mathrm{R}}_{\eta\xi\kappa}(\omega) = \frac{-i}{\hbar}\int_0^\infty dt e^{i\omega t}\mathrm{Tr}[\rho,\mu_\kappa]\alpha_{\eta\xi}(t), \tag{2.37}$$

where the index (η, ξ or κ) is one of x, y and z labels of the laboratory coordinate frame. In Eq. (2.37) $\rho = e^{-\beta H}/Z$ for a system with Hamiltonian H and partition function Z at reciprocal temperature $\beta = 1/k_\mathrm{B}T$; μ_κ is the κ-th component of the system electric dipole and $\alpha_{\eta\xi}$ is the $\eta\xi$-th component of the polarizabiltiy tensor[208]. Besides the vibrational resonance, $\chi^{(2),\mathrm{R}}$, which reflects the vibrational and orientational characteristics of the surface species, the VSFG signal also includes the contribution from the non-resonant signal background $\chi^{(2),\mathrm{NR}}$, due to static hyperpolarizability of the interface itself[60]. For example, there are strong non-resonant second-order nonlinear responses[203, 209, 210] of the interface in the case of some metal(-oxide). Generally, experiments employ visible light and VSFG frequencies far from resonant conditions, therefore, the non-resonant term $\chi^{(2),\mathrm{NR}}$ is approximately off-resonant to the light frequencies involved[211].

Microscopic expression of molecular hyperpolarizability As the electric field is increased, the description of the induced dipole moment $\boldsymbol{\mu}$ should include the normally insignificant nonlinear terms. We can express the induced dipole moment as

$$\boldsymbol{\mu} = \boldsymbol{\mu}_0 + \alpha\mathbf{E} + \beta\mathbf{EE}. \tag{2.38}$$

The VSFG spectra are determined by the frequency-dependent hyperpolarizability in molecular level description. The frequency-dependent hyperpolarizability can be expressed as a sum of resonant and non-resonant terms:

$$\beta_{\eta\xi\kappa}(\omega_\mathrm{SFG}, \omega_\mathrm{vis}, \omega) = \beta^\mathrm{R}_{\eta\xi\kappa} + \beta^\mathrm{NR}_{\eta\xi\kappa}, \tag{2.39}$$

where η, ξ and κ are space-fixed axes. The resonant term of the frequency-dependent hyperpolarizability is

$$\beta^\mathrm{R}_{\eta\xi\kappa}(\omega_\mathrm{SFG}, \omega_\mathrm{vis}, \omega) = \sum_{v',v}\frac{\langle v|\alpha_{\eta\xi}|v'\rangle\langle v'|\mu_\kappa|v\rangle}{(\omega_{v'}-\omega_v)-\omega-i\gamma_{v'v}}\rho_v, \tag{2.40}$$

where the subscripts η, ξ and κ denote body-fixed axes, $\omega_{v'} - \omega_v$ is the vibrational energy gap, ρ_v is the thermal distribution function of the initial vibrational states v, $\alpha_{\eta\xi}$ is the $\eta\xi$-th component of the molecular dipole polarizability, μ_κ is the κ-th component of the molecular dipole moment, and $\gamma_{v'v}$ is the damping rate. We can rewrite Eq. (2.40) as (Appendix A)

$$\begin{aligned}\beta^\mathrm{R}_{\eta\xi\kappa} &= i\int_0^\infty dt\sum_{v'v} e^{-i[(\omega_{v'}-\omega_v)-\omega-i\gamma_{v'v}]t}\langle v|\alpha_{\eta\xi}|v'\rangle\langle v'|\mu_\kappa|v\rangle\rho_v \\ &= i\int_0^\infty dt\sum_{v'v} e^{i\omega t}\langle v|e^{iHt}\alpha_{\eta\xi}e^{-iHt}|v'\rangle\langle v'|\mu_\kappa|v\rangle\rho_v \\ &= i\int_0^\infty dt e^{i\omega t}\langle\alpha_{\eta\xi}(t)\mu_{\eta\xi}(0)\rangle, \end{aligned} \tag{2.41}$$

where H is the Hamiltonian of the system without external field. Eq. (2.41) indicates that the resonant term $\beta^{(2),\mathrm{R}}_{\eta\xi\kappa}$ is the FT of the quantity $\langle\alpha_{\eta\xi}(t)\mu_\kappa(0)\rangle$, i.e., the ensemble average of the time correlation function $\alpha(t)\mu_r(0)$. The damping rate $\gamma_{v'v}$ is not explicitly included in Eq. (2.41), because the dephasing is incorporated in the time development of the off-diagonal matrix elements of $\alpha_{\eta\xi}(t)$ and $\mu_\kappa(0)$.

The tensor elements $\chi^{(2),\mathrm{R}}_{\eta\xi\kappa}$ is microscopically represented as the average sum of first-order hyperpolarizability of the constituent molecules β in the space-fixed frame

$$\chi^{(2),\mathrm{R}}_{\eta\xi\kappa} = \langle \sum_{i}^{N} \sum_{pqr} D_{\eta p}(\Omega_i) D_{\xi q}(\Omega_i) D_{\kappa r}(\Omega_i) \beta_{pqr} \rangle \tag{2.42}$$

where $D(\Omega_i)$ is the direction cosine matrix of the i-th molecule, projecting β onto the space-fixed frame[212].

Fresnel Factors Because of screening and dipole-dipole coupling, the local electric fields felt by molecules is different from the macroscopic fields[210]. The VSFG signal depends on the magnitude of the local electric fields of the interacting optical beams at the interfaces. While the magnitude of the local electric fields is related to both the intensity of the incident beams and the linear refractive indices of the different layers (bulk) of the sample[106]. Fresnel coefficients define the magnitude of the electric fields at the interface. Therefore, to find out the magnitude of the local electric fields, we need to evaluate Fresnel factors. The VSFG intensity I_{SFG}, is proportional to the intensities of the incident visible and infrared beams, I_{vis}, I, and to the square of the second-order nonlinear susceptibilities, $\chi^{(2)}_{\eta\xi\kappa}(\omega_{\mathrm{SFG}})$, of the interface:

$$\chi^{(2)}_{\eta\xi\kappa}(\omega_{\mathrm{SFG}}) \propto |\sum_{\eta,\xi,\kappa} L_{\eta\eta}(\omega_{\mathrm{SFG}}) \chi^{(2)}_{\eta\xi\kappa}(\omega_{\mathrm{SFG}}) L_{\xi\xi}(\omega_{\mathrm{vis}}) L_{\kappa\kappa}(\omega)|^2 \sec^2(\theta_{\mathrm{SFG}}) I_{\mathrm{vis}} I \tag{2.43}$$

where η, ξ, κ are the Descartes coordinates of the reference frame; $\omega_{\mathrm{SFG}} = \omega_{\mathrm{vis}} + \omega$ is the frequency of VSFG beam; $L_{\eta\eta}$, $L_{\xi\xi}$ and $L_{\kappa\kappa}$ are the Fresnel coefficients; θ_{SFG} is the reflected angle of VSFG beam with respect to the normal direction in the medium.

2.5.2 VSFG spectra from velocity auto-correlation functions

This paragraph gives the derivation for the calculation of the sum frequency generation spectra of water interfaces that is based on the projection of the atomic velocities on the local normal modes, such an approach permits one to obtain VSFG signals from suitable velocity ACFs, reducing the computational cost to that of the accumulation of a molecular dynamics trajectory, and therefore cutting the overhead costs associated with the explicit calculation of the dipole and polarizability tensor. Moreover, the method permits to interpret the peaks in the spectrum in terms of local modes. Components of the resonant term $\chi^{(2),\mathrm{R}}_{\eta\xi\kappa}$ of the second order susceptibility can be calculated according to the classical formula[54, 211, 213]

$$\chi^{(2),\mathrm{R}}_{\eta\xi\kappa} = \frac{-i}{k_{\mathrm{B}} T \omega} \int_0^\infty dt e^{i\omega t} \left\langle \dot{A}_{\eta\xi}(t) \dot{M}_\kappa(0) \right\rangle \tag{2.44}$$

where k_{B} is the Boltzmann constant, ω is the frequency of the IR beam, $\mathbf{M}$ (A) is the dipole moment (dipole polarizability) of the system, and $\langle \dots \rangle$ denotes the average over all starting time points.

The total dipole moment and dipole polarizability derivatives for the system can be expressed in terms of the water and bond contributions:

$$\dot{A} = \sum_{i=1}^{N} \sum_{\epsilon} \dot{\alpha}^{i,\mathrm{l},\epsilon} \tag{2.45}$$

$$\dot{\mathbf{M}} = \sum_{i=1}^{N} \sum_{\epsilon} \dot{\mu}^{i,\mathrm{l},\epsilon} \tag{2.46}$$

where $\mu^{i,\mathrm{l},\epsilon}$ ($\alpha^{i,\mathrm{l},\epsilon}$) is the dipole moment (polarizability) of the bond ϵ of the i-th water molecule, the superscript (l) denote these quantities are measured in the lab frame, and N is the total number of water molecules. Therefore, the correlation function in Eq. (2.44) can be written as

$$\begin{aligned}\langle \dot{A}_{\eta\xi}(t)\dot{M}_{\kappa}(0)\rangle &= \sum_{i=1}^{N} \sum_{\epsilon} \left\langle \dot{\alpha}^{\mathrm{l}}_{\eta\xi,i,\epsilon}(t)\dot{\mu}^{\mathrm{l}}_{\kappa,i,\epsilon}(0) \right\rangle \\ &+ \sum_{i=1}^{N} \sum_{\epsilon} \left\langle \dot{\alpha}^{\mathrm{l}}_{\eta\xi,i,\epsilon}(t)\dot{\mu}^{\mathrm{l}}_{\kappa,i,-\epsilon}(0) \right\rangle \\ &+ \sum_{i,j=1;i\neq j}^{N} \sum_{\epsilon,\epsilon'} \left\langle \dot{\alpha}^{\mathrm{l}}_{\eta\xi,i,\epsilon}(t)\dot{\mu}^{\mathrm{l}}_{\kappa,i,\epsilon'}(0) \right\rangle. \end{aligned} \tag{2.47}$$

In Eq. (2.47), the first term of the right-hand side is the bond auto-correlation, the second term accounts for the correlation between the two bonds in the same water molecule, and the third them for the correlation between bonds in two different water molecules.

We assume that the bond elongation are small compared to the total bond length and stretching frequencies of the bond are much larger than frequencies of bond reorientation, for example, the libration. Therefore, we can approximately write $\dot{\mu}(0)$ by

$$\begin{aligned}\dot{\mu}_{\kappa}(0) &= \sum_{i}^{x,y,z} D_{\kappa i}(0)\dot{\mu}_i(0) \\ &= \sum_{i}^{x,y,z} D_{\kappa i}(0)\Big(\sum_{j}^{x,y,z} \frac{d\mu_i}{dr_j}\frac{dr_j}{dt}|_{t=0}\Big) \\ &= \sum_{i}^{x,y,z} D_{\kappa i}(0)\frac{d\mu_i}{dr_z}v_z(0), \end{aligned} \tag{2.48}$$

where $D_{\kappa i}$ is the direction cosine between the laboratory-fixed κ axis and the molecular-fixed i axis, and $v_z = \frac{dr_z}{dt}|_{t=0}$ is the projection of the velocity on the bond axis.

Similarly, for the dipole polarizability, we have

$$\dot{\alpha}_{\eta\xi}(t) = \sum_{i,j}^{x,y,z} \Big(D_{\eta i}(t)\frac{\partial \alpha_{ij}}{\partial r_z}D_{\xi j}(t)\Big)v_z(t). \tag{2.49}$$

The Eq. (2.48) and Eq. (2.49) simplify the calculation of the $\left\langle \dot{A}_{\eta\xi}(t)\dot{M}_{\kappa}(0) \right\rangle$ in Eq. (2.44), because $v_z(t)$ and $D(t)$ can be readily determined from the DFTMD trajectory, and $\frac{d\mu_i}{dr_z}$ and $\frac{d\alpha_{ij}}{dr_z}$ can be parameterized[106, 214].

We used three different frameworks: the lab framework $(x^{\mathrm{l}}, y^{\mathrm{l}}, z^{\mathrm{l}})$, the molecular

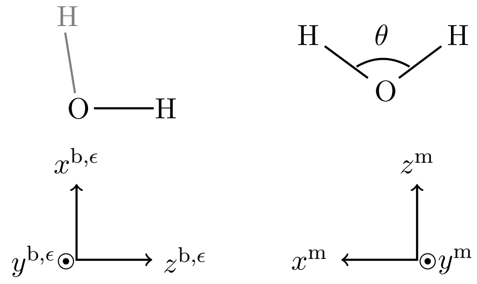
H
O
H
$x^{\mathrm{b},\epsilon}$
$y^{\mathrm{b},\epsilon}$
$z^{\mathrm{b},\epsilon}$
H
θ
H
O
z^{m}
x^{m}
y^{m}

(a) (b)

FIGURE 2.2: The representation of the bond (a) and the molecular (b) frameworks[114].

framework $(x^{\mathrm{m}}, y^{\mathrm{m}}, z^{\mathrm{m}})$ and the bond framework $(x^{\mathrm{b}}, y^{\mathrm{b}}, z^{\mathrm{b}})$ (Fig. 2.2). In the lab framework, the z^{l}-axis is perpendicular to the interface. The molecular frame will be used to decompose the signal into normal modes of water monomers. For the j-th molecule, the z^{m} axis is along the bisector of the H-O-H angle, the x^{m} axis is in the molecular plane, and the y^{m} axis is out of the molecular plane[114].

In the bond framework, $z^{\mathrm{b},\epsilon}$ axis is along the bond ϵ of a molecule, $z^{\mathrm{b},\epsilon}$ is in the molecular plane and $y^{\mathrm{b},\epsilon}$ is out of the molecular plane.

$$\dot{\alpha}^{\mathrm{l},\epsilon} = D^{\mathrm{m}} D^{\mathrm{b},\epsilon} \left(\frac{\partial \alpha^{\mathrm{b}}}{\partial r} \dot{r}^{\epsilon}\right) (D^{\mathrm{b},\epsilon})^{\mathrm{T}} (D^{\mathrm{m}})^{\mathrm{T}}, \tag{2.50}$$

$$\dot{\mu}^{\mathrm{l},\epsilon} = D^{\mathrm{m}} D^{\mathrm{b},\epsilon} \left(\frac{\partial \mu^{\mathrm{b}}}{\partial r} \dot{r}^{\epsilon}\right). \tag{2.51}$$

The direction cosine matrix $D^{\mathrm{b},\epsilon=1}$ and $D^{\mathrm{b},\epsilon=-1}$ can be expressed as

$$D^{\mathrm{b},1} = \begin{pmatrix} \cos\frac{\theta}{2} & 0 & -\sin\frac{\theta}{2} \\ 0 & 1 & 0 \\ \sin\frac{\theta}{2} & 0 & \cos\frac{\theta}{2} \end{pmatrix}, \quad D^{\mathrm{b},-1} = \begin{pmatrix} -\cos\frac{\theta}{2} & 0 & \sin\frac{\theta}{2} \\ 0 & 1 & 0 \\ \sin\frac{\theta}{2} & 0 & \cos\frac{\theta}{2} \end{pmatrix}, \tag{2.52}$$

where θ is the H-O-H angle in a water molecule. We use D^{m} to transform the coordinates in a molecular framework to coordinates in the lab framework. Because the orientation of water molecules is changing during the simulation, D^{m} is time dependent.

Based on DFTMD simulations, we can implement the parameterization of $\frac{\partial \mu_k}{\partial r_z}$ and $\frac{\partial \alpha_{ij}}{\partial r_z}$ and calculate the correlation function $\langle \dot{A}_{\eta\xi}(t) \dot{M}_{\kappa}(0) \rangle$ through the velocity ACF. This approximation for estimating the susceptibility retains the details of the interface, including the full electronic structure. And it reduces the computational cost for a total calculation with the instantaneous evaluation of the molecular dipoles and polarizabilities[102]. The parametrization of $\frac{\partial \mu_k}{\partial r_z}$ and $\frac{\partial \alpha_{ij}}{\partial r_z}$ is based on the calculation of the MLWF[215] and can be done through the approach developed by Salanne *et al.*[216] and Khatib *et al.*[114]. The implementation of this parametrization is given in Appendix A.

2.6 Definitions of HB population and correlation functions

Luzar and Chandler[217] have pioneered the analysis of HB dynamics of pure water, and subsequently such analysis has been extended to more complex systems, e.g., electrolytes[218], proteins[219, 220], biomolecules[221] and micellar surfaces[222]. There are geometric[223] and energetic[224] criteria to define a HB. Here we use the geometric one: Two water molecules are H-bonded if their inter-oxygen distance between a specific tagged pair of water molecules is less than cutoff radius $r^{\mathrm{c}}_{\mathrm{OO}}$ and the H-O$\cdots$O angle is less than cutoff angle ϕ^{c}[225–227]. The value $r^{\mathrm{c}}_{\mathrm{OO}}$ corresponds to the first-minimum position of the O–O radial distribution function (RDF) of water[224]. The choice for ϕ^{c} for water-water molecules is obtained by studying the average number of H-bonds, as a function of ϕ^{c}[228]. We call this definition of HB the acceptor-donor-hydrogen (ADH) criterion. To compare the impact of different HB definitions on HB dynamics, we also use another definition of HB in our analysis. When the distance between the oxygen atoms of two water molecules is less than $r^{\mathrm{c}}_{\mathrm{OO}}$, and the O-H$\cdots$O included angle is greater than cutoff angle θ^{c}, then we say that there is a HB between the two molecules. We denote this definition as acceptor-hydrogen-donor (AHD) criterion. In this thesis, we use $r^{\mathrm{c}}_{\mathrm{OO}} = 3.5$ Å both for the ADH and AHD criteria, $\phi^{\mathrm{c}} = 30^\circ$ for the ADH criterion, and $\theta^{\mathrm{c}} = 120^\circ$ for the AHD criterion.

The configuration criterion above allows us to define a variable $h[r(t)] = h(t)$, the HB population. Here a configuration $r(t)$ denotes the positions of all the atoms in the system at time t[217]. The $h(t)$ has a value 1 when the particular tagged pair of molecules are bonded, and 0 otherwise. The fluctuation or deviation in the dynamical variable $h(t)$ from its time-independent equilibrium average $\langle h \rangle$, is defined by[229]

$$\delta h = h(t) - \langle h \rangle.$$

Since the probability that a specific pair of molecules is bonded in a large system is extremely small, i.e., the time average of h is zero, or $\langle h \rangle = 0$, then

$$\delta h(t) = h(t).$$

Therefore, $h(t)$ describe the fluctuation $\delta h(t)$ of the HB population.

While the equilibrium average of $\delta h(t)$ is zero, we can obtain useful information by considering the equilibrium correlations between fluctuations at different times. The correlation between $\delta h(t)$ and $\delta h(0)$ can be written as

$$\langle \delta h(0) \delta h(t) \rangle = \langle h(0) h(t) \rangle - \langle h \rangle^2 = \langle h(0) h(t) \rangle,$$

where the averaging $\langle \cdots \rangle$ is to be performed over the ensemble of initial conditions.

In this paragraph, we use the following three correlation functions to describe the HB dynamics of the water/vapor interface: the HB population ACF $c(t)$, the continuum HB population correlation function (also called survival probability) $s(t)$ and the reactive flux $k(t)$[230].

Hydrogen bond population auto-correlation function $c(t)$ The structural relaxation of H-bonds is described by the ACF $c(t)$ of the HB population, i.e.,

$$c(t) = \langle h(0) h(t) \rangle / \langle h \rangle. \tag{2.53}$$

With the aid of the ergodic principle, the ensemble average $\langle \cdots \rangle$ is implemented by the time average. The $\langle h \rangle$ is the probability that a pair of randomly chosen water molecules in the system is H-bonded at any time t. As examples, the dynamics of the inter-oxygen distance $r_{\mathrm{OO}}(t)$, the cosine of the H$-$O$\cdots$O angle ($\cos\phi(t)$) and the HB population operator $h(t)$ for a HB in a DFTMD simulated water cluster $(\mathrm{H_2O})_n$ (n=5) at 300 K is displayed in Fig. 2.3, respectively.

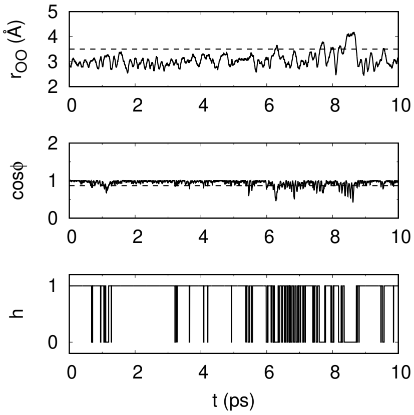

FIGURE 2.3: Dynamics of $r_{\mathrm{OO}}(t)$ (top panel), $\cos\phi(t)$ (middle panel), and $h(t)$ (bottom panel) for a typical HB in a water cluster. The dashed lines show the inter-oxygen distance boundary $r^{\mathrm{c}}_{\mathrm{OO}}$=3.5 Å (top panel) and criterion of cosine of H$-$O$\cdots$O angle $\cos\phi^{\mathrm{c}}$ with ϕ^{c}=30° (middle panel), respectively.

In a large system that consists of many water molecules, the probability that a specific pair of water molecules are H-bonded is extremely small. Therefore, $c(t)$ relaxes to zero when t is large. The function $c(t)$ measures correlation in $h(t)$ independent of any possible bond breaking events. It is one of the intermittent HB correlation functions, introduced by Stillinger, Rapaport and others[224, 230–237], and can be studied by a continuous function, the probability density. From $c(t)$, the HB relaxation time τ_{R} can be computed by

$$\tau_{\mathrm{R}} = \frac{\int t c(t) \mathrm{d}t}{\int c(t) \mathrm{d}t}. \tag{2.54}$$

The ACF $c(t)$ for the simulated bulk water is shown in Fig. 2.4 a (for computational details see Appendix B). We can obtain the relaxation time from Eq. 2.54: $\tau_R = 14.01$ ps for the ADH definition, and $\tau_R = 14.16$ ps for the AHD definition.

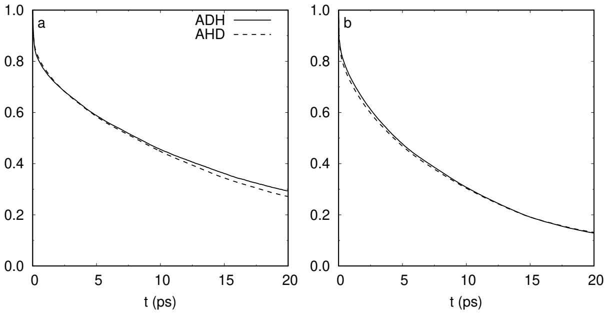

FIGURE 2.4: The $c(t)$ for bulk water, as computed from the ADH (solid line) and AHD (dashed line) criterion of H-bonds. (a) the interchange processes are included; (b) The interchange processes are neglected.

The method of HB population-based HB dynamics has been frequently used in previous literature[217, 218, 238]. The basis is the population operator $h(t)$ of the HB formed between two water molecules. The function $c(t)$ is interpreted as the probability that the HB is intact at time t, if the pair of water molecules are H-bonded at time zero.

When a pair of water molecules a and b are H-bonded, there are 4 different forms of possible H-bonds . In other words, there are exchange processes, i.e., interchange tunneling and bifurcation tunneling, during the dynamics. After an exchange process, a pair of bonded molecules still form H-bonds. In the above definition, we have not included this interexchange process, i.e., H-bonds before and after the interexchange process are regarded as the same HB. If we consider this interexchange process in the definition of HB population, the corresponding function $c(t)$ will be slightly different (Fig. 2.4 b). In the next paragraphs, for the sake of simplicity, we will ignore this interchange process and simply regard the H-bonds before and after the exchange process as the same HB. Comparing Fig. 2.4 a and b, we find that the relaxation in the latter is faster than that in the former, because the bifurcation tunneling (hydrogen exchange) is considered.

Besides, in Fig.s 2.4 a and 2.4 b, we plotted $c(t)$ for bulk water, using the ADH and AHD criteria of HB. We find that the relaxation time of H-bonds is not affected by the HB criteria.

Because the thermal motion can cause distortions of H-bonds from the perfectly tetrahedral configuration, water molecules show a librational motion on a time scale of ~ 0.1 ps superimposed to rotational and diffusional motions (> 1 ps), which causes a time variation of interaction parameters. A new HB population $h^{(d)}(t)$ was also defined to obviate the distortion of real HB dynamics[218, 224]. The $h^{(d)}(t)$ is 1 when the inter-oxygen distance of a particular tagged pair of water molecules is less than $r^{\mathrm{c}}_{\mathrm{OO}} = 3.5$ Å at time t and 0 otherwise. The difference between the operators $h^{(d)}(t)$ and $h(t)$ is that there is no restriction on the angle. Therefore, those molecular pairs that meet the condition of $h^{(d)}(t) = 1$ may not meet the condition of $h(t) = 1$. That is, the H-bonds between the tagged molecular pairs that satisfy the condition $h^{(d)}(t) = 1$ may have been broken, but they may more easily form H-bonds again. The function

$$c^{(d)}(t) = \langle h(0)h^{(d)}(t)\rangle / \langle h\rangle \tag{2.55}$$

is the probability that the specific two water molecules are located in reformable region ($r_{\mathrm{OO}} < r^{\mathrm{c}}_{\mathrm{OO}}$) at time t, if they were H-bonded at time zero. The time correlation function

$$n(t) = \langle h(0)[1 - h(t)]h^{(d)}(t)\rangle / \langle h\rangle \tag{2.56}$$

represents the probability at time t that a tagged pair of initially H-bonded water molecules are not bonded but remain separated by less than $r^{\mathrm{c}}_{\mathrm{OO}}$, $1 - h(t)$ describes the breaking of a HB at time t after its formation at time $t = 0$. The probability at time t that a pair of water molecules bonded at the initial moment does not be bonded but the distance between their oxygen atoms is still less than $r^{\mathrm{c}}_{\mathrm{OO}}$ is calculated according to

$$n(t) = \int_0^t dt' k_{\mathrm{in}}(t'), \tag{2.57}$$

where $k_{\mathrm{in}}(t) = -\langle \dot{h}(0)[1 - h(t)]h^{d}(t)\rangle / \langle h\rangle$ is the restricted rate function.

Continuum HB population correlation function $s(t)$ Another scheme to describe the HB dynamics is the continuum HB population correlation function $s(t)$, or survival probability[218] for a newly generated HB. It is defined as

$$s(t) = \langle h(0)H(t)\rangle / \langle h\rangle, \tag{2.58}$$

where $H(t) = 1$ if the tagged pair of molecules, remains *continuously* H-bonded till time t and 0 otherwise. It describes the probability that an initially H-bonded molecular pair remains bonded at all times up to t[239]. The $s(t)$ for the simulated bulk water according to the formula 2.58 is shown in Fig. 2.5.

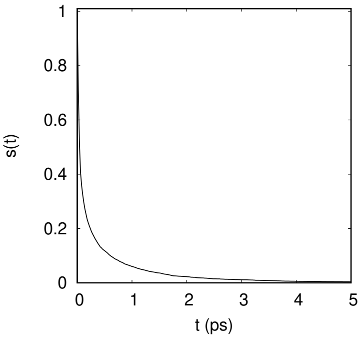

FIGURE 2.5: Time dependence of $s(t)$ for bulk water.

The average continuum HB lifetime $\langle\tau_\mathrm{a}\rangle$ is calculated by the integration of $s(t)$ over t (for detailed derivation see Appendix C.1) :

$$\langle\tau_\mathrm{a}\rangle = \int_0^\infty s(t)dt. \tag{2.59}$$

The time derivative of $s(t)$

$$P_a(t) = -\frac{\mathrm{d}s(t)}{\mathrm{d}t}$$

represents the first passage time probability density of H bonds. $P_a(t)$ is also called probability distribution of HB lifetimes[240–243], or histogram of HB lifetimes[232, 244]. It denotes the probability of the first HB breaking in time t after it has been detected at $t = 0$, i.e.,

$$s(t) = \int_t^\infty P_a(t')dt'. \tag{2.60}$$

Reactive Flux $k(t)$ The rate of relaxation to equilibrium is characterized by the reactive flux correlation function,

$$k(t) = -\frac{\mathrm{d}c(t)}{\mathrm{d}t}, \tag{2.61}$$

i.e., $k(t) = \langle j(0)[1 - h(t)]\rangle / \langle h\rangle$[149, 217], where $j(0) = -\mathrm{d}h/\mathrm{d}t|_{t=0}$ is the integrated flux departing the HB configuration space at time $t = 0$ (for detailed derivation see Appendix C.2). $-k(t)$ is the average rate of change of HB population for the trajectories in which the HB is broken at a time t later[217], independent of possible breaking and reforming events in the interval from 0 to t. Therefore, $k(t)$ measures the effective decay rate of an initial set of H-bonds[229, 235].

Assuming that each HB acts independently of other H-bonds, from detailed balance condition, we obtain

$$\tau_{\mathrm{HB}} = \frac{1-\langle h \rangle}{k}, \tag{2.62}$$

where k is the rate constant of breaking a HB (forward rate constant)[245, 246]. For an aqueous interface, the probability that a given tagged molecule pair forms a HB is very low, i.e., $\langle h \rangle \ll 1$. Therefore, from Eq. 2.62, k is related to the average HB lifetime by $\tau_{\mathrm{HB}} = 1/k$. Using k' to represent the rate constant from the HB *on* state to the HB *off* state for a tagged pair of molecules (backward rate constant), the reaction time constant τ_{re} is

$$\tau_{\mathrm{re}} = \frac{1}{k+k'}.$$

Chapter 3

Alkali nitrate clusters

There are two ways of obtaining highly specific information on solvation structures: studying gas-phase clusters consisting of ions surrounded by a few water molecules[247, 248], and exciting and detecting a dissolved prob molecule[249]. Due to the experimental difficulties, most information on the dynamics of aqueous solvation shells was obtained from MD simulations[218, 250]. In this chapter, DFTMD simulations of gas phase clusters including alkali metal cations, nitrate ions and a few water molecules have been used to obtain these specific information and to understand the effects of alkali cations and nitrate anions on H-bonding[251, 252]. The VDOS is used to extract the vibrational signatures for water molecules in these systems. In Paragraphs 3.1 and 3.2, the effect of the anion and the cation are separately investigated. The two clusters, $[NO_3{\cdot}(H_2O)_3]^-$ and $[Li{\cdot}(H_2O)_4]^+$, are used to study the structural and dynamical properties of water clusters with nitrate ions and with alkali cations. In Paragraph 3.3, the effects of alkali metal cations and nitrate anion are discussed within clusters containing both cations and anions and an increasing number of water molecules.

3.1 Cluster of nitrate and water molecules

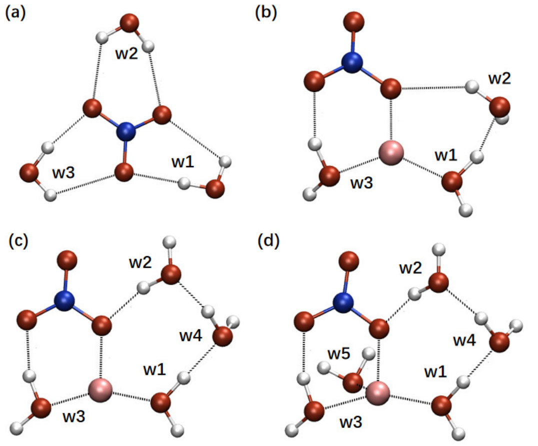

FIGURE 3.1: Geometry optimized structure of clusters: (a) $[NO_3{\cdot}(H_2O)_3]^-$; (b) $RNO_3(H_2O)_3$; (c) $RNO_3(H_2O)_4$; (d) $RNO_3(H_2O)_5$ (R=Li, Na, K). More structural properties are given in Appendix D.

First, we consider the nitrate–water cluster, $[NO_3{\cdot}(H_2O)_3]^-$. The symmetric isomer of the cluster, as shown in Fig. 3.1 a, is obtained by geometry optimization at the BLYP/TZV2P level of theory. According to the definition of HB[226, 227], there are three H-bonds in it, i.e., only one of the two OH bonds is H-bonded to NO_3^- in each water molecule. Therefore, the two OH bonds in each water molecule exhibit different vibrational features. Fig. 3.2 shows the VDOS for OH bonds in the cluster. For each water molecule, one OH bond is vibrating in the frequency range 3680–3700 cm^{-1}, while the other in the range 3380–3440 cm^{-1}. The difference of frequencies between these vibrational modes is about $\Delta\nu = 180$ cm^{-1}.

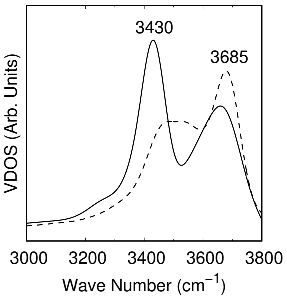

FIGURE 3.2: VDOS for the two OH bonds in w1 (Fig. 3.1 a) of $[NO_3{\cdot}(H_2O)_3]^-$.

Additionally, we label the three water molecules as w1, w2, and w3, respectively (Fig. 3.1 a). For the three water molecules, we find some differences in the structural parameters. Table D.5 gives the calculated lengths of H-bonds in the cluster $[NO_3{\cdot}(H_2O)_3]^-$. The average differences Δd between the H-bonds and other three bonds are 0.69 Å (Table D.2).

3.2 Cluster of alkali metal cation and water molecules

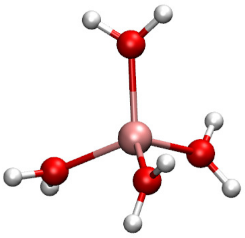

FIGURE 3.3: The cluster $[Li{\cdot}(H_2O)_4]^+$.

To find the effects of alkali cations on the structural properties of water, we investigated the cluster $[Li{\cdot}(H_2O)_4]^+$(Fig. 3.3). We concentrate on two aspects: the radial distribution function (RDF), and the VDOS for water molecules of this cluster.

Sharp peaks in the RDF (Fig. 3.4) show that the solvation shell of Li^+ is bound to all the four water molecules. The peak for g_{LiO} is at 2.02 Å, and for g_{LiH} is at 2.69 Å. The VDOS for water molecules in the cluster $[Li{\cdot}(H_2O)_4]^+$ is calculated from a 20-ps trajectory, during which one water molecule escaped from the bonding of the Li and then formed a new HB to another water

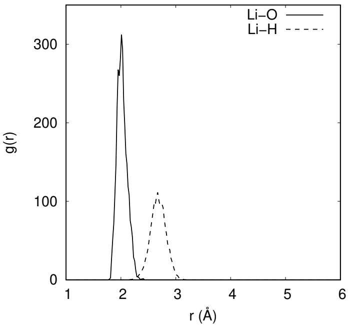

FIGURE 3.4: RDFs $g_{\text{Li-O}}$ and $g_{\text{Li-H}}$ for the cluster $[Li{\cdot}(H_2O)_4]^+$.

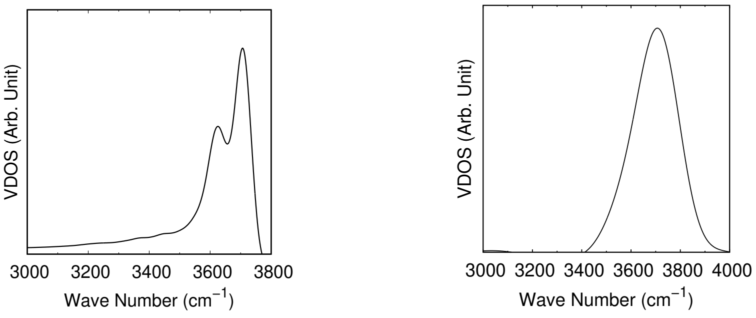

(A) (B)

FIGURE 3.5: (A) The VDOS for the four water molecules (all water molecules) in the cluster $[Li{\cdot}(H_2O)_4]^+$. (B) The VDOS for water molecules (three water molecules) bound to Li in the cluster $[Li{\cdot}(H_2O)_4]^+$.

molecule. Figure 3.5 A shows that there are two types of OH stretching modes in the cluster $[Li{\cdot}(H_2O)_4]^+$: free OH stretch which peaks at 3705 cm^{-1} and bonded OH stretch at 3625 cm^{-1}. However, water molecules just bound to Li has two degenerate free O-H stretching modes. The VDOS for water molecules only bound to Li (Fig. 3.5 B) shows that these water molecules only have free OH stretch, since there is only a broad stretching mode at 3705 cm^{-1}.

3.3 Clusters of alkali nitrate and water molecules

As a first minimal model system for the interface of alkali nitrate solution, we consider alkali nitrate water clusters including 3 to 5 waters. The idea is to investigate the effect of alkali nitrate on the vibrational properties of those water molecules which are directly H-bonded to the ions. In our simulations, clusters are geometry optimized and the most stable configurations are determined (Fig.s 3.1 b–d). The first interesting result is that for all the clusters containing 3 to 5 water molecules, a contact ion pair is maintained during the simulation trajectories where a *direct* interaction involves the cation and one of the nitrate oxygen's.

In the $LiNO_3(H_2O)_3$ cluster, there are three H-bonds and three Li-O bonds. The average lengths of them are given in Table 3.1. We use HB1, HB2 and HB3 to denote the HB between w1 and w2, w2 and NO_3^-, and w3 and NO_3^-, respectively (Fig. 3.1 b). Both the average lengths of HB1 and HB3 are very close to each other and both of them are smaller than that of HB2. Since both w1 and w3 are bound to Li^+, we calculate an average value $\bar{d}_{\mathrm{HB}} = 1.81$ Å of the lengths of HB1 and HB3. The difference between length of HB2 and $\bar{d}_{\mathrm{HB}}$ is $\delta d_{\mathrm{HB}} = 0.19$ Å. By testing the difference of environment of each H-bonds, we obtain that δd_{HB} comes from the difference between Li-O bonds and H-bonds.

Besides, the RDF between the alkali (Li^+, Na^+ or K^+) and the water O (panel a) and the nitrate O – water H (panel b) are reported in Fig. 3.6. The sharp and left-shifted peaks in the RDF (Fig. 3.6 b) show that the nitrate is solvated and in particular a stronger HB is formed in the presence of the cation in all three clusters.

The vibrational features associated to these small clusters are calculated from the VDOS and reported in Fig. 3.7. In the frequency range 3000–3800 cm^{-1}, each water molecule has two vibrational bands. In addition to the free OH peak at ~3700 cm^{-1},

TABLE 3.1: The average length r_a of H-bonds (Li-O bonds) in the cluster $LiNO_3(H_2O)_3$.

Bonds	r_a(Å)
HB1	1.83 ± 0.14
HB2	2.00 ± 0.25
HB3	1.79 ± 0.16
O(w1)–Li	1.95 ± 0.09
O(w3)–Li	1.92 ± 0.07
nitrate O–Li	1.91 ± 0.08

we see that the H-bonded band (HB band) is characterized by quite strong *red-shifted* peaks around 3200 cm^{-1}. These red-shifted peaks are associated to water molecules which are bound either to the cation or to both cation and anion and are different with respect to the peaks associated to the water molecules which only bound to the nitrate in the cluster $[NO_3{\cdot}(H_2O)_3]^-$ (3430 cm^{-1}, see Fig. 3.2).

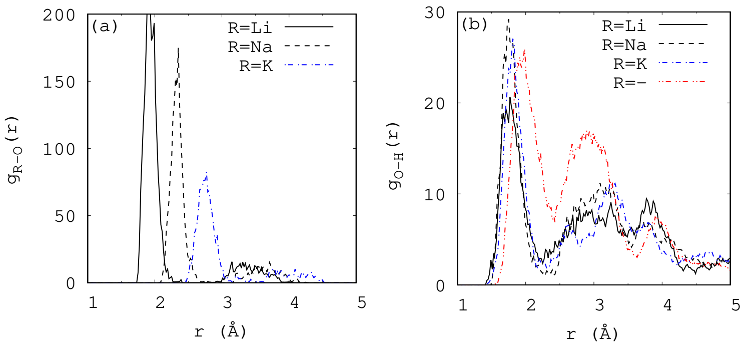

FIGURE 3.6: (a) RDF $g_{\text{R-O}}$ for clusters $RNO_3(H_2O)_3$ (R=Li, Na, K); (b) RDF $g_{\text{O-H}}$ for clusters $RNO_3(H_2O)_3$ and $[NO_3{\cdot}(H_2O)_3]^-$ (no alkali metal cation, denoted as "R=-").

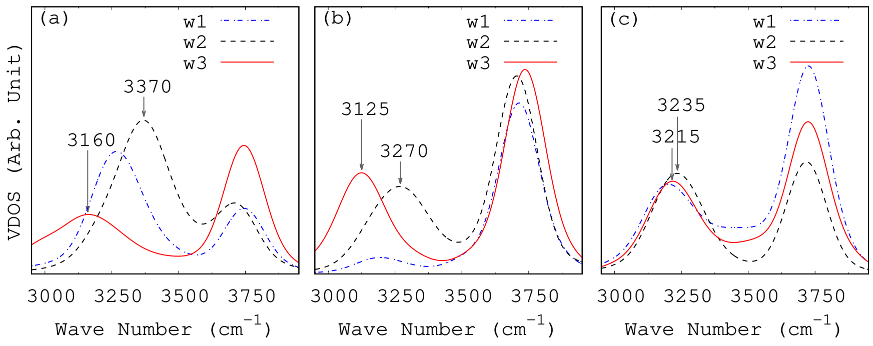

FIGURE 3.7: VDOS for H_2O in clusters: (a) $LiNO_3(H_2O)_3$, (b) $NaNO_3(H_2O)_3$ and (c) $KNO_3(H_2O)_3$. w1: H_2O bound to R and H_2O; w2: H_2O bound to nitrate and H_2O; w3: H_2O bound to R and nitrate.

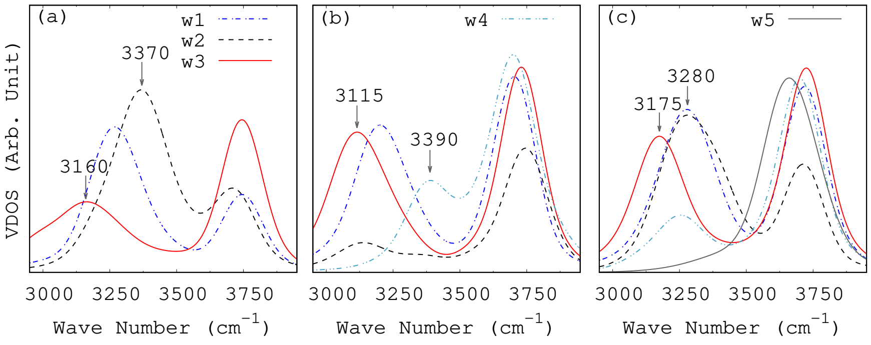

FIGURE 3.8: VDOS for H_2O in clusters $LiNO_3(H_2O)_n$: (a) $n = 3$; (b) $n = 4$; (c) $n = 5$. w1: H_2O bound to Li and H_2O; w2: H_2O bound to nitrate and H_2O; w3: H_2O bound to Li and nitrate; w4: H_2O bound to H_2O; w5: H_2O only bound to Li.

To explore the effect of adding some additional water molecules to the cluster, we considered clusters $RNO_3(H_2O)_n$ (n=4, 5; R=Li, Na, K). The most stable configurations are shown in Fig.s 3.1 c and d, and the corresponding VDOS for water molecules are shown in Fig.s 3.8 b and c for the clusters $LiNO_3(H_2O)_n$ (n=4 and 5). We find that the OH stretching peaks in the HB region are also quite red-shifted. The red shift is particularly strong for the water molecules which are directly interacting with the Li and those which are simultaneously bound to the Li and to the nitrate O's (e.g. w3).

We also calculated the effects of other alkali metal cations, namely Na^+ and K^+. The calculated VDOS for water molecules in clusters $NaNO_3(H_2O)_3$ and $KNO_3(H_2O)_3$ are shown in Fig.s 3.7 b and c, respectively. As in the case of $LiNO_3(H_2O)_3$, the HB bands are also characterized by red-shifted peaks around 3200 cm^{-1}. In addition, the peaks in the OH-stretching region are also compatible with infrared predissociation (IRPD) spectra which have been recorded for the $[Li{\cdot}(H_2O)_{3-4}Ar]^+$ clusters[253–255] and for $[Na{\cdot}(H_2O)_{4-7}]^+$ and $[K{\cdot}(H_2O)_{4-7}]^+$ clusters[256], although there no nitrate is present and only the effect of the cation was investigated.

To summarize, the vibrational spectra from the clusters clearly point to red-shifted peaks which are not recorded in VSFG spectra at the solution/vapor interface for the $LiNO_3$ solution. In other words, these clusters are not really representative of the solvation structures presents in the $LiNO_3$ solution. Therefore, these small clusters cannot be directly used to describe the topmost layer of the $LiNO_3$ solution, and we need to build more realistic models to capture main features of the interface. In particular, according to the cluster picture one would be tempted to rule out the possibility of a contact ion pair at the interface.

Chapter 4

VSFG spectroscopy of the water/vapor and solution/vapor interfaces

In Chapter 3, we investigated the VDOS for water clusters containing nitrate and alkali metal ions. We found that small clusters cannot be directly used to model interfaces of aqueous solutions, and we need to build more realistic ones to capture the main features of interfaces. In this chapter, we will analyze the structure and dynamics of solutions containing an alkali cation and a nitrate (iodide) ion and to provide a microscopic interpretation of recent experimental results[124, 127, 134].

The goal of this chapter is to find the origin of the main characteristics of the VSFG spectrum of the $LiNO_3$ solution, and provide a molecular picture to interpret the recorded spectra. To achieve this goal, we simulate a solution/vapor interface including Li^+ and NO_3^-, as shown in Fig. 4.1, and extract the vibrational spectroscopic properties of the interface.

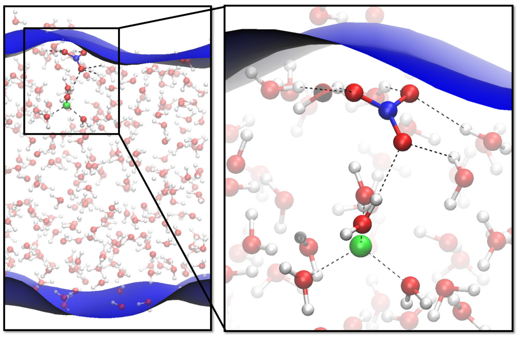

Figure 4.1: The salty water interface of $LiNO_3$ solution (left, top) and the water/vapor interface (left, bottom). The right panel shows that the Li^+ and the NO_3^- ions are separated by a water molecule at the salty interface.

We consider a model for the interface where a slab of 256 water molecules containing one Li^+ and one NO_3^- ($LiNO_3(H_2O)_{256}$) is included in a periodic simulation box of $19.70 \times 19.70 \times 40.00$ Å^3 at 300 K. The slab is 20 Å thick and infinite in the x and y direction, while the separation between the periodic slabs in the z direction is 20 Å. The $LiNO_3$ was inserted at one of the two interfaces, with the NO_3^- residing in the topmost layer and the Li^+ residing somewhat deeper at about 5 Å from the surface. In this way we have a model with one *salty* interface and one *neat* interface which can be used as a reference. To provide the interpretation to the above experimental results, the following analysis tools are used: (1) VDOS; (2) calculation of the nonlinear susceptibility; (3) reconcile of the interface and cluster picture. In

Paragraph 4.1, the VSFG spectrum of the alkali nitrate interface of aqueous solutions is calculated, to find the connection between these two kind of models: the interface and cluster picture. Additionally, to study the effect of cations, interfaces of alkali iodide solutions are also studied in Paragraph 4.2.

4.1 VSFG spectra of the $LiNO_3$ solution/vapor interface

It has been often put forward the idea that in nitrate solution anion and cation are paired at the interface and form a double layer. Based on the relatively high propensity of NO_3^- for the interface[257] we decided to start DFTMD simulations with the anion at the water surface and to investigate the possibility that $LiNO_3$ forms a stable water-separated ion pair at the interface. The idea that nitrate ions form water-separated pair where the Coulomb interaction is shielded was already suggested for divalent cation nitrate[129]. The first result is that such model system is stable and the NO_3^- remains within the topmost water layer during all the simulation time. This result can be found in the probability distribution along z-axis of the simulation box (Fig. 4.2). This is in agreement with previous simulation results based on polarizable classical force field[258] and also with some DFTMD work on nitric acid, which was also found stable at the interface[259]. Moreover, the Li^+ remains relatively close to the surface, in a water sub-layer forming a water separated ion pair with NO_3^- at the interface.

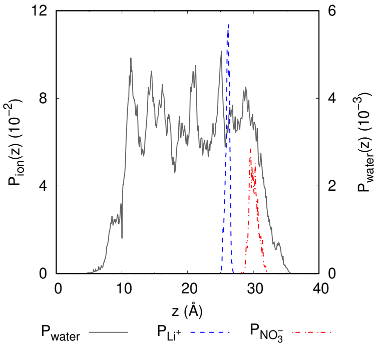

FIGURE 4.2: Probability distributions of ions and water molecules for $LiNO_3$ water interface along the normal direction.

We have calculated the nonlinear susceptibility for the two interfaces, namely the one containing the $LiNO_3$ pair (salty interface) and the neat one which does not include any ion. The calculated imaginary part is reported in panel a and the intensity in panel b of Fig. 4.3. The calculated intensity spectra show a depletion of the 3200 cm^{-1} region as in the experiments (Fig. 4.4). The same feature is also shown in the imaginary part. Also the calculated spectra show that the free OH region is less intense in the salty interface with respect to the water/vapor interface.

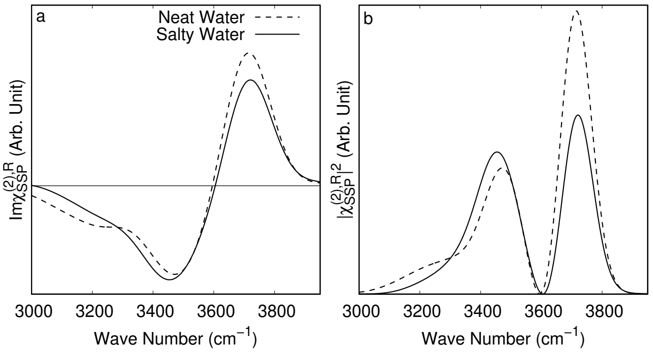

FIGURE 4.3: (a) The $\Im\chi^{(2),R}_{SSP}$ and (b) $|\chi^{(2),R}_{SSP}|^2$ for water molecules at the interface of LiNO$_3$ solution.

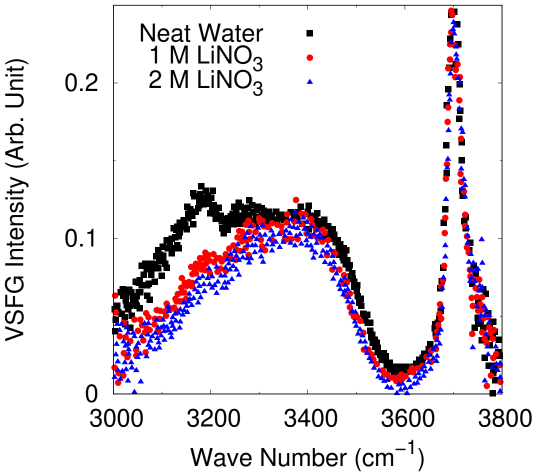

FIGURE 4.4: Experimental VSFG intensity of LiNO$_3$ solutions, compared with that of neat water[134].

To find the microscopic origin of the depression of the lower frequency region, we have also decomposed the salty water interface VDOS into the contributions coming from the different water molecules. The VDOS $g_z(\nu)$ for the water molecules at the interface, which is calculated from the FT of atoms' ACF of velocity in the z-axis projection, gives a rough value of the thickness d of the interface. Using 1, 2 and 5 Å thicknesses, we have defined three different interfacial regions. For the LiNO$_3$ solution, $g_z(\nu)$ of the salty and neat water interfaces in the slab is reported in Fig. 4.5. When d is equal to 1 Å, water molecules at the solution surface have lower free OH stretching frequency than that in pure water. This means that there are less water molecules with free OH stretch at the interface of LiNO$_3$ solution than at the water/vapor interface. It compares very well with the experimental result of the surface propensity of nitrate anions in water solution[127]. Meanwhile, compared to the result of the water/vapor interface, the H-bonded band of the VDOS for the salty interface has a blue shift of $\Delta\nu \approx 80$ cm^{-1}. As we increase the value of d, the difference between the VDOS of the water/vapor and solution/vapor interface is gradually reduced. When d is equal to 2 Å, the amount of blue shift $\Delta\nu$ reduces to 55 cm^{-1}(Fig. 4.5 b); when d is 5 Å, $\Delta\nu$ is almost zero (Fig. 4.5 c). This tendency indicates that ions' (Li$^+$, Na$^+$, K$^+$ and NO$_3^-$) effects can be found only on the water molecules in the top ~5-Å layer of the interface. As the thickness of the interfacial water layer included in $g_z(\nu)$ increases, the free OH signal is depressed and at the same time the H-bonded OH bands for the salty and neat water interfaces become more similar.

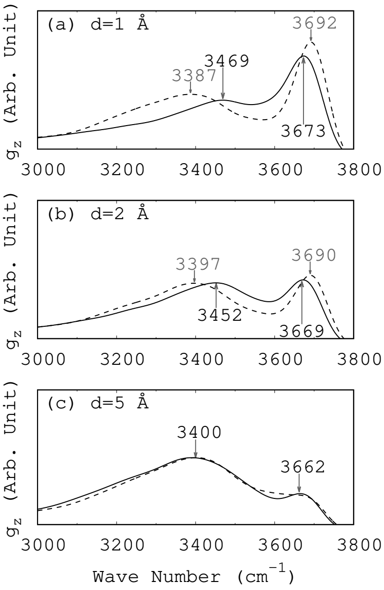

FIGURE 4.5: VDOS $g_z(\nu)$ for water molecules at the interface of $LiNO_3$ solution (solid line) and at the water/vapor interface (dashed line). (a): $d = 1$ Å; (b): $d = 2$ Å; (c): $d = 5$ Å.

To explore the reason for the blue shift of the H-bonded OH stretch at the interface, we also calculated the VDOS $g(\nu)$ for the six water molecules in the subsystems $NO_3^-(H_2O)_6$ (the structure of this cluster is shown in Fig. 4.1). Compared to the VDOS for H-bonded water molecules at the water/vapor interface, a blue shift of $\Delta\nu' \approx 80$ cm^{-1} on the vibrational modes of water molecules is found at the interface (Fig. 4.6). It indicates that a HB with nitrate acceptor (nitrate–water bond) is weaker than that with water acceptor (water–water bonds), since the amount of O–H frequency shift reflects the strength of the H-bonds[212, 260]. This feature agrees with experimental result obtained by Jubb *et al.*[124]. The OH stretching band at 3394 cm^{-1} (for T = 300 K) also agrees with that of liquid pure water (3400 cm^{-1}[261]). Since $\Delta\nu'$ is almost equal to $\Delta\nu$ for the case of $d = 1$ Å, we conclude that the blue shift of the VDOS at the salty water interface is mainly caused by the H-bonds between the uppermost nitrate and water molecules at the solution/vapor interface.

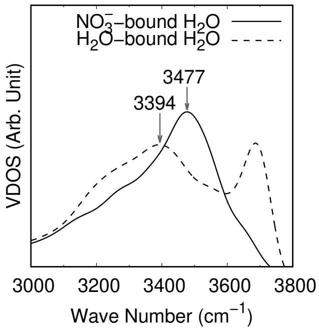

FIGURE 4.6: VDOS for the six water molecules bound to NO_3^- at the $LiNO_3$ solution/vapor ($LiNO_3$/vapor) interface (salty water) and that for 15 water molecules at the top layer (d=1 Å) of the neat water.

First, there are two reasons to support the view that NO_3^- is located at the top layer of the surface. (1) The reduced intensity of the free OH peak can be explained by that NO_3^- is at the surface. The 3700 cm^{-1}-peak is the character of free OH stretch in water molecules with their dipole moment pointing to the vapor phase[74, 262]. NO_3^- binds to water molecules from the water surfaces which have less free OH, therefore reduce the intensity of the free OH peak. (2) Those water molecules directly H-bonded to the NO_3^- ion show an higher frequency band with respect to the neat water at the interface, which explain the increased intensity of the 3400 cm^{-1} band.

Second, the statement that Li^+ and NO_3^- are separated is confirmed by Ref. [32, 263], which show that the alkali metal cations are of *small* composite partition coefficients ($k_{p,K^+} = 0.00 \pm 0.03$, $k_{p,Na^+} = 0.05 \pm 0.17$, $k_{p,Li^+} = 0.14 \pm 0.18$), i.e., these cations are more surface-excluded than NO_3^- ($k_{p,NO_3^-} \approx 1.0$). How do we reconcile the interface picture and the cluster picture? In the small clusters (with 3, 4 and 5 water molecules) the contact ion pair is the most stable configuration, while at the interface the water *separated* configuration is the most stable. This result suggests that a sufficiently large number of water molecules is required to stabilize a water separated ion pair where NO_3^- still reside at the surface. To verify this idea we extracted a relatively large cluster with 30 water molecules from the full interface, centered around the Li^+ ion and we simulate it in the gas phase. For this medium size cluster we calculated the free energy difference between the water separated and the contact ion pair. The details of the calculation is given in Appendix D.3. The blue-moon ensemble method[264–266] is used to calculate the free energy as a function of the distance r between alkali metal cation and the nitrogen of NO_3^- in $LiNO_3(H_2O)_{30}$. We find that (Fig. 4.7) there are two minima in the free energy at $r = 2.9$ Å (configuration A) and $r = 4.3$ Å (configuration B). Li^+ and NO_3^- are bonded in configuration A, but are water-separated in configuration B. The free energy difference $\Delta F_{AB} = F_A - F_B$ is equal to 0.3 kcal/mol. The energy barrier between C and A (B) is $\Delta F_{CA} = 1.2$ kcal/mol ($\Delta F_{CB} = 1.5$ kcal/mol), i.e., configuration B is more stable than A. For the interface system, NO_3^- resides on the surface and Li^+ in the layer below, separated from NO_3^- by water molecules. Therefore, no obvious red-shift induced by alkali metal cation and nitrate is obtained in the VSFG spectrum. Our results show that as the number of waters increases, the first solvation shell around the Li^+ is stabilized and the water separated ion pair is equally stable as the contact ion.

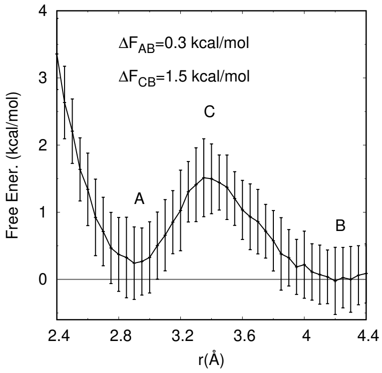

FIGURE 4.7: Free energy profile with respect to the distance r between Li^+ and the nitrogen in NO_3^- in the cluster $LiNO_3(H_2O)_{30}$. *A*: configuration A where r is equal to 2.9 Å; *B*: configuration B where r is equal to 4.3 Å; *C*: the transition states.

Finally, at the salty interface, one single water is constantly shared between the

Li^+ and the NO_3^- and indeed this water shows a vibrational peak with a very pronounced red shift. This clearly reminds the water peak we already observed in the small clusters, however if the full interface is considered its signature do not emerge from the spectra, as it can be seen in Fig. 4.3.

From the three arguments above, our conclusion is thus that in the VSFG spectrum we do only see the changes induced by the NO_3^- at the interface. This points to a clear 3400 cm^{-1} band in the vibrational spectra. The Li^+ resides in the sub-layer forming a water separated ion pair at the interface.

Until now, we have analyzed the behaviour of a salty interface containing $LiNO_3$. Both the measured and calculated VSFG spectra show a reduced intensity of the lower frequency portion of the HB region, namely around 3200 cm^{-1}, when compared to the water/vapor interface. This reduction can be attributed to the H-bonds which are established between the NO_3^- and the surrounding water molecules at the interface. This effect is only related to the presence of NO_3^- at the water surface and is not affected by the Li^+ ions. Indeed we have shown that although Li^+ can reside relative close to the water surface, also forming a water mediated ion pair with NO_3^-, its effect on the VSFG spectrum is not visible. The water which mediate the interaction between the NO_3^- and Li^+ ions would produce a red-shifted peak in small water cluster, but its influence is not visible neither in the calculated or the measured VSFG spectra. We have also shown that the very simple models, such as small clusters are not suitable to reproduce the experimental spectra and cannot provide a microscopic interpretation of the spectra. A realistic model of the interface is required to address the perturbation of the ion on the water surface. Besides, how do other ions, such as Li^+, Na^+, and K^+, etc., affect the VSFG spectra of the interface? To apply our method and explain the experimental observations, we constructed the interface of lithium iodide, sodium iodide, and potassium iodide solutions and calculated the VSFG spectra. Experiments have proved that iodide ions have similar properties to nitrate ions in many aspects. For example, they tend to the interface and are easily polarized. On the other hand, when we analyze the effects of cations, the model containing iodide ions is more simplified than the model containing nitrate ions.

4.2 VSFG spectra of the alkali iodide solution/vapor interfaces

Direct investigations of the dynamics of simple ions, such as I^- and Br^-, at water interfaces, by the x-ray photoelectron spectroscopy[267] and MD simulations[82, 83] have shown that these ions could accumulate at the interface. To provide a molecular interpretation of the recorded spectra we perform here AIMD simulations of salty solutions containing alkali metal cations and iodide.

A model for the electrolyte solution/vapor interface is built, in which a slab of 118 water molecules containing two Li^+ cations and two I^- anions is included in a period simulation box of $15.60 \times 15.60 \times 31.00$ Å^3 (0.9 M). The slab is about 20 Å thick and infinite in the x and y direction, while the separation between the periodic slabs in the z direction is about 20 Å. In the initial configuration, the LiI was inserted at one of the two interfaces, with the I^- residing in the topmost layer and the Li^+ residing somewhat deeper at about 5 Å from the surface. Using the same method, we also constructed interface models of NaI and KI solutions for DFTMD simulations. In all the cases the systems were equilibrated for 30 ps and then a production time of 60 ps was considered for the analysis.

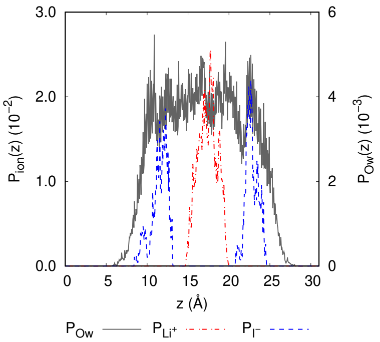

FIGURE 4.8: Probability distribution $P(z)$, along the normal direction (z-axis), of Li^+, I^- and O in LiI solution/vapor interface.

Structural Properties First, we have calculated the probability distributions of Li^+, I^- and O with respect to the normal direction (z-axis) of the LiI solution surface. The results are given in Fig. 4.8, where we see that the I^- anions prefer to be located at the surface of the solution, while the Li^+ cations prefer to stay below the surface. This result is consistent with the calculations by Ishiyama and Morita[85, 88] on a similar system.

The effects of Li^+ and I^- on the organization of water molecules are shown in Li–water (Fig. 4.9 a) and I–water RDFs (Fig. 4.9 b), respectively. In Fig. 4.9 a, the first two peaks of $g_{\text{Li-O}}$ and $g_{\text{Li-H}}$ are located at 1.97 Å and 4.12 Å, and, 2.61 Å and 4.73 Å, respectively. Here we consider the *difference* δ_1 between the first peaks' positions of $g_{\text{X-O}}$ and $g_{\text{X-H}}$. Thus, one can determine the differences of the peaks' positions, which are shown in Table 4.1. The difference δ_1 between the first peaks, 0.67 Å, is shorter than the OH bond length R_{OH} in a water molecule which is about 0.98 Å, i.e.,

$$\delta_1 < R_{\text{OH}}. \tag{4.1}$$

This relation reflects that all the water molecules around Li^+ have their O atom facing Li^+. Similarly, we find from Fig. 4.9 b that the distance δ_1 between the first peaks of the two RDFs is 0.93 Å, and it can be seen that δ_1 is slightly equal to R_{OH} (about 0.98 Å), i.e.,

$$\delta_1 \approx R_{\text{OH}}. \tag{4.2}$$

This relation shows that for the water molecules around I^-, only one H atom forms an I–H bond with I^-. This relation also implies that I^- is essentially at the outermost layer of the solution interface. This is consistent with many of the previous results from MD simulations[82, 268] and experimental results for the increase in surface tension relative to neat water for aqueous solutions of sodium halide salts[83, 269–271].

TABLE 4.1: Peaks of $g_{\text{Li-O}}$ and $g_{\text{Li-H}}$ for the LiI solution. (unit: Å, the same for Tables 4.2 and 4.3)

$g_{\text{Li-O}}$	$g_{\text{Li-H}}$	δ_1
1.97	2.64	0.67
4.12	4.73	0.61
6.13	6.93	0.80

For the NaI and the KI interfaces, the effects can be seen from Fig.s 4.10 and 4.11. For Na^+ and K^+, the relation $\delta_1 < R_{\text{OH}}$ remains, i.e., δ_1 is equal to 0.61 Å for Na^+ and δ_1 is 0.56 Å for K^+. For I^-, the relation $\delta_1 \approx R_{\text{OH}}$ still holds (Fig.s 4.10 a

TABLE 4.2: Peaks of $g_{\text{Na-O}}$ and $g_{\text{Na-H}}$ for the NaI solution.

$g_{\text{Na-O}}$	$g_{\text{Na-H}}$	δ_1
2.41	3.02	0.61
4.55	4.96	0.41
6.48	7.20	0.72

TABLE 4.3: Peaks of $g_{\text{K-O}}$ and $g_{\text{K-H}}$ for the KI solution.

$g_{\text{K-O}}$	$g_{\text{K-H}}$	δ_1
2.84	3.40	0.56
4.71	5.51	0.80
6.78	7.49	0.71

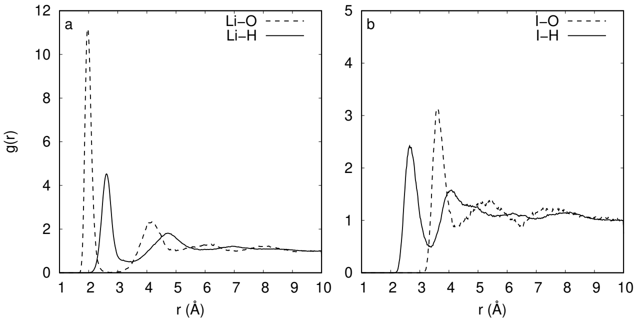

FIGURE 4.9: RDFs for the LiI solution/vapor interface: (a) $g_{\text{Li-O}}$ and $g_{\text{Li-H}}$. The first two peaks of $g_{\text{Li-O}}$ and $g_{\text{Li-H}}$: 1.97 and 4.12 Å, and, 2.61 and 4.73 Å, respectively. (b) $g_{\text{I-O}}$ and $g_{\text{I-H}}$. The first two peaks of $g_{\text{I-O}}$ and $g_{\text{I-H}}$: 3.62 and 5.28 Å; and, 2.69 and 4.11 Å, respectively.

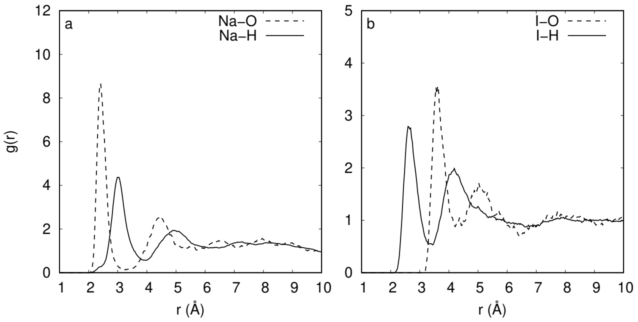

FIGURE 4.10: RDFs for the NaI solution/vapor interface: (a) $g_{\text{Na-O}}$ and $g_{\text{Na-H}}$. The first two peaks of $g_{\text{Na-O}}$ and $g_{\text{Na-H}}$: 2.41 and 4.55 Å, and, 3.02 and 4.96 Å, respectively. (b) $g_{\text{I-O}}$ and $g_{\text{I-H}}$. The first two peaks of $g_{\text{I-O}}$ and $g_{\text{I-H}}$: 3.59 and 5.04 Å; and, 2.63 and 4.15 Å, respectively.

and 4.11 a, and Tables 4.2 and 4.3). For I^- in the NaI interface, δ_1 is equal to 0.96 Å; and for I^- in the KI interface, δ_1 is 0.94 Å (Fig.s 4.10 b and 4.11 b). Therefore, these structural properties are similar to that in the LiI interface, except the larger solvation shells.

VSFG spectra The calculated VSFG spectra for the LiI, NaI and KI interfaces, are shown in Fig.s 4.12 to 4.14. In all the cases there is one free OH stretching band (3600–3800 cm^{-1}) and one bonded OH stretching band (3000–3600 cm^{-1}). These features are the same as that of the water/vapor interface. The sign of $\Im\chi^{(2),\text{R}}$ is

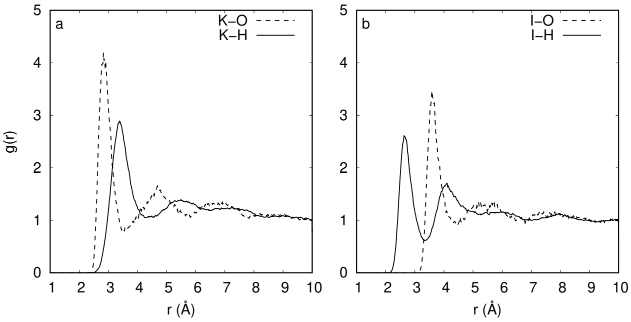

FIGURE 4.11: RDFs for the KI solution/vapor interface: (a) $g_{\text{K-O}}$ and $g_{\text{K-H}}$. The first two peaks of $g_{\text{K-O}}$ and $g_{\text{K-H}}$: 2.84 and 4.71 Å, and, 3.40 and 5.51 Å, respectively. (b) $g_{\text{I-O}}$ and $g_{\text{I-H}}$. The first two peaks of $g_{\text{I-O}}$ and $g_{\text{I-H}}$: 3.59 and 5.43 Å; and, 2.65 and 4.10 Å, respectively.

positive for the free OH peak while it is negative in the H-bonded region. This result is consistent with the VSFG spectrum calculated in Paragraph 4.1, i.e., (1) the anion–water bonds at interfaces decrease the amount of free stretching OH bonds (2) the free stretching peak in the intensity of VSFG decrease and the H-bonded stretching peak is shifted at the interfaces of LiNO_3 (or alkali iodide) solution.

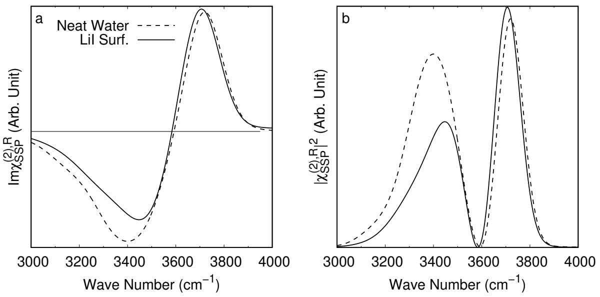

FIGURE 4.12: (a) $\Im\chi^{(2),\text{R}}_{SSP}$ and (b) $|\chi^{(2),\text{R}}_{SSP}|^2$ of the LiI solution/vapor (solid line) and the water/vapor (dashed line) interface. The data for the water/vapor interface is calculated from the DFTMD simulation for the water interface with the same thickness (5 Å) (the same for Fig.s 4.13 and 4.14).

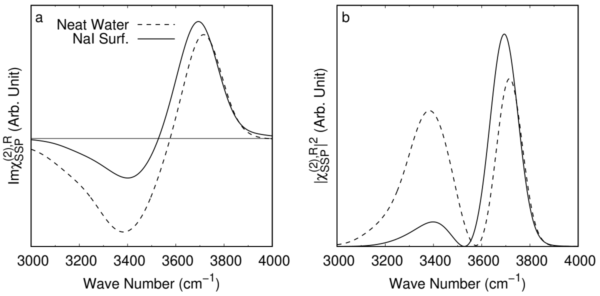

FIGURE 4.13: (a) $\Im\chi^{(2),\text{R}}_{SSP}$ and (b) $|\chi^{(2),\text{R}}_{SSP}|^2$ of the NaI solution/vapor (solid line) and the water/vapor (dashed line) interface.

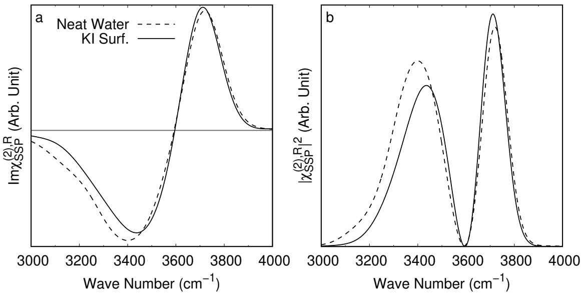

FIGURE 4.14: (a) $\Im\chi^{(2),R}_{SSP}$ and (b) $|\chi^{(2),R}_{SSP}|^2$ of the KI solution/vapor (solid line) and the water/vapor (dashed line) interface.

Compared with the water/vapor interface, the H-bonded peak of $|\chi^{(2),R}_{SSP}|^2$ for the NaI solution is blue-shifted, which is consistent with experimental results on the NaI solution[33, 69, 124, 272]. The H-bonded OH-stretching peak of $|\chi^{(2),R}_{SSP}|^2$ for the LiI and the KI solutions are also blue-shifted. These results support the idea that I^- is a strong structure-breaking anion. Secondly, the bonded OH-stretching region of the NaI solution is narrower than that of pure water. This result has also been obtained for the interface of the $LiNO_3$ solution. The retained high frequencies of these bonded OH-stretching peaks indicate that these molecules at the interfaces of these solutions are participating in weak H-bonding. The introduction of I^-, caused a slight decrease in the strong H-bonding region at 3200 cm^{-1} and relatively an increase in the weak H-bonding region at 3400 cm^{-1}. This result is consistent with experimental results in Ref.[124, 272].

Because of surface isotropy of the solutions[273], the $\chi^{(2),R}_{SSP}$ can be calculated either through $\chi^{(2),R}_{XXZ}$, or $\chi^{(2),R}_{YYZ}$. Here we report the comparison between $\Im\chi^{(2),R}_{XXZ}$ and $Im\chi^{(2),R}_{YYZ}$ for the KI solution in Fig. 4.15. They should be very close to each other, because the interfaces have rotational symmetry about the z-axis. It can be seen that the calculated spectra are very close to each other. From the results of the nonlinear susceptibilities, we conclude that water molecules at the interfaces of the LiI, NaI, and KI solutions are participating in weaker H-bonds, compared with those at the water/vapor interface. The simulation results permit to interpret the features present in the experimental spectra, which can be explained as consequence of the double layer formed by I^- on the topmost water layer and the alkali ion in the sublayer. Therefore, the VSFG experimental characteristics on alkali nitrate and alkali iodide solutions can be reproduced from our calculation method, which verifies the reliability of the method used in the current thesis to calculate VSFG spectra.

In view of the close relationship between the HB network and the VSFG spectra of solution interfaces, we will continue to study the properties of the water/vapor interface and the solution/vapor interface from the perspectives of HB dynamics and reorientation of water molecules in Chapters 5 and 6.

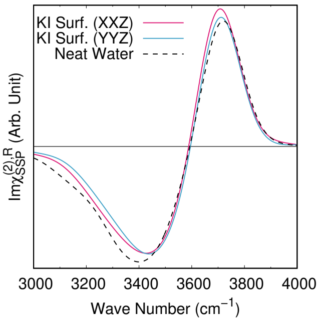

FIGURE 4.15: $\Im\chi^{(2),R}_{XXZ}$ and $\Im\chi^{(2),R}_{YYZ}$ spectra for the KNO_3 solution/-vapor interface.

Chapter 5

Hydrogen bond dynamics at the water/vapor interface

Hydrogen bonds play a critical role in the behaviour of bulk water[35, 148, 274], aqueous solutions[275], and water near interfaces[276]. There are many methods to study HB dynamics in water, solutions and interfaces, such as molecular dynamics simulation[130, 276–279], neutron scattering[280, 281], IR spectroscopy[282, 283], 2D-IR spectroscopy[144, 284] and 2D-SFG spectroscopy[285]. In this chapter, we will use the general concepts and methods of HB dynamics [148, 217, 229] introduced in Paragraph 2.6 in Chapter 2 to analyze the structure and dynamic properties of bulk water and the water/vapor interface.

5.1 Dynamical properties of H-bonds in bulk water and at the water/vapor interface

The bulk water and the interface between pure water and vacuum, i.e., the water/-vapor interface, are considered in this paragraph. All simulations in this chapter were performed at 300 K within the canonical (NVT) ensemble. The BLYP exchange and correlation functional[184, 185], and D3 dispersion corrections[98, 191] have been employed. The electron-ion interactions are described by GTH pseudopotentials[286, 287]. The length of the trajectory is 60 ps of physical time. The simulated bulk water consisted of 128 water molecules in a periodic cubic box of length $L = 15.64$ Å, which corresponds to a density of 1.00 g cm^{-3}. The simulated water/vapor interface consisted of 128 water molecules in a periodic box with size $15.64 \times 15.64 \times 31.28$ Å^3 (with a ∼15 Å separation between the periodic slabs in the z-direction).

Correlation functions $c(t)$, $n(t)$ and $k(t)$ As we have seen in the definition of the HB population $h(t)$, the cutoff radius depends on the RDFs of water. To provide a basis for subsequent calculation, we calculated the basic structural properties of the simulated bulk water. The O-O RDF is characterized by the first peak, which corresponds to the first solvation shell, followed by a minimum at 3.5 Å, which corresponds to the cutoff chosen in the definition of the HB criterium. The RDFs $g_{\mathrm{OO}}(r)$ and $g_{\mathrm{OH}}(r)$ for bulk water system are shown in Fig. 5.1.

The correlation functions $c(t)$ from the trajectory of a bulk water simulation calculated according to Eq. 2.53 with the ADH (solid line) and AHD (dashed line) definition of H-bonds are shown in Fig. 5.2 a. The reactive flux $k(t)$ calculated according to Eq. 2.61 (see Fig. 5.2 b) is consistent with the result in Ref.[288]. For bulk water, there exists a ∼ 0.2-ps transient period, during which $k(t)$ quickly changes from its initial value[235]. However, at longer times, the $k(t)$ is independent of the HB definitions. The results in Fig. 5.2 b show that the difference in $k(t)$ caused by different HB

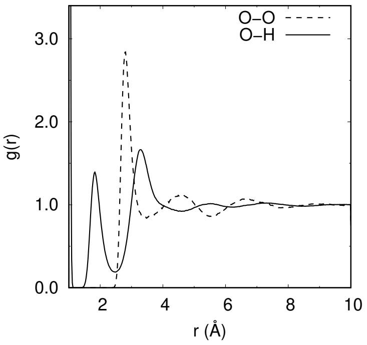

FIGURE 5.1: Partial RDFs of the simulated bulk water.

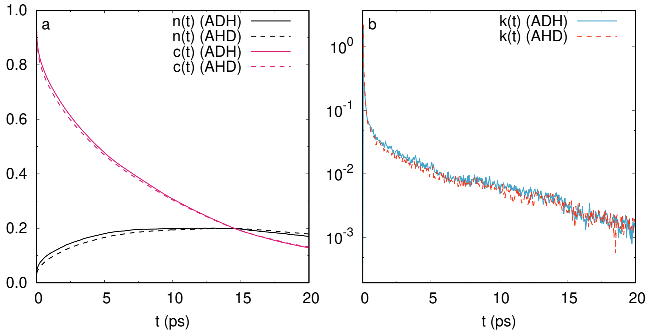

FIGURE 5.2: Time dependence of (a) $n(t)$, $c(t)$ and (b) $k(t)$ for *bulk* water.

definitions is relatively small. Therefore, the long time decay of $k(t)$ reflects the general properties of H-bonds, and calculating the reactive flux HB correlation functions is a more rigorous way to obtain the nature of H-bonds[149].

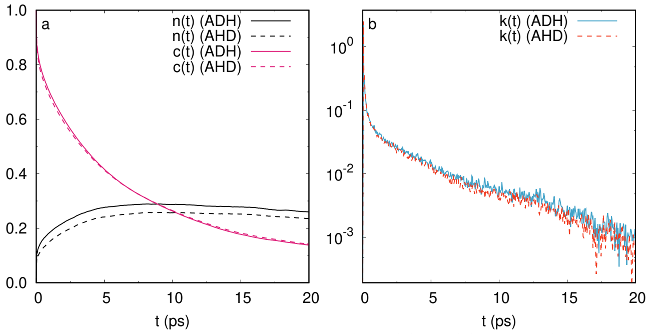

FIGURE 5.3: Time dependence of (a) $n(t)$, $c(t)$ and (b) $k(t)$ for the water/vapor *interface*.

Now we discuss the result for the water/vapor interface. At first we consider the water/vapor interface as a whole. We reported $c(t)$ and $n(t)$ in Fig. 5.3 a and the reactive flux $k(t)$ in Fig. 5.3 b. Also at the interface cases, $k(t)$ quickly changes from its initial value on a time scale of less than 0.2 ps. This can be seen from Fig. 5.4, where $k(t)$ in Fig.s 5.2 and 5.3 is reported in double logarithmic coordinates. This log-log plot of the $k(t)$ shows that, as in bulk water, this decay behaviour cannot be described with a power-law decay for the water/vapor interface. This result is also in good agreement with that of the classical molecular simulation of bulk water[148, 288].

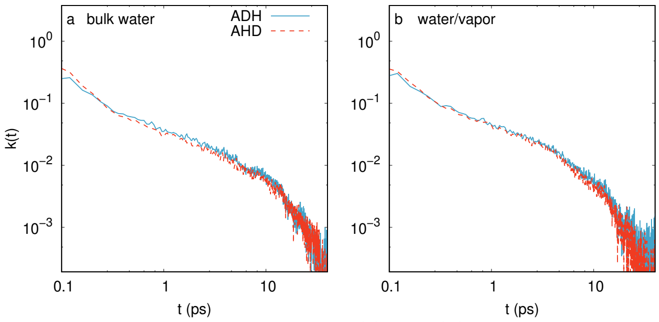

FIGURE 5.4: Time dependence of $k(t)$ for (a) bulk water and (b) the water/vapor interface.

For the water/vapor interface, we focus on the reactive flux $k(t)$, which had been used in the study of HB dynamics of liquid water[156, 217]. The $k(t)$ calculated from the trajectory of water molecules in simulations, is reported in Fig. 5.5. Beyond the 0.2-ps transient period, $k(t)$ decays to zero monotonically (see Fig. 5.4). This property has been found for bulk water using the SPC water model by Luzar and Chandler[217].

The functions $n(t)$ calculated according to Eq. 2.57 for bulk water and the water/-vapor interface are shown in Fig. 5.6. It shows that the overall trend of $n(t)$ does not depend on the choice of HB definition. i.e., as t increases, $n(t)$ increases rapidly from 0, and it reaches a maximum at $t \approx 10$ ps, and then gradually decreases. We find that the maximum of $n(t)$ for the water/vapor interface is slightly higher than that in bulk water, for both HB definitions. We interpret this result as the fact that at time t, there is a greater probability that H-bonds at the interface are broken compared to H-bonds in bulk water.

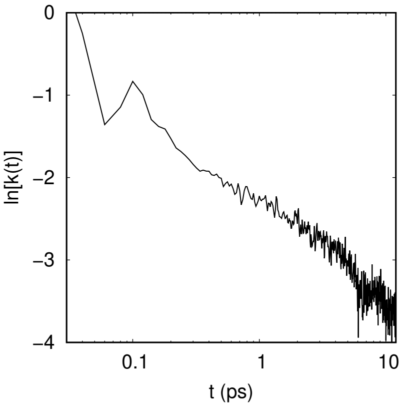

FIGURE 5.5: Time dependence of $k(t)$ for the water/vapor interface, according to Eq. 2.61.

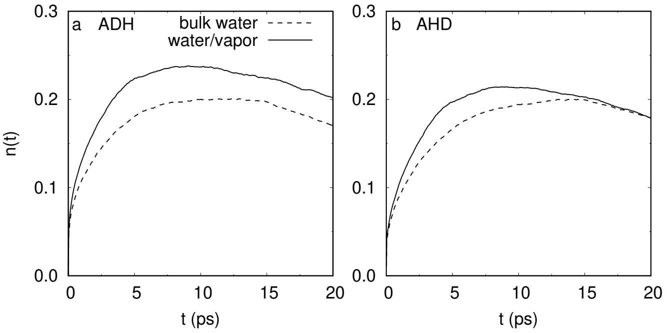

FIGURE 5.6: Time dependence of $n(t)$ for bulk water and the water/-vapor interface from the (a) ADH and (b) AHD criteria.

Reaction rate constants To calculate the HB relaxation times in bulk water and the water/vapor interface, we make connection between microscopic HB dynamics and the phenomenological description of the HB breaking/reforming reaction

$$A \rightleftharpoons B, \tag{5.1}$$

with k and k' as the forward and backward rate constants, respectively. Here, A denotes reactants (HB *on*, $\langle h \rangle$), and B denotes products (HB *off*, $\langle 1-h \rangle$)[218]. Khaliullin and Kühne have studied HB dynamics of bulk water using AIMD simulations[156]. Based on the HB population operators $h(t)$ and $h^{(d)}(t)$, and correlation functions $n(t)$ and $k(t)$, they have used the simulation data to obtain the ratio k/k' in bulk water, and then the lifetime and relaxation time of the H-bonds. Here, we study HB dynamics at the water/vapor interface. We can obtain the optimal solution range of k and k' from the relationship between the reactive flux and the HB population correlation function $c(t)$ and $n(t)$, and the two rate constants k and k', i.e.,

$$k(t) = kc(t) - k'n(t). \tag{5.2}$$

We have found the optimal value of the rate constants, k and k', by a least squares fit of the calculated data $k(t)$, $c(t)$ and $n(t)$ beyond the transition phase. The function $c(t)$ is regarded as a P-dimensional column vector composed by $(c(1), c(2), \cdots, c(P))^{\mathsf{T}}$, and denoted as $\mathbf{c}$, with $c(i)$ representing the value of the correlation $c(t)$ at $t = i$. Similarly, the functions $n(t)$ and $k(t)$ are also viewed as P-dimensional column vectors and are denoted as $\mathbf{n}$ and $\mathbf{k}$, respectively. Therefore, k and k' are determined from the matrix $A = \begin{bmatrix} \mathbf{c} & \mathbf{n} \end{bmatrix}$, i.e.,

$$\begin{bmatrix} k \\ -k' \end{bmatrix} = (A^{\mathsf{T}}A)^{-1}A^{\mathsf{T}}\mathbf{k}. \tag{5.3}$$

For bulk water and the water/vapor interface, the optimal k and k' are reported in Tables 5.1 and 5.2.

TABLE 5.1: The forward and backward rate constants, k and k', for bulk water (bulk) and the water/vapor interface (w/v). We carried on the short time region 0.2 ps $< t <$ 2 ps. The unit for k (k') is ps^{-1}, and that for τ_{HB} ($= 1/k$) is ps. (Same for Table 5.2.)

Criterion	k (bulk)	k' (bulk)	τ_{HB} (bulk)	k (w/v)	k' (w/v)	τ_{HB} (w/v)
ADH	0.30	0.99	3.38	0.32	0.77	3.10
AHD	0.29	1.15	3.47	0.31	0.89	3.18

TABLE 5.2: The forward and backward rate constants, k and k', for bulk water (bulk) and the water/vapor interface (w/v). We carried on the long time region 2 ps $< t <$ 12 ps.

Criterion	k (bulk)	k' (bulk)	τ_{HB} (bulk)	k (w/v)	k' (w/v)	τ_{HB} (w/v)
ADH	0.12	0.04	8.72	0.16	0.07	6.37
AHD	0.11	0.05	9.50	0.16	0.09	6.47

To obtain the forward and backward rate constants (k and k'), we performed the fitting in different time region $0.2 < t < 2$ ps and $2 < t < 12$ ps, respectively. We note that in the larger time region, i.e., $2 < t < 12$ ps, the value of HB lifetime τ_{HB} is larger than that in shorter time region, $0.2 < t < 2$ ps, no matter for bulk water or for the water/vapor interface. A larger τ_{re} value means that the distance between two water molecules stays within $r^c_{\mathrm{OO}} = 3.5$ Å for a longer time. For the long time region, these values of the k are comparable in magnitude to that obtained by Ref. [156].

5.2 Instantaneous interfacial HB dynamics

It can be seen from Tables 5.1 and 5.2 that if we analyze the simulated water/vapor interface as a whole, the behavior of the water surface is masked by the behavior of the bulk contribution. To selectively identify the properties at the interface, it is necessary to selectively identify the surface molecules. Therefore, we define a instantaneous interface using the procedure of Willard and Chandler[157] and then selectively analyze HB dynamics of the water molecules at the water interface.

To study HB dynamics for the water/vapor interface, we first determine the instantaneous interface and then define the interfacial HB population operator. Based on these two definitions, we can derive the correlation functions and reaction rate constants, for interfacial layers. Using these quantities we can discuss the change in HB dynamics at the interface as function of the interface layer's thickness.

Instantaneous Interfaces As shown by Willard and Chandler, due to molecular motions, interfacial configurations change with time, and the identity of molecules that lie at the interface also changes with time. Generally, useful procedures for identifying interfaces must take into account these motions[157]. To determine the instantaneous interface of the system, we adopted the Willard-Chandler method based on spatial density[157]. The coarse-grained density at a space-time point $(\mathbf{r}, t)$ can be expressed as polynomial

$$\bar{\rho}(\mathbf{r}, t) = \sum_i \phi(|\mathbf{r} - \mathbf{r}_i(t)|; \xi) \tag{5.4}$$

where $\mathbf{r}_i(t)$ is the position of the ith particle at time t and the sum is over all such particles, and

$$\phi(\mathbf{r}; \xi) = (2\pi\xi^2)^{-3/2} \exp(-r^2/2\xi^2) \tag{5.5}$$

is a normalized Gaussian functions for a 3-dimensional system, where r is the magnitude of $\mathbf{r}$, and ξ is the coarse-graining length. Equation 5.5 is introduced to improve the accuracy of the interface, such that we can extend the domain and make it a single unicom, i.e., no cavity exists in the domain. With the parameter ξ set, the

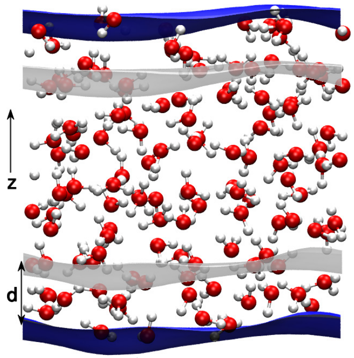

FIGURE 5.7: A slab of water (128 water molecules are included) with the instantaneous interface represented as a blue mesh on the upper and lower phase boundary. The normal is along the z-axis and the parameter d is the thickness of the interfacial layer. The grey surfaces are obtained by translating the interfaces to the interior of the slab along the z-axis (or the opposite direction) by d.

interface can be defined to be the two-dimensional manifold $\mathbf{r} = \mathbf{s}$ such that

$$\bar{\rho}(\mathbf{s}; t) = \rho_c, \tag{5.6}$$

where ρ_c is a reference density. This interface depends on molecular configurations, i.e., $\mathbf{s}(t) = \mathbf{s}(\{\mathbf{r}_i(t)\})$.

After the instantaneous interface is defined, we can define an instantaneous interface layer for any non-uniform fluid system. Specifically, for the simulated water/vapor interface system in the cuboid simulation box, we can get another two-dimensional manifold $\mathbf{s}_0(t)$ by moving the surface $\mathbf{s}(t)$ along the system's normal coordinate to a certain distance d (two grey surfaces are shown in Fig. 5.7). At any time t, the volume between the two surfaces $\mathbf{s}(t)$ and $\mathbf{s}_0(t)$ is defined as an *instantaneous interface layer*, or *instantaneous interface*. In other words, these two surfaces are the two boundaries of the instantaneous interface, and d is its thickness. Different values of d give us different layering strategies for the interface system. See Fig. 5.7 as an example, two instantaneous interface layers with thickness d are shown.

Below we will combine the instantaneous interface and Luzar-Chandler's HB population operator[217] to identify the H-bonds at the water/vapor interface. The dynamics of these H-bonds will vary with the thickness d of the interface layer. By investigating HB dynamics for these layers, we can obtain the dynamical characteristics of the water/vapor interfaces.

Interfacial HB population After we have determined the instantaneous surface $\mathbf{s}(t) = \mathbf{s}(\{r_i(t)\})$, we can define *interfacial H-bonds*. Now we define the interface HB population operator $h^{(\mathrm{s})}[r(t)]$ as follows: It has a value 1 when the particular tagged molecular pair i, j are H-bonded, *and* both molecules are inside the instantaneous interface with a thickness d, and zero otherwise:

$$h^{(\mathrm{s})}[r(t)] = \begin{cases} 1 & i, j \text{ are H-bonded, and} \\ & i, j \text{ are inside the interfacial layer} \\ 0 & \text{otherwise} \end{cases} \tag{5.7}$$

From the definition, we know that $h^{(\mathrm{s})}(t)$ depends on the thickness d, therefore, $h^{(\mathrm{s})}(t)$ can help to efficiently obtain H-bonds' dynamic characteristics of the interfacial layer. In this paragraph, we discuss H-bonds based on water molecule pairs for simplicity.

Similar to $c(t)$ in Eq. 2.53, which describes the fluctuation of general H-bonds, we define a correlation function $c^{(\mathrm{s})}(t)$ that describes the fluctuation of the interfacial H-bonds:

$$c^{(\mathrm{s})}(t) = \langle h^{(\mathrm{s})}(0)h^{(\mathrm{s})}(t)\rangle / \langle h^{(\mathrm{s})}\rangle. \tag{5.8}$$

Similarly, we define correlation functions

$$n^{(\mathrm{s})}(t) = \langle h^{(\mathrm{s})}(0)[1 - h^{s}(t)]h^{(\mathrm{d,s})}\rangle / \langle h^{(\mathrm{s})}\rangle, \tag{5.9}$$

and

$$k^{(\mathrm{s})}(t) = -\frac{dc^{(\mathrm{s})}}{dt}. \tag{5.10}$$

Using these functions, we can determine the reaction rate constant of breaking and reforming and the lifetimes of interfacial H-bonding. We will discuss the dependence of the correlation functions $c(t)$, $c^{(\mathrm{s})}(t)$, and the reaction rates k and k' on the interface thickness d in the next two paragraphs.

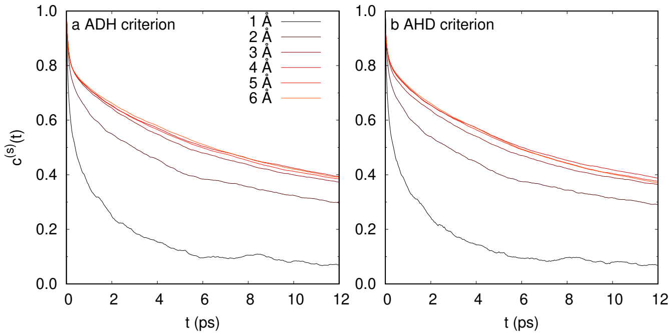

FIGURE 5.8: The $c^{(\mathrm{s})}(t)$ for the instantaneous interfacial H-bonds with different thicknesses, as computed from the (a) ADH and (b) AHD criteria through the IHB method.

Depth-dependence of $c^{(\mathrm{s})}(t)$ For the water/vapor interface, we used two geometric criteria of H-bonds to calculate $h^{(\mathrm{s})}(t)$ and therefore $c^{(\mathrm{s})}(t)$ from Eq. 5.8. The calculated results of $c^{(\mathrm{s})}(t)$ are shown in Fig. 5.8. We find that HB dynamics is faster at the water/vapor interface when compared to bulk water. As d increases, HB dynamics gets slower and it recovers the bulk value. This behavior is independent of the HB definition as shown by the comparison of results in panel a and b of Fig. 5.8.

For comparison, we also calculate HB dynamics of water molecules at the interface obtained by interfacial molecule sampling (IMS, see Appendix E.1 for details). In this method, we first select molecules at the interface at each sampling time and then make a statistical average of the calculated correlation functions for those molecules. Specifically, to determine the water molecules in the interface layer, we sample at regular intervals, and then calculate $c(t)$ for these water molecules in the interface layer and then their a statistical average. Figure 5.9 shows how $c(t)$ depends on the thickness d. The panel a and b use HB definition criterion ADH, and AHD, respectively. Comparing Fig.s 5.8 and 5.9, we find that when we use the method of IMS, the dependence of the correlation function $c(t)$ on the interface thickness is consistent with that of $c^{(\mathrm{s})}(t)$ for large d. Moreover, regardless of the ADH or AHD definition of a HB, this conclusion is valid.

Beside the correlation functions $c(t)$ or $c^{(\mathrm{s})}(t)$ for the interface, we will further examine the correlation functions $n(t)$, $k(t)$ ($n^{(\mathrm{s})}(t)$, $k^{(\mathrm{s})}(t)$), and the rate constants k, k'.

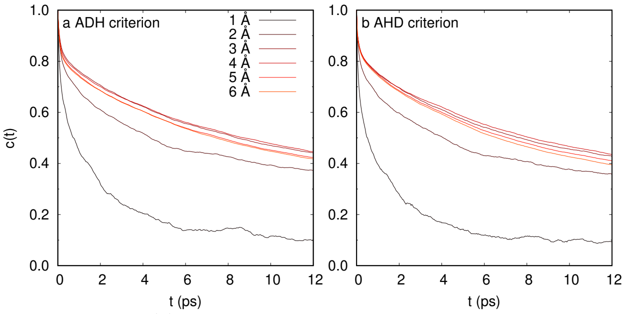

FIGURE 5.9: The $c(t)$ for the instantaneous interfacial H-bonds with different thicknesses, as computed from the (a) ADH and (b) AHD criteria. The IMS method is used, and the sampling rate is 1/4 per ps.

Depth-dependence of reaction rate constants To find the reaction rate constants k and k', we have two statistical methods: (1) Instantaneous interfacial hydrogen bond (IHB), by which we can calculate the correlation functions $c^{(\mathrm{s})}(t)$, $n^{(\mathrm{s})}(t)$, and $k^{(\mathrm{s})}(t)$; (2) IMS, by which we first identify the water molecules at the instantaneous interface at each time t, and start from the corresponding correlation functions $c(t)$, $n(t)$, and $k(t)$ of H-bonds of the identified water molecules. Figure 5.10 shows the rate constants (k and k') and the lifetime τ_{HB} obtained by the two methods. We find that, for all the three parameters k, k' and τ_{HB}, the behavior as function of the thickness of the interface is only slightly affected by the calculation methods.

As we can see from Fig. 5.10, when d is large enough ($d > d_0 \sim 4$ Å), the constants k an k' obtained by the two methods agree quantitatively. This result shows that the two statistical methods (Appendix E.1) for HB dynamics of the interface do not produce much difference.

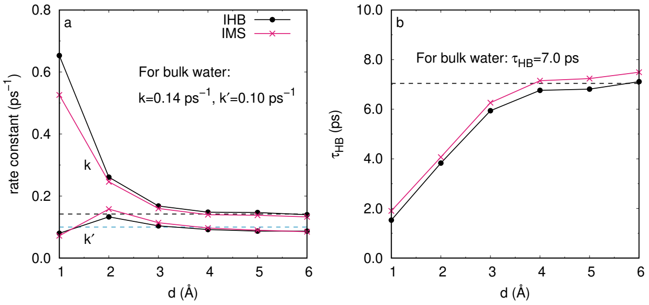

FIGURE 5.10: Dependence of (a) the reaction rate constants k and k' and (b) the HB lifetime τ_{HB} on the interface thickness d, obtained by the IHB and the IMS method, respectively. The corresponding k, k' and τ_{HB} in bulk water are drawn with dashed lines as references. In panel a, the k of bulk water is represented by a *black dashed* line, and the k' of bulk water by a *blue dashed* line; in panel b, the τ_{HB} of bulk water by a *black dashed* line. The ADH criterion of H-bonds is used and the least square fits are carried on the time region 0.2 ps $< t <$ 12 ps.

We also find that when we focus on molecules in the interface layer with $d < d_0$, the values of the reaction rate constants does depend on the method we use. That is, the k obtained by the IHB method is slightly larger than by the IMS and k' is smaller. Since $\tau_{\mathrm{HB}} = 1/k$, a larger value of k directly leads to a relatively shorter HB lifetime. This result is related to our definition of the IHB, and it is the same as our expectation: the definition of interfacial H-bonds ($h^{(\mathrm{s})}(t)$) makes the HB break rate on the interface artificially increased. At the same time, the IMS retains the original rate constant of H-bonds, but it may include the contribution of bulk water molecules to the rate constant.

In Fig. 5.10, the k, k', and τ_{HB} for *bulk* water are also reported with dashed lines as a reference. Comparing the above-mentioned quantities for the water/vapor interface and bulk water, we find that when d is larger than d_0, no matter which statistical method is used, the calculated reaction rate constants of the interface water is *greater* than that in bulk water. Therefore, the HB lifetime τ_{HB} at the water/vapor interface, is smaller than in bulk water.

Furthermore, we have found from Fig. 5.10 that as d increases, the values of k and k' also tend to bulk values at the same condition. These results are obtained by the least squares method in the same interval (0.2–12 ps). This verifies that the IHB method can get as good results as the IMS method when d is larger than d_0. Because the IHB method is concise to operate, it can be used to calculate HB dynamics and thus HB lifetime for the water/vapor interface when d is larger than d_0. For the water/vapor interface, d_0 is approximately 4 Å or equals to the size of $\sim$2 layers of water molecules. This result coincides with the previous theoretical results based on MD simulation[212, 289, 290] and VSFG spectroscopy[291], which have shown that isotropic properties are already recovered at sub-nanometer distances from the surface of ordered hydrophobic monolayers. For example, Stiopkin and coworkers suggested a "healing length" of about 3 Å with the bulk-phase properties of water recovered within the top few monolayers[292].

Finally, because the real HB dynamical properties of interface molecules are between the results of the above two methods, we can approximate the interfacial HB dynamics, by either the IHB or the IMS method if the thickness of the interface is large enough, i.e., $d > d_0$.

To illustrate this point more clearly, we compare the k, k', and τ_{HB} obtained under the two methods. We listed more detailed data in Tables 5.3 to 5.6.

TABLE 5.3: The k and k' for the interfacial HB dynamics of the water/vapor interface, through the IHB method, with the ADH criteria. We carried on the longer time region 0.2 ps $< t <$ 12 ps (same below).

d (Å)	k (ps^{-1})	k' (ps^{-1})	$\tau_{\mathrm{HB}}(= 1/k)$ (ps)
1.0	0.653	0.080	1.53
2.0	0.261	0.133	3.83
3.0	0.168	0.104	5.94
4.0	0.148	0.092	6.76
5.0	0.147	0.087	6.81
6.0	0.139	0.087	7.17

TABLE 5.4: The k and k' for the interfacial HB dynamics of the water/vapor interface through the IHB method, with the AHD criteria.

d (Å)	k (ps^{-1})	k' (ps^{-1})	$\tau_{\mathrm{HB}}(=1/k)$ (ps)
1.0	0.661	0.080	1.51
2.0	0.265	0.133	3.77
3.0	0.172	0.102	5.82
4.0	0.148	0.090	6.74
5.0	0.149	0.084	6.72
6.0	0.144	0.078	6.93

TABLE 5.5: The k and k' for the interfacial HB dynamics of the water/vapor interface through the IMS method, with the ADH criteria.

d (Å)	k (ps^{-1})	k' (ps^{-1})	$\tau_{\mathrm{HB}}(=1/k)$ (ps)
1.0	0.526	0.072	1.90
2.0	0.246	0.158	4.07
3.0	0.160	0.114	6.26
4.0	0.140	0.097	7.15
5.0	0.138	0.090	7.24
6.0	0.133	0.085	7.49

TABLE 5.6: The k and k' for the interfacial HB dynamics of the water/vapor interface through the IMS method, with the AHD criteria.

d (Å)	k (ps^{-1})	k' (ps^{-1})	$\tau_{\mathrm{HB}}(=1/k)$ (ps)
1.0	0.610	0.083	1.64
2.0	0.235	0.142	4.62
3.0	0.138	0.102	7.22
4.0	0.141	0.098	7.07
5.0	0.120	0.078	8.40
6.0	0.119	0.071	8.39

5.3 Summary

In this chapter, the HB population operator and associated correlation functions based on it are used for studying HB dynamics. The HB dynamics in bulk water can be calculated from these correlation functions: $c(t)$ describes the relaxation of H-bonds; $s(t)$ gives the average lifetime $\langle\tau_a\rangle$ of the continuous H-bonds. Using DFTMD simulations, starting from the functions $c(t)$, $n(t)$, and $k(t)$, we have calculated the reaction rate constants k and k' for HB rupture and regeneration, and the average HB lifetime τ_{HB} for bulk water.

We have also studied HB dynamics at *instantaneous* water/vapor interfaces using the combination of two statistical methods, the IMS and the newly introduced IHB. In the IHB method, correlation functions based on the instantaneous interfacial HB population operator, i.e., $c^{(\mathrm{s})}(t)$, $s^{(\mathrm{s})}(t)$, $n^{(\mathrm{s})}(t)$, and $k^{(\mathrm{s})}(t)$ are defined for the water/vapor interface. Based on the instantaneous interface, the combination of the IMS and IHB methods provides more realistic interfacial HB dynamics of the water/vapor interface. The instantaneous interface describes the microscopic interface more accurately, and both the IHB and IMS methods provide partial information on the HB breaking and reforming reaction rates for the interface. As the thickness of the interface increases, comparing the calculation results obtained from the IHB and IMS methods, respectively, we found that HB dynamics in the instantaneous layer *below* the surface recovers bulk values. Therefore, the real HB dynamical characteristics at the water/vapor interface, such as the HB breaking and reforming rate constants and the HB lifetime, can be calculated from the combination of IMS and IHB methods.

In particular, we have found that as the thickness of the interface layer increases, the HB reaction rate constants tends to the ones in bulk water. From the results for the water/vapor interface, we conclude that from the perspective of HB dynamics, the thickness of the water/vapor interface is 4 Å. This value is smaller than that obtained from the VSFG spectra (Ref. Paragraph 4.1) for the $LiNO_3$/vapor interface. This result is reasonable, because the presence of ions in solutions affects the HB network.

The idea of IHB can be extended to electrolyte solutions, and can be used to study ions' effects on HB dynamics. We will analyze HB dynamics in electrolyte solutions in the next chapter.

Chapter 6

Hydrogen bond dynamics in electrolyte solutions

In this chapter, we explore the effects of nitrate, iodide and alkali metal ions on HB dynamics and water reorientation dynamics at the interface of alkali nitrate solutions and alkali iodide solutions. In Paragraph 6.1, we discuss the ion-water HB dynamics for the whole interface. Then in Paragraph 6.2, we study HB dynamics and HB lifetime specifically in solvation shells of ions. In Paragraphs 6.3 and 6.4, we focus on reorientation dynamics of water molecules at the interface and in the solvation shells of ions in electrolyte solutions. All simulations in this chapter were performed at the DFT (BLYP + D3) level and at 300 K within the canonical ensemble. The length of each trajectory is about 60 ps. For each solution, we have performed simulations for the solution/vapor interface and bulk system, respectively. The detailed parameter settings of different systems can be found in Appendix B.

6.1 Ion-water HB dynamics at electrolyte/vapor interface

6.1.1 Lithium nitrate solutions

We simulated a solution/vapor interface including Li^+ and NO_3^-, as shown in Fig. 6.1 A (for clarity water molecules are not shown), the $LiNO_3$ molarity of the solution is 0.4 M (for computational details see Appendix B).

The HB population correlation functions $c(t)$ and $s(t)$ for both nitrate–water (N–W) and water–water (W–W) H-bonds in the slab are shown in Fig.s 6.2 a and b, respectively. For both the ADH and AHD definitions, we find that the decay rates of $c(t)$ and $s(t)$ for N–W bonds are much faster than that for W–W bonds. From Eq. 2.59, the faster relaxation of $s(t)$ implies that N–W bonds have shorter lifetime than W–W bonds in bulk phase. The calculation results are in good agreement with numerous experimental and simulation results[127, 257, 269, 277]: nitrate has structure-breaking ability, or that N–W interaction is weaker, compared with W–W interaction.

Since the structure-breaking ability of ions is closely related to surface propensity, we speculate that the rate of relaxation of the correlation functions ($c(t)$ and $s(t)$) of N–W bonds may be related to the distribution of NO_3^- ions at various depths under the surface. Therefore, we calculated the distribution of ions at different depths relative to the instantaneous interfaces of the $LiNO_3$ solution.

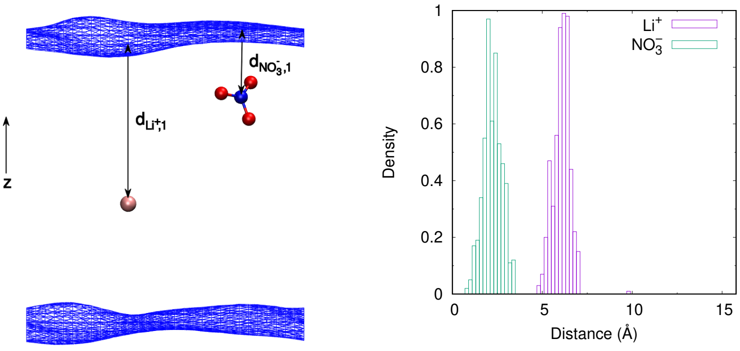

(A) (B)

Figure 6.1: Distribution of ions at the LiNO$_3$/vapor interface. (A) Distances between ions and one of the instantaneous surfaces (blue meshes) for a slab of aqueous LiNO$_3$ solution. (B) Density distribution of the Li$^+$–surface and NO$_3^-$–surface distances at the LiNO$_3$/vapor interface. The horizontal axis represents the distance between the ion and the instantaneous surface, which is defined in Eq. 6.1. The *distance* refers specifically to $d_{\mathrm{X},1}$, the distance between the ion X and one of the instantaneous surfaces. Zero distance denotes the instantaneous surface of the interfacial system of LiNO$_3$ solution.

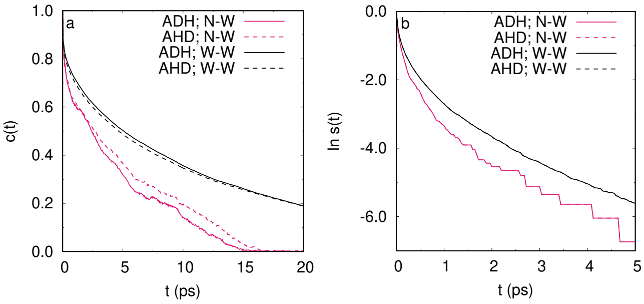

Figure 6.2: Time dependence of (a) $c(t)$ and (b) $\ln s(t)$ of all W–W and N–W bonds for the slab of LiNO$_3$ solution, as computed from the ADH (solid line) and AHD (dashed line) criteria of H-bonds. The W–W bonds represents H-bonds between all pairs of water molecules in the entire slab.

For any molecule or ion X in such a solution/vapor interface, we can define its distance from the instantaneous surface (the blue mesh reported in Fig. 6.1 A)). Assuming that the z-axis is the normal direction, the distances between the particle and the two instantaneous surfaces are:

$$d_{\mathrm{X},1}(t) = z_{\mathrm{X},1}^{\mathrm{surf}}(t) - z_{\mathrm{X}}(t), \tag{6.1}$$

$$d_{\mathrm{X},2}(t) = z_{\mathrm{X}}(t) - z_{\mathrm{X},2}^{\mathrm{surf}}(t), \tag{6.2}$$

where z_{X} is the z coordinate of the particle X in the normal direction at time t, $z_{\mathrm{X},i}^{\mathrm{surf}}(t)$ is the z coordinate of the surface position corresponding to particle X at time t, and the subscripts $i = 1$ and 2 respectively identify the lower and upper instantaneous surface. As an example, Fig. 6.1 A shows the distance, $d_{\mathrm{Li}^+,1}$ ($d_{\mathrm{NO}_3^-,1}$), between the Li$^+$ (NO$_3^-$) ion and one of the instantaneous surfaces at a certain moment. Fig. 6.1 B shows the probability density of the distance between the ion and the instantaneous surface for the LiNO$_3$/vapor interface. We find that when the system reaches an equilibrium state, the Li^+ ion is stable within a few angstroms below the instantaneous interface, while the NO_3^- ion resides near the surface. When the system is in equilibrium ($t > 10$ ps), the distance $d_{\mathrm{NO}_3^-,1}$ is around 2 Å, which indicates that the nitrate ion is in the top layer of the instantaneous interface.

The result for HB dynamics is in agreement with what we have obtained in Chapter 4 from the vibrational spectroscopy. From the calculation of the VSFG spectrum of the $\mathrm{LiNO_3}$/vapor interface and the VDOS for water molecules in the water cluster $\mathrm{NO}_3^-(\mathrm{H_2O})_3$, we have shown that: (1) Compared with the water/vapor interface, the VSFG spectrum of the $\mathrm{LiNO_3}$/vapor interface has a blue-shifted HB band (see Fig. 4.3); (2) The vibration frequency of water molecules at the $\mathrm{LiNO_3}$/vapor interface is higher than that at the water/vapor interface (see Fig. 4.5). The two conclusions indicate that nitrate ions have surface propensity. Here, the probability distribution of the nitrate ion in the slab shows that the average position of the nitrate ion relative to the solution/vapor interface is 2 Å, which is consistent with the conclusion from the VSFG spectra and the VDOS.

6.1.2 Alkaline iodide solutions

We also calculated the distribution of ions at different depths at the instantaneous interface for the alkali iodide solutions. Figures 6.3–6.4 show the density of the distance between the anions (cations) and the instantaneous surface in the simulated solution/vapor interface of the LiI, NaI and KI solution, respectively. As an example, the distances between ions and one of the instantaneous surfaces (grey meshes) for a slab of aqueous KI solution are shown in Fig. 6.4 A. We find that the I^- ion resides near the surface, while alkali metal ions does not have such a strong tendency. The experimental data of the concentration dependence of surface tension $d\gamma/dm_2$ of solutions containing Li^+, Na^+ and K^+ ions also show that they do not have the strong surface propensity of I^- ions (see Chapter 1).

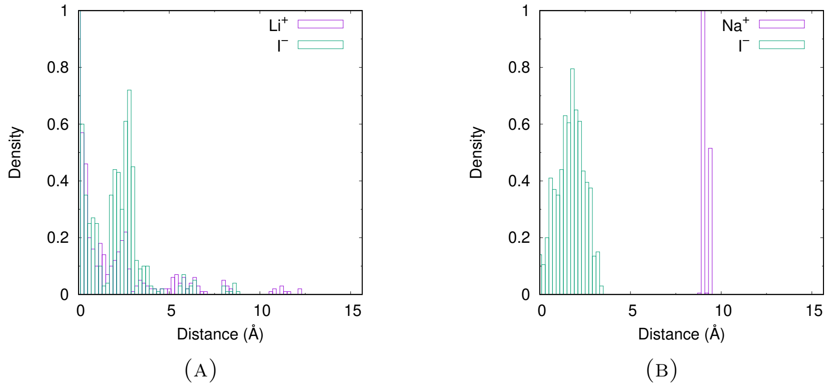

(A) (B)

FIGURE 6.3: Density distribution of ions at the LiI/vapor and NaI/-vapor interfaces. (A) The Li^+–surface and I^-–surface distances. (B) The Na^+–surface and I^-–surface distances.

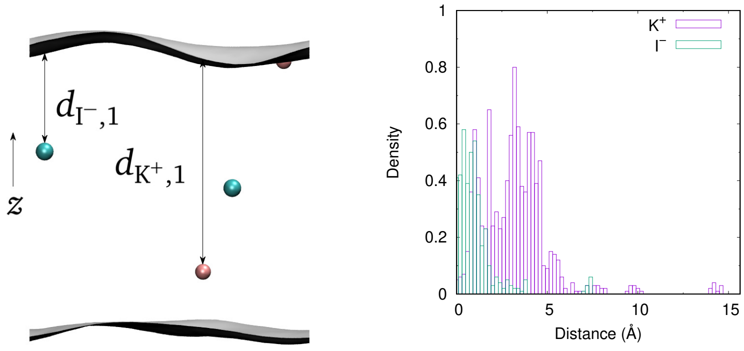

(A) (B)

FIGURE 6.4: (A) Distances between ions and one of the instantaneous surfaces (grey meshes) for a slab of the KI solution. (B) Density distribution of the K^+–surface and I^-–surface distances at the KI/vapor interface, respectively.

TABLE 6.1: The average of the continuum HB lifetimes $\langle\tau_\mathrm{a}\rangle = \int_0^\infty s(t)dt$ (unit: ps) in the first solvation shell of I^- ion and of alkali metal ion at the interface of three 0.9 M alkali iodide solutions.

	I^--shell	cation-shell	bulk water	w/v interface
LiI	0.22	0.24	0.25	0.23
NaI	0.24	0.28	0.25	0.23
KI	0.20	0.23	0.25	0.23

To investigate ions' effects, we calculated HB population correlation functions for H-bonds between ions' first and second solvation shells at aqueous electrolyte interfaces. We denote these H-bonds as H-bonds *in the solvation shell.* Then we compared these correlation functions to that of the water/vapor interface obtained in the previous chapter (see Paragraph 5.2 in Chapter 5). Here, we consider $s(t)$, from which the HB lifetime τ_a can be calculated. Table 6.1 lists the continuum HB lifetime of H-bonds in the solvation shell of I^- ion and of alkali metal ion, respectively, at interfaces of alkali iodide solutions: LiI, NaI and KI. For reference, we also give the $\langle\tau_\mathrm{a}\rangle$ for bulk water and the water/vapor interface in Table 6.1. The $\langle\tau_\mathrm{a}\rangle$ values obtained under these different environments are only slightly different. The continuum HB lifetime $\langle\tau_\mathrm{a}\rangle$ for the H-bonds in the solvation shell of alkali metal (iodine) ions is larger (smaller) than that at the water/vapor interface. For the LiI solution, the water molecules bound to Li^+, on average, have a continuum HB lifetime $\langle\tau_\mathrm{a}\rangle \sim 0.24$ ps, which is longer than that of molecules bound to I^- and at the water/vapor interface. Besides, we find that $\langle\tau_\mathrm{a}\rangle$ for the I^--shell is smaller than that at the water/vapor interface in general.

Effects of the ion concentration To investigate the effect of the ion concentration we considered additional systems with higher concentration, namely 1.8 M. We calculated the $c(t)$ for the interfaces of the alkali iodide solutions, and the relaxation time τ_R for each of them, which can be determined according to Eq. 2.54. Here, the *interface* means *all* the water molecules in each model. The τ_R for the interfaces of the LiI (NaI) solutions are given in Table 6.2. Generally, they are in the range 1–10 ps. The values of τ_R decrease as the concentration of the solutions increases.

TABLE 6.2: The relaxation time τ_{R} (unit: ps) of the $c(t)$ for the interface of the LiI (NaI) solutions.

concentration	τ_{R} (LiI)	τ_{R} (NaI)
0	11.50	11.50
0.9 M	7.04	10.60
1.8 M	4.40	1.96

The concentration dependence of the $s(t)$ was also calculated. Figure 6.5 a (b) gives the $s(t)$ for the interfaces of 0.9 M and 1.8 M LiI (NaI) solutions. This result indicates that, for the interface of alkali iodide solution, the continuum HB lifetime decrease as the concentration of the LiI (or NaI) solution increase. This can be explained as following: As the ion concentration increases, more iodide ions gather on the surface. The *ratio* of the number of iodide ions to the number of water molecules among the neighbors of the surface water molecules is set to r_{I^-}. For the water molecules in the first solvation shell of the cation, the ratio of the number of cations to the number of water molecules in its neighbors is set to r_{cation}. Water molecules below the surface are surrounded by more water molecule neighbors than those at the interface. Since the upper half of the surface is vacuum and the cations here do not aggregate on the surface. Therefore, $r_{\mathrm{I}^-}$is larger than r_{cation}, so the influence of the cation on HB relaxation is not as strong as the influence of the I^- ion on the surface. We believe that this fact is the reason that HB relaxation of the water molecules at the interface becomes faster as the alkali iodide concentration increases. Therefore, HB relaxation of the interface and the lifetime of H-bonds at the interface will be more dominated by the concentration of ions accumulated at the interface.

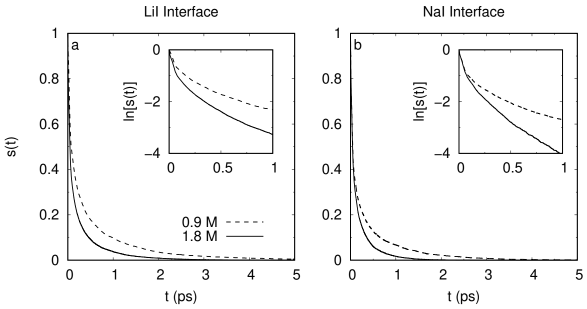

FIGURE 6.5: Time dependence of $s(t)$: (a) the LiI/vapor interface; (b) the NaI/vapor interface. The insets show the plots of $\ln s(t)$.

To summarize, we have investigated the effect of alkali nitrate and alkali iodide on HB dynamics of water molecules at solution/vapor interfaces, obtained from *ab initio* simulations. N-W's $c(t)$ and $s(t)$ decay faster than W-W's, which proves that the N-W bonds is weaker than W-W ones. The result calculated from $\Im\chi^{(2),\mathrm{R}}$ spectra in Paragraph 2.6 is that the blue shift of the HB band in the $\Im\chi^{(2)}$, or, the nitrate ion in the solution tends to be distributed at the interface, which is consistent with the smaller relaxation time given by $c(t)$ and $s(t)$. Compared with the water/vapor interface, the characteristic relaxation time of H-bonds between water molecules at the interface of the alkali metal salt solution as a whole is smaller and increases with the increase of the solute concentration.

6.1.3 Ion-water bond dynamics: breaking and reforming

For ion–water bonds, some results obtained by molecular simulations have been obtained. For example, HB dynamics of surfactant–water and W–W bonds at the interface has been analyzed by Chanda and Bandyopadhyay[278]. Similar analysis for N–W bonds is also done by Yadav, Choudhary and Chandra by first-principles MD simulations[132]. As for the effect of the interface on HB dynamics in electrolyte solutions, we also calculate the functions $c(t)$ and $s(t)$.

Alkali nitrate solutions First, let us discuss the changes in H-bonds of water molecules by nitrate ions in bulk solution. The $\ln s(t)$ for the W–W bonds and N–W bonds at the $LiNO_3$/vapor interface is shown in Fig. 6.6. The $\ln S_{\mathrm{HB}}(t)$ shows that N–W bonds are weaker than W–W bonds, i.e., nitrate ions accelerate HB dynamics in water.

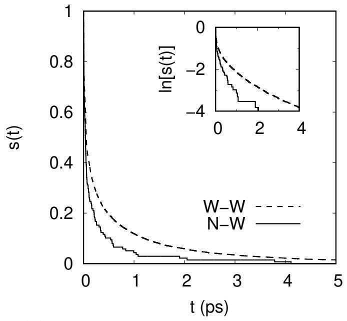

FIGURE 6.6: The $s(t)$ of W–W and N–W bonds at the $LiNO_3$/vapor interface. The inset is the plot of $\ln s(t)$. The results are calculated for the temporal resolution $t_{\mathrm{t}} = 1$ fs. For the definition of t_{t} see Appendix E.

The difference between N–W and W–W bonds is also analyzed in terms of the survival probability $s(t)$ [217, 225, 226], reported in Fig. 6.6. The integration of $s(t)$ from 0 to $t_{\max} = 5.0$ ps[293], gives the approximate lifetime τ_{a}[294]. The values of τ_{a} depend on the temporal resolution t_t, during which the H-bonds that break and reform are treated as intact[149]. Here, we choose the temporal resolution as $t_t = 1$ fs. Then, Fig. 6.6 gives $\tau_{\mathrm{a}} = 0.20$ ps for N–W bonds at the interface, and $\tau_{\mathrm{a}} = 0.42$ ps for W–W bonds. This result of τ_{a} is consistent with the experimental result of Kropman and Bakker ($\tau_{\mathrm{a}} = 0.5 \pm 0.2$ ps) for W–W bonds [248]. The smaller value of τ_{a} for N–W bonds implies that N–W bonds are weaker than W–W bonds. This is consistent with the VDOS analysis and the blue-shifted frequency (of 55 cm^{-1} towards the blue) of the OH stretching in N–W bonds (Fig. 4.6).

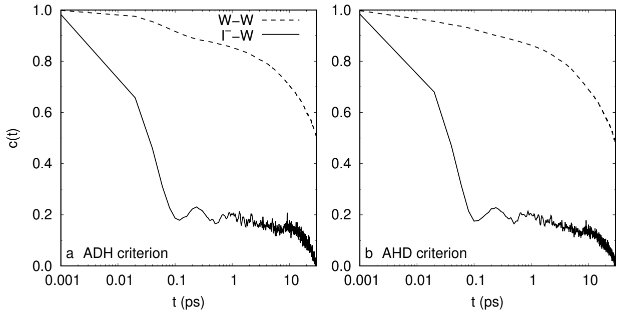

FIGURE 6.7: Time dependence of $c(t)$ of I^-–water (I^-–W) and W–W bonds: (a) ADH; (b) ADH. A base-10 log scale is used for the x-axis.

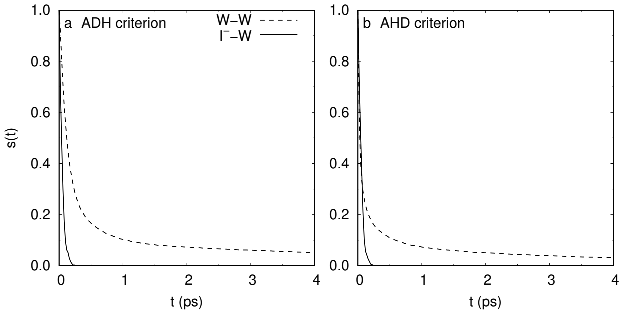

FIGURE 6.8: Time dependence of $s(t)$ of I$^-$–water (I$^-$–W) and W–W bonds.

Alkaline iodide solutions For anion-oxygen (X–O) bonds, we can use a similar criteria. The cutoff values for X–oxygen distance are obtained from the positions of the first minimum of the X–oxygen RDF, i.e., $R^{\mathrm{c}}_{\mathrm{XO}}$=4.1 Å for X = I$^-$ (Fig. 4.9). We have used $\phi^{\mathrm{c}} = 30°$ for the angular cutoff[239]. The function $c(t)$ of I$^-$–water and W–W bonds describes the structural relaxation of these H-bonds. The intermittent correlation functions $c(t)$ are shown in Fig. 6.7, and the results of the continuous correlation functions for both definitions (the ADH and AHD criteria) for the H-bonds are shown in Fig. 6.8 for I$^-$–water bonds. The results of W–W bonds are also included for comparison in both Fig.s 6.7 and 6.8. For both the ADH and AHD definitions of H-bonds, it is found that I$^-$–water bonds show faster dynamics than W–W bonds [239] (consistent to previous MD results by Chowdhuri and Chandra).

The time scales of the relaxation of I$^-$–water bonds are obtained for both definitions. In Table 6.3, we have included the average lifetimes $\langle\tau_{\mathrm{a}}\rangle$ for I$^-$–water and N–W bonds. We have performed the fitting in the time region 0.2 ps $< t <$ 12 ps to calculate the forward and backward rate constants for HB reactive flux. From both ADH and AHD criteria, the average lifetime $\langle\tau_{\mathrm{a}}\rangle$ of I$^-$–water bonds is shorter than that of N–W bonds. In addition, based on HB population operator for ion–molecule pairs, we also calculated the HB lifetime $1/k$ for these two H-bonds. The results show that the lifetime of I$^-$–water bonds is only half of lifetime of N–W bonds. Therefore, from the perspective of HB dynamics, we can draw the following conclusion: I$^-$–water bonds and N–W bonds are both weaker than W–W bonds. In particular, I$^-$–water bonds is slightly weaker than N–W bonds.

TABLE 6.3: Dynamical properties of I$^-$–water and N–W bonds within the ADH (AHD) criterion.

Quantities	I$^-$–water	NO$_3^-$–water
$\langle\tau_a\rangle$ (ps)	0.10 (0.11)	4.35 (7.91)
$1/k$ (ps)	2.80 (2.40)	4.15(6.02)

6.2 Water-water HB dynamics within ions' solvation shells

We will extend the IHB dynamics in Paragraph 5.2 in Chapter 5 to H-bonds around ions in aqueous solutions. Similar to the determination of the instantaneous surface, we can define interfaces for molecules or ions in aqueous solutions, i.e., their solvation shells. Below we will combine the interface defined by the first and the second solvation shells of ions, and Luzar-Chandler's HB population [217] to calculate HB dynamics for the H-bonds in solvation shells of ions. From characteristics of HB dynamics in the solvation shells, we can obtain the effect of ions on the structure and dynamics of aqueous solutions.

Solvation shell HB population Given the solvation shell $\mathbf{k}(t) = \mathbf{k}(\{\mathbf{r}_i(t)\})$, we can define the solvation Shell H-Bonds (SHBs). We use a parameter r_{shell} to denote the radius of the first or the second solvation shell (We also use r_{shell} to denote the radius of the second solvation shell, for the case of alkali iodide solutions). We define the solvation shell HB population operator $h^{(\text{k,X})}(t) = h^{(\text{k,X})}[r(t)]$ as follows: It has a value 1 when the particular tagged molecular pair are H-bonded *and* one of the water molecules are inside the first solvation shell of species X with a radius r_{shell}, and zero otherwise. The definition of $h^{(\text{k,X})}(t)$ is similar to $h^{(\text{s})}(t)$ in Paragraph 5.2 in Chapter 5 for studying the interfacial H-bonds, and it is used to obtain the dynamic characteristics of H-bonds in the solvation shell of species X.

Similar to the definition of $c^{(\text{s})}(t)$ in Eq. 5.8 in Chapter 5, for a given r_{shell}, we define a correlation function $c^{(\text{k,X})}(t)$ that describes the fluctuation of *the solvation shell H-bonds* for ion X:

$$c^{(\text{k,X})}(t) = \langle h^{(\text{k,X})}(0) h^{(\text{k,X})}(t)\rangle / \langle h^{(\text{k,X})}\rangle. \tag{6.3}$$

(When not considering specific ions, we denote $c^{(\text{k,X})}(t)$ as $c^{(\text{k})}(t)$ for short.) Similarly, we define a correlation function

$$n^{(\text{k,X})}(t) = \langle h^{(\text{k,X})}(0)[1 - h^{(\text{k,X})}(t)] h^{(\text{d,k,X})}\rangle / \langle h^{(\text{k,X})}\rangle, \tag{6.4}$$

and a reactive flux function

$$k^{(\text{k,X})}(t) = -\frac{dc^{(\text{k,X})}}{dt}. \tag{6.5}$$

Using these correlation functions, we can determine rate constants of breaking and reforming and lifetimes for the solvation shell H-bonds.

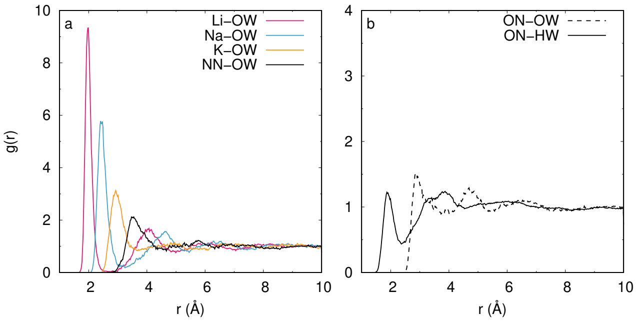

FIGURE 6.9: RDFs for the alkali nitrate solutions.

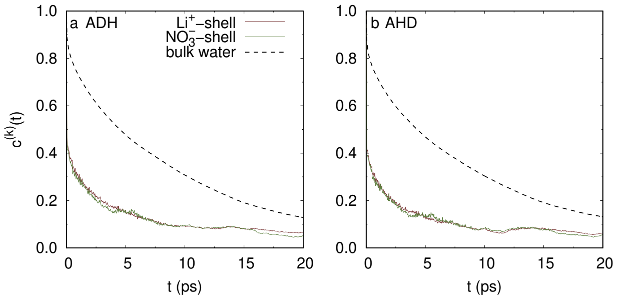

FIGURE 6.10: The $c^{(\mathrm{k})}(t)$ for the second solvation shell H-bonds as computed from different HB definitions: (a) ADH; (b) AHD. The r_{shell} is set to be 5.0 and 4.0 Å for Li^{+} an Nitrate O, respectively. The $c(t)$ (dashed line) for bulk water is also plotted in panel a and b, respectively.

Alkaline nitrate solutions For the $\mathrm{LiNO_3}$ solution, we calculated HB dynamics for the solvation shell H-bonds. The choice of the shell radius r_{shell} comes from the RDFs (Fig.6.9). From the previous paragraph, Fig. 6.2 a shows that N–W bonds, or H-bonds in the first solvation shell of $\mathrm{NO_3^-}$, is significantly weaker than W–W bonds. And from the VDOS for the $\mathrm{Li^+(H_2O)_4}$ cluster (Fig. 3.5 A), we know that Li^+-bound water has a red-shifted peak, i.e., the Li^+–water bonds slow down the vibrational relaxations of W–W bonds formed by molecules in the first solvation shell of Li^+. If the above two properties were still valid outside the first solvation shell of $\mathrm{NO_3^-}$ or Li^+ ions, then we could conclude that the H-bonds in the second solvation shell of $\mathrm{NO_3^-}$ will be weaker than that of the Li^+ ion, i.e., the relaxation time of $c^{(\mathrm{k},\mathrm{NO_3^-})}(t)$ will be significantly less than the relaxation time of $c^{(\mathrm{k},\mathrm{Li}^+)}(t)$. However, as we can see from Fig.s 6.10 a and b, the relaxation of $c^{(\mathrm{k},\mathrm{NO_3^-})}$ is almost the same as that of $c^{(\mathrm{k},\mathrm{Li}^+)}(t)$, or the former will not be faster than the latter. Specifically, Fig.6.10 shows that the relaxation process of H-bonds between the water molecules in the second solvation shell of $\mathrm{NO_3^-}$ is *not* faster than the relaxation process of H-bonds between water molecules in the second solvation shell of the Li^+ion. In general, this result implies that the HB strength between water molecules in the ions' second solvation shells are not affected by the nature of the ions evidently. In other words, the strength of the H-bonds does not significantly affect the surrounding H-bonds.

Alkaline iodide solutions In Paragraph 6.1, the probability distributions of ions in the solution/vapor interface of the LiI and NaI solutions with respect to the depth of ions in the solutions are calculated. The distributions in Fig.s 6.3–6.4 indicate that I^- ions prefer to staying at the topmost layer of surface of solutions. The probability distribution shows that I^- ions tend to the surface of solutions, while Na^+ and Li^+ tend to stay in bulk phase. This result is consistent with the calculations from Ishiyama and Morita[85, 88]. We choose the LiI solution to calculate HB correlation function $c^{(\mathrm{k})}(t)$, and the results are shown in Fig.6.11. The values of r_{shell} are obtained from the RDFs $g_{\mathrm{LiO}}(r)$ and $g_{\mathrm{IO}}(t)$, which represent the radius of the second solvation shell of Li^+ and I^- ions, respectively. Like the $\mathrm{LiNO_3}$ solution, the relaxation functions $c^{(\mathrm{k},\mathrm{Li}^+)}(t)$ and $c^{(\mathrm{k},\mathrm{I}^-)}(t)$ are very close to each other. This result shows that the presence of ions has no significant effect on the relaxation of H-bonds outside the first solvation shell.

Moreover, the $s^{(\mathrm{k},\mathrm{Li}^+)}(t)$ and $s^{(\mathrm{k},\mathrm{I}^-)}(t)$ have no significant difference. This result also implies that Li^+ ions have not significantly affected the relaxation process of H-bonds between the water molecules in the second solvation shells. Comparing the results in Fig. 3.8 in Chapter 3, we can summarize the influence of lithium ions on the dynamics of water molecules in clusters (solutions) as follows: Although in water molecule clusters, the vibration frequency of the water molecules directly connected to the Li^+ ion has a redshift, HB relaxation between water molecules in the second solvation shell of the ion is no longer significantly affected by the ion.

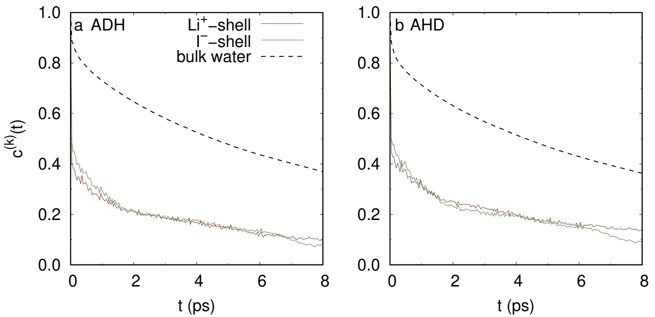

FIGURE 6.11: The $c^{(\mathrm{k})}(t)$ for the second solvation shell H-bonds as computed from different HB definitions: (a) ADH; (b) AHD. The r_{shell} is set to be 5.0 and 6.5 Å for Li^+ an I^-, respectively. The $c(t)$ (dashed line) for bulk water is also plotted in panel a and b, respectively.

6.3 Rotational anisotropy decay of water molecules at the water/vapor interface

The effect of ions on the dynamics of water molecules can also be characterized by rotational anisotropy decay of water molecules. The pump-probe polarization anisotropy monitors electronic alignment[295, 296]. The anisotropy decay can be determined from experimental signal in two different polarization configurations—parallel and perpendicular polarizations, by[297, 298]

$$R(t) = \frac{I_{\|}(t) - I_{\perp}(t)}{I_{\|}(t) + 2I_{\perp}(t)} \tag{6.6}$$

where $I_{\|}(t)$ is the absorption change when the probe laser pulse is parallel to the pump laser pulse, $I_{\perp}(t)$ is the absorption change when the probe laser pulse is perpendicular to the pump, and t is the time between pump and probe laser pulses. The effects of ion environment on structure and dynamics of water are obtained by comparing the second-order Legendre polynomial[232, 233], i.e., $P_2(x) = \frac{1}{2}(3x^2 - 1)$, orientational correlation function of the transition dipole. The anisotropy decay can also be obtained by simulations, and calculated by the third-order response functions[299, 300]. If the anisotropy decay is only due to the orientational relaxation of water molecules and within the Condon approximation[301], it is directly related to the orientational correlation function $C_2(t)$[302–305]

$$R(t) = \frac{2}{5} C_2(t). \tag{6.7}$$

The $C_2(t)$ is given by the rotational time-correlation function

$$C_2(t) = \langle P_2(\hat{u}(0) \cdot \hat{u}(t)) \rangle, \tag{6.8}$$

where $\hat{u}(t)$ is the time dependent unit vector of the transition dipole, and $\langle\rangle$ indicate equilibrium ensemble average[214, 306]. In our simulations, we concentrate on water molecules and consider a unit vector that is directed along the OH bond.

Water/vapor interface For the water/vapor interface, using the method introduced in Paragraph 5.2 in Chapter 5, we first obtained the instantaneous interface with thickness $d = 1, \cdots, 6$ Å. Then for each thickness, the method of IMS (Paragraph 5.2) is used to obtain the $C_2(t)$ for the water molecules at the water/vapor interface. The result is shown in Fig. 6.12 A.

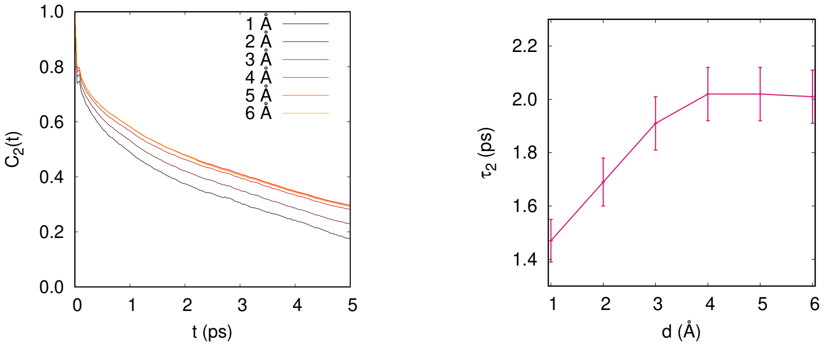

(A) (B)

FIGURE 6.12: (A) Time dependence of $C_2(t)$ for water molecules at the water/vapor interface with different thickness in the range of 1 Å to 6 Å. (B) The dependence of decay time τ_2 on the thickness d in the exponential fitting of $C_2(t)$ for water molecules at the water/vapor interface.

Here we introduce a fitting with an exponential and provide a decay time τ_2, i.e.:

$$C_2(t) = Ae^{-t/\tau_2}, \tag{6.9}$$

with $A = 1.0$ for all thickness values ($d = 1, \cdots, 6$ Å), and the thickness dependence of τ_2 is shown in Fig. 6.12 B. We see that when the interface thickness d is small, the decay time τ_2 increases linearly with d. That is, the orientation relaxation process of OH bonds in the thinner interface is faster than in the thicker interface. Similar to the correlation functions $c(t)$ and $s(t)$ for interfacial water molecules, as the interface thickness increases, the τ_2 converges to a fixed value, which characterizes the decay time of the orientation relaxation process of OH bonds in bulk water. Therefore, we have reached a conclusion that the orientation of OH at the water/vapor interface relaxes faster than in bulk water. From the convergence trend of τ_2 in Fig. 6.12, we found that at the interface with a thickness greater than 4 Å, the OH orientation relaxation of the water/vapor interface is no longer different from bulk water.

Therefore, starting from the instantaneous interface, we reach a consistent conclusion on the issue of estimating the thickness of the water/vapor interface, no matter from the perspective of OH reorientation relaxation or from HB dynamics.

Lithium nitrate solution The anisotropy decay of OH bonds in water molecules at 0.4 M $LiNO_3$/vapor interface is shown in Fig. 6.13. This result implies that the reorientation relaxation rate of water molecules at the interface of the alkali nitrate solution is very close to that at the water/vapor interface.

We also introduced the fitting with an exponential according to Eq. 6.9. As we known in Paragraph 4.1 in Chapter 4, the $LiNO_3$ was inserted at one of the two interfaces, we have a model with one salty interface and one neat interface which can be used as a reference. We obtained $A = 0.70 \pm 0.01$ for both the salty and neat interface, and τ_2 is 3.88 ± 0.09 ps and 4.04 ± 0.09 ps for the salty and neat water interface, respectively. Therefore, the close reorientation decay time (τ_2) for the salty interface and the water/vapor interface is also obtained from this fitting.

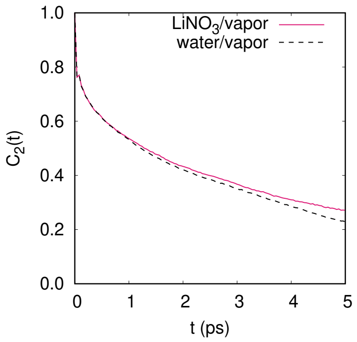

FIGURE 6.13: Anisotropy decay of OH bonds in water molecules at the $LiNO_3$/vapor interface. The water molecules considered are in an instantaneous layer with $d = 2$ Å.

To understand the reason of the difference between alkali nitrate solution/vapor interfaces and the water/vapor interface, we consider the water dangling OH bonds (or free OH bonds) at the interfaces. First, we calculated the distribution of the number (n) of H-bonds per OH group at a given instantaneous interface by

$$P(n) = \frac{\sum_j^J N_{l,j}}{\sum_j^J \sum_{i=1}^M N_{i,j}}, \tag{6.10}$$

where $N_{l,j}$ denotes the number of OH bonds which own l H-bonds at the j-th sampling time, and $l = 1, \cdots, l_{\max}$. The parameter $l_{\max}$ is defined as the largest number of H-bonds that a OH bond can form. For the solution/vapor interface, we use $l_{\max} = 5$.

For the $LiNO_3$/vapor interface with different thickness, the distributions $P(n)$'s are shown in Fig.s 6.14 a–d and Fig. 6.15 b. The same calculations for the water/vapor interface are plotted as a reference in these Fig. 6.14 and Fig. 6.15 a.

From Fig.s 6.14 and 6.15, we find: (1) For thinner layers (Fig.s 6.14 a–c, i.e., $d = 1, 2, 3$ Å), $P(n = 0)$ for the $LiNO_3$/vapor interface is smaller than that for the water/vapor interface. This result implies that there are less water dangling OH bonds at the $LiNO_3$/vapor interface, compared to the water/vapor interface. (2) The $P(n = 1)$ for the $LiNO_3$/vapor interface is larger if d is thin enough. This means that the water at the topmost interface layer are more H-bonded than those at the water/vapor interface. (3) In particular, for $d = 2$ Å, we have $P(n = 2)$ for the $LiNO_3$/vapor interface is larger than that for the water/vapor interface, which is approximately zero. This character means that for the water/vapor interface there are less possibility for a OH bond to form *two* H-bonds at the topmost instantaneous layer. (4) From the distribution $P(n)$, we again obtain the consistent result, i.e., when d is large enough, or $d \geq 4$ Å, the difference between the $LiNO_3$/vapor and the water/vapor interface disappears. Both distributions converge to $P(n)$ for bulk water.

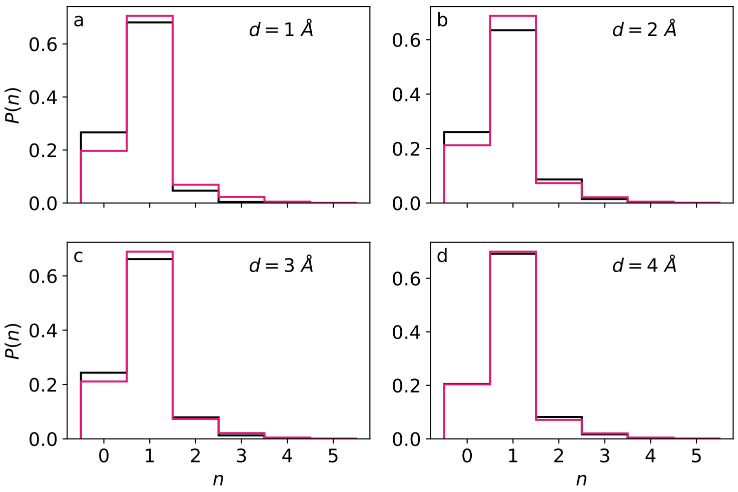

FIGURE 6.14: Distribution $P(n)$ of the number of H-bonds per OH group at instantaneous layers with thickness d. The red (black) line is for the $LiNO_3$/vapor (water/vapor) interface.

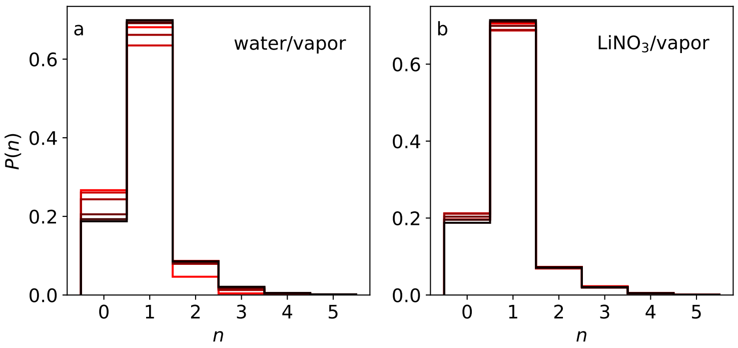

FIGURE 6.15: Distribution $P(n)$ of the number of H-bonds per OH group at instantaneous layers with thickness d ($d = 1, \cdots, 6$ Å). The red (black) line is for the interfaces (bulk) phase.

These results demonstrate that the structural properties in the instantaneous layer with $d \leq 4$ Å is the main source of interfacial properties, such as HB lifetime, anisotropy decays and VSFG spectroscopy.

Alkaline iodide solutions We also calculated $C_2(t)$ for the LiI/vapor interface (the whole slab). The result of $C_2(t)$ for the solution/vapor interface is shown in Fig. 6.16. It decays significantly faster than $C_2(t)$ for the water/vapor interface, indicating that H-bonds at the LiI/vapor interface are orientated more frequently than that of the water/vapor interface. From the single exponent fitting by Eq. 6.9, we obtained $\tau_2 = 2.1 \pm 0.1$ ps (2.7 ± 0.1 ps) for the LiI interface (the water/vapor interface). i.e., water molecules at the LiI/vapor interface have larger reorientation relaxation rate than that at the water/vapor interface. It shows that the LiI accelerate the dynamics of molecular reorientation of water molecules at the interface.

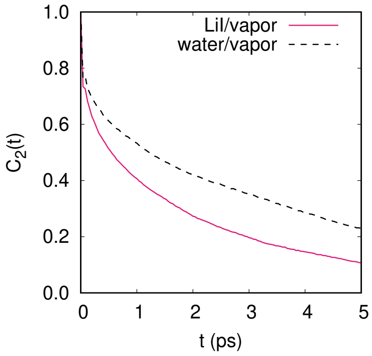

FIGURE 6.16: Time dependence of $C_2(t)$ for OH bonds at the LiI/vapor (solid line) and the water/vapor (dashed line) interface. The water molecules considered are in instantaneous layer with $d = 2$ Å.

The distribution of the number of H-bonds per OH bond for the LiI/vapor interface is also calculated and analyzed. For the LiI/vapor interface, the distribution $P(n)$ is shown in Fig. 6.17 a–d and Fig. 6.18. (1) From both Fig.s 6.17 and 6.18, we find that the ratio of water dangling OH bonds for the LiI/vapor interface is smaller than that for the water/vapor interface. (2) When $d > 4$ Å the distribution $P(n)$ does not change anymore. (3) At top layer, $P(n = 1)$ is larger than that for the water/vapor interface, this result implies that OH bonds are bonded to ions. From the probability distribution of ions for the LiI/vapor interface (Fig. 6.3 a), which shows that the I^- has more propensity for surface than the Li^+. Therefore, there are more O–H$\cdots$I bonds at the LiI/vapor interface than in bulk phase. (4) $P(n = 0)$ of the LiI/vapor interface is larger than that of the water/vapor interface, this implies that at the LiI/vapor interface, the O–H$\cdots$I bonds replace the role of O–H$\cdots$O bonds at these layers.

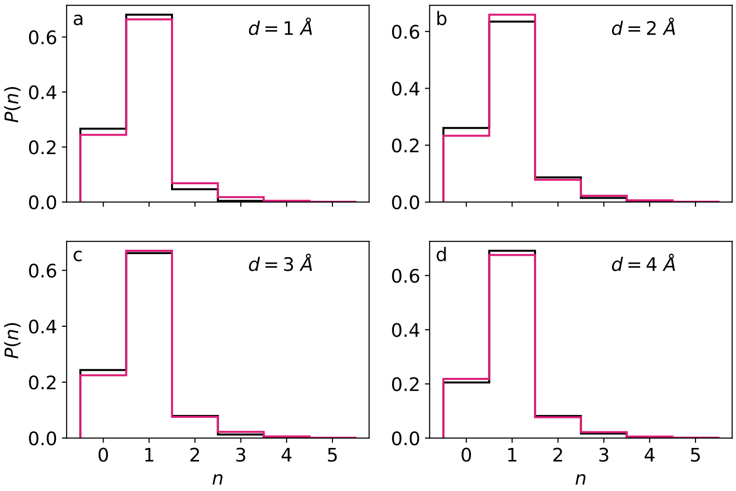

FIGURE 6.17: Distribution $P(n)$ of the number of H-bonds per OH group at instantaneous layers with thickness d. The red (black) line is for the LiI/vapor (water/vapor) interface.

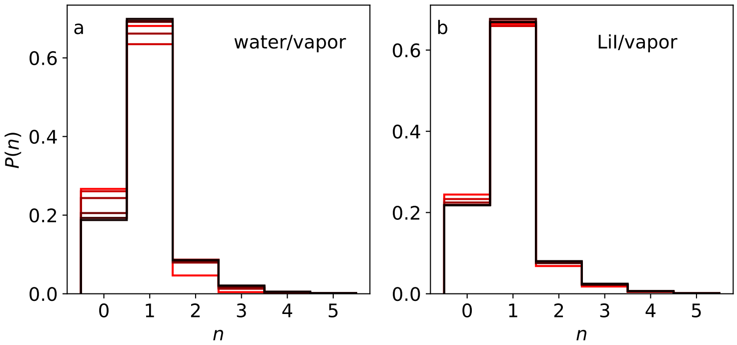

FIGURE 6.18: Distribution $P(n)$ of the number of H-bonds per OH group at instantaneous layers with thickness d ($d = 1, \cdots, 6$ Å). The red (black) line is for the interfaces (bulk) phase.

Therefore, the increasing density of the O–H$\cdots$I bonds, and decreasing density of water dangling OH bonds are two clear structural properties of solution/vapor interface. The decreasing of water dangling OH bonds explains reduction of the intensity of the 3700 cm^{-1} peak in the alkali iodide solutions (see Fig.s 4.4 and 4.5 for LiNO$_3$ solution), and the increasing density of the O–H$\cdots$I bonds explains the blue-shift of the 3200–3600 cm^{-1} band (see ref.s [52, 64] for VSFG spectra for NaI solution).

6.4 Rotational anisotropy decay of water molecules in ions' solvation shells

In this paragraph, we investigate the effects of ions on water molecules' orientation dynamics of water molecules in the ions' solvation shells.

We calculated the anisotropy decay of water molecules in ions' solvation shells in alkali nitrate (alkali iodide) solution/vapor interfaces. The calculated average of $C_2(t)$ is shown in Fig. 6.19. It is obtained by averaging the $C_2(t)$'s for 6 different trajectories. The radius of the solvation shell of nitrate O, Li$^+$, and water molecules are taken as 4.0, 2.8 and 3.5 Å, respectively. These values are obtained from the position of the first minimum of the RDFs $g_{\text{NN-OW}}(r)$ (NN: nitrate nitrogen), $g_{\text{Li-OW}}(r)$ and $g_{\text{OW-OW}}(r)$, for bulk alkali nitrate solution, as shown in Fig. 6.9. To avoid that the considered molecules diffuse out of the first solvation shell, we only consider trajectories with a duration of 10 ps.

For the NaNO$_3$/vapor interface, the average values of the $C_2(t)$ are also shown in Fig. 6.19. The radius of the solvation shell of nitrate O, Na$^+$, and water molecules are taken as 4.0, 3.2 and 3.5 Å, respectively. (Also in this case ,they are obtained from the RDFs $g_{\text{NN-OW}}(r)$, $g_{\text{Na-OW}}(r)$ and $g_{\text{OW-OW}}(r)$, see Fig. 6.9.)

Finally we also calculated $C_2(t)$ for the KNO$_3$/vapor interface. The average values of $C_2(t)$ are shown in Fig. 6.19. The radius of the solvation shell of nitrate O, K$^+$, and water molecules are taken as 4.0, 3.6 and 3.5 Å, respectively. (Also in this case, they are obtained from the RDFs $g_{\text{NN-OW}}(r)$, $g_{\text{K-OW}}(r)$ and $g_{\text{OW-OW}}(r)$, see Fig. 6.9.)

From the above calculation of $C_2(t)$, we find that in the interfacial systems of alkali metal nitrate solution, NO$_3^-$ always accelerates the reorientation dynamics of water molecules in the solvation shells of nitrate ions. However, the reorientation dynamics of water molecules in the solvation shells of alkali metal ions may slow down (for $LiNO_3$ and $NaNO_3$ solutions, respectively) or accelerate (for the KNO_3 solution), due to the presence of alkali metal ions.

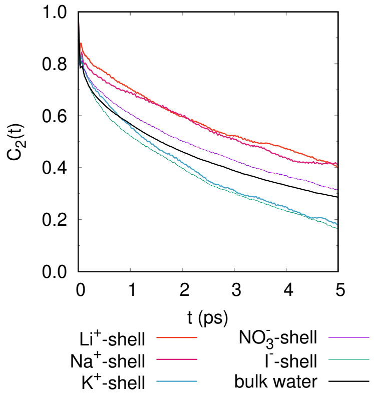

FIGURE 6.19: The $C_2(t)$ for water molecules in the solvation shell of Li^+, Na^+, K^+, I^- and NO_3^- ions at alkali nitrate (alkali iodide) solution/vapor interfaces. For comparison, the $C_2(t)$ for bulk water (black line) is shown.

For the dynamic process in a short time, we find a relation between the reorientation relaxation time and the radius of solvation shell. Using a single exponential fit of $C_2(t)$ we obtain the values of τ_2 as reported in Table 6.4. The anisotropy decay is a single exponential given by

$$C_2(t) = e^{-t/\tau_2}.$$

It can be seen that the reorientation relaxation time τ_2 of the water molecules in the solvation shell decreases with the increase of the radius of the solvation shell, as shown in Fig. 6.20. We also give a linear regression function (solid line) to fit this relation, obtained from the data from alkali nitrate (iodide) solutions. The relation between orientation relaxation time τ_2 and the radius is as following:

$$\tau_2(r) = -ar + b, \tag{6.11}$$

where $a = -1.5 \pm 0.5$ and $b = 8.6 \pm 1.7$.

TABLE 6.4: The radius r of the first solvation shells and corresponding relaxation times τ_2 at the interface of alkali nitrate (alkali iodide) solutions. For NO_3^-, we use the O–OW distance, instead of the N–OW distance to define the radius of the ion's solvation shell.

ion (molecule)	r (Å)	τ_2 (ps)
Li^+	2.8	4.57(3)
Na^+	3.2	4.35(2)
K^+	3.6	2.37(2)
H_2O	3.5	2.92(2)
NO_3^-	4.0	3.32(2)
I^-	4.3	2.22(2)

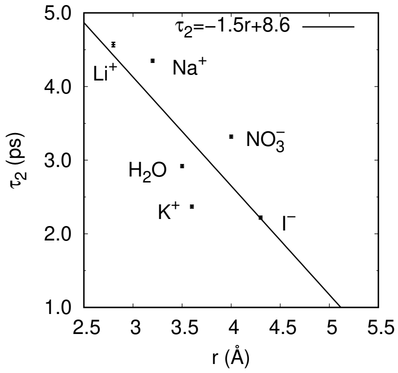

FIGURE 6.20: Dependence of τ_2 on the radius of the first solvation shell of molecules and ions (H_2O, Li^+, Na^+, K^+, I^- and NO_3^- ions) in the slab of alkali nitrate (iodide) solutions.

Using the same approach as above, we calculated τ_2 with a single exponential fitting. We also find that τ_2 of the water molecules in the solvation shell decreases with the increase of the radius of the solvation shell (see the data for I^- in Table 6.4).

To explain the $C_2(t)$ for the $LiNO_3$/vapor and the LiI/vapor interfaces, we list the peaks of RDFs for the LiI/vapor, the $LiNO_3$/vapor and the water/vapor interfaces (Fig. 6.5). We find that there is a correlation between reorientation and the strength of the H-bonds: Nitrate–water and W–W bonds have very close local structure, while the iodide-water (I^-–W) bonds are of significantly different local structure. This result can be found from the larger value (3.61 Å and 2.66 Å, see the first two rows in Table 6.5) of the first peaks' locations in $g_{\text{I-OW}}$ and $g_{\text{I-HW}}$, and close first peak locations for ON–OW and OW–OW RDFs (2.80 Å and 2.79 Å, see the 3rd and 5th row in Table 6.5). The difference between water molecules with W–W and N–W bonds is discussed in Paragraph D.4.

TABLE 6.5: The peaks' position (unit: Å) of RDFs for the LiI/vapor, the $LiNO_3$/vapor and the water/vapor interfaces (see Table D.5 and D.6).

g(r)	1st peak	2nd peak
I-OW	3.61	-
I-HW	2.66	4.07
ON-OW	2.80	-
ON-HW	1.83	3.30
OW-OW	2.79	-
OW-HW	1.83	3.25

6.5 Summary

We have investigated the effects of ions on HB dynamics of water molecules at alkali nitrate and alkali iodide solution/vapor interfaces. Nitrate–water HB dynamics decay faster than water–water's, which proves that N–W bonds is weaker than W–W bonds. The result from the calculated $\Im\chi^{(2),\mathrm{R}}$ spectra is that the blue shift of the HB band in the nonlinear susceptibility, or, the nitrate ion in the solution tends to be distributed on the surface, which is consistent with the smaller relaxation time given by HB population correlation functions $c(t)$ and $s(t)$.

From a detailed analysis of the dynamics of water molecules in the second solvation shell of ions, we found that HB relaxation between water molecules in the second solvation shell of the ion is no longer significantly affected by the ion. However, the reorientation relaxation time τ_2 of the water molecules in the first solvation shell decreases linearly with the increase of the radius of the ions' solvation shell.

The rotational anisotropy decay of water molecules at the water/vapor and solution/vapor interfaces was investigated to understand the effects of ions on the dynamics of water at interfaces. The instantaneous interfaces are used in the analysis. The main result is that the ratio of the free OH bonds for the water/vapor interface is an important factor that affect the decay rate of the reorientation relaxation of water molecules. Single exponential decay is a good model for water molecules at the interface of alkali iodide solutions, and the faster anisotropy decay of water molecules at the interface is the effects of free OH stretch and hydrogen–iodide bond. This difference of HB dynamics from the water/vapor interface is the source of the $\Im\chi^{(2)}$ spectrum of the interface of alkali iodide solutions.

Chapter 7

Conclusions and Perspectives

Using density functional theory-based molecular dynamics (DFTMD) simulations, we have analyzed the interfacial structure and dynamics of electrolyte solutions containing alkali nitrates and alkali halides, which share some similarities in terms of surface propensity. In particular we have presented a detailed analysis of the vibrational sum-frequency generation (VSFG) spectra, hydrogen bond (HB) dynamics, and reorientation dynamics of water molecules at the solution/vapor interfaces. We have also provided a molecular interpretation of the interface vibrational spectra.

We have shown that the use of simple models, such as small clusters are not suitable to reproduce the experimental spectra and cannot provide a microscopic interpretation of the VSFG spectra. Realistic models of the interface are required to address the perturbation of ions on the water surface.

As a first system we have analyzed the behaviour of a salty interface containing alkali nitrates. Both measured and calculated VSFG spectra shows a reduced intensity of the lower frequency portion region, when compared to the water/vapor interface. This reduction is attributed to the H-bonds established between nitrate and the surrounding water molecules at the interface. This effects is only related to the presence of nitrate at the water surface and is *not* due to the alkali metal ions. We have shown that although the Li^+ can reside relative close to the water surface, also forming a water mediated ion pair with NO_3^-, its effect on the VSFG spectrum is not visible. The water molecule which mediate the interaction between nitrate and the alkali metal ions would produce a red-shifted peak in small water cluster's VDOS, but its influence is not visible in the VSFG spectra. Our simulations permit to describe the distribution of ions relative to the interface: nitrate ions are located in the uppermost layer of the interface, and alkali metal ions are located in the layer below and form with the anion a water separated ion pair. The higher stability of the water-separated ion configuration is also proved by our calculation of the free energy difference between the different configurations.

Using the instantaneous interface layer, we discussed the thickness of the water/-vapor interface, the relaxation time of the interfacial H-bonds, and the distribution of free OH bonds, which have an important contribution to the VSFG spectrum. These properties all converge when the interface thickness is about 4 Å. In particular, the distribution of the number of H-bonds per OH group is consistent with the frequency shift of the H-bonded OH stretching band of the VSFG spectrum. These results suggest that considering instantaneous interfaces is essential for understanding the microscopic structure about aqueous interfaces.

To obtain information on the HB lifetime and its rate of breaking and forming, we have used the Luzar-Chandler HB population operator and calculated the correlation functions $c(t)$, $n(t)$, and $k(t)$ for bulk water. We find that both NO_3^-–water and I^-–water bonds have shorter lifetime than water–water bonds. The HB relaxation and the lifetime of H-bonds at the interface are dominated by the concentration of ions accumulated at the interface. Another general conclusion is that the HB strength between water molecules in the ions' second solvation shell is independent of the ion–water interactions in ions' first solvation shell.

In Chapter 5 we have shown that, the method of interfacial molecule sampling (IMS) can give information on the HB breaking and reforming rates at the water/vapor interface and permits to determine how far from the surface the interface affects the dynamics of H-bonds in water. Due to the movement of water molecules at the interface and in the bulk phase, the number of molecules at the interface will fluctuate. Therefore, this method *underestimates* the HB breaking rate constant of the water/-vapor interface. We have provided a method based on the instantaneous surface and the new-defined interfacial hydrogen bond (IHB) operator to obtain the interfacial HB dynamics of instantaneous water/vapor interfaces, and the thickness of the interface. The IHB method avoids sampling the molecules reside in the interfacial layer and it also provide partial information on the HB breaking and reforming rates at the interface. Because of the definition of the IHB population, the IHB method *overestimates* the HB breaking rate constant. The results for the two methods indicate that, as the thickness of the water layer increases, the HB breaking and reforming rate constants in the water layer below the instantaneous surface tends to be uniform. The real HB dynamical characteristics at the water/vapor interface are derived from the two extreme cases using the convergence behavior of the HB reaction rate constants and relaxation time of HB population correlation functions. Therefore, the result has given an estimate of the thickness of the water/vapor interface. The combination of the IMS method and the IHB population operator is extended to the solution/vapor interface. Due to the specific ions distribution in the normal direction of the interface, the thickness of the solution/vapor interface is greater than the thickness of the water/vapor interface.

In the last part of the thesis, the concept of instantaneous interface has been extended to analyze the first solvation shell around the ions. For the alkali iodide solution/vapor interfaces, we found that the cations does not alter the H-bonding network outside the first hydration shell. It is concluded that no long-range structural-changing effects for alkali metal cations. Moreover, the solvation shell HB method shows that, as far as the Li^+, Na^+, K^+, NO_3^- and I^- ions are concerned, the HB dynamics for water molecule pairs does not vary significantly with these ions.

To sum up, from the results of nonlinear susceptibilities, which show bonded OH-stretching peaks with higher frequencies, we conclude that the water molecules at the interfaces of the alkali iodide solutions are participating in weaker H-bonds, compared with those at the water/vapor interface. The origin of these features can be found in the distribution of I^- and the alkali metal cations over the thickness on the order of 5 Å. Therefore, both the VSFG spectra of alkali nitrate and iodide solutions can be explained in the same way, in that the anions has propensity for the surface, and the weaker anion–H bonds at the topmost interface layer contribute to the blue-shifted H-bond band, and the relative less free OH bonds produce a lower free OH stretching band. This conclusion is verified by the distribution $P(n)$ of the number of H-bonds owned by a OH group at the instantaneous interface layer. By calculating the rotational anisotropy decay for water molecules at the instantaneous interface, we obtain that the average density of free OH bonds is an important factor that affect the decay rate of the reorientation relaxation of water molecules.

Some of the methods discussed in this thesis can be extended to other systems. In particular, the combination of IHB and IMS can provide a basis for determining the thickness of the interface layer in other systems or environments, for example, to study the dynamics of water molecules around proteins. In recent years, there is a lot of experimental and simulation progress, for example, the diffusion acceleration effect on the glass surface[307, 308], and the aging effect of the non-equilibrium dynamics of the protein molecules on cell surface[309]. To describe these effects quantitatively, it is important to define the size of the interface accurately. We believe that combining the VSFG method, IHB and IMS methods will help us more accurately identify the range and size of the interface in these systems. This will likely promote our understanding of the nature of these effects at interfaces.

Finally, as shown in this thesis, *ab initio* simulations permit to widen our understanding of interface properties and the interactions between atoms. However, the high computational cost prevents applications of AIMD calculations to larger systems. One possible solution to this problem is to using the *ab initio* data accumulated for small systems to train potentials (e.g. with machine learning approaches[310]), and then use these potentials to investigate larger systems such as more extended interfaces, e.g., at different ions concentrations[311–314].

Appendix A

Calculation of nonlinear optical susceptibilities

Definitions and relations 1. Definition of double product of a m-order tensor A and a n-order tensor B is a tensor with order $m+n-2$.

$$A : B = A_{ij}B_{lm}\delta_{jl}\delta_{im}. \tag{A.1}$$

2. The components of product of AB is defined by

$$(AB)_{ijlm} = A_{ij}B_{lm}. \tag{A.2}$$

3. For vectors $\mathbf{a}$, $\mathbf{b}$, $\mathbf{c}$ and $\mathbf{d}$, $\mathbf{ab} : \mathbf{cd} = (\mathbf{a}\cdot\mathbf{d})(\mathbf{b}\cdot\mathbf{c})$.
Proof:

$$\begin{aligned}\mathbf{ab} : \mathbf{cd} &= (\mathbf{ab})_{ij}(\mathbf{cd})_{lm}\delta_{jl}\delta_{im}\\ &= (\mathbf{ab})_{ij}(\mathbf{cd})_{ji}\\ &= (a_i b_j)(c_j d_i)\\ &= (\mathbf{b}\cdot\mathbf{c})(\mathbf{a}\cdot\mathbf{d})\end{aligned} \tag{A.3}$$

Proof of Eq. 2.41 Since

$$\lim_{t\to\infty} |e^{-it(a-ib)}| \le \lim_{t\to\infty} |e^{-bt}| = 0,$$

we can obtain

$$\int_0^\infty dt e^{-it(a-ib)} = \frac{1}{b+ia},$$

i.e.,

$$i\int_0^\infty dt e^{-it(a-ib)} = \frac{1}{a-ib}.$$

Set $a = (\omega_{v'} - \omega_v) - \omega$, and $b = \gamma_{v'v}$, then we have

$$\int_0^\infty dt e^{-it[(\omega_{v'}-\omega_v)-\omega-i\gamma_{v'v}]} = \frac{-i}{(\omega_{v'}-\omega_v)-\omega-i\gamma_{v'v}}. \tag{A.4}$$

Using Eq.A.4, express Eq.2.40 in integral form, we obtain

$$\beta^{\mathrm{R}}_{\eta\xi\kappa} = i\int_0^\infty dt e^{i\omega t}\langle\alpha_{\eta\xi}(t)\mu_{\eta\xi}(0)\rangle,$$

which is Eq.2.41.

Properties of $\chi^{(2)}$ Theoretically, the interaction of electromagnetic radiation with mater in the long-wavelength limit is treated within the *electric dipole approximation* (EDA). The EDA is usually expressed in terms of a scalar potential $-\mathbf{E}(0,t)\cdot\mathbf{r}$, where $\mathbf{E}(0,t)$ is the electric field at the origin, and $\mathbf{r}$ is the displacement vector, and a zero vector potential[315]. Within the EDA, the magnetic multipoles are neglected. A material system under external electric field $\mathbf{E}$ induces dipole moment, or polarization. The polarization $\mathbf{P}$ is defined as the dipole moment per a unit volume of a bulk material. When the system indicates a surface, $\mathbf{P}$ is defined as the dipole moment per a unit area. The induced polarization $\mathbf{P}$ is represented as a power series of the electric field[52]

$$P_i = \chi^{(1)}_{ij}E_j + \chi^{(2)}_{ijk}E_jE_k + \cdots \,, \tag{A.5}$$

where the subscripts i, j, k denote the Cartesian components. The first term describes the linear response of polarization with respect to electric field, where $\chi^{(1)}$ is a second-rank tensor, which is called *linear susceptibility*. The second term is responsible to the second-order nonlinear optical processes, and $\chi^{(2)}$ is the second-order nonlinear susceptibility. Therefore, the generation of a polarization in a nonlinear medium by an optical electric field $\mathbf{E}$ can be presented by

$$P^{(2)}_i = \chi^{(2)}_{ijk}E_jE_k. \tag{A.6}$$

The second-order nonlinear susceptibility $\chi^{(2)}$ is a $3\times3\times3$ third-rank tensor, which characterizes the process and whose components $\chi^{(2)}_{ijk}$ are restricted by the symmetry of the sample. The components of nonlinear susceptibility represented in different coordinate frames, $\chi^{(2)}_{\alpha\beta\gamma}$ and $\chi^{(2)}_{ijk}$, satisfy the condition

$$\chi^{(2)}_{\alpha\beta\gamma} = a_{\alpha i}a_{\beta j}a_{\gamma k}\chi^{(2)}_{ijk}, \tag{A.7}$$

where a can be written as a 3×3 matrix representing an arbitrary combination of rotation and inversion. If a is restricted to be a symmetry transformation A, then all the properties of the sample are identically described in both coordinate frames. Then the elements of $\chi^{(2)}$ are the same in both coordinate frames so that

$$\chi^{(2)}_{\alpha\beta\gamma} = A_{\alpha i}A_{\beta j}A_{\gamma k}\chi^{(2)}_{ijk}. \tag{A.8}$$

If the sample has inversion symmetry[59], i.e., $A_{\alpha i} = -\delta_{\alpha i}$, Eq. A.8 yields

$$\begin{aligned}\chi^{(2)}_{\alpha\beta\gamma} &= (-\delta_{\alpha i})(-\delta_{\beta j})(-\delta_{\gamma k})\chi^{(2)}_{ijk}\\ &= -\chi^{(2)}_{\alpha\beta\gamma}\\ &= 0.\end{aligned} \tag{A.9}$$

Therefore, for any material exhibiting inversion symmetry, $\chi^{(2)}$ is identically 0, and SFG is precluded. This result implies that, within the EDA, the VSFG process is forbidden in any centrosymmetric bulk medium[60], such as isotropic liquids and glasses, but it is allowed at interfaces because of the broken inversion symmetry[61]. The advantage is its wide applicability to almost every interface which lack a center of inversion, as long as light can reach them.

The second important property of $\chi^{(2)}$ is that it is a polar tensor, which has vectorial nature[66]. $\chi^{(2)}$ can also be represented as $\chi^{(2)}$ can be expressed as the sum of β of all molecules in a probed volume

$$\chi^{(2)} = \sum \beta,$$

or more quantitative expression

$$\chi^{(2)} = N_{\mathrm{s}} \beta_{lmn} R(\langle \cos\theta \rangle, \langle \cos^3\theta \rangle), \tag{A.10}$$

where N_{s} is the number of molecules in a unit area, $R(\langle \cos\theta \rangle, \langle \cos^3\theta \rangle)$ is an orientation function, θ is the polar orientation angle of a molecule and $\langle \cdots \rangle$ denotes the ensemble average. Thus $\chi^{(2)}$ has a sign relating to the molecular orientation when $\chi^{(2)} \neq 0$. From Eq. A.10, if $\chi^{(2)}$ and β_{lmn} is known, the sign of $\langle \cos\theta \rangle$ can be determined. Therefore, the up/down orientation of interfacial molecules can be experimentally determined.

Molecular dipole moment and dipole polarizability derivatives The polarizability tensor α is defined by the relation

$$\delta \boldsymbol{\mu} = \alpha \mathscr{E} \tag{A.11}$$

where $\delta\boldsymbol{\mu}$ is the electric dipole moment (a vector) induced in the molecule by the electric field $\mathscr{E}$, with the components $\mathscr{E}_x$,$\mathscr{E}_y$ and $\mathscr{E}_z$. Now we describe the main algorithm to implement the parametrization of the molecular dipole moment derivative $\frac{\partial \mu_k}{\partial r}$ and dipole polarizability derivative $\frac{\partial \alpha_{\eta\xi}}{\partial r}$. This result can be used in the VACF-based method for calculating the VSFG spectroscopy intensity.

Given a DFTMD trajectory of total length $\sim 10^2$ ps for bulk water, sampled with a frequency ~ 1 ps^{-1}. For the j-th water molecule in the n-th snapshot of the trajectory, we denote the two OH bonds as $\mathrm{H}^{n,j,\epsilon=1}$ and $\mathrm{H}^{n,j,\epsilon=-1}$. We will calculate statistical average over all time steps and all OH bonds, therefore, we just denote the corresponding OH bonds by $\epsilon = 1$ and $\epsilon = -1$, respectively. The H atoms in a water molecule are denoted by $\mathrm{H}^{\epsilon=1}$ and $\mathrm{H}^{\epsilon=-1}$, and the O atom by O^0.

We used three different coordinate frames: the lab frame $(x^{\mathrm{l}}, y^{\mathrm{l}}, z^{\mathrm{l}})$, the molecular frame $(x^{\mathrm{m}}, y^{\mathrm{m}}, z^{\mathrm{m}})$ and the bond frame $(x^{\mathrm{b}}, y^{\mathrm{b}}, z^{\mathrm{b}})$ (Fig. 2.2). In the lab frame, the z^{l}-axis is perpendicular to the interface. The molecular frame will be used to decompose the signal into normal modes of water monomers. For the j-th molecule, the z^{m} axis is along the bisector of the H-O-H angle, the x^{m} axis is in the molecular plane, and the y^{m} axis is out of the molecular plane. In the bond frame, $z^{\mathrm{b},\epsilon}$ axis is along the bond ϵ of a molecule, $z^{\mathrm{b},\epsilon}$ is in the molecular plane and $y^{\mathrm{b},\epsilon}$ is out of the molecular plane.

There are two direction cosine matrices between the bond frames and molecular frame, we name them as $D^{\mathrm{b},\epsilon=-1}$ and $D^{\mathrm{b},\epsilon=1}$[114], or $D^{\mathrm{b},-1}$ and $D^{\mathrm{b},1}$ for short. Then the direction matrix $D^{\mathrm{b},\epsilon}$ can be represented by direction cosines between $\mathbf{x}^{\mathrm{b},\epsilon}$ and $\mathbf{x}^{\mathrm{m}}$, where $\epsilon = \pm 1$ and θ denotes the H-O-H angle in the j-th water molecule for the n-step:

$$\hat{x}_1^{\mathrm{b},\epsilon} = \epsilon \cos\frac{\theta}{2} \hat{x}_1^{\mathrm{m}} + \sin\frac{\theta}{2} \hat{x}_3^{\mathrm{m}} \tag{A.12a}$$

$$\hat{x}_2^{\mathrm{b},\epsilon} = \epsilon \hat{x}_2^{m} \tag{A.12b}$$

$$\hat{x}_3^{\mathrm{b},\epsilon} = -\epsilon \sin\frac{\theta}{2} \hat{x}_1^{\mathrm{m}} + \cos\frac{\theta}{2} \hat{x}_3^{\mathrm{m}} \tag{A.12c}$$

i.e.,

$$D^{\mathrm{b},\epsilon} = \begin{pmatrix} \epsilon\cos\frac{\theta}{2} & 0 & \sin\frac{\theta}{2} \\ 0 & \epsilon & 0 \\ -\epsilon\sin\frac{\theta}{2} & 0 & \cos\frac{\theta}{2} \end{pmatrix}. \tag{A.13}$$

The molecular frame is given by the direction cosine matrix $D^{\mathrm{m,l}}$ (or D^{m}) between molecular frame and the lab frame

$$\hat{\mathbf{x}}^{\mathrm{m}} = D^{\mathrm{m}}\hat{\mathbf{x}}^{\mathrm{l}}. \tag{A.14a}$$

The dipole moment of each OH bond with different length is required to determine the dipole moment derivative. Therefore, we elongate (reduce) one bond ϵ by $\Delta r = 0.05$ Å ($\Delta r = -0.05$ Å), and keep other bonds in the total system still, then we obtain a updated coordinate. Then the MLWF centers for the system can be calculated from the updated coordinate, using force and energy calculation at the DFT level. From the Wannier centers of the j-th water molecule, we can calculate the dipole moment for the elongated (reduced) bond ϵ. In the bond frame, $|\mu^b| = |\mu^b_z|$. Therefore, we can calculate the $k = z$ component of the dipole moment for ϵ in water molecule j from the MLWF centers[316]. The MLWF centers are computed and the partial dipole moment for a given molecular species I is defined as[216]

$$\mu^I = \sum_{i\in I}(Z_i\mathbf{R}_i - 2\sum_{n\in i}\mathbf{r}^{\mathrm{w}}_n). \tag{A.15}$$

In particular, here it is expressed as

$$\mu^{\mathrm{b},r+\Delta r,\epsilon} = \frac{1}{2}Z_{\mathrm{O}}\mathbf{R}^0 + Z_{\mathrm{H}}\mathbf{R}^{\epsilon} - 2r^{\mathrm{w},\epsilon} - 2r^{\mathrm{w},0}, \tag{A.16}$$

where $\epsilon = \pm 1$. In the ϵ frame, the $k = z$ component dipole moment derivative with respect to bond length[317] for the single OH bond ϵ in water molecule j is

$$\frac{\partial \mu^{\mathrm{b},\epsilon}}{\partial r} = (\mu^{\mathrm{b},r+\Delta r,\epsilon} - \mu^{\mathrm{b},r,\epsilon})/\Delta r. \tag{A.17}$$

Since the components of the dipole moment in the molecular frame are given by the transformation:

$$\begin{pmatrix} (\frac{\partial \mu^{\mathrm{m}}}{\partial r})_1 \\ (\frac{\partial \mu^{\mathrm{m}}}{\partial r})_2 \\ (\frac{\partial \mu^{\mathrm{m}}}{\partial r})_3 \end{pmatrix} = D^{\mathrm{b},\epsilon}\begin{pmatrix} 0 \\ 0 \\ \frac{\partial \mu^{\mathrm{b},\epsilon}}{\partial r} \end{pmatrix}, \tag{A.18a}$$

then, to calculate the individual polarizability for a OH bond from Wannier centers, calculations involving finite electric fields (of 0.0001 au intensity) were performed independently along x, y, and z directions at each sampled time step[102]. For the electric field $\mathscr{E} \in \{\mathscr{E}_x, \mathscr{E}_y, \mathscr{E}_z\}$, like in the case of no external electric field, the MLWF centers are calculated. For a finite Δr, the dipole moment is given by

$$\mu^{\mathrm{b},r+\Delta r,\epsilon,\mathscr{E}} = Z_H\mathbf{R}^{\epsilon,\mathscr{E}} + \frac{1}{2}Z^0\mathbf{R}^{0,\mathscr{E}} - 2\mathbf{r}^{\mathrm{w},\epsilon,\mathscr{E}} - 2\mathbf{r}^{\mathrm{w},0,\mathscr{E}}. \tag{A.19}$$

From the relation (obtained from Eq. A.11)

$$0 = \alpha_{11}^{\mathrm{b},r+\Delta r}\mathscr{E}_1 + \alpha_{12}^{\mathrm{b},r+\Delta r}\mathscr{E}_2 + \alpha_{13}^{\mathrm{b},r+\Delta r}\mathscr{E}_3 \tag{A.20a}$$

$$0 = \alpha_{21}^{\mathrm{b},r+\Delta r}\mathscr{E}_1 + \alpha_{22}^{\mathrm{b},r+\Delta r}\mathscr{E}_2 + \alpha_{23}^{\mathrm{b},r+\Delta r}\mathscr{E}_3 \tag{A.20b}$$

$$\delta\mu_3^{\mathrm{b},r+\Delta r} = \alpha_{31}^{\mathrm{b},r+\Delta r}\mathscr{E}_1 + \alpha_{32}^{\mathrm{b},r+\Delta r}\mathscr{E}_2 + \alpha_{33}^{\mathrm{b},r+\Delta r}\mathscr{E}_3. \tag{A.20c}$$

where

$$\delta\mu_3^{\mathrm{b},r+\Delta r} = \mu_3^{\mathrm{b},\epsilon,r+\Delta r,\mathscr{E}} - \mu_3^{\mathrm{b},\epsilon,r+\Delta r}. \tag{A.21}$$

and the expressions of the electric filed $\mathscr{E}^{\mathrm{b}}$ in a OH frame for the three cases of external electric field which is along x, y and z axis in the lab frame, respectively, we obtain 9 equations. For

$$\mathscr{E}^{\mathrm{l}} = (\mathscr{E}_0\ 0\ 0)^{\mathsf{T}}$$

where $\mathscr{E}_0 = 0.0001$ au, we can obtain the intensity of the external electric filed in the molecular frame

$$\mathscr{E}_1^{\mathrm{m}} = D_{12}^{\mathrm{m}}\mathscr{E}_2^{\mathrm{l}} \tag{A.22a}$$

$$\mathscr{E}_2^{\mathrm{m}} = D_{22}^{\mathrm{m}}\mathscr{E}_2^{\mathrm{l}} \tag{A.22b}$$

$$\mathscr{E}_3^{\mathrm{m}} = D_{32}^{\mathrm{m}}\mathscr{E}_2^{\mathrm{l}}, \tag{A.22c}$$

where D_{pq}^{m} is the pq-component of D^{m}. In OH bond frame,

$$\mathscr{E}^{\mathrm{b}} = D^{\mathrm{b}}\mathscr{E}^{\mathrm{m}}. \tag{A.23}$$

Similarly, we obtain expansions of the intensity of the electric field for the other two cases: when $\mathscr{E}^{\mathrm{l}} = (0, \mathscr{E}_0, 0)^{\mathrm{T}}$ and when $\mathscr{E}^{\mathrm{l}} = (0, 0, \mathscr{E}_0)^{\mathrm{T}}$, respectively. Here, $\mathscr{E}_x$ is the electric field along x-axis in the lab frame. Then the dipole polarizability for the bond ϵ is as follows:

$$\frac{\partial\alpha_{31}^{\mathrm{b},\epsilon}}{\partial r} = (\alpha_{31}^{\mathrm{b},\epsilon,r+\Delta r} - \alpha_{31}^{\mathrm{b},\epsilon,r})/\Delta r \tag{A.24a}$$

$$\frac{\partial\alpha_{32}^{\mathrm{b},\epsilon}}{\partial r} = (\alpha_{32}^{\mathrm{b},\epsilon,r+\Delta r} - \alpha_{32}^{\mathrm{b},\epsilon,r})/\Delta r \tag{A.24b}$$

$$\frac{\partial\alpha_{33}^{\mathrm{b},\epsilon}}{\partial r} = (\alpha_{33}^{\mathrm{b},\epsilon,r+\Delta r} - \alpha_{33}^{\mathrm{b},\epsilon,r})/\Delta r. \tag{A.24c}$$

Therefore, the average for $(\frac{\partial\mu^{\mathrm{b},\epsilon}}{\partial r})_\kappa$ and $(\frac{\partial\alpha^{\mathrm{b},\epsilon}}{\partial r})_{\eta\xi}$ (the subscripts $\kappa, \eta, \xi = x^{\mathrm{m}}, y^{\mathrm{m}}, z^{\mathrm{m}}$, or $1, 2, 3$) over all OH bonds gives the molecular dipole and polarizability derivatives.

Appendix B

Computational details of the DFTMD simulations

The DFT calculations were done with the CP2K program[93, 177], which incorporates the Gaussian and Plane Waves (GPW) method[287]. Core electrons were described by Goedecker-Teter-Hutter pseudopotentials[318, 319], while the valence electrons were expanded as a double-zeta Gaussian basis set[320]. The cutoff for the auxiliary plane wave basis was set to 280 Ry. The discretized integration time step Δt was set to 0.5 fs. The Brillouin zone was sampled at the Γ-point only and, the BLYP XC functional has been employed. All simulations for the water/vapor interface and aqueous solutions were performed within the canonical NVT ensemble.

Bulk water To simulate the bulk water, we constructed the following model. The number of water molecules in the simulation system is 128, the temperature is $T =$ 300 K, and the box is a cube with a side length of 15.64 Å. In this simulation, we relax the value of the target accuracy for the SCF convergence to 10^{-6}. The size of the simulation box is obtained as follows: According to the experimentally obtained relations between water density, temperature and ion concentration (if ions are present), a nonlinear equation set is established, and then the equation set is solved to find the box size.

Lithium nitrate solutions The simulated interfacial system consisted of 127 water molecules and a Li^+–nitrate pair in a periodic box of size $15.78 \times 15.78 \times 31.56$ Å^3, which corresponds to a density of 0.997 g/cm^3. At each DFTMD step the corrector was applied only once, which implies just one preconditioned gradient calculation. For a given molecular configuration, $\{\mathbf{r}_i(t)\}$, Eq. 5.6 can be solved through interpolation on a spatial grid[157]. We have taken $\{\mathbf{r}_i(t)\}$ to refer to the positions of all atoms except hydrogen atoms in the system, and because the bulk correlation length of liquid water is about one molecular diameter, we have used ξ =2.4 Å; further, we have used $\rho_0 = 0.016$ Å^{-3}, which is approximately one-half the bulk density of water.

The calculation of the $\chi^{(2,\mathrm{R})}$ is done for a model for the water/vapor interface where a slab of 117 water molecules containing one Li^+ and one NO_3^- is included in a period simulation box of 15.60 Å ×15.60 Å ×31.00 Å at 300 K.

For the interface of the $\mathrm{LiNO_3}$ solution, we performed the simulation on a system containing one Li^+ ion, one nitrate ion and 127 water molecules (concentration: $\sim$ 0.4 M). The size of periodic box is $15.78 \times 15.78 \times 31.56$ Å^3.

For the interface of the $\mathrm{NaNO_3}$ solution, the size of periodic box is $15.65 \times 15.65 \times 31.31$ Å^3. For the interface of the $\mathrm{KNO_3}$ solution, the size of periodic box is $15.72 \times 15.72 \times 31.43$ Å^3.

The simulated bulk alkali metal nitrate $\mathrm{LiNO_3}$, $\mathrm{NaNO_3}$, and $\mathrm{KNO_3}$ solution consisted of one alkali metal ion, one nitrate ion and 127 water molecules in a periodic cubic box of length L, which corresponds to their density of $\sim$ 1.00 g cm^{-3}. Here, $L = 15.78$, 15.65, and 15.72 for $LiNO_3$, $NaNO_3$, and KNO_3 solution, respectively.

Water/vapor interface For the calculation of the nonlinear susceptibility $\chi^{(2,\mathrm{R})}$ of water/vapor interface, the water/vapor interface is modeled with a slab made of 121 water molecules in a simulation box of size 15.60 × 15.60 × 31.00 Å^3. For this water/vapor interface, the DFTMD simulations at 300 and 330 K are also calculated.

Interface of alkaline iodide solution The calculation of the $\chi^{(2,\mathrm{R})}$ is done for a model for the water/vapor interface where a slab of 118 water molecules containing one Li^+ and one I^- is included in a period simulation box of 15.60 Å × 15.60 Å × 31.00 Å.

Appendix C

HB dynamics and instantaneous interfaces

C.1 Relations between HB lifetime distributions

The HB lifetime is a significant feature of HB dynamics in liquids. The peculiar properties of water are a direct consequence of water's H-bond lifetime distribution[224, 240, 321]. For example, understanding of HB dynamics is essential when investigating proton transfer reactions in protein environments[322]. The statistical properties of lifetime of H-bonds can be described by a variety of distribution functions[230, 232, 323, 324]. Below we discuss the three probability distribution functions of HB lifetime, so that we can study the dynamic characteristics of H-bonds in liquids and interfaces.

Probability distribution of HB lifetimes in a configuration Suppose that there are n_{tot} H-bonds in a system at time t, and we can distinguish a part of H-bonds from these H-bonds. The lifetime of this part of H-bonds is in a certain range $[\tau, \tau + d\tau]$. We can assume that their number of those bonds is n_τ. One can easily find that $n_{\mathrm{tot}} > n_\tau$. If we observe this part of H-bonds in the next time period $[t, t+\tau]$, then they will be broken once during $[t, t+\tau]$. That is to say, within $[t, t+\tau]$, we will detect the breaking of all H-bonds with lifetime τ (Fig. C.1). Therefore, in a very short period of time $d\tau$, the probability of detecting these H-bonds is $(1/\tau)d\tau$. Since the probability for the HB to have the lifetime $\in [\tau, \tau + d\tau]$ is $P_{\mathrm{t}}(\tau)$. Therefore, the relation between $P_{\mathrm{a}}(t)$ and $P_{\mathrm{t}}(t)$ is

$$P_{\mathrm{a}}(t) = \int_t^\infty P_{\mathrm{t}}(\tau) \frac{d\tau}{\tau}, \tag{C.1}$$

i.e., the probability of the HB breaking for the first time in the time t after detection at the initial moment depends on the number of those H-bonds whose lifetime exceeds the given time t[243].

Hydrogen bond lifetime distributions From the probability $P_{\mathrm{tc}}(t)$ of the total HB lifetime in a configuration, and the probability P_{a} of the first HB breaking in time t after it have been detected at the moment t, one can introduce the average time $\langle \tau_{\mathrm{tc}} \rangle$ and $\langle \tau_{\mathrm{a}} \rangle$:

$$\langle \tau_{\mathrm{tc}} \rangle = \int_0^\infty t P_{\mathrm{tc}}(t) dt, \tag{C.2}$$

$$\langle \tau_{\mathrm{a}} \rangle = \int_0^\infty t P_{\mathrm{a}}(t) dt. \tag{C.3}$$

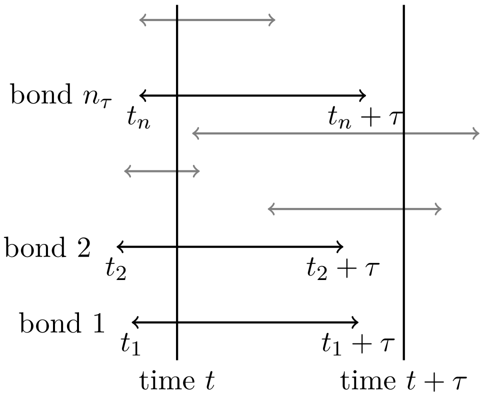

FIGURE C.1: The H-bonds with lifetime τ in a certain configuration. At time t, we assume that there are totally n_{tot} H-bonds can be detected, and n_τ H-bonds are of lifetime τ, therefore, the fraction of H-bonds that have the lifetime τ in the configuration at time t is $P_{\text{tc}}(\tau) = n_\tau/n_{\text{tot}}$. Let τ take all the values in the interval $[0,\infty]$, we can get the HB lifetime distribution $P_{\text{tc}}(t)$.

Since $P_{\text{a}}(t) = \int_t^\infty P_{\text{tc}}(\tau)\frac{d\tau}{\tau}$, i.e.,

$$P_{\text{tc}}(t) = -t\frac{dP_{\text{a}}(t)}{dt},$$

integrating by parts, we obtain

$$\begin{aligned}\langle\tau_{\text{tc}}\rangle &= -\int_0^\infty t^2\frac{dP_{\text{a}}(t)}{dt}dt\\ &= -\int_0^\infty t^2 dP_{\text{a}}(t)\\ &= 2\langle\tau_{\text{a}}\rangle,\end{aligned}$$

in which we used $\int_0^\infty d(t^2P_{\text{a}}) = 0$. Therefore, there is a relationship between $\langle\tau_{\text{tc}}\rangle$ and $\langle\tau_{\text{a}}\rangle$:

$$\langle\tau_{\text{tc}}\rangle = 2\langle\tau_{\text{a}}\rangle. \tag{C.4}$$

We denote the probability of the total HB lifetime along a trajectory as $P_{\text{tt}}(t)$, then the average HB lifetime over the trajectory is

$$\langle\tau_{\text{tt}}\rangle = \int_0^\infty tP_{\text{tt}}(t)dt. \tag{C.5}$$

Because $\int_0^\infty P_{\text{tc}}(t)dt = \frac{1}{\langle\tau_{\text{tt}}\rangle}\int_0^\infty tP_{\text{tt}}(t)dt = 1$, we get

$$P_{\text{tt}}(t) = \langle\tau_{\text{tt}}\rangle\, P_{\text{tc}}(t)/t. \tag{C.6}$$

The difference between the distribution functions, $P_{\text{tt}}(t)$ and $P_{\text{tc}}(t)$, can be described as follows. $P_{\text{tt}}(t)$ represents the percentage of pairs of molecules that had a continuous H-bonds during time t, while $P_{\text{tc}}(t)$ the percentage of the number of H-bonds with a given lifetime t to the number of all H-bonds in any configuration[243].

Since $P_{\mathrm{a}}(t) = \int_t^\infty P_{\mathrm{tc}}(\tau)\frac{d\tau}{\tau}$, we can obtain

$$\begin{aligned} P_{\mathrm{a}}(t) &= \int_t^\infty \frac{P_{\mathrm{tt}}}{\langle \tau_{\mathrm{tt}} \rangle}\frac{\tau}{\tau} d\tau \\ &= \int_t^\infty \frac{P_{\mathrm{tt}}}{\langle \tau_{\mathrm{tt}} \rangle} d\tau. \end{aligned}$$

Let $t = 0$, we obtain

$$P_{\mathrm{a}}(0) = 1/\left\langle t_{\mathrm{tt}}\right\rangle = 1/\left\langle t_{\mathrm{HB}}\right\rangle. \tag{C.7}$$

From Eq. C.2 and the relation between $s(t)$ and $P_{\mathrm{a}}(t)$

$$S_{\mathrm{HB}}(t) = \int_t^\infty P_{\mathrm{a}}(\tau) d\tau, \tag{C.8}$$

we can obtain

$$\begin{aligned} \int_0^\infty \int_t^\infty P_{\mathrm{a}}(t) d\tau dt &= \int_0^\infty \int_0^\tau P_{\mathrm{a}}(\tau) dt d\tau \\ &= \int_0^\infty \tau P_{\mathrm{a}}(\tau) d\tau \\ &= \langle \tau_{\mathrm{a}} \rangle, \end{aligned}$$

i.e.,

$$\int_0^\infty S_{\mathrm{HB}}(t) dt = \langle \tau_{\mathrm{a}} \rangle. \tag{C.9}$$

Calculation of HB lifetime distributions In this paragraph, we describe the method to calculate the above lifetime distributions $P_{\mathrm{tc}}(\tau)$, $P_{\mathrm{a}}(\tau)$, and $P_{\mathrm{tt}}(\tau)$.

First, we describe the method of calculating $P_{\mathrm{tc}}(\tau)$. Theoretically speaking, in order to calculate $P_{\mathrm{tc}}(\tau)$, our detection time t must meet the following conditions: $t - t_0 > \tau_{\mathrm{hb}}^{\mathrm{max}}$, where t_0 is the initial time and $\tau_{\mathrm{hb}}^{\mathrm{max}}$ is the maximum lifetime value of the H-bonds in the system. However, the value of τ_{hb} cannot be known in advance. In order to reduce the error, the method we can adopt is to set an empirical value as large as possible for $\tau_{\mathrm{hb}}^{\mathrm{max}}$ if conditions permit. Since the value of $\tau_{\mathrm{hb}}^{\mathrm{max}}$ is limited, in principle the lifetime value of the HB can always be greater than $\tau_{\mathrm{hb}}^{\mathrm{max}}$. Therefore, the average value of the HB lifetime distribution calculated in this approximate way will move to a shorter lifetime than the average value of the true HB lifetime distribution:

$$\int_0^\infty \tau P_{\mathrm{tc}}^{\mathrm{approx}}(\tau) d\tau < \left\langle \tau_{\mathrm{tc}}\right\rangle. \tag{C.10}$$

Among H-bonds detected at time t, if there are some H-bonds that have existed at the beginning t_0 and remain in existence until time t, then we can approximately express the lifetime of these H-bonds as $\delta t^{(j)} = t^{(j)} - t_0$, where $j = 1, \cdots, m$ is the labels of the m H-bonds and $t^{(j)}$ is the moment when the j-th HB is broken. If we use $\tau^{(j)}, j = 1, \cdots, m$ to represent the true lifetimes of these m H-bonds, then we can find that $\tau^{(j)} - \delta t^{(j)} > 0$. Since we cannot judge the true lifetime of these m hydrogen bonds, we can use $\delta t^{(j)}$ to approximate the lifetime of these m H-bonds, that is

$$\tau^{(j)} = \delta t^{(j)}. \tag{C.11}$$

For those H-bonds that did not exist at the beginning, the method of calculating their lifetime is very straightforward, the lifetime $\tau^{(j)}$ is equal to the time $t^{(j)}$ when the HB is broken minus the moment $t_0^{(j)}$ of its formation:

$$\tau^{(j)} = t^{(j)} - t_0^{(j)}, \tag{C.12}$$

where the superscript $j = 1, \cdots, m'$, identifies m' H-bonds detected at time t, and formed after t_0 and broken at $t^{(j)}$.

Specifically, for DFTMD results, we also approximate P_{tc} as follows: We select evenly distributed n time points $t = t_1, ..., t_n$, from the trajectory obtained by the simulation, and count the HB lifetime at each time point t_i. The distribution function $P_{\mathrm{tc}}(\tau)$ can be obtained by the average of the lifetime distribution detected at a certain time t_i, $i = 1, \cdots, n$, where $t_i - t_{i-1} = \tau_{\mathrm{hb}}^{\mathrm{max}}$.

If only from the perspective of simulation data, we have another way to obtain $P_{\mathrm{tc}}(\tau)$: Count the lifetimes of H-bonds that are formed after the initial time t_0 and are broken before the end time t_{f}.

C.2 Hydrogen bond population operator

Calculation of the reactive flux For dynamical variables $x_i(t)$ and $x_k(t)$, their correlation functions have the following relationship[325]:

$$\langle x_i(t')x_k(t)\rangle = -\langle x_i(t)x_k(t')\rangle. \tag{C.13}$$

Let $x_i = h$, $x_k = \dot{h}$, then, we obtain

$$\langle h(0)\dot{h}(t)\rangle = -\langle \dot{h}(0)h(t)\rangle. \tag{C.14}$$

From the definition of the reactive flux $k(t) = -dc/dt$, we obtain

$$k(t) = -\langle h(0)\dot{h}(t)\rangle / \langle h\rangle. \tag{C.15}$$

Then from Eq. C.14, we get

$$k(t) = \langle \dot{h}(0)h(t)\rangle / \langle h\rangle.$$

Since $\langle \dot{h}(0)\rangle = 0$, $k(t)$ can be calculated by

$$k(t) = -\langle \dot{h}(0)[1 - h(t)]\rangle / \langle h\rangle. \tag{C.16}$$

Relaxation time of hydrogen bonds in bulk water For the dynamic trajectory of such a system, we also calculated the self-correlation function $c(t)$ of the HB population operator, and the functions $k(t)$ and $n(t)$ derived from it. Tables C.1 and C.2 show the rate constants k and k', and the relaxation time τ_{HB} obtained by the least squares fit method.

TABLE C.1: The k and k' for bulk water. We carried on the short time region 0.2 ps $< t <$ 2 ps. The unit for k (k') is ps^{-1}, and that for τ_{HB} ($= 1/k$) is ps. The $h(t)$ is bond-based.

Criterion	k (bulk)	k' (bulk)	τ_{HB} (bulk)
ADH	0.299	1.029	3.347
AHD	0.288	1.121	3.468

TABLE C.2: The k and k' for bulk water. We carried on the long time region 2 ps $< t <$ 12 ps. The unit for k (k') is ps^{-1}, and that for τ_{HB} ($= 1/k$) is ps. The $h(t)$ is bond-based.

Criterion	k (bulk)	k' (bulk)	τ_{HB} (bulk)
ADH	0.103	0.028	9.728
AHD	0.103	0.040	9.702

C.3 Reorientation dynamics of water molecules at solution/vapor interfaces

Double exponential fit In general, the rotational motion of water molecules are not simply characterized by a well-defined rate constant. Similar non-single-exponential kinetics is also obtained in HB dynamics in liquid water[217, 326] and in the time variation of the average frequency shifts of the remaining modes after excitation in hole burning technique[327, 328]. We can understand the non-single-exponential kinetics of rotational anisotropy decay by fitting the rotational anisotropy decay by a biexponential function.

To obtain the effects of diffusion and HB decay of water molecules in solutions respectively, we assume that the correlation function $C_2(t)$ has the form[329]

$$C_2(t) = A_1 e^{-t/\tau_{2,1}} + A_2 e^{-t/\tau_{2,2}}, \tag{C.17}$$

where A_i are amplitudes and $1/\tau_{2,i}$ ($i = 1, 2$) are decay rates of $C_2(t)$, and the $\tau_{2,i}$ represent the relaxation times of the $C_2(t)$. Here, we assume that the orientation relaxation $C_2(t)$ is composed of two independent relaxation processes with different time scales, and each process can be described by an exponential decay function, respectively. For alkali-iodine solutions (LiI and NaI), the A_i and $\tau_{2,i}$ of the biexponentials fits for functions $C_2(t)$ are shown in Table C.3. We found that Eq. C.17, the biexponential kinetics is sufficiently accurate to describe the characteristics of anisotropy decay.

Then we considered the effect of ion species in solution/vapor interfaces on the anisotropy decay of water molecules. From Table C.3, we found that for both LiI and NaI solutions, there are two decay processes — amplitude ~ 1, decay time $\tau_{2,2} \sim 10.0$ ps, and for the other describe the initial fast decay of the anisotropy, with amplitude ~ 0.1, decay time $\tau_{2,1} \sim$ 0.1–1.0 ps, due to the inertial–librational motion preceding the orientational diffusion.

TABLE C.3: The fitted parameters of anisotropy decay of water molecules at the LiI (NaI, KI) solution/vapor interface according to Eq. C.17 for the time range [0,10] ps. The standard errors: $\delta A_i \sim 0.01$, $\delta\tau_{2,i} \sim 0.1$ ps ($i = 1, 2$).

H_2O	A_1	$\tau_{2,1}$ (ps)	A_2	$\tau_{2,2}$ (ps)
Li^+-shell	0.56	8.3	0.33	50.0
I^--shell	0.86	7.1	0.08	0.1
Na^+-shell	0.71	16.7	0.19	1.3
LiI/vapor	0.84	4.9	0.09	0.6
NaI/vapor	0.77	9.1	0.13	0.4
KI/vapor	0.80	6.1	0.12	1.1

The orientation relaxation time constants $\tau_{2,i}$ and amplitudes A_i $(i = 1, 2)$ of the single exponential fits (10 ps) for $C_2(t)$ are in Table C.3. For comparison, we also fit the $C_2(t)$ function of water molecules at each interface in Table 1 with a single exponential. The results are shown in Table C.4. It can be seen that the value of τ_2 is between the two characteristic times $\tau_{2,1}$ and $\tau_{2,2}$, obtained by biexponential fitting. At the same time, we can see the obvious difference in water molecules under various conditions: the reorientation characteristic time τ_2 in the first solvation shell of alkali metal ions is 2 to 3 times that of I^- ion. This is a reasonable result. However, the single exponential model describes the reorientation of water molecules as an exponential decay process. Our above biexponential function model (Eq. C.17) can be explained as: the reorientation dynamics of each water molecule is composed of two independent decay processes. One has amplitude ~ 1, decay time ~ 10 ps, which describes the initial fast decay of the anisotropy, and the other is of amplitude ~ 0.1, decay time ~ 0.1 ps, due to the inertial-librational motion preceding the orientational diffusion.

Table C.4: The fitted (single exponential) parameters of anisotropy decay of water molecules at the LiI (NaI, KI) solution/vapor interface according to Eq. C.17 for the time range [0,10] ps. The standard errors: $\delta A \sim 0.01$, $\delta\tau_2 \sim 0.1$ ps.

H_2O	A	τ_2 (ps)
Li^+-shell	0.88	13.7
I^--shell	0.83	3.9
Na^+-shell	0.84	10.1
LiI/vapor	0.80	3.0
NaI/vapor	0.86	4.2
KI/vapor	0.86	5.7

Appendix D

Structural characterization of water clusters and solutions

D.1 Water clusters

The structural parameters of the considered water clusters are shown here. Table D.1 gives the average HB lengths r_a (with standard deviations)in $[NO_3{\cdot}(H_2O)_3]^-$. Table D.2 (D.3) reports the selected distances characterizing $[NO_3{\cdot}(H_2O)_3]^-$ ($RNO_3(H_2O)_3$), and Table D.4 the selected parameters for RNO_3 $(H_2O)_3$ (R=Li, Na, K). The unit for length and angle are Å and degree (°), respectively.

TABLE D.1: Hydrogen bond lengths r_a in $[NO_3{\cdot}(H_2O)_3]^-$.

HB bound to	r_a
w1	2.40±0.52; 3.02±0.72
w2	2.56±0.48; 3.20±0.41
w3	2.29±0.47; 3.11±0.72

TABLE D.2: Parameters of water molecules and H-bonds in $[NO_3{\cdot}(H_2O)_3]^-$.

water	R_{OH}	∠HOH	r_{OH}
w1	0.98±0.02	101±4	2.40±0.52, 3.02±0.72
w2	0.98±0.02	101±5	2.56±0.48, 3.20±0.41
w3	0.98±0.02	101±4	2.29±0.47, 3.11±0.72

TABLE D.3: Structural parameters of $RNO_3(H_2O)_3$ from geometry optimization.

Parameters	$LiNO_3(H_2O)_3$	$NaNO_3(H_2O)_3$	$KNO_3(H_2O)_3$
r_{HB1}	1.67	1.71	1.82
r_{HB2}	1.91	1.78	1.92
r_{HB3}	1.82	1.69	1.94
$r_{\text{R-O(w1)}}$	1.91	2.31	2.70
$r_{\text{R-O(w2)}}$	1.90	2.26	2.70
$r_{\text{R-O(NO}_3^-)}$	1.84	2.29	2.69
∠HOH(w1)	109	106	107
∠HOH(w2)	106	105	105
∠HOH(w3)	108	107	106

Table D.5: Lengths of H-bonds in $[NO_3{\cdot}(H_2O)_3]^-$. Indices of H atoms: H6, H7 in w1; H9, H10 in w2; and H12, H13 in w3.

HBs	$r_a \pm \delta$ (100 K)(Å)	$r_a \pm \delta$ (300 K) (Å)
H6-O2	2.75±0.62	2.40±0.52
H7-O4	2.79±0.58	3.02±0.72
H9-O3	2.89±0.60	2.56±0.48
H10-O4	2.74±0.49	3.20±0.41
H12-O3	2.46±0.45	2.29±0.47
H13-O2	2.75±0.59	3.11±0.72

Table D.4: Parameters of $RNO_3(H_2O)_3$ at 300 K, obtained from the averaging during a DFTMD trajectory. For $RNO_3(H_2O)_3$, R_{OH} and R'_{OH} denote the lengths of O-H bonds in which H atoms is H-bonded and is free, respectively.

Parameters	$LiNO_3(H_2O)_3$	$NaNO_3(H_2O)_3$	$KNO_3(H_2O)_3$
r_{HB1}	1.83 ± 0.14	1.78 ± 0.09	1.82 ± 0.13
r_{HB2}	2.00 ± 0.25	1.91 ± 0.24	1.80 ± 0.12
r_{HB3}	1.79 ± 0.16	1.76 ± 0.11	1.89 ± 0.18
R_{OH}(w1)	0.97 ± 0.01	0.98 ± 0.04	0.97 ± 0.03
R'_{OH}(w1)	1.00 ± 0.02	1.00 ± 0.02	1.00 ± 0.03
R_{OH}(w2)	0.97 ± 0.01	0.98 ± 0.02	0.97 ± 0.02
R'_{OH}(w2)	0.99 ± 0.01	1.00 ± 0.02	1.00 ± 0.03
R_{OH}(w3)	0.97 ± 0.01	0.97 ± 0.02	0.97 ± 0.03
R'_{OH}(w3)	1.00 ± 0.02	1.00 ± 0.02	1.00 ± 0.03
$r_{\text{R-O(w1)}}$	1.95 ± 0.09	2.34 ± 0.08	2.76 ± 0.11
$r_{\text{R-O(w3)}}$	1.92 ± 0.07	2.32 ± 0.11	2.74 ± 0.13
$r_{\text{R-O}(NO_3^-)}$	1.91 ± 0.08	2.31 ± 0.09	2.74 ± 0.12
∠HOH (w1)	107 ± 4	106 ± 4	105 ± 5
∠HOH (w2)	106 ± 6	105 ± 4	106 ± 4
∠HOH (w3)	108 ± 5	106 ± 3	106 ± 3

Structural and vibrational properties of $[NO_3{\cdot}(H_2O)_3]^-$ To find possible source of the vibrational features of water molecules in the cluster $[NO_3{\cdot}(H_2O)_3]^-$, we consider structural properties and VDOS for water molecules in it. Lengths of H-bonds are shown in Table D.5. The nitrate O (ON)–water O (OW) and nitrate O–water H (HW) RDFs are shown in Fig. D.1.

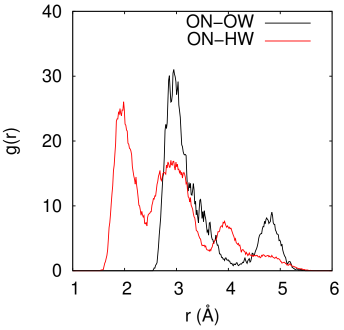

FIGURE D.1: The nitrate O (ON)–water O (OW) and nitrate O–water H (HW) RDFs for $[NO_3{\cdot}(H_2O)_3]^-$. Peaks for the former are 1.93, 2.95 and 3.95 Å, and for the later are 2.95 and 4.80 Å.

When $T = 300$ K, the difference r_a between different hydrogen atoms in one water molecule is $\Delta r_a = 0.69$ Å, while $\Delta r_a = 0.13$ Å for $T = 100$ K. It shows that the vibrational peaks for the three water molecules are much closer than that at the higher temperature 300 K.

The calculated VDOS for water molecules in the cluster at a lower temperature 100 K is given in Fig. D.2. It shows that the vibrational peaks for the three water molecules are very close to each other ($\Delta\nu < 10$ cm^{-1}) for both vibrational and bending modes. At the lower temperature, the three water molecules are more symmetric distributed bound to the central nitrate. Therefore, the difference between H-bonds in the symmetric isomer of $[NO_3{\cdot}(H_2O)_3]^-$ is likely a finite temperature effect, which can be verified by the calculation of the VDOS for water molecules.

Both differences $\Delta\nu$ and Δd decrease as the temperature decrease, Therefore, the different vibrational features are T-dependent effect.

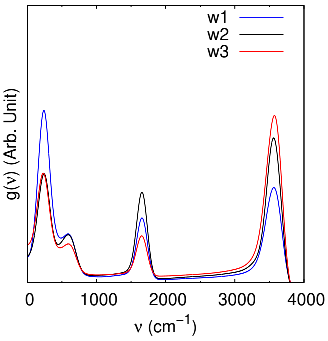

FIGURE D.2: The VDOS $g(\nu)$ for water molecules in the cluster $[NO_3{\cdot}(H_2O)_3]^-$ at 100 K.

D.2 Solution/vapor interfaces

Dipole orientation distribution of water at aqueous/vapor interfaces Set θ as the angle between the dipole moment of water molecules and the normal vector of the interface, and $P(\theta)$ as the probability. The data used to statistics is the dipole tilt angle θ_i. We use the θ_i instead of $\langle\theta\rangle$ to do the statistics. With picking up θ_l, $l = 0, 10, 20, ...$ from the series θ_i, we find that pure water's dipole moment tilt angle is smaller than that of water molecules at the salty water surface. This result means that at the pure water surface, water molecules have more p-polarization components than those at the salty water surface. However, water molecules at the salty water surface has more s-polarization component. The result is shown in Fig. D.3.

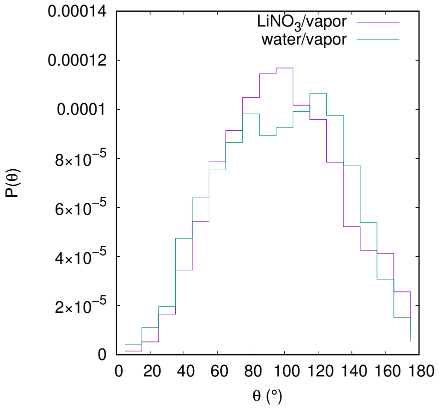

FIGURE D.3: The dipole orientation distribution of water molecules at the water/vapor and the $LiNO_3$ solution/vapor interfaces.

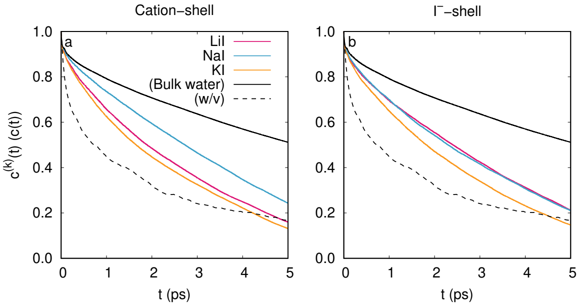

FIGURE D.4: The $c^{(k)}(t)$ of W–W bonds in the solvation shell of (a) cations and (b) I^- at the interfaces of 0.9 M LiI, NaI and KI solutions, respectively. As a reference, the $c(t)$ for the 1-Å water/vapor interface (Paragraph 5.2 in Chapter 5) and bulk water are also shown.

Solvation shell HB dynamics of W–W bonds at the alkali iodide/vapor interfaces Figures D.4 a and b report the $c^{(k)}(t)$ of W–W bonds in the solvation shell of cations and I^- at the interfaces of the alkali iodide solutions. The interface of the LiI solution contains H-bonds between water molecules similar to those in bulk water, i.e., water molecules participating in these H-bonds are not in the solvation shell of ions. This result is consistent with the observation of femtosecond mid-infrared pump-probe experiments on the O–H stretch vibration of water molecules in aqueous solution, that changing the nature of the cation does not affect the dynamics of solvating water[248]. It is also in agreement with to the following *ab initio* simulation results: water molecules that directly surround the cation, the O–H groups point away from the cation and form O–H···O hydrogen bonds with bulk water molecules[248, 330, 331]. From Fig. D.4 b, we found that for all three alkali iodide solutions, $c^{(k)}(t)$ for solvation shell of I^- decays faster than that for molecules in bulk water. The simulation produces similar result as Omta and coworker's experiments of femtosecond pump-probe spectroscopy, which demonstrate that anions (SO_4^{2-}, ClO_4^-, etc) have no influence on the dynamics of bulk water, even at high concentration up to 6 M[332, 333]. Here, we have found that the cations Li^+ and Na^+ do not alter the H-bonding network outside the first solvation shell of cations. It is concluded that no long-range structural-changing effects for alkali metal cations.

In addition, $c(t)$ for the instantaneous interface layer of thickness d = 1 Å in pure water is also shown in Fig. D.4. Its ultrafast relaxation process has a shorter relaxation time, which shows that the effects of ions (alkali cations and I^-) are not as obvious as that of the water/vapor interface.

RDFs in alkali nitrate solutions RDFs $g_{\text{Li-OW}}(r)$, $g_{\text{Li-HW}}(r)$, $g_{\text{ON-OW}}(r)$ and $g_{\text{ON-HW}}(r)$ in bulk $LiNO_3$ solution are shown in Fig. D.5.

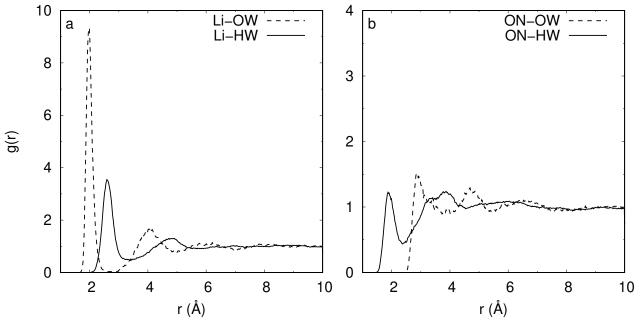

FIGURE D.5: RDFs $g_{\text{Li-OW}}(r)$, $g_{\text{Li-HW}}(r)$, $g_{\text{ON-OW}}(r)$ and $g_{\text{ON-HW}}(r)$ in bulk $LiNO_3$ solution.

RDFs in alkali iodide solutions RDFs $g_{\text{Li-OW}}(r)$, $g_{\text{Li-HW}}(r)$, $g_{\text{I-OW}}(r)$ and $g_{\text{I-HW}}(r)$ for the LiI/vapor interface are shown in Fig. D.6.

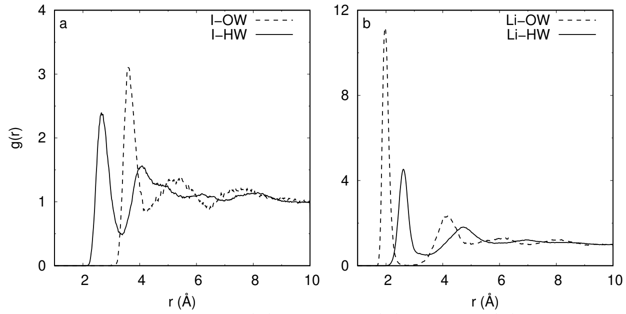

FIGURE D.6: RDFs $g_{\text{Li-OW}}(r)$, $g_{\text{Li-HW}}(r)$, $g_{\text{I-OW}}(r)$ and $g_{\text{I-HW}}(r)$ for the LiI/vapor interface.

The radii of the second solvation shell are: 5.0 Å for Li^+, 5.38 Å for Na^+, and 6.0 Å for I^- ions, which are obtained from the RDFs. The RDFs $g_{\text{X-O}}$ ($X=Li^+$, Na^+, K^+) for the interfaces of LiI (NaI,KI) solutions are shown in Fig. D.7 a, and the coordination numbers are in Fig. D.7 b. We see that the radius of the solvation shells of Li^+ ions, Na^+ ions, and K^+ ions increase sequentially, and the number of coordination molecules also increase sequentially. However, this order is not true for the relaxation time of HB dynamics between water molecules in the first solvation shell of the ion and other water molecules. As can be seen in Fig. D.4, the effects of the alkali metal ions and iodide ions are similar, that is, the relaxation time of HB dynamics in the outer layer is smaller than that in bulk water.

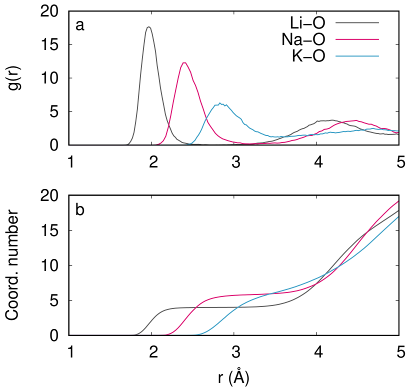

FIGURE D.7: (a) RDFs $g_{\text{X-O}}(r)$(X=Li$^+$, Na$^+$, K$^+$) and (b) the coordination number of Li$^+$ (Na$^+$, K$^+$) ions at the interfaces of LiI (NaI, KI) solution. The coordination numbers are n_{Li^+}=4, n_{Na^+}=5 and n_{K^+}=6.

D.3 Free energy of the water separated and the contact ion pair

From the blue-moon ensemble method[264, 265], we can obtain the constraint force (unit: a.u.force) acting on the atoms. If the distance between the ion pair (unit: Å) is chosen as the reaction coordinate, the formula for calculating the free energy (unit: kcal/mol) is given as follows. The relative free energy is given by

$$F = \sum_{i}^{N} f_i \Delta r,$$

where i denote a point on the one-dimensional reaction coordinate, N is the number of the sampling points of the reaction coordinates, and f_i denotes the average force on atoms over the trajectory when i is fixed. Now we estimate the error of the free energy δF from the summation approximation. It reads

$$\delta F = \frac{1}{N} \sum_{i}^{N} \delta f_i \Delta r. \tag{D.1}$$

Usually, $\delta f_i \approx \delta f$, thus

$$\delta F = \frac{1}{N} \delta f \sum_{i}^{N} \Delta r. \tag{D.2}$$

Particularly, if $\Delta r = 0.2$ Å, $\delta f = 0.0075$ a.u.force, we get

$$\delta F \approx 1.78 \text{ kcal/mol}.$$

D.4 Classification of water molecules based on H-bonds

Here we discuss the relation between the reorientation relaxation time of water molecules and their environment. The basic method is to classify the water molecules at solution/vapor interfaces based on the types of H-bonds and the number of H-bonds.

Alkali nitrate solutions For alkali nitrate solution/vapor interfaces, we can classify the water molecules into three types: nitrate-bound water, water at the water/-vapor interface, and bulk water. Because nitrate ions have more surface propensity (Fig. 4.2), and we have studied the effect of alkali cations on the reorientation relaxation of water molecules, here we consider $LiNO_3$ solution/vapor interface. We have known that nitrate-bound water are located at the solution/vapor interface (the thickness ~ 2 Å, see Fig. 4.5). Therefore, among the three types, the first two types of water molecules are interfacial ones. For each type of water molecules, we have chosen *six* water molecules for obtaining the correlation function $C_2(t)$. The IMS method (Paragraph E.1) is used to choose the water molecules for each type.

Lithium iodide solution Following the definition used in Ref.[8], we use the following labels to denote water molecules in an alkali iodide solution: D denotes that the water molecule donates a HB, D′ donates a H-I bond, and A accepts a HB. DDAA represents a water molecule with two H-Bonds donated to water molecules and two H-bonds accepted from water molecules (Fig. D.8 a); DD′AA represents a water molecule with two H-bonds donated to a water molecule and I^- (Fig. D.8 b), and with two H-bonds accepted from other water molecules (Fig. D.8 c), D′AA represents a water molecule bonded to I^- at the water/vapor interface and other H-bonds to water molecules (Fig. D.8 d). Clearly, we found that D′AA molecules are of free OH stretching during the dynamics.

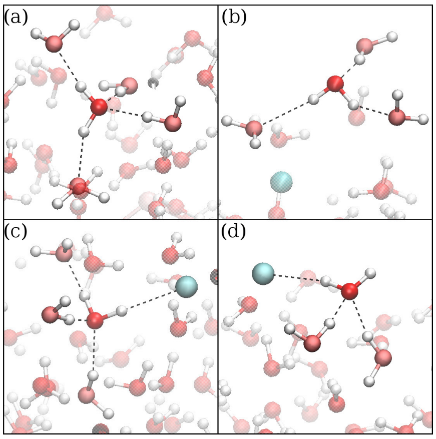

FIGURE D.8: Four types of water molecules at the LiI/vapor interface, regarding the HB environments: (a) DDAA; (b) DDA; (c) DD′AA; (d) D′AA. The cyan balls denote I^- ions.

It is evident that $C_2(t)$ for DDAA and DD′AA molecules do not decay exponentially (Fig. D.9 and Table D.6). This result is similar to the reactive flux function $k(t)$, i.e., the escaping rate kinetics of H-bonds in bulk water. The relaxation of H-bonds in water appears complicated, with no simple characterization in terms of a few relaxation rate constants. Most of the authors believe that the cooperation between neighbouring H-bonds[224, 334] or self evident coupling between translational diffusion and HB dynamics is the source of the complexity. However, for D′AA molecules at the LiI/vapor interface, the $C_2(t)$ decays exponentially,

$$C_2(t) \quad = \quad Ce^{-t/\tau_2},$$

where the amplitude is $C = 0.76$, and the reorientation rate is $1/\tau_2 = 7.14$ ps^{-1}. The single exponential decay of $C_2(t)$ for D′AA molecules, indicates that each D′AA molecule reorientate independently to each other.

Furthermore, the $C_2(t)$ for D′AA molecules decays much faster than that for DDAA or DD′AA molecules. From the definitions, the D′AA molecule accepts two H-bonds and donates only one H-bond, while both DDAA and DD′AA molecules own *four* H-bonds. Therefore, the correlation between H-bonds around the D′AA molecule is weaker than those around a DDAA or DD′AA molecule. Faster decay of $C_2(t)$ for D′AA molecules shows that the reorientation process of D′AA molecules is faster than water molecules in bulk phase, e.g., DDAA or DD′AA molecules.

Additionally, a D′AA molecule has a free OH bond, which can stretch and vibrate freely. This feature is not available in other types of molecules such as DDAA, DD′A, DD′AA, etc. Therefore, at the LiI/vapor interface, the most closely related feature of the molecular orientation relaxation process is the number of H-bonds *donated* by water molecules. The result that D′AA molecules have shortest relaxation time among the four types of water molecules implies that the factor $\langle n\rangle_{\mathrm{HB}}$, the average number of H-bonds per water molecule, plays a dominate role. This conclusion is consistent with the one obtained from above discussion for $LiNO_3$/vapor interface.

Besides, the type (or strength) of H-bonds (water–water, or ion–water) also affects the orientation relaxation process, which is also consistent with the above conclusion about $LiNO_3$/vapor interface. However, from our calculation, the number of H-bonds *accepted* by water molecules has no major effect on the orientation relaxation of the water molecules at the interface.

Finally, D′AA molecules' inertial-librational motion can not be seen in Fig. D.9. This result implies that the rotational anisotropy decay of D′AA molecules are of the same time scale of the inertial libration, i.e., ~ 0.2 ps. This conclusion can be verified from the value of τ_2 in Table D.6: $\tau_2 = 0.97$ for D′AA molecules, which is smaller than the τ_2 for DDAA, DD′A, and DD′AA molecules.

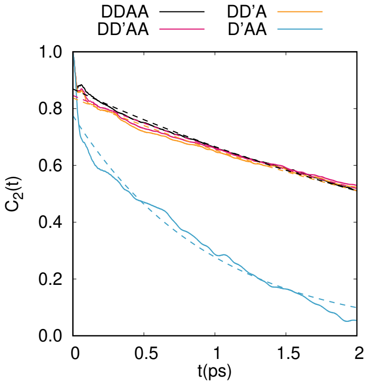

FIGURE D.9: Time dependence of $C_2(t)$ for DD′A, DD′AA, and D′AA water molecules at the LiI/vapor interface.

To summarize, rotational anisotropy decay of water molecules under different local environments is calculated at the LiI/vapor interface. The result comes from a different HB types from the usual DDAA HB type in bulk water. The faster anisotropy decay for D′AA molecules reflects the less correlation between different H-bonds for D′AA molecules, which comes from Hydrogen–Iodide bond at the interfaces and the existence of free OH stretching. As we already known from Fig. 4.8, in the LiI solution, I^- ions prefer to locate at the interface. Therefore, we infer that the reduction of the inter-correlations between H-bonds occurs at the interface. Slower rotational anisotropy decay exists for water molecules at the alkali-iodide solution/vapor interfaces, which is the result of a different HB types (D′AA) from DDAA molecules in bulk water. The slowing down of anisotropy decay is the effect of Hydrogen-Iodide bonds at the interface. Since the iodide's surface propensity is high, this difference of HB structure from the water/vapor interface changed the Im$\chi^{(2)}$ spectrum and the total HB dynamics of the interface of alkali-iodide solutions.

Table D.6: Biexponential fitting of $C_2(t)$ for water molecules in the LiI solution. The relative standard errors: $\Delta A/A \leq 10^{-2}$, $\Delta\tau_2/\tau_2 \leq 3 \times 10^{-2}$.

water molecules	A	τ_2 (ps)
DD′A	0.84	4.04
DD′AA	0.85	4.08
DDAA	0.87	3.76
D′AA	0.78	0.97

Appendix E

Thickness of the interface of aqueous solutions

E.1 Interfacial HB dynamics

Instantaneous Surfaces At a certain time t, the instantaneous surface $\mathbf{s}^0(x(t), y(t))$ for the water/vapor interface system can be determined by calculating the coarse-graining density field: we can specify that the coarse-grained density is the reference density $\rho_{\text{ref}} = 0.016$ Å^{-3}, and those grid points constitute the surface $\mathbf{s}^0(x, y)$ of pure water. In our simulated pure water system, there are two such surfaces. The code for calculating the instantaneous surfaces of interfacial systems can be found on `https://github.com/hg08/interface`.

Griding and layering We assume that the normal is along the z-axis direction. First, we discretize the coordinates of the xy plane. The xy plane can be approximated by $N \times N$ discrete points. Then $N \times N$ ordinates of the surface $\mathbf{s}^0(x(t_0), y(t_0))$ at the initial time t_0 can be represented as components of an $N \times N$-vector $\mathbf{z}^0(t_0)$. The surface $\mathbf{s}^0(x(t_0), y(t_0))$ is also the upper boundary of the interface. Secondly, we define a layering strategy, or define the thickness d of the interface layer. We then determine the lower boundary $\mathbf{s}^1(x(t_0), y(t_0))$ of the interface. It can be expressed as a $N \times N$-vector $\mathbf{z}^1(t_0) = \mathbf{z}^0(t_0) - \mathbf{d}$, and $\mathbf{d}$ is a $N \times N$-dimensional constant vector in which all the entries are equal to d. The superscripts 0 and 1 identify the upper and lower boundaries of the interface layer, respectively. Similarly, other instantaneous interfaces can also be determined if one change the value of d.

Next, the instantaneous interfaces can be defined for different moments naturally. Therefore, according to the same method, for the molecular motion trajectory of an interface system, we can obtain the dynamically changing interface layer, i.e., $\mathbf{z}^1(t) = \mathbf{z}^0(t) - \mathbf{d}$. To answer the question that whether an atom with coordinates (x, y, z) at any time t is in the interface layer, we map the atom's coordinates (x, y) to an integer pair (i, j), $i, j \in \{0, \cdots, N\}$, where $i = \text{int}(x/\Delta x), j = \text{int}(y/\Delta y)$, $\Delta x = a/N$, and $\Delta y = b/N$, where $\text{int}(x)$ converts a real number x to the nearest integer. At a certain time t, the coordinate z of an atom can be approximately represented as a function defined on point (i, j), $z = z(i, j)$. Then we compare $z(i, j)$ and $z^l_{i,j}$ $(l = 0, 1)$ to determine if the atom is in the interface layer. If $z^0_{i,j}(t) < z(i, j) < z^1_{ij}(t)$, then the atom at (x, y, z) is located in the interface layer at time t.

Interfacial molecule sampling The steps of the IMS method is as follows. 1) Determine the instantaneous surface of the water/vapor interface system; 2) Define a interfacial layer with a thickness d below the surface; 3) Identify the atoms which are located between the two instantaneous surface; 4) Obtain HB dynamics for molecules in interface layer at different time t. Given the thickness of layer d, at any sampling time t_0, t_1, t_2, $\cdots$, t_n, the set of molecules in the interface layer can be determined. The t_j is given by

$$t_j = t_0 + j\delta t \quad (j = 0, 1, \cdots, n). \tag{E.1}$$

We denote the set $S^0(t_i)$ of the molecules in the interface layer at two time t_i and t_j as $S^0(t_i)$ and $S^0(t_j)$, respectively. Since the molecules are always in motion, generally, we have $S^0(t_j) \neq S^0(t_i)$. Therefore, to calculate HB dynamics of molecules in the interface layer, we calculate the correlation functions of the HB population $h(t)$ of the molecules in the interface layer at different times, and calculate the *average* of the obtained correlation functions over these functions, e.g., $C_{\text{HB},j}(t), j = 1, \cdots, n$.

Interfacial HB population operator $h^{(\mathbf{s})}(t)$ The IHB method to identify the interfacial molecules is as follows. It shares the same procedures to define the instantaneously interfacial layer as we described in the above paragraph. Then we define the interfacial hydrogen bond population operator $h^{(\text{s})}(t)$, and calculate the autocorrelation function of $h^{(\text{s})}(t)$ and then the related observations.

None of the two methods (IMS and IHB) for obtaining HB dynamics of the interface water molecules can give the true interface HB dynamics completely. However, they respectively give an extreme case of interface HB dynamics. In the IMS method, the formation and breaking of intermolecular H-bonds can be truly described, but the selection of interface water molecules is not accurate enough, because of the sampling rate $1/\delta t$. Since the configuration of the molecule changes over time, the contribution of H-bonds in bulk phase will be included. In the IHB method, we are very accurate in choosing the interfacial water molecules and interfacial H-bonds, but we may miss some intact H-bonds intersecting the boundary of the interface layer. To a certain extent, the HB dynamics obtained by the IHB method is *accelerated*. Therefore, the comparison of the results obtained by the two methods may give a true picture of the interfacial HB dynamics. In particular, as the interface thickness increases, they achieve the same results. The code for calculating HB dynamics for instantaneous interfaces can be found on `https://github.com/hg08/hb_in_interface`.

E.2 Thickness of the solution/vapor interfaces

To determine the thickness of the solution/vapor interface of alkali solutions, we chose several different thickness values of slab of the interface and calculate the corresponding susceptibility for these slabs, respectively. Take the $LiNO_3$ solution/vapor interface as an example. We chose several different thickness values—from 2 to 8 Å, and calculate VSFG intensities $I_{SSP} \propto |\chi^{(2),\text{R}}_{SSP}|^2$ for the water/vapor interface with a thickness of each of these values. The result is given in Fig.s E.1 a and b. It shows that $|\chi^{(2),\text{R}}_{SSP}|^2$ converges as the thickness increases.

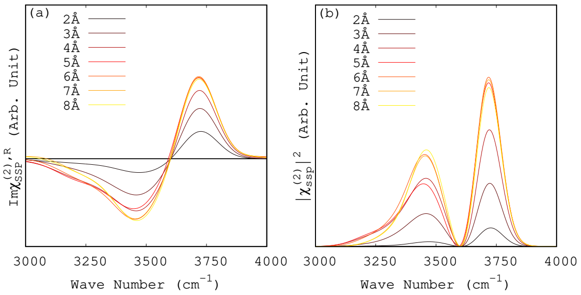

FIGURE E.1: The calculated $|\chi^{(2),\mathrm{R}}_{SSP}|^2$, of water molecules at the $LiNO_3$ solution/vapor interfaces with different thickness.

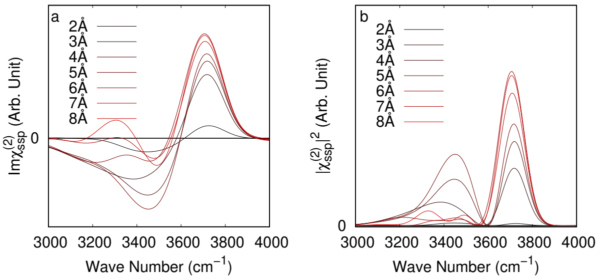

FIGURE E.2: The calculated $|\chi^{(2),R}_{SSP}|^2$, of water molecules at the LiI solution/vapor interface with different thickness.

The VSFG intensities $I_{SSP} \propto |\chi^{(2),R}_{SSP}|^2$ for the LiI solution/vapor interface are given in Fig.s E.2 a and b. The results show that $|\chi^{(2),R}_{SSP}|^2$ converges as the thickness increase from 0 to 8 Å.

Furthermore, we also estimated the thickness of a solution/vapor interface by calculating the HB dynamics for it. Fig. E.3 shows the dependence of the logarithm of survival probability on the thickness of the LiI solution/vapor interface. We found that when $d = 6$ Å the correlation function $s(t)$ of the interface converges as the thickness increases, indicating the thickness of the interface.

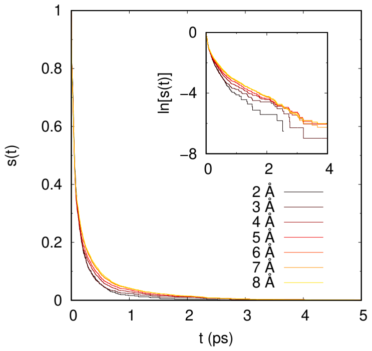

FIGURE E.3: The function $s(t)$ and its logarithm for water-water H-bonds at interfaces with different thickness in the LiI solution.

In addition, the survival probability $s(t)$ is dependent on the temporal resolution t_t, which is the time interval between two adjacent states in time used to calculate the survival probability. As an example, the t_t dependence of the τ_HB of the three alkali-iodine solution interfaces in DFTMD simulations is reported in Fig. E.4. It shows that, if one decrease t_t, the number of times that H-bonds break and form again in this period of time (t_t) will be reduced. The value of τ_HB corresponding to the intersections of the $\tau_{\mathrm{HB}}(t_{\mathrm{t}})$ functions and the line $t_{\mathrm{t}} = 5$ fs approximately give the continuum HB lifetimes. For $t_{\mathrm{t}} = 5$ fs, the calculated continuum HB lifetime is 0.30, 0.31 and 0.23 ps, for the interface of LiI, NaI and KI solution, respectively. Then, the estimated value of τ_{a} is ~ 0.2 ps. Moreover, we can obtain the continuum HB lifetime independent of the t_{t} by $\tau_{\mathrm{HB}} = \lim_{t_{\mathrm{t}}\to 0} \tau_{\mathrm{HB}}(t_{\mathrm{t}})$.

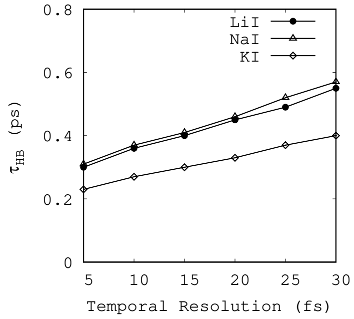

Figure E.4: The resolution dependence of the continuum lifetime τ_{HB} of water–water H-bonds at interfaces of different alkali-iodine solutions at 330 K, calculated for six temporal resolutions (t_{t})[335–337].

Bibliography

[1] J. G. Irwin and M. L. Williams. “Acid rain: chemistry and transport”. In: *Environ. Pollut.* 50 (1988), pp. 29–59. DOI: 10.1016/0269-7491(88)90184-4. URL: https://www.sciencedirect.com/science/article/pii/0269749188901844.

[2] D. J. Tobias. “A workshop on MD simulations”. In: *NATO Sci. Ser., Ser. A* 305 (1999), pp. 293–310.

[3] A. V. Benderskii and K. B. Eisenthal. “Effect of organic surfactant on femtosecond solvation dynamics at the air-water interface”. In: *J. Phys. Chem. B* 104 (2000), pp. 11723–11728. DOI: 10.1021/jp0025429. URL: https://pubs.acs.org/doi/abs/10.1021/jp0025429.

[4] R. Asahi et al. “Visible-light photocatalysis in nitrogen-doped titanium oxides”. In: *Science* 293 (2001), pp. 269–271. DOI: 10.1126/science.1061051. URL: https://science.sciencemag.org/content/293/5528/269.abstract.

[5] A. V. Benderskii and K. B. Eisenthal. “Dynamical time scales of aqueous solvation at negatively charged lipid/water interfaces”. In: *J. Phys. Chem. A* 106 (2002), pp. 7482–7490. DOI: 10.1021/jp0120155. URL: https://pubs.acs.org/doi/abs/10.1021/jp0120155.

[6] G. L. Richmond. “Molecular bonding and interactions at aqueous surfaces as probed by vibrational sum frequency spectroscopy”. In: *Chem. Rev.* 102 (2002), pp. 2693–2724. DOI: 10.1021/cr0006876. URL: https://doi.org/10.1021/cr0006876.

[7] H. Liu and B. E. Logan. “Electricity generation using an air-cathode single chamber microbial fuel cell in the presence and absence of a proton exchange membrane”. In: *Environ. Sci. Technol.* 38 (2004), p. 4040. DOI: 10.1021/es0499344. URL: https://pubs.acs.org/doi/abs/10.1021/es0499344.

[8] C. S. Tian et al. “Interfacial structures of acidic and basic aqueous solutions”. In: *J. Am. Chem. Soc* 130 (2008), p. 13033. DOI: 10.1021/ja8021297. URL: https://doi.org/10.1021/ja8021297.

[9] S. Yamamoto et al. “In situ X-ray photoelectron spectroscopy studies of water on metals and oxides at ambient conditions”. In: *J. Phys.: Condens. Matter* 20.18 (2008), p. 184025. DOI: 10.1088/0953-8984/20/18/184025. URL: https://iopscience.iop.org/article/10.1088/0953-8984/20/18/184025/meta.

[10] M. Salmeron et al. “Water growth on metals and oxides: binding, dissociation and role of hydroxyl groups”. In: *Faraday Discuss.* 141 (0 2009), pp. 221–229. DOI: 10.1039/B806516K. URL: http://dx.doi.org/10.1039/B806516K.

[11] L. Y. Zhang et al. “Protein hydration dynamics and molecular mechanism of coupled water-protein fluctuations”. In: *J. Am. Chem. Soc.* 131 (2009), pp. 10677–10691. DOI: 10.1021/ja902918p. URL: https://pubs.acs.org/doi/pdf/10.1021/ja902918p.

[12] P. Lo Nostro and B. W. Ninham. “Hofmeister phenomena: an update on ion specificity in biology”. In: *Chem. Rev.* 112 (2012), pp. 2286–2322. DOI: `10.1021/cr200271j`. URL: `https://pubs.acs.org/doi/pdf/10.1021/cr200271j`.

[13] L. Piatkowski et al. “Extreme surface propensity of halide ions in water”. In: *Nat. Commun.* 5 (2014), p. 4083. URL: `https://doi.org/10.1038/ncomms5083`.

[14] J. Balajka et al. “High-affinity adsorption leads to molecularly ordered interfaces on TiO_2 in air and solution”. In: *Science* 361 (2018), pp. 786–789. DOI: `10.1126/science.aat6752`. URL: `https://science.sciencemag.org/content/361/6404/786`.

[15] Ilan Benjamin. “Chemical reactions and solvation at liquid interfaces: a microscopic perspective”. In: *Chem. Rev.* 96.4 (1996), pp. 1449–1476. DOI: `10.1021/cr950230+`. URL: `https://doi.org/10.1021/cr950230+`.

[16] Tsun-Mei Chang and Liem X. Dang. “Recent advances in molecular simulations of ion solvation at liquid interfaces”. In: *Chem. Rev.* 106 (2006), pp. 1305–1322. DOI: `10.1021/cr0403640`. URL: `https://doi.org/10.1021/cr0403640`.

[17] V. S. Craig, B. W. Ninham, and R. M. Pashley. “Effects of electrolytes on bubble coalescence”. In: *Nature* 364 (1993), p. 317. DOI: `10.1038/364317a0`. URL: `https://www.nature.com/articles/364317a0`.

[18] V. S. Craig, B. W. Ninham, and R. M. Pashley. “The effects of electrolytes on bubble coalescence in water”. In: *J. Phys. Chem.* 97 (1993), pp. 10192–10197. DOI: `10.1021/j100141a047`. URL: `https://pubs.acs.org/doi/pdf/10.1021/j100141a047`.

[19] P. K. Weissenborn and R. J. Pugh. “Surface tension and bubble coalescence phenomena of aqueous solutions of electrolytes”. In: *Langmuir* 11.5 (1995), pp. 1422–1426. DOI: `10.1021/la00005a002`. URL: `https://pubs.acs.org/doi/abs/10.1021/la00005a002`.

[20] S. Marčelja. “Short-range forces in surface and bubble interaction”. In: *Curr. Opin. Colloid Interface Sci.* 9 (2004), p. 165. DOI: `10.1016/j.cocis.2004.05.024`. URL: `https://www.sciencedirect.com/science/article/pii/S1359029404000524`.

[21] V. S. Craig. “Bubble coalescence and specific-ion effects”. In: *Curr. Opin. Colloid Interface Sci.* 9 (2004), p. 178. DOI: `10.1016/j.cocis.2004.06.002`. URL: `https://www.sciencedirect.com/science/article/pii/S1359029404000627`.

[22] P. Ball. “Water as an active constituent in cell biology”. In: *Chem. Rev.* 108 (2008), pp. 74–108. DOI: `10.1021/cr068037a`. URL: `https://pubs.acs.org/doi/abs/10.1021/cr068037a`.

[23] I.-F. W. Kuo and C. J. Mundy. “An ab initio molecular dynamics study of the aqueous liquid-vapor interface”. In: *Science* 303 (2004), p. 658. DOI: `10.1126/science.1092787`. URL: `https://science.sciencemag.org/content/303/5658/658`.

[24] Prashant Chandra Singh et al. “Communication: Ultrafast vibrational dynamics of hydrogen bond network terminated at the air/water interface: a two-dimensional heterodyne-detected vibrational sum frequency generation study”. In: *J. Chem. Phys.* 139.16 (2013), p. 161101. DOI: `10.1063/1.4826095`. URL: `https://doi.org/10.1063/1.4826095`.

[25] P. Jedlovszky, Á. Vincze, and G. Horvai. “Full description of the orientational statistics of molecules near to interfaces. Water at the interface with CCl_4”. In: *Phys. Chem. Chem. Phys.* 6.8 (2004), pp. 1874–1879. DOI: 10.1039/b313231p. URL: https://pubs.rsc.org/en/content/articlelanding/2004/cp/b313231p/unauth#!divAbstract.

[26] Darryl C. Rideout and Ronald Breslow. “Hydrophobic acceleration of Diels-Alder reactions”. In: *J. Am. Chem. Soc* 102.26 (1980), pp. 7816–7817. DOI: 10.1021/ja00546a048. URL: https://doi.org/10.1021/ja00546a048.

[27] Sridhar Narayan et al. “’On water’: unique reactivity of organic compounds in aqueous suspension”. In: *Angew. Chem. Int. Ed.* 44 (2005), pp. 3275–3279. DOI: 10.1002/anie.200462883. URL: https://onlinelibrary.wiley.com/doi/full/10.1002/anie.200462883.

[28] James K. Beattie, Christopher S. P. McErlean, and Christopher B. W. Phippen. “The mechanism of on-water catalysis”. In: *Chem. A European Journal* 16.30 (2010), pp. 8972–8974. DOI: 10.1002/chem.201001705. URL: https://doi.org/10.1002/chem.201001705.

[29] Mohammadhasan Dinpajooh and Dmitry V. Matyushov. “Dielectric constant of water in the interface”. In: *J. Chem. Phys.* 145.1 (2016), p. 014504. DOI: 10.1063/1.4955203. URL: https://doi.org/10.1063/1.4955203.

[30] T. N. Veziriglu. *Environmental problems and solutions: Greenhouse effect, acid rain, pollution.* New York: Hemisphere, 1990.

[31] C. M. Starks, C. L. Liotta, and M. Halpern. *Phase transfer catalysis.* New York: Chapman & Hall, 1994.

[32] L. M. Pegram and Jr. M. T. Record. “Partitioning of atmospherically relevant ions between bulk water and the water/vapor interface”. In: *Proc. Natl. Acad. Sci. USA* 103.39 (2006), pp. 14278–14281. DOI: 10.1073/pnas.0606256103. URL: https://doi.org/10.1073/pnas.0606256103.

[33] E. A. Raymond and G. L. Richmond. “Probing the molecular structure and bonding of the surface of aqueous salt solutions”. In: *J. Phys. Chem. B* 108 (2004), p. 5051. DOI: 10.1021/jp037725k. URL: https://pubs.acs.org/doi/10.1021/jp037725k.

[34] S. E. McLain and A. K. Soper. “Structural studies on the hydration of l-glutamic acid in solution”. In: *J. Phys. Chem. B* 110 (2006), pp. 21251–21258. DOI: 10.1021/jp062383e. URL: https://pubs.acs.org/doi/abs/10.1021/jp062383e.

[35] D. Eisenberg and W. Kauzmann. *The structure and properties of water.* Oxford University press, Oxford, 1969. ISBN: ISBN:9780198570264. URL: https://global.oup.com/academic/product/the-structure-and-properties-of-water-9780198570264?cc=cn&lang=en&#.

[36] R. J. Speedy and C. A. Angell. “Isothermal compressibility of supercooled water and evidence for a thermodynamic singularity at -45 °C”. In: *J. Chem. Phys.* 65.3 (1976), pp. 851–858. DOI: 10.1063/1.433153. URL: https://doi.org/10.1063/1.433153.

[37] Peter H. Poole et al. “Effect of hydrogen bonds on the thermodynamic behavior of liquid water”. In: *Phys. Rev. Lett.* 73 (12 1994), pp. 1632–1635. DOI: 10.1103/PhysRevLett.73.1632. URL: https://link.aps.org/doi/10.1103/PhysRevLett.73.1632.

[38] A. K. Soper. “Structural transformations in amorphous ice and supercooled water and their relevance to the phase diagram of water”. In: *Molecular Physics* 106.16-18 (2008), pp. 2053–2076. DOI: 10.1080/00268970802116146. URL: https://doi.org/10.1080/00268970802116146.

[39] P. Ball. *Life’s matrix: a biography of water*. Berkeley and Los Angeles, California: University of California Press, 2001.

[40] A. Nilsson and L. G. M. Pettersson. “Perspective on the structure of liquid water”. In: *Chem. Phys.* 389.1 (2011), pp. 1–34. ISSN: 0301-0104. DOI: https://doi.org/10.1016/j.chemphys.2011.07.021. URL: http://www.sciencedirect.com/science/article/pii/S0301010411003247.

[41] L. G. M. Pettersson and A. Nilsson. “The structure of water: from ambient to deeply supercooled”. In: *Journal of Non-Crystalline Solids* 407 (2015). 7th IDMRCS: Relaxation in Complex Systems, pp. 399 –417. ISSN: 0022-3093. DOI: https://doi.org/10.1016/j.jnoncrysol.2014.08.026. URL: http://www.sciencedirect.com/science/article/pii/S0022309314004104.

[42] P. Allongue. “Molecular imaging and local density of states characterization at the Si(111)/NaOH interface”. In: *Phys. Rev. Lett.* 77 (1996), p. 1986. DOI: 10.1103/PhysRevLett.77.1986. URL: https://journals.aps.org/prl/abstract/10.1103/PhysRevLett.77.1986.

[43] J.-J. Velasco-Velez et al. “The structure of interfacial water on gold electrodes studied by X-ray absorption spectroscopy”. In: *Science* 346 (2014), p. 831. DOI: 10.1126/science.1259437. URL: https://www.science.org/doi/full/10.1126/science.1259437.

[44] H. S. Frank. “Free volume and entropy in condensed systems I. general principles, fluctuation entropy and free volume in some monatomic crystals”. In: *J. Chem. Phys.* 13 (1945), p. 478. DOI: 10.1063/1.1723983. URL: https://doi.org/10.1063/1.1723983.

[45] H. S. Frank. “Free volume and entropy in condensed systems II. Entropy of vaporization in liquids and the pictorial theory of the liquid state”. In: *J. Chem. Phys.* 13 (1945), p. 493. DOI: 10.1063/1.1723984. URL: https://doi.org/10.1063/1.1723984.

[46] H. S. Frank and M. W. Evans. “Free volume and entropy in condensed systems III. Entropy in binary liquid mixtures; partial molal entropy in dilute solutions; structure and thermodynamics in aqueous electrolytes”. In: *J. Chem. Phys.* 13 (1945), p. 507. DOI: 10.1063/1.1723985. URL: https://doi.org/10.1063/1.1723985.

[47] R. E. Pattle. “Production of electric power by mixing fresh and salt water in the hydroelectric pile”. In: *Nature* 174 (1954), p. 660. DOI: 10.1038/174660a0. URL: https://www.nature.com/articles/174660a0.

[48] S. Loeb et al. “The osmotic power plant”. In: *Science* 189.4203 (1976), pp. 654–655. DOI: 10.1126/science.189.4203.654. URL: https://www.science.org/doi/pdf/10.1126/science.189.4203.654.

[49] S. R. Schill et al. “The impact of aerosol particle mixing state on the hygroscopicity of sea spray aerosol”. In: *ACS Cent. Sci.* 1 (2015), pp. 132–141. DOI: 10.1021/acscentsci.5b00174. URL: https://pubs.acs.org/doi/10.1021/acscentsci.5b00174.

[50] R. E. Cochran et al. “Sea spray aerosol: the chemical link between the oceans, atmosphere, and climate”. In: *Acc. Chem. Res.* 50 (2017), pp. 599–604. DOI: `10.1021/acs.accounts.6b00603`. URL: `https://pubs.acs.org/doi/full/10.1021/acs.accounts.6b00603`.

[51] Y. R. Shen. *Fundamentals of sum-frequency spectroscopy.* Cambridge University Press, 2016.

[52] A. Morita. *Theory of sum frequency generation spectroscopy.* Singapore: Springer Nature Singapore Pte Ltd., 2018.

[53] Y. R. Shen. “Revisiting the basic theory of sum-frequency generation”. In: *J. Chem. Phys.* 153 (2020), p. 180901. DOI: `10.1063/5.0030947`. URL: `https://aip.scitation.org/doi/10.1063/5.0030947`.

[54] A. Morita and T. Ishiyama. “Recent progress in theoretical analysis of vibrational sum frequency generation spectroscopy”. In: *Phys. Chem. Chem. Phys.* 10 (2008), pp. 5801–5816. DOI: `10.1039/b808110g`. URL: `http://dx.doi.org/10.1039/B808110G`.

[55] H.-F. Wang et al. “Quantitative sum-frequency generation vibrational spectroscopy of molecular surfaces and interfaces: lineshape, polarization, and orientation”. In: *Annual Review of Physical Chemistry* 66.1 (2015), pp. 189–216. DOI: `10.1146/annurev-physchem-040214-121322`.

[56] Yu-Chieh. Wen et al. “Unveiling microscopic structures of charged water interfaces by surface-specific vibrational spectroscopy”. In: *Phys. Rev. Lett.* 116.1 (2016), p. 016101. DOI: `10.1103/physrevlett.116.016101`.

[57] Tatsuya Ishiyama and Akihiro Morita. “Computational analysis of vibrational sum frequency generation spectroscopy”. In: *Annual Review of Physical Chemistry* 68.1 (2017), pp. 355–377. DOI: `10.1146/annurev-physchem-052516-044806`.

[58] Chariz Peñalber-Johnstone et al. “Sum frequency generation spectroscopy of tetraalkylphosphonium ionic liquids at the air-liquid interface”. In: *J. Chem. Phys.* 148.19 (2018), p. 193841. DOI: `10.1063/1.5009674`. URL: `https://doi.org/10.1063/1.5009674`.

[59] P. A. Franken and J. F. Ward. “Optical harmonics and nonlinear phenomena”. In: *Rev. Mod. Phys.* 35.1 (1963), p. 23. DOI: `10.1103/RevModPhys.35.23`. URL: `https://doi.org/10.1103/RevModPhys.35.23`.

[60] M Che and J. C. Védrine (Ed.) *Characterization of solid materials and heterogeneous catalysts: From structure to surface reactivity.* Vol. 1. Wiley-VCH, 2012, pp. 1075–1117.

[61] Peer Fischer et al. “Three-wave mixing in chiral liquids”. In: *Phys. Rev. Lett.* 85 (20 2000), pp. 4253–4256. DOI: `10.1103/PhysRevLett.85.4253`. URL: `https://link.aps.org/doi/10.1103/PhysRevLett.85.4253`.

[62] Y. R. Shen. *Principle of nonlinear optics.* Wiley, New York, 1984.

[63] P. Guyot-Sionnest, W Chen, and Y. R. Shen. “General considerations on optical second-harmonic generation from surfaces and interfaces”. In: *Phys. Rev. B* 33 (1986), p. 8254. DOI: `10.1103/PhysRevB.33.8254`.

[64] N. Ji et al. “Characterization of vibrational resonances of water-vapor interfaces by phase-sensitive sum-frequency spectroscopy”. In: *Phys. Rev. Lett.* 100 (9 2008), p. 096102. DOI: `10.1103/PhysRevLett.100.096102`. URL: `http://link.aps.org/doi/10.1103/PhysRevLett.100.096102`.

[65] I. V. Stiopkin et al. “Heterodyne-detected vibrational sum frequency generation spectroscopy”. In: *J. Am. Chem. Soc.* 130 (2008), pp. 2271–2275. DOI: 10.1021/ja076708w. URL: https://doi.org/10.1021/ja076708w.

[66] Satoshi Nihonyanagi et al. “Structure and dynamics of interfacial water studied by heterodyne-detected vibrational sum-frequency generation”. In: *Annu. Rev. Phys. Chem.* 64 (2013), pp. 579–603. DOI: 10.1146/annurev-physchem-040412-110138. URL: https://www.annualreviews.org/doi/abs/10.1146/annurev-physchem-040412-110138.

[67] C. Tian et al. “Interfacial structures of acidic and basic aqueous solutions”. In: *J. Am. Chem. Soc.* 130.39 (2008), pp. 13033–13039. DOI: 10.1021/ja8021297. URL: http://dx.doi.org/10.1021/ja8021297.

[68] C. S. Tian and Y. R. Shen. “Sum-frequency vibrational spectroscopic studies of water/vapor interfaces”. In: *Chem. Phys. Lett.* 470 (2009), pp. 1–6. ISSN: 0009-2614. DOI: http://dx.doi.org/10.1016/j.cplett.2009.01.016. URL: http://www.sciencedirect.com/science/article/pii/S0009261409000281.

[69] C. Tian et al. “Surface propensities of atmospherically relevant ions in salt solutions revealed by phase-sensitive sum frequency vibrational spectroscopy”. In: *J. Phys. Chem. Lett.* 2 (2011), pp. 1946–1949. DOI: 10.1021/jz200791c. URL: https://pubs.acs.org/doi/abs/10.1021/jz200791c.

[70] Satoshi Nihonyanagi, Shoichi Yamaguchi, and Tahei Tahara. “Direct evidence for orientational flip-flop of water molecules at charged interfaces: A heterodyne-detected vibrational sum frequency generation study”. In: *J. Chem. Phys.* 130 (2009), p. 204704. DOI: 10.1063/1.3135147. URL: https://doi.org/10.1063/1.3135147.

[71] Y. R. Shen. “Phase-sensitive sum-frequency spectroscopy”. In: *Annu. Rev. Phys. Chem.* 64 (2013), pp. 129–150. DOI: 10.1146/annurev-physchem-040412-110110. URL: https://doi.org/10.1146/annurev-physchem-040412-110110.

[72] P. Guyot-Sionnest, J. H. Hunt, and Y. R. Shen. “Sum-frequency vibrational spectroscopy of a Langmuir film: Study of molecular orientation of a two-dimensional system”. In: *Phys. Rev. Lett.* 59 (14 1987), pp. 1597–1600. DOI: 10.1103/PhysRevLett.59.1597. URL: https://link.aps.org/doi/10.1103/PhysRevLett.59.1597.

[73] R. Superfine, J. H. Huang, and Y. R. Shen. “Nonlinear optical studies of the pure liquid/vapor interface: vibrational spectra and polar ordering”. In: *Phys. Rev. Lett.* 66 (1991), pp. 1066–1069. DOI: 10.1103/PhysRevLett.66.1066. URL: https://ui.adsabs.harvard.edu/abs/1991PhRvL..66.1066S.

[74] Q. Du et al. “Vibrational spectroscopy of water at the vapor/water interface”. In: *Phys. Rev. Lett.* 70 (15 1993), pp. 2313–2316. DOI: 10.1103/PhysRevLett.70.2313. URL: https://link.aps.org/doi/10.1103/PhysRevLett.70.2313.

[75] Q. Du, E. Freysz, and Y. R. Shen. “Vibrational spectra of water molecules at quartz/water interfaces”. In: *Phys. Rev. Lett.* 72 (2 1994), pp. 238–241. DOI: 10.1103/PhysRevLett.72.238. URL: http://link.aps.org/doi/10.1103/PhysRevLett.72.238.

[76] S. Gopalakrishnan et al. “Vibrational spectroscopic studies of aqueous interfaces: Salts, acids, bases, and nanodrops”. In: *Chem. Rev.* 106 (2006), pp. 1155–1175. DOI: `10.1021/cr040361n`. URL: `http://www.ncbi.nlm.nih.gov/pubmed/16608176`.

[77] Y. R. Shen and V. Ostroverkhov. “Sum-frequency vibrational spectroscopy on water interfaces: Polar orientation of water molecules at interfaces”. In: *Chem. Rev.* 106 (2006), pp. 1140–1154. DOI: `10.1021/cr040377d`. URL: `https://www.ncbi.nlm.nih.gov/pubmed/16608175`.

[78] A. L. Harris et al. “Monolayer vibrational spectroscopy by infrared-visible sum generation at metal and semiconductor surfaces”. In: *Chem Phys. Lett.* 141 (1987), pp. 350–356. DOI: `10.1016/0009-2614(87)85037-6`. URL: `https://www.sciencedirect.com/science/article/abs/pii/0009261487850376`.

[79] R. Superfine et al. “Surface vibrational spectroscopy of molecular adsorbates on metals and semiconductors by infrared-visible sum-frequency generation”. In: *Surf. Sci.* 200 (1988), pp. L445–L450. DOI: `10.1016/0039-6028(88)90422-0`. URL: `https://www.sciencedirect.com/science/article/pii/0039602888904220`.

[80] F. Vidal and A. Tadjeddine. “Sum-frequency generation spectroscopy of interfaces”. In: *Rep. Prog. Phys.* 68 (2005), pp. 1095–1127. DOI: `10.1088/0034-4885/68/5/r03`. URL: `https://www.onacademic.com/detail/journal_1000035594033610_0ae5.html`.

[81] R. Rotenberg. “Water in Clay Nanopores”. In: *MRS Bulletin* 39 (2014), p. 1074.

[82] P. Jungwirth and D. J. Tobias. “Molecular structure of salt solutions: A new view of the interface with implications for heterogeneous atmospheric chemistry”. In: *J. Phys. Chem. B* 105 (2001), pp. 10468–10472. DOI: `10.1021/jp012750g`. URL: `https://pubs.acs.org/doi/abs/10.1021/jp012750g`.

[83] P. Jungwirth and D. J. Tobias. “Ions at air/water interface”. In: *J. Phys. Chem. B* 106 (2002), pp. 6361–6373. DOI: `10.1021/jp020242g`. URL: `https://pubs.acs.org/doi/abs/10.1021/jp020242g`.

[84] C. M. Johnson and S. Baldelli. “Vibrational sum frequency spectroscopy studies of the influence of solutes and phospholipids at vapor/water interfaces relevant to biological and environmental systems”. In: *Chem. Rev.* 114 (2014), pp. 8416–8446. DOI: `10.1021/cr4004902`. URL: `https://pubs.acs.org/doi/abs/10.1021/cr4004902`.

[85] T. Ishiyama, T. Imamura, and A. Morita. “Theoretical studies of structures and vibrational sum frequency generation spectra at aqueous interfaces”. In: *Chem. Rev.* 114 (2014), pp. 8447–8470. DOI: `10.1021/cr4004133`. URL: `https://pubs.acs.org/doi/pdf/10.1021/cr4004133`.

[86] L. X. Dang. “Solvation of the hydronium ion at the water liquid/vapor interface”. In: *J. Chem. Phys.* 119 (2003), p. 6351. DOI: `10.1063/1.1599274`. URL: `https://aip.scitation.org/doi/abs/10.1063/1.1599274`.

[87] M. K. Petersen et al. “The hydrated proton at the water liquid/vapor interface”. In: *J. Phys. Chem. B* 108 (2004), pp. 14804–14806. DOI: `10.1021/jp046716o`. URL: `https://pubs.acs.org/doi/abs/10.1021/jp046716o`.

[88] T. Ishiyama and A. Morita. “Molecular dynamics analysis of interfacial structures and sum frequency generation spectra of aqueous hydrogen halide solutions”. In: *J. Phys. Chem. A* 111.38 (2007), pp. 9277–9285. DOI: `10.1021/jp072997z`. URL: `http://dx.doi.org/10.1021/jp072997z`.

[89] M. Mucha et al. "Unified molecular picture of the surfaces of aqueous acid, base, and salt solutions". In: *J. Phys. Chem. B* 109 (2005), pp. 7617–7623. DOI: 10.1021/jp0445730. URL: https://pubs.acs.org/doi/abs/10.1021/jp0445730.

[90] R. Car and M. Parrinello. "Unified approach for molecular dynamics and density functional theory". In: *Phys. Rev. Lett.* 55 (22 1985), pp. 2471–2474. DOI: 10.1103/PhysRevLett.55.2471. URL: https://link.aps.org/doi/10.1103/PhysRevLett.55.2471.

[91] G. Pastore, E. Smargiassi, and F. Buda. "Theory of ab initio molecular-dynamics calculations". In: *Phys. Rev. A* 44 (10 1991), pp. 6334–6347. DOI: 10.1103/PhysRevA.44.6334. URL: https://link.aps.org/doi/10.1103/PhysRevA.44.6334.

[92] J. Hutter. "Car-Parrinello molecular dynamics". In: *Wiley Interdiscip. Rev.: Comput. Mol. Sci.* 2 (2012), pp. 604–612. DOI: 10.1002/wcms.90. URL: https://doi.org/10.1002/wcms.90.

[93] Thomas D. Kühne et al. "CP2K: An electronic structure and molecular dynamics software package - Quickstep: Efficient and accurate electronic structure calculations". In: *J. Chem. Phys.* 152.19 (2020), p. 194103. DOI: 10.1063/5.0007045. URL: https://doi.org/10.1063/5.0007045.

[94] Ivan S. Ufimtsev, Nathan Luehr, and Todd J. Martinez. "Charge transfer and polarization in solvated proteins from ab initio molecular dynamics". In: *J. Phys. Chem. Lett.* 2.14 (2011), pp. 1789–1793. DOI: 10.1021/jz200697c. URL: https://pubs.acs.org/doi/abs/10.1021/jz200697c.

[95] Stefan Grimme. "Accurate description of van der Waals complexes by density functional theory including empirical corrections". In: *J. Comp. Chem.* 25.12 (2004), pp. 1463–1473. ISSN: 01928651. DOI: 10.1002/jcc.20078. URL: https://onlinelibrary.wiley.com/doi/abs/10.1002/jcc.20078.

[96] S. Grimme. "Semiempirical GGA-type density functional constructed with a long-range dispersion correction". In: *J. Comput. Chem.* 27 (2006), pp. 1787–1799. DOI: 10.1002/jcc.20495. URL: https://onlinelibrary.wiley.com/doi/abs/10.1002/jcc.20495.

[97] Stefan Grimme et al. "Density functional theory with dispersion corrections for supramolecular structures, aggregates, and complexes of (bio)organic molecules". In: *Org. Biomol. Chem.* 5 (5 2007), pp. 741–758. DOI: 10.1039/B615319B. URL: http://dx.doi.org/10.1039/B615319B.

[98] S. Grimme et al. "A consistent and accurate ab initio parametrization of density functional dispersion correction (DFT-D) for the 94 elements H-Pu". In: *J. Chem. Phys.* 132 (2010), p. 154104. DOI: 10.1063/1.3382344. URL: https://aip.scitation.org/doi/abs/10.1063/1.3382344.

[99] Marcel D. Baer et al. "Re-examining the properties of the aqueous vapor-liquid interface using dispersion corrected density functional theory". In: *J. Chem. Phys.* 135 (2011), p. 124712. DOI: 10.1063/1.3633239. URL: https://aip.scitation.org/doi/abs/10.1063/1.3633239.

[100] Christopher M. Lee et al. "Sum-Frequency-Generation Vibration Spectroscopy and Density Functional Theory Calculations with Dispersion Corrections (DFT-D2) for Cellulose Iα and Iβ". In: *J. Phys. Chem. B* 117.22 (2013), pp. 6681–6692. DOI: 10.1021/jp402998s. URL: https://doi.org/10.1021/jp402998s.

[101] Christopher M. Lee James D. Kubicki Bingxin Fan Linghao Zhong Michael C. Jarvis and Seong H. Kim. “Hydrogen-bonding network and OH stretch vibration of cellulose: Comparison of computational modeling with polarized IR and SFG spectra”. In: *J. Phys. Chem. B* 119.49 (2015), pp. 15138–15149. DOI: `10.1021/acs.jpcb.5b08015`. URL: `https://doi.org/10.1021/acs.jpcb.5b08015`.

[102] M. Sulpizi et al. “Vibrational sum frequency generation spectroscopy of the water liquid-vapor interface from density functional theory-based molecular dynamics simulations”. In: *J. Phys. Chem. Lett.* 4.1 (2013), pp. 83–87. DOI: `10.1021/jz301858g`. URL: `http://dx.doi.org/10.1021/jz301858g`.

[103] Tatsuhiko Ohto et al. “Toward ab initio molecular dynamics modeling for sum-frequency generation spectra; an efficient algorithm based on surface-specific velocity-velocity correlation function”. In: *J. Chem. Phys.* 143.12 (2015), p. 124702. DOI: `10.1063/1.4931106`. URL: `https://doi.org/10.1063/1.4931106`.

[104] T. Ohto et al. “Lipid carbonyl groups terminate the hydrogen bond network of membrane-bound water”. In: *J. Phys. Chem. Lett.* 6.22 (2015), pp. 4499–4503. DOI: `10.1021/acs.jpclett.5b02141`. URL: `http://dx.doi.org/10.1021/acs.jpclett.5b02141`.

[105] Teresa Fornaro et al. “Dispersion corrected DFT approaches for anharmonic vibrational frequency calculations: Nucleobases and their dimers”. In: *Phys. Chem. Chem. Phys.* 16 (21 2014), pp. 10112–10128. DOI: `10.1039/C3CP54724H`. URL: `http://dx.doi.org/10.1039/C3CP54724H`.

[106] R. Khatib et al. “Water orientation and hydrogen-bond structure at the fluorite/water interface”. In: *Scientific Reports* 6 (2016), p. 24287. DOI: `10.1038/srep24287`. URL: `https://www.nature.com/articles/srep24287`.

[107] Yuki Nagata et al. “Surface tension of ab initio liquid water at the water-air interface”. In: *J. Chem. Phys.* 144.20 (2016), p. 204705. DOI: `10.1063/1.4951710`. URL: `https://doi.org/10.1063/1.4951710`.

[108] Tatsuhiko Ohto et al. “Unveiling the amphiphilic nature of TMAO by vibrational sum frequency generation spectroscopy”. In: *J. Phys. Chem. C* 120.31 (2016), pp. 17435–17443. DOI: `10.1021/acs.jpcc.6b04852`. URL: `https://doi.org/10.1021/acs.jpcc.6b04852`.

[109] Yuki Nagata et al. “Molecular modeling of water interfaces: From molecular spectroscopy to thermodynamics”. In: *J. Phys. Chem. B* 120.16 (2016), pp. 3785–3796. DOI: `10.1021/acs.jpcb.6b01012`. URL: `https://doi.org/10.1021/acs.jpcb.6b01012`.

[110] Saman Hosseinpour et al. “Chemisorbed and physisorbed water at the TiO_2/water interface”. In: *J. Phys. Chem. Lett.* 8 (2017), pp. 2095–2199. DOI: `10.1021/acs.jpclett.7b00564`. URL: `https://doi.org/10.1021/acs.jpclett.7b00564`.

[111] Jaciara C. C. Santos et al. “Interaction of water with the gypsum (010) surface: Structure and dynamics from nonlinear vibrational spectroscopy and ab initio molecular dynamics”. In: *J. Am. Chem. Soc.* 140.49 (2018), pp. 17141–17152. DOI: `10.1021/jacs.8b09907`. URL: `https://doi.org/10.1021/jacs.8b09907`.

[112] Tatsuhiko Ohto, Hirokazu Tadaa, and Yuki Nagata. "Structure and dynamics of water at water-graphene and water-hexagonal boron-nitride sheet interfaces revealed by ab initio sum-frequency generation spectroscopy". In: *Phys. Chem. Chem. Phys* 20 (2018), p. 12979. DOI: `10.1039/c8cp01351a`. URL: `https://pubs.rsc.org/en/content/articlepdf/2018/cp/c8cp01351a`.

[113] R. Khatib et al. "Molecular dynamics simulations of SFG librational modes spectra of water at the water-air interface". In: *J. Phys. Chem. C* 120 (2016), pp. 18665–18673. DOI: `10.1021/acs.jpcc.6b06371`. URL: `https://pubs.acs.org/doi/abs/10.1021/acs.jpcc.6b06371`.

[114] R. Khatib and M Sulpizi. "Sum frequency generation spectra from velocity-velocity correlation functions". In: *J. Phys. Chem. Lett.* 8 (2017), pp. 1310–1314. DOI: `10.1021/acs.jpclett.7b00207`. URL: `https://pubs.acs.org/doi/abs/10.1021/acs.jpclett.7b00207`.

[115] Alexandre P dosSantos, Alexandre Diehl, and Yan Levin. "Surface tensions, surface potentials, and the Hofmeister series of electrolyte solutions". In: *Langmuir* 26.13 (2010), pp. 10778–10783. DOI: `10.1021/la100604k`. URL: `https://doi.org/10.1021/la100604k`.

[116] P. Jungwirth and D. J. Tobias. "Specific ion effects at the air/water interface". In: *Chem. Rev.* 106 (2006), pp. 1259–1281. DOI: `10.1021/cr0403741`. URL: `https://pubs.acs.org/doi/abs/10.1021/cr0403741`.

[117] L. M. Pegram and M. T. Record, Jr. "Hofmeister salt effects on surface tension arise from partitioning of anions and cations between bulk water and the air-water interface". In: *J. Phys. Chem. B* 111.19 (2007), pp. 5411–5417. DOI: `10.1021/jp070245z`. URL: `https://pubs.acs.org/doi/pdf/10.1021/jp070245z`.

[118] Y. J. Zhang and P. S. Cremer. "Chemistry of Hofmeister anions and osmolytes". In: *Annu. Rev. Phys. Chem.* 61 (2010), pp. 63–83. DOI: `10.1146/annurev.physchem.59.032607.093635`. URL: `https://www.annualreviews.org/doi/abs/10.1146/annurev.physchem.59.032607.093635`.

[119] D. Tobias and J. C. Hemminger. "Getting specific about specific ion effects". In: *Science* 319 (2008), pp. 1197–1198. DOI: `10.1126/science.1152799`. URL: `https://www.jstor.org/stable/20053465`.

[120] D. F. Parsons et al. "Hofmeister effects: Interplay of hydration, nonelectrostatic potentials, and ion size". In: *Phys. Chem. Chem. Phys.* 13 (27 2011), pp. 12352–12367. DOI: `10.1039/C1CP20538B`. URL: `http://dx.doi.org/10.1039/C1CP20538B`.

[121] Wei Hua, Dominique Verreault, and Heather C. Allen. "Surface prevalence of perchlorate anions at the air/aqueous interface". In: *J. Phys. Chem. Lett.* 4 (2013), pp. 4231–4236. DOI: `10.1021/jz402009f`. URL: `https://doi.org/10.1021/jz402009f`.

[122] I. Langmuir. "The constitution and fundamental properties of solids and liquids. II. Liquids". In: *J. Am. Chem. Soc.* 39 (1917), p. 1848. DOI: `10.1021/ja02254a006`. URL: `https://doi.org/10.1021/ja02254a006`.

[123] N. L. Jarvis and M. A. Scheiman. "Surface potentials of aqueous electrolyte solution". In: *J. Phys. Chem.* 72.1 (1968), pp. 74–78. ISSN: 00223654. DOI: `10.1021/j100847a014`. URL: `https://pubs.acs.org/doi/abs/10.1021/j100847a014`.

[124] A. M. Jubb, W. Hua, and H. C. Allen. “Organization of water and atmospherically relevant ions and solutes: Vibrational sum frequency spectroscopy at the vapor/liquid and liquid/solid interfaces”. In: *Accounts of Chemical Research* 45.1 (2012), pp. 110–119. DOI: `10.1021/ar200152v`. URL: `https://pubs.acs.org/doi/abs/10.1021/ar200152v`.

[125] A. G. Lambert, P. B. Davies, and D. J. Neivandt. “Implementing the theory of sum frequency generation vibrational spectroscopy: A tutorial review”. In: *Applied Spectroscopy Reviews* 40:2 (2005), pp. 103–145. DOI: `10.1081/ASR-200038326`. URL: `https://doi.org/10.1081/ASR-200038326`.

[126] S. Gopalakrishnan et al. “Air-liquid interfaces of aqueous solutions containing ammonium and sulfate: Spectroscopic and molecular dynamics studies”. In: *J. Phys. B* 109 (2005), pp. 8861–8872. DOI: `10.1021/jp0500236`. URL: `https://pubs.acs.org/doi/abs/10.1021/jp0500236`.

[127] P. Salvador et al. “Polarizability of the nitrate anion and its solvation at the air/water interface”. In: *Phys. Chem. Chem. Phys.* 5 (17 2003), pp. 3752–3757. DOI: `10.1039/B304537D`. URL: `http://dx.doi.org/10.1039/B304537D`.

[128] B. J. Finlayson-Pitts and J. N. Pitts Jr. *Chemistry of the upper and lower atmosphere: Theory, experiments and applications.* Academic Press: San Diego,CA, 2000.

[129] M. Xu et al. “Nitrate anions and ion pairing at the air-aqueous interface”. In: *J. Phys. Chem. C* 113 (2009), pp. 2082–2087. DOI: `10.1021/jp805376x`. URL: `https://pubs.acs.org/doi/abs/10.1021/jp805376x`.

[130] Puja Banerjee, Subramanian Yashonath, and Biman Bagchi. “Coupled jump rotational dynamics in aqueous nitrate solutions”. In: *J. Chem. Phys.* 145.23 (2016), p. 234502. DOI: `10.1063/1.4971864`. URL: `https://aip.scitation.org/doi/abs/10.1063/1.4971864`.

[131] Sushma Yadav and Amalendu Chandra. “Preferential solvation, ion pairing, and dynamics of concentrated aqueous solutions of divalent metal nitrate salts”. In: *J. Chem. Phys.* 147.24 (2017), p. 244503. DOI: `10.1063/1.4996273`. URL: `https://doi.org/10.1063/1.4996273`.

[132] S. Yadav, A. Choudhary, and A. Chandra. “A first-principles molecular dynamics study of the solvation shell structure, vibrational spectra, polarity, and dynamics around a nitrate ion in aqueous solution”. In: *J. Phys. Chem. B* 121 (2017), pp. 9032–9044. DOI: `10.1021/acs.jpcb.7b06809`. URL: `https://doi.org/10.1021/acs.jpcb.7b06809`.

[133] Joshua F. Robinson et al. “Drying kinetics and nucleation in evaporating sodium nitrate aerosols”. In: *J. Chem. Phys.* 152.7 (2020), p. 074503. DOI: `10.1063/1.5139106`. URL: `https://doi.org/10.1063/1.5139106`.

[134] W. Hua, D. Verreault, and H. C. Allen. “Surface electric fields of aqueous solutions of NH_4NO_3, $Mg(NO_3)_2$, $NaNO_3$, and $LiNO_3$: Implications of atmospheric aerosol chemistry”. In: *J. Phys. Chem. C* 118 (2014), pp. 24941–24949. DOI: `10.1021/jp505770t`. URL: `https://pubs.acs.org/doi/abs/10.1021/jp505770t`.

[135] W. Hua, A. M. Jubb, and H. C. Allen. “Electric field reversal of Na_2SO_4, $(NH_4)_2SO_4$, and Na_2CO_3 relative to $CaCl_2$ and NaCl at the air/aqueous interface revealed by heterodyne detected phase-sensitive sum frequency”. In: *J. Phys. Chem. Lett.* 2 (2011), pp. 2515–2520. DOI: `10.1021/jz200888t`. URL: `https://pubs.acs.org/doi/abs/10.1021/jz200888t`.

[136] W. Hua, X. Chen, and H. C. Allen. "Phase-sensitive sum frequency revealing accommodation of bicarbonate ions, and charge separation of sodium and carbonate ions within the air/water interface". In: *J. Phys. Chem. A* 115 (2011), pp. 6233–6238. DOI: `10.1021/jp111552f`. URL: `https://pubs.acs.org/doi/abs/10.1021/jp111552f`.

[137] X. Chen, W. Hua, and H. C. Allen. "Interfacial water structure associated with phospholipid membranes studied by phase-sensitive vibrational sum frequency generation spectroscopy". In: *J. Am. Chem. Soc.* 132.32 (2010), pp. 11336–11342. DOI: `10.1021/ja1048237`. URL: `https://pubs.acs.org/doi/abs/10.1021/ja1048237`.

[138] D. Verreault and H. C. Allen. "Bridging the Gap between Microscopic and Macroscopic Views of Air/Aqueous Salt Interfaces". In: *Chem. Phys. Lett.* 586 (2013), pp. 1–9. DOI: `10.1016/j.cplett.2013.08.054`. URL: `http://www.sciencedirect.com/science/article/pii/S0009261413010646`.

[139] D. Verreault and H. C. Allen. "Reactions at surfaces in the atmosphere: Integration of experiments and theory as necessary (but not necessarily sufficient) for predicting the physical chemistry of aerosols". In: *Phys. Chem. Chem. Phys.* 11 (2009), pp. 7760–7779. DOI: `10.1039/b906540g`. URL: `http://pubs.rsc.org/en/content/articlepdf/2009/cp/b906540g`.

[140] K. Mizoguchi, T. Ujike, and Y. Tominaga. "Dynamics structure of water in NaCl aqueous solution". In: *J. Chem. Phys.* 109.5 (1998), pp. 1867–1872. DOI: `10.1063/1.476763`. URL: `https://doi.org/10.1063/1.476763`.

[141] John B. Asbury et al. "Water dynamics: vibrational echo correlation spectroscopy and comparison to molecular dynamics simulations". In: *J. Phys. Chem. A* 108.7 (2012), pp. 1107–1119. DOI: `10.1021/jp036266k`. URL: `https://doi.org/10.1021/jp036266k`.

[142] J. D. Eaves et al. "Hydrogen bonds in liquid water are broken only fleetingly". In: *Proc. Natl. Acad. Sci. USA*. 102.37 (2005), pp. 13019–13022. DOI: `10.1073/pnas.0505125102`. URL: `https://doi.org/10.1073/pnas.0505125102`.

[143] Sean T. Roberts Joseph J. Loparo and Andrei Tokmakoff. "Multidimensional infrared spectroscopy of water. II. Hydrogen bond switching dynamics". In: *J. Chem. Phys.* 125 (2006), p. 194522. DOI: `10.1063/1.2382896`. URL: `https://doi.org/10.1063/1.2382896`.

[144] B. Auer et al. "Hydrogen bonding and Raman, IR, and 2D-IR spectroscopy of dilute HOD in liquid D2O ". In: *Proc. Natl. Acad. Sci. USA* 104.36 (2007), pp. 14215–14220. DOI: `10.1073/pnas.0701482104`. URL: `https://doi.org/10.1073/pnas.0701482104`.

[145] Rebecca A. Nicodemus et al. "Hydrogen bond rearrangements in water probed with temperature-dependent 2D IR". In: *J. Phys. Chem. Lett.* 1.7 (2010), pp. 1068–1072. DOI: `10.1021/jz100138z`. URL: `https://doi.org/10.1021/jz100138z`.

[146] Krupa Ramasesha et al. "Ultrafast 2D IR anisotropy of water reveals reorientation during hydrogen-bond switching". In: *J. Chem. Phys.* 135 (2011), p. 054509. DOI: `10.1063/1.3623008`. URL: `https://doi.org/10.1063/1.3623008`.

[147] Yicun Ni, Scott M. Gruenbaum, and James L. Skinner. "Slow hydrogen-bond switching dynamics at the water surface revealed by theoretical two-dimensional sum-frequency spectroscopy". In: *Proc. Natl. Acad. Sci. USA.* 110.6 (2012), pp. 1992–1998. DOI: `10.1073/pnas.1222017110`. URL: `https://doi.org/10.1073/pnas.1222017110`.

[148] A. Luzar. "Water hydrogen-bond dynamics close to hydrophobic and hydrophilic groups". In: *Faraday Discuss.* 103 (0 1996), pp. 29–40. DOI: `10.1039/FD9960300029`. URL: `http://dx.doi.org/10.1039/FD9960300029`.

[149] A. Luzar. "Resolving the hydrogen bond dynamics conundrum". In: *J. Chem. Phys.* 113 (2000), p. 10663. DOI: `10.1063/1.1320826`. URL: `https://aip.scitation.org/doi/abs/10.1063/1.1320826`.

[150] Pu Liu, Edward Harder, and B. J. Berne. "Hydrogen–bond dynamics in the air-water interface". In: *J. Phys. Chem. B* 109.7 (2005), pp. 2949–2955. DOI: `10.1021/jp046807l`. URL: `https://doi.org/10.1021/jp046807l`.

[151] Ilan Benjamin. "Hydrogen bond dynamics at water/organic liquid interfaces". In: *J. Phys. Chem. B* 109.28 (2005), pp. 13711–13715. DOI: `10.1021/jp044157f`. URL: `https://doi.org/10.1021/jp044157f`.

[152] Kota Usui et al. "Ab initio liquid water dynamics in aqueous TMAO solution". In: *J. Phys. Chem. B* 119.33 (2015), pp. 10597–10606. DOI: `10.1021/acs.jpcb.5b02579`. URL: `https://pubs.acs.org/doi/abs/10.1021/acs.jpcb.5b02579`.

[153] Thomas D. Kühne et al. "Efficient and accurate Car-Parrinello-like approach to Born-Oppenheimer molecular dynamics". In: *Phys. Rev. Lett.* 98 (6 2007), p. 066401. DOI: `10.1103/PhysRevLett.98.066401`. URL: `https://link.aps.org/doi/10.1103/PhysRevLett.98.066401`.

[154] Bhabani S. Mallik, A. Semparithi, and Amalendu Chandra. "A first principles theoretical study of vibrational spectral diffusion and hydrogen bond dynamics in aqueous ionic solutions: D_2O in hydration shells of Cl^- ions". In: *J. Chem. Phys.* 129.19 (2008), p. 194512. DOI: `10.1063/1.3006032`. URL: `https://doi.org/10.1063/1.3006032`.

[155] Timothy C. Berkelbach, Hee-Seung Lee, and Mark E. Tuckerman. "Concerted hydrogen-bond dynamics in the transport mechanism of the hydrated proton: a first-principles molecular dynamics study". In: *Phys. Rev. Lett.* 103 (23 2009), p. 238302. DOI: `10.1103/PhysRevLett.103.238302`. URL: `https://link.aps.org/doi/10.1103/PhysRevLett.103.238302`.

[156] Rustam Z. Khaliullin and Thomas D. Kühne. "Microscopic properties of liquid water from combined ab initio molecular dynamics and energy decomposition studies". In: *Phys. Chem. Chem. Phys.* 15 (38 2013), pp. 15746–15766. DOI: `10.1039/C3CP51039E`. URL: `http://dx.doi.org/10.1039/C3CP51039E`.

[157] A. P. Willard and D. Chandler. "Instantaneous liquid interfaces". In: *J. Phys. Chem. B* 114.5 (2010), p. 1954. DOI: `10.1021/jp909219k`. URL: `https://doi.org/10.1021/jp909219k`.

[158] F. H. Stillinger. "Water revisited". In: *Science* 209 (1980), p. 451. DOI: `10.1126/science.209.4455.451`. URL: `https://science.sciencemag.org/content/209/4455/451.abstract`.

[159] M. E. Tuckerman. *Statistical mechanics: Theory and molecular simulation.* Oxford University Express, 2010.

[160] S. W. Rick, S. J. Stuart, and B. J. Berne. “Dynamical fluctuating force fields: Application to liquid water”. In: *J. Chem. Phys.* 101(7) (1994), p. 6141. DOI: 10.1063/1.468398. URL: arXiv:chem-ph/9406002.

[161] S. W. Rick and S. J. Stuart. “Potentials and algorithms for incorporating polarizability in computer simulations”. In: *Rev. Comput. Chem.* 18 (2002), pp. 89–146. DOI: 10.1002/0471433519.ch3. URL: https://onlinelibrary.wiley.com/doi/abs/10.1002/0471433519.ch3.

[162] G. Lamoureux, A. D. MacKerell, Jr., and B. Roux. “A simple polarizable model of water based on classical Drude oscillators”. In: *J. Chem. Phys.* 119 (2003), p. 5185. DOI: 10.1063/1.1598191. URL: https://aip.scitation.org/doi/abs/10.1063/1.1598191.

[163] M. E. Tuckerman. “Ab initio molecular dynamics: Basic concepts, current trends and novel applications”. In: *J. Phys.: Condens. Matter* 14 (2002), R1297–R1355. DOI: 10.1088/0953-8984/14/50/202. URL: https://ui.adsabs.harvard.edu/abs/2002JPCM...14R1297T.

[164] A. Warshel and R. M. Weiss. “An empirical valence bond approach for comparing reactions in solutions and in enzymes”. In: *J. Am. Chem. Soc.* 102 (1980), pp. 6218–6226. DOI: 10.1021/ja00540a008. URL: http://pubs.acs.org/doi/10.1021/ja00540a008.

[165] D. K. Remler and P. A. Madden. “Molecular dynamics without effective potentials via the Car-Parrinello approach”. In: *Mol. Phys.* 70 (1990), pp. 921–966. DOI: 10.1080/00268979000101451. URL: https://doi.org/10.1080/00268979000101451.

[166] M. C. Payne et al. “Iterative minimization techniques for ab initio total-energy calculations: Molecular dynamics and conjugate gradients”. In: *Rev. Mod. Phys.* 64 (4 1992), pp. 1045–1097. DOI: 10.1103/RevModPhys.64.1045. URL: https://link.aps.org/doi/10.1103/RevModPhys.64.1045.

[167] M. P. Allen and D. J. Tildesley (Ed.) *Computer simulation in chemical physics, chapter 8, first-principles molecular dynamics.* NATO ASI Series C, 1993, p. 261. URL: https://link.springer.com/chapter/10.1007/978-94-011-1679-4_8.

[168] M. E. Tuckerman et al. “Ab initio molecular dynamics simulations”. In: *J. Phys. Chem.* 100 (1996), pp. 12878–12887. DOI: 10.1021/jp960480+. URL: https://pubs.acs.org/doi/abs/10.1021/jp960480+.

[169] M. Parrinello. “From silicon to RNA: The coming of age of ab initio molecular dynamics”. In: *Solid State Commun.* 102 (1997), pp. 107–120. DOI: 10.1016/S0038-1098(96)00723-5. URL: https://www.sciencedirect.com/science/article/abs/pii/S0038109896007235.

[170] D. Marx and J. Hutter. “Ab initio molecular dynamics: theory and implementation”. In: *Modern Methods and Algorithms of Quantum Chemistry, J.Grotendorst (Ed.) John von Neumann Institute for Computing, Jülich, NIC Series* 1 (2000), pp. 301–499. URL: https://juser.fz-juelich.de/record/44687/files/NIC-Band-1.pdf#page=311.

[171] R. Car. “Introduction to density-functional theory and ab-initio molecular dynamics”. In: *Quant. Struct. Act. Rel.* 21 (2002), pp. 97–104. URL: https://onlinelibrary.wiley.com/doi/abs/10.1002/1521-3838(200207)21:2%3C97::AID-QSAR97%3E3.0.CO;2-6.

[172] R. P. Feynman and A. R. Hibbs. *Quantum mechanics and path integrals.* New York: McGraw-Hill, 1965.

[173] R. P. Feynman. *Statistical mechanics: A set of lectures.* Benjamin, 1972.

[174] D. Marx and M. Parrinello. "Ab initio path integral molecular dynamics: Basic ideas". In: *J. Chem. Phys.* 104 (1996), p. 4077. DOI: `10.1063/1.471221`. URL: `https://aip.scitation.org/doi/abs/10.1063/1.471221`.

[175] M. Tuckerman et al. "Efficient and general algorithms for path integral Car-Parrinello molecular dynamics". In: *J. Chem. Phys.* 104 (1996), pp. 5579–5588. DOI: `10.1063/1.471771`. URL: `https://doi.org/10.1063/1.471771`.

[176] D. Marx, M. E. Tuckerman, and G. J. Martyna. "Quantum dynamics via adiabatic ab initio centroid molecular dynamics". In: *Comput. Phys. Commun.* 118 (1999), p. 166.

[177] J. VandeVondele et al. "Quickstep: Fast and accurate density functional calculations using a mixed Gaussian and plane waves approach". In: *Comput. Phys. Commun.* 167.2 (2005), pp. 103–128. ISSN: 0010–4655. DOI: `10.1016/j.cpc.2004.12.014`. URL: `https://doi.org/10.1016/j.cpc.2004.12.014`.

[178] M. Born and J. R. Oppenheimer. "Zur Quantentheorie er Molekeln". In: *Ann. Physik* 84 (1927), p. 457.

[179] P. Hohenberg and W. Kohn. "Inhomogeneous electron gas". In: *Phys. Rev.* 136 (3B 1964), B864–B871. DOI: `10.1103/PhysRev.136.B864`. URL: `https://link.aps.org/doi/10.1103/PhysRev.136.B864`.

[180] W. Kohn and L. J. Sham. "Quantum density oscillations in an inhomogeneous electron gas". In: *Phys. Rev.* 137 (6A 1965), A1697–A1705. DOI: `10.1103/PhysRev.137.A1697`. URL: `https://link.aps.org/doi/10.1103/PhysRev.137.A1697`.

[181] M. Levy. "Universal variational functionals of electron densities, first-order density matrices, and natural spin-orbitals and solution of the v-representability problem". In: *Proc. Natl. Acad. Sci. USA.* 76 (1979), pp. 6062–6065. DOI: `10.1073/pnas.76.12.6062`. URL: `https://www.pnas.org/content/76/12/6062.short`.

[182] Kieron Burke. *ABC of density functional theory.* Department of Chemistry, University of California, Irvine, 2007.

[183] J. P. Perdew, K. Burke, and M. Ernzerhof. "Generalized gradient approximation made simple". In: *Phys. Rev. Lett.* 77 (1996), pp. 3865–3868. DOI: `10.1103/PhysRevLett.77.3865`. URL: `http://link.aps.org/doi/10.1103/PhysRevLett.77.3865`.

[184] A. D. Becke. "Density-functional exchange-energy approximation with correct asymptotic behavior". In: *Phys. Rev. A* 38 (1988), p. 3098. DOI: `10.1103/PhysRevA.38.3098`. URL: `https://doi.org/10.1103/PhysRevA.38.3098`.

[185] C. Lee, W. Yang, and R. G. Parr. "Development of the colic-salvetti correlation-energy formula into a functional of the electron density". In: *Phys. Rev. B* 37 (1988), p. 785. DOI: `10.1103/PhysRevB.37.785`. URL: `https://doi.org/10.1103/PhysRevB.37.785`.

[186] G. D. Zeiss and William J. Meath. “Dispersion energy constants C_6(A,B), dipole oscillator strength sums and refractivities for Li, N, O, H_2, N_2, O_2, NH_3, H_2O, NO and N_2O”. In: *Molecular Physics* 33.4 (1977), pp. 1155–1176. DOI: 10.1080/00268977700100991. URL: https://doi.org/10.1080/00268977700100991.

[187] J. Kohanoff. *Electronic structrue calculations for solids and materials: theory and computational methods*. Cambridge University Press, 2006.

[188] X. Wu et al. “Towards extending the applicability of density functional theory to weakly bound systems”. In: *J. Chem. Phys.* 115 (2001), pp. 8748–8757. DOI: 10.1063/1.1412004. URL: https://doi.org/10.1063/1.1412004.

[189] Q. Wu and W. Yang. “Empirical correction to density functional theory for van der Waals interactions”. In: *J. Chem. Phys.* 116 (2002), pp. 515–524. DOI: 10.1063/1.1424928. URL: https://aip.scitation.org/doi/abs/10.1063/1.1424928.

[190] U. Zimmerli, M. Parrinello, and P. Koumoutsakos. “Dispersion corrections to density functionals for water aromatic interactions”. In: *J. Chem. Phys.* 120 (2004), p. 2693. DOI: 10.1063/1.1637034. URL: https://aip.scitation.org/doi/abs/10.1063/1.1637034.

[191] J. Klimeš and A. Michaelides. “Perspective: Advances and challenges in treating van der Waals dispersion forces in density functional theory”. In: *J. Chem. Phys.* 137.1 (2012), pp. 120901–120912. DOI: 10.1063/1.4754130. URL: https://aip.scitation.org/doi/full/10.1063/1.4754130.

[192] P Pulay. “Ab initio calculation of force constants and equilibrium geometries in polyatomic molecules: I. Theory”. In: *Mol. Phys.* 17.2 (1969), pp. 197–204. DOI: 10.1080/00268976900100941. URL: https://doi.org/10.1080/00268976900100941.

[193] D. Frenkel and B. Smit. *Understanding molecular simulation*. Computational Science Series (Academic Press), 2nd ed, 2002.

[194] G. Kresse and J. Hafner. “Ab initio molecular dynamics for liquid metals”. In: *Phys. Rev. B* 47 (1 1993), pp. 558–561. DOI: 10.1103/PhysRevB.47.558. URL: https://link.aps.org/doi/10.1103/PhysRevB.47.558.

[195] M. T. Dove. *Introduction to lattice dynamics*. Cambridge: Cambridge University Press, 1993.

[196] J. M. Dickey and A. Paskin. “Computer simulation of the lattice dynamics of solids”. In: *Phys. Rev.* 188 (1969), p. 1407. DOI: 10.1103/physrev.188.1407. URL: https://journals.aps.org/pr/abstract/10.1103/PhysRev.188.1407.

[197] T. Ishiyama and A. Morita. “Molecular dynamics analysis of interfacial structures and sum frequency generation spectra of aqueous hydrogen halide solutions”. In: *J. Phys. Chem. A* 111.38 (2007), pp. 9277–9285. DOI: 10.1021/jp072997z. URL: http://dx.doi.org/10.1021/jp072997z.

[198] M. P. Allen and D. J. Tildesley. *Computer simulation of liquids*. Oxford Science Publ. Clarendon Press, 1989. ISBN: 9780198556459. URL: https://books.google.de/books?id=032VXB9e5P4C.

[199] A. L. Harris et al. “Vibrational energy transfer to metal surfaces probed by sum generation: CO/Cu(100) and CH_3S/Ag(111)”. In: *J. Electron Spec. Related Phenomena* 54155 (1990), pp. 5–16. DOI: `10.1016/0368-2048(90)80196-H`. URL: `https://www.sciencedirect.com/science/article/abs/pii/036820489080196H`.

[200] A. L. Harris et al. “Molecular vibrational energy relaxation at metal surfaces by picosecond infrared-visible sum spectroscopy”. In: Optical Society of America, 1990, QTHK1. URL: `http://www.osapublishing.org/abstract.cfm?URI=IQEC-1990-QTHK1`.

[201] H.-L. Dai and W. Ho. *Laser spectroscopy and photochemistry on metal surfaces: Part 1*. World Scientific Publishing Co. Pte. Ldt., 1995.

[202] P. Halevi (Ed.) *Photonic probes of surfaces*. Progress in Quantum Electronics, 1996, p. 255.

[203] A. Wieckowski. *Interfacial electrochemistry: Theory, experiment and applications*. CRC Press, 1999, p. 992.

[204] Z. Chen, D. Gracias, and G. Somorjai. “Sum frequency generation (SFG)-surface vibrational spectroscopy studies of buried interfaces: Catalytic reaction intermediates on transition metal crystal surfaces at high reactant pressures; Polymer surface structures at the solid-gas and solid-liquid interfaces”. In: *Appl. Phys. B* 68 (1999), p. 549. DOI: `10.1007/s003400050664`. URL: `https://link.springer.com/article/10.1007/s003400050664`.

[205] Z. Chen. “Understanding surfaces and buried interfaces of polymer materials at the molecular level using sum frequency generation vibrational spectroscopy”. In: *Polymer International* 56(5) (2007), pp. 577–587. DOI: `10.1002/pi.2201`. URL: `https://deepblue.lib.umich.edu/bitstream/handle/2027.42/56019/2201_ftp.pdf?sequence=1`.

[206] A. Morita. “Theory of sum frequency generation spectroscopy”. In: Singapore: Springer Nature Singapore Pte Ltd., 2018. Chap. 1, p. 2.

[207] For OH vibrations at room temperature, the energy difference between vibrational states $|\nu = 0\rangle$ and $|\nu = 1\rangle$ is about 4500 K, or 0.4 eV, which is much larger than $k_\mathrm{B}T$. Therefore, we can treat the OH like a linear harmonic oscillator.

[208] S. Mukamel. *Principles of nonlinear optical spectroscopy*. Oxford University Press, Oxford, 1995.

[209] C. M. Pradier and Y. J. Chabal (Ed.) *Biointerface Characterization by Advanced IR Spectroscopy*. Elsevier, 2011, p. 344.

[210] R. Vanselow and R. Howe. *Chemistry and physics of solid surfaces VIII*. Springer Science + Business Media, 2012, p. 464.

[211] A. Morita and J. T. Hynes. “A theoretical analysis of the sum frequency generation spectrum of the water surface. II. Time-dependent approach”. In: *J. Phys. Chem. B* 106 (2002), pp. 673–685. DOI: `10.1021/jp0133438`. URL: `https://pubs.acs.org/doi/abs/10.1021/jp0133438`.

[212] A. Morita and J. T. Hynes. “A Theoretical analysis of the sum frequency generation spectrum of the water surface”. In: *J. Chem. Phys.* 258 (2000), pp. 371–390. DOI: `http://dx.doi.org/10.1016/S0301-0104(00)00127-0`. URL: `http://www.sciencedirect.com/science/article/pii/S0301010400001270`.

[213] S. Nihonyanagi et al. “Unified molecular view of the air/water interface based on experimental and theoretical $\chi^{(2)}$ spectra of an isotopically diluted water surface”. In: *J. Am. Chem. Soc.* 133 (2011), pp. 16875–16880. DOI: `10.1021/ja2053754`. URL: `https://pubs.acs.org/doi/abs/10.1021/ja2053754`.

[214] S. A. Corcelli and J. L. Skinner. “Infrared and raman line shapes of dilute HOD in liquid H_2O and D_2O from 10 to 90 °C”. In: *J. Phys. Chem. A* 109 (2005), pp. 6154–6165. DOI: `10.1021/jp0506540`. URL: `https://pubs.acs.org/doi/abs/10.1021/jp0506540`.

[215] N. Marzari and D. Vanderbilt. “Maximally localized generalized wannier functions for composite energy bands”. In: *Phys. Rev. B* 56 (20 1997), pp. 12847–12865. DOI: `10.1103/PhysRevB.56.12847`. URL: `https://link.aps.org/doi/10.1103/PhysRevB.56.12847`.

[216] M. Salanne et al. “Polarizabilities of individual molecules and ions in liquids from first principles”. In: *J. Phys. Condens. Matter.* 20.49 (2008), p. 494207. URL: `http://stacks.iop.org/0953-8984/20/i=49/a=494207`.

[217] A. Luzar and D. Chandler. “Effect of environment on hydrogen bond dynamics in liquid water”. In: *Phys. Rev. Lett.* 76 (6 1996), pp. 928–931. DOI: `10.1103/PhysRevLett.76.928`. URL: `https://link.aps.org/doi/10.1103/PhysRevLett.76.928`.

[218] Amalendu Chandra. “Effects of ion atmosphere on hydrogen-bond dynamics in aqueous electrolyte solutions”. In: *Phys. Rev. Lett.* 85 (2000), pp. 768–771. DOI: `10.1103/PhysRevLett.85.768`. URL: `https://link.aps.org/doi/10.1103/PhysRevLett.85.768`.

[219] M. Tarek and D. J. Tobias. “Role of protein-water hydrogen bond dynamics in the protein dynamical transition”. In: *Phys. Rev. Lett.* 88 (13 2002), p. 138101. DOI: `10.1103/PhysRevLett.88.138101`. URL: `https://link.aps.org/doi/10.1103/PhysRevLett.88.138101`.

[220] Matthias Heyden and Douglas J. Tobias. “Spatial dependence of protein-water collective hydrogen-bond dynamics”. In: *Phys. Rev. Lett.* 111 (21 2013), p. 218101. DOI: `10.1103/PhysRevLett.111.218101`. URL: `https://link.aps.org/doi/10.1103/PhysRevLett.111.218101`.

[221] Christoph Kolano et al. “Watching hydrogen-bond dynamics in a β-turn by transient two-dimensional infrared spectroscopy”. In: *Nature* 444.7118 (2006), pp. 469–472. ISSN: 14764687. DOI: `10.1038/nature05352`. URL: `https://www.nature.com/articles/nature05352`.

[222] S. Pal, B. Bagchi, and S. Balasubramanian. “Hydration layer of a cationic micelle, C_{10}TAB: Structure, rigidity, slow reorientation, hydrogen bond lifetime, and solvation dynamics”. In: *J. Phys. Chem. B* 109 (2005), pp. 12879–12890. DOI: `10.1021/jp0510793`. URL: `https://pubs.acs.org/doi/abs/10.1021/jp0510793`.

[223] R. Kumar, J. R. Schmidt, and J. L. Skinner. “Hydrogen Bonding Definitions and Dynamics in Liquid Water”. In: *J. Chem. Phys.* 126.20 (2007), p. 204107. DOI: `10.1063/1.2742385`. URL: `https://doi.org/10.1063/1.2742385`.

[224] F. Sciortino and S. L. Fornili. “Hydrogen bond cooperativity in simulated water: Time dependence analysis of pair interactions”. In: *J. Chem. Phys.* 90.5 (1989), pp. 2786–2792. DOI: `10.1063/1.455927`. URL: `https://doi.org/10.1063/1.455927`.

[225] A. K. Soper and M. G. Phillips. “A new determination of the structure of water at 25 ° C”. In: *Chem. Phys* 107 (1986), pp. 47–60. DOI: `10.1016/0301-0104(86)85058-3`. URL: `https://www.sciencedirect.com/science/article/abs/pii/0301010486850583`.

[226] J. Teixeira, M. C. Bellisent-Funel, and S. H. Chen. “Dynamics of water studied by neutron scattering”. In: *J. Phys. Condens. Matter* 2 (1990), SA105. DOI: `10.1088/0953-8984/2/S/011`. URL: `http://iopscience.iop.org/0953-8984/2/S/011`.

[227] Sundaram Balasubramanian, Subrata Pal, and Biman Bagchi. “Hydrogen-bond dynamics near a micellar surface: Origin of the universal slow relaxation at complex aqueous interfaces”. In: *Phys. Rev. Lett.* 89 (2002), p. 115505. DOI: `10.1103/PhysRevLett.89.115505`. URL: `https://link.aps.org/doi/10.1103/PhysRevLett.89.115505`.

[228] Alenka Luzar and David Chandler. “Structure and hydrogen bond dynamics of water-dimethyl sulfoxide mixtures by computer simulations”. In: *J. Chem. Phys.* 98.10 (1993), pp. 8160–8173. DOI: `10.1063/1.464521`. URL: `https://doi.org/10.1063/1.464521`.

[229] D. Chandler. *Introduction to morden statistical mechanics.* Oxford University press, Oxford, 1987.

[230] D. C. Rapaport. “Hydrogen bonds in water: Network organization and life-times”. In: *Mol. Phys.* 50 (1983), pp. 1151–1162. DOI: `10.1080/00268978300102931`. URL: `https://doi.org/10.1080/00268978300102931`.

[231] F. H. Stillinger. “Theory and molecular models for water”. In: *Adv. Chem. Phys* 31 (1975), pp. 1–101. DOI: `10.1002/9780470143834.ch1`. URL: `https://onlinelibrary.wiley.com/doi/abs/10.1002/9780470143834.ch1`.

[232] A. Geiger et al. “Structure and dynamics of the hydrogen bond network in water by computer simulations”. In: *J. Phys. (Paris)* 45 (1984), pp. C7–13–C7–30. DOI: `10.1051/jphyscol:1984702`. URL: `https://doi.org/10.1051/jphyscol:1984702`.

[233] Dominic A. Zichi and Peter J. Rossky. “Solvent molecular dynamics in regions of hydrophobic hydration”. In: *J. Chem. Phys.* 84.5 (1986), pp. 2814–2822. DOI: `10.1063/1.450307`. URL: `https://doi.org/10.1063/1.450307`.

[234] F. Sciortino. *Dynamics of the hydrogen bond networks in simulated liquid water. In: Stanley H. E., Ostrowsky N. (eds) Correlations and Connectivity. NATO ASI Series (Series E: Applied Sciences).* Vol. 188. Springer, Dordrecht, 1990. ISBN: 978-94-009-2157-3. DOI: `10.1007/978-94-009-2157-3_17`. URL: `https://doi.org/10.1007/978-94-009-2157-3_17`.

[235] Francis W. Starr, Johannes K. Nielsen, and H. Eugene Stanley. “Hydrogen-bond dynamics for the extended simple point-charge model of water”. In: *Phys. Rev. E* 62 (1 2000), pp. 579–587. DOI: `10.1103/PhysRevE.62.579`. URL: `https://link.aps.org/doi/10.1103/PhysRevE.62.579`.

[236] D. van der Spoel et al. “Thermodynamics of hydrogen bonding in hydrophilic and hydrophobic media”. In: *J. Phys. Chem. B* 110.9 (2006), pp. 4393–4398. DOI: `10.1021/jp0572535`. URL: `https://pubs.acs.org/doi/10.1021/jp0572535`.

[237] Johanna Busch, Jan Neumann, and Dietmar Paschek. “An exact *a posteriori* correction for hydrogen bond population correlation functions and other reversible geminate recombinations obtained from simulations with periodic boundary conditions. Liquid water as a test case”. In: *The Journal of Chemical Physics* 154.21 (2021), p. 214501. DOI: 10.1063/5.0053445. URL: https://doi.org/10.1063/5.0053445.

[238] A Luzar and D Chandler. *Application of the reactive flux formalism to study water hydrogen bond dynamics. In: Bellissent-Funel MC., Dore J. C. (eds) Hydrogen bond networks.* Vol. 435. Springer, Dordrecht, 1994.

[239] S. Chowdhuri and A. Chandra. “Dynamics of halide ion-water hydrogen bonds in aqueous solutions: dependence on ion size and temperature”. In: *J. Phys. Chem. B* 110 (2006), pp. 9674–9680. DOI: 10.1021/jp057544d. URL: https://pubs.acs.org/doi/abs/10.1021/jp057544d.

[240] F. Sciortino et al. “Lifetime of the bond network and gel-like anomalies in supercooled water”. In: *Phys. Rev. Lett.* 64.14 (1990), pp. 1686–1689. DOI: 10.1103/PhysRevLett.64.1686. URL: https://link.aps.org/doi/10.1103/PhysRevLett.64.1686.

[241] T. Krausche and W. Nadler. “Statistical mechanics of hydrogen bond networks”. In: *Z. Phys. B: Condens. Matter* 86.5 (1992), p. 433. URL: https://link.springer.com/content/pdf/10.1007/BF01323737.pdf.

[242] F. W. Starr, J. K. Nielsen, and H. E. Stanley. “Fast and slow dynamics of hydrogen bonds in liquid water”. In: *Phys. Rev. Lett.* 82.11 (1999), p. 2294. DOI: 10.1103/PhysRevLett.82.2294. URL: https://doi.org/10.1103/PhysRevLett.82.2294.

[243] V. P. Voloshin and Yu. I. Naberukhin. “Hydrogen bond lifetime distributions in computer-simulated water”. In: *J. Structural Chem.* 50 (2009), pp. 78–89. URL: https://link.springer.com/content/pdf/10.1007/s10947-009-0010-6.pdf.

[244] H. E. Stanley et al. “Unsolved mysteries of water in its liquid and glassy phases”. In: *J. Phys.: Condens. Matter* 12 (2000), A403–A412. URL: https://iopscience.iop.org/article/10.1088/0953-8984/12/8A/355/pdf.

[245] D. Chandler. “Roles of classical dynamics and quantum dynamics on activated processes occurring in liquids”. In: *J. Stat. Phys.* 42 (1986), pp. 49–67. DOI: 10.1007/BF01010840. URL: https://link.springer.com/article/10.1007/BF01010840.

[246] D. Chandler. “Statistical mechanics of isomerization dynamics in liquids and the transition state approximation”. In: *J. Chem. Phys.* 68 (1978), pp. 2959–2970. DOI: 10.1063/1.436049. URL: https://aip.scitation.org/doi/abs/10.1063/1.436049.

[247] J. Mathias Weber et al. “Isolating the spectroscopic signature of a hydration shell with the use of clusters: Superoxide tetrahydrate”. In: *Science* 287.5462 (2000), pp. 2461–2463. ISSN: 0036-8075. DOI: 10.1126/science.287.5462.2461. URL: https://science.sciencemag.org/content/287/5462/2461.

[248] M. F. Kropman and H. J. Bakker. “Negligible effect of ions on the hydrogen-bond structure in liquid water”. In: *Science* 291 (2001), p. 2118. DOI: 10.1126/science.1084801. URL: https://science.sciencemag.org/content/301/5631/347.

[249] R. Jimenez et al. “Femtosecond solvation dynamics of water”. In: *Nature* 369 (1994), pp. 471–473. DOI: `https://doi.org/10.1038/369471a0`.

[250] David E. Smith and Liem X. Dang. “Computer simulations of NaCl association in polarizable water”. In: *J. Chem. Phys.* 100.5 (1994), pp. 3757–3766. DOI: `10.1063/1.466363`. URL: `https://doi.org/10.1063/1.466363`.

[251] L. Jiang et al. “Gas-phase vibrational spectroscopy of microhydrated magnesium nitrate ions $[MgNO_3(H_2O)_{1-4}]^+$”. In: *J. Am. Chem. Soc.* 132 (2010), pp. 7398–7404. DOI: `10.1021/ja1011806`. URL: `https://pubs.acs.org/doi/abs/10.1021/ja1011806`.

[252] N. Heinea and K. R. Asmis. “Cryogenic ion trap vibrational spectroscopy of hydrogen-bonded clusters relevant to atmospheric chemistry”. In: *J. Am. Chem. Soc.* 34.1 (2015), pp. 1–34. DOI: `https://doi.org/10.1080/0144235X.2014.979659`. URL: `https://www.tandfonline.com/doi/full/10.1080/0144235X.2014.979659`.

[253] Jr. O. Rodriguez and J. M. Lisy. “Revisiting $Li^+(H_2O)_{3-4}Ar_1$ clusters: Evidence of high-energy conformers from infrared spectra”. In: *J. Phys. Chem. Lett.* 2 (2011), p. 1444. DOI: `10.1021/jp112087e`. URL: `https://doi.org/10.1021/jp112087e`.

[254] D. J. Miller and J. M. Lisy. “Hydrated alkali-metal cations: Infrared spectroscopy and ab Initio calculations of $M^+(H_2O)_{x=2-5}Ar$ cluster ions for M = Li, Na, K, and Cs”. In: *J. Am. Chem. Soc.* 130 (2008), pp. 15381–15392. DOI: `10.1021/ja803665q`. URL: `https://pubs.acs.org/doi/abs/10.1021/ja803665q`.

[255] D. J. Miller and J. M. Lisy. “Entropic effects on hydrated alkali-metal cations: Infrared spectroscopy and ab initio calculations of $M^+(H_2O)_{x=2-5}$ cluster ions for M = Li, Na, K, and Cs”. In: *J. Am. Chem. Soc.* 130 (2008), p. 15393. DOI: `10.1021/ja803666m`. URL: `https://pubs.acs.org/doi/abs/10.1021/ja803666m`.

[256] J. P. Beck and J. M. Lisy. “Infrared spectroscopy of hydrated alkali metal cations: Evidence of multiple photon absorption”. In: *J. Chem. Phys.* 135 (2011), p. 044302. DOI: `10.1063/1.3609760`. URL: `https://aip.scitation.org/doi/abs/10.1063/1.3609760`.

[257] D. E. Otten, P. B. Petersen, and R. Saykally. “Observation of nitrate ions at the air/water interface by UV-second harmonic generation”. In: *J. Chem. Phys. Lett.* 449 (4–6 2007), pp. 261–265. DOI: `10.1016/j.cplett.2007.10.081`. URL: `https://www.sciencedirect.com/science/article/abs/pii/S0009261407014017`.

[258] D. J. Tobias et al. “Simulation and theory of ions at atmospherically relevant aqueous liquid-air interfaces”. In: *Annu. Rev. Phys. Chem.* 64 (2013), p. 33959.

[259] E. S. Shamay et al. “At the water’s edge: nitric acid as weak acid”. In: *J. Am. Chem. Soc.* 129.43 (2007), p. 12910. DOI: `10.1021/ja074811f`. URL: `https://doi.org/10.1021/ja074811f`.

[260] G. C. Pimentel and A. L. MClellan. *The hydrogen bond.* W. H. Freemann, San Francisco, 1960.

[261] Y. Marechál. “The molecular structure of liquid water delivered by absorption spectroscopy in the whole IR region completed with thermodynamics data”. In: *J. molecular structure* 1004 (2011), pp. 146–155. DOI: `10.1016/j.molstruc.2011.07.054`. URL: `https://www.sciencedirect.com/science/article/abs/pii/S0022286011006247`.

[262] S. Baldelli, C. Schnitzer, and M. J. Shultz. “Sum Frequency Generation Investigation of Water at the Surface of H_2O/H_2SO_4 Binary Systems”. In: *J. Phys. Chem. B* 101 (1997), pp. 10435–10441. DOI: `10.1021/jp972376d`. URL: `https://pubs.acs.org/doi/abs/10.1021/jp972376d`.

[263] L. M. Pegram and M. T. Record, Jr. “Thermodynamic origin of Hofmeister ion effects”. In: *J. Phys. Chem. B* 112 (2008), pp. 9428–9436. DOI: `10.1021/jp800816a`. URL: `https://pubs.acs.org/doi/abs/10.1021/jp800816a`.

[264] E. A. Carter et al. “Constrained reaction coordinate dynamics for the simulation of rare events”. In: *Chem. Phys. Lett.* 156 (1989), p. 472. DOI: `10.1016/S0009-2614(89)87314-2`. URL: `https://www.sciencedirect.com/science/article/abs/pii/S0009261489873142`.

[265] M. Sprik and G. Ciccotti. “Free energy from constrained molecular dynamics”. In: *J. Chem. Phys.* 109 (1998), pp. 7737–7744. DOI: `10.1063/1.477419`. URL: `https://ui.adsabs.harvard.edu/abs/1998JChPh.109.7737S`.

[266] M. E. Tuckerman. *Statistical Mechanics: Theory and Molecular Simulation*. Oxford University Press, 2010.

[267] Sutapa Ghosal et al. “Electron spectroscopy of aqueous solution interfaces reveals surface enhancement of halides”. In: *Science* 307.5709 (2005), pp. 563–566. ISSN: 0036-8075. DOI: `10.1126/science.1106525`. URL: `https://science.sciencemag.org/content/307/5709/563`.

[268] L. X. Dang and T.-M. Chang. “Molecular mechanism of ion binding to the liquid/vapor interface of water”. In: *J. Phys. Chem. B* 106 (2002), pp. 235–238. DOI: `10.1021/jp011853w`. URL: `https://pubs.acs.org/doi/abs/10.1021/jp011853w`.

[269] L. Vrbka et al. “Propensity of soft ions for the air/water interface”. In: *Curr. Opin. Coll. Interface Sci.* 9 (2004), pp. 67–73. DOI: `10.1016/j.cocis.2004.05.028`. URL: `https://www.sciencedirect.com/science/article/pii/S1359029404000330`.

[270] B. C. Garrett. “Ions at the air/water interface”. In: *Science* 303.5661 (2004), pp. 1146–1147. DOI: `10.1126/science.1089801`. URL: `https://science.sciencemag.org/content/303/5661/1146`.

[271] P. Bajaj, A. W. Götz, and F. Paesani. “Toward chemical accuracy in the description of ion-water interactions through many-body representations. I. Halide-water dimer potential energy surfaces”. In: *J. Chem. Theory Comput.* 12 (2016), pp. 2698–2705. DOI: `10.1021/acs.jctc.6b00302`. URL: `https://pubs.acs.org/doi/abs/10.1021/acs.jctc.6b00302`.

[272] D. F. Liu et al. “Vibrational spectroscopy of aqueous sodium halide solutions and air-liquid interfaces: Observation of increased interfacial depth”. In: *J. Phys. Chem. B* 108 (2004), pp. 2252–2260. DOI: `10.1021/jp036169r`. URL: `https://pubs.acs.org/doi/abs/10.1021/jp036169r`.

[273] M. J. Shultz et al. “Sum frequency generation spectroscopy of the aqueous interface: Ionic and soluble molecular solutions”. In: *Int. Rev. Phys. Chem.* 19.1 (2000), pp. 123–153. DOI: `10.1080/014423500229882`. URL: `https://doi.org/10.1080/014423500229882`.

[274] Bernard Cabane and Rodolphe Vuilleumier. “The physics of liquid water”. In: *Comptes Rendus Geoscience* 337.1 (2005), pp. 159–171. ISSN: 1631-0713. DOI: `https://doi.org/10.1016/j.crte.2004.09.018`. URL: `http://www.sciencedirect.com/science/article/pii/S1631071304002780`.

[275] L.-Å. Näslund et al. “X-ray absorption spectroscopy study of the hydrogen bond network in the bulk water of aqueous solutions”. In: *J. Phys. Chem. A* 109.27 (2005), pp. 5995–6002. DOI: `10.1021/jp050413s`. URL: `https://doi.org/10.1021/jp050413s`.

[276] Janamejaya Chowdhary and Branka M. Ladanyi. “Hydrogen bond dynamics at the water/hydrocarbon interface”. In: *J. Phys. Chem. B* 113.13 (2008), pp. 4045–4053. DOI: `10.1021/jp8061509`. URL: `https://doi.org/10.1021/jp8061509`.

[277] A. Tongraar, P. Tangkawanwanit, and B. M. Rode. “A Combined QM/MM Molecular Dynamics Simulations Study of Nitrate Anion (NO_3^-) in Aqueous Solution”. In: *J. Phys. Chem. A* 110.47 (2006), pp. 12918–12926. DOI: `10.1021/jp064779w`. URL: `https://pubs.acs.org/doi/abs/10.1021/jp064779w`.

[278] J. Chanda and S. Bandyopadhyay. “Hydrogen bond lifetime dynamics at the interface of a surfactant monolayer”. In: *J. Phys. Chem. B* 110.46 (2006), pp. 23443–23449. DOI: `10.1021/jp065203`. URL: `https://doi.org/10.1021/jp065203`.

[279] A. Tongraar, S. Hannongbua, and B. M. Rode. “QM/MM MD simulations of iodide ion (I^-) in aqueous solution: A delicate balance between ion-water and water-water h-bond interactions”. In: *J. Phys. Chem. A* 114.12 (2010), pp. 4334–4339. DOI: `10.1021/jp910435d`. URL: `https://www.ncbi.nlm.nih.gov/pubmed/20196599`.

[280] Sow-Hsin Chen et al. “Hydrogen-bond spectroscopy of water by neutron scattering”. In: *Phys. Rev. Lett.* 53 (14 1984), pp. 1360–1363. DOI: `10.1103/PhysRevLett.53.1360`. URL: `https://link.aps.org/doi/10.1103/PhysRevLett.53.1360`.

[281] J. Teixeira and M. C Bellissent-Funel1. “Dynamics of water studied by neutron scattering”. In: *J. Phys.: Condens. Matter* 2.SA (1990), pp. 105–108. URL: `https://iopscience.iop.org/article/10.1088/0953-8984/2/S/011/meta`.

[282] Jasper C. Werhahn et al. “Dynamics of weak, bifurcated, and strong hydrogen bonds in lithium nitrate trihydrate”. In: *J. Phys. Chem. Lett.* 2 (2011), pp. 1633–1638. DOI: `dx.doi.org/10.1021/jz200591v`. URL: `https://pubs.acs.org/doi/abs/10.1021/jz200591v`.

[283] Joseph A. Fournier et al. “Interplay of ion-water and water-water interactions within the hydration shells of nitrate and carbonate directly probed with 2D IR spectroscopy”. In: *J. Am. Chem. Soc.* 138.30 (2016), pp. 9634–9645. DOI: `10.1021/jacs.6b05122`. URL: `https://pubs.acs.org/doi/full/10.1021/jacs.6b05122`.

[284] Yung Sam Kim and Robin M. Hochstrasser. “Applications of 2D IR spectroscopy to peptides, proteins, and hydrogen-bond dynamics”. In: *J. Phys. Chem. B* 113.24 (2009), pp. 8231–8251. DOI: `10.1021/jp8113978`. URL: `https://doi.org/10.1021/jp8113978`.

[285] Zhen Zhang et al. “Ultrafast vibrational energy transfer at the water/air interface revealed by two-dimensional surface vibrational spectroscopy”. In: *Nature Chem.* 3 (2011), pp. 888–893. DOI: `10.1038/nchem.1158`. URL: `https://www.nature.com/articles/nchem.1158`.

[286] C. Hartwigsen, S. Goedecker, and J. Hutter. “Relativistic separable dual-space Gaussian pseudopotentials from H to Rn”. In: *Phys. Rev. B* 58 (7 1998), pp. 3641–3662. DOI: `10.1103/PhysRevB.58.3641`. URL: `http://link.aps.org/doi/10.1103/PhysRevB.58.3641`.

[287] G. Lippert, J. Hutter, and M. Parrinello. “The Gaussian and augmented-plane-wave density functional method for ab initio molecular dynamics simulations”. In: *Theor. Chem. Acc.* 103 (1999), pp. 124–140. DOI: `10.1007/s002140050523`. URL: `https://doi.org/10.1007/s002140050523`.

[288] A. Luzar and D. Chandler. “Hydrogen-bond kinetics in liquid water”. In: *Nature* 379 (1996), pp. 55–57. DOI: `10.1038/379055a0`. URL: `https://doi.org/10.1038/379055a0`.

[289] R. Michael Townsend, Jan Gryko, and Stuart A. Rice. “Structure of the liquid–vapor interface of water”. In: *J. Chem. Phys.* 82.9 (1985), pp. 4391–4392. DOI: `10.1063/1.448808`. URL: `https://doi.org/10.1063/1.448808`.

[290] Ramona S. Taylor, Liem X. Dang, and Bruce C. Garrett. “Molecular dynamics simulations of the liquid/vapor interface of SPC/E water”. In: *J. Phys. Chem.* 100 (1996), pp. 11720–11725. DOI: `10.1021/jp960615b`. URL: `https://doi.org/10.1021/jp960615b`.

[291] Eric Tyrode and Jonathan F. D. Liljeblad. “Water structure next to ordered and disordered hydrophobic silane monolayers: A vibrational sum frequency spectroscopy study”. In: *J. Phys. Chem. C* 117.4 (2013), pp. 1780–1790. DOI: `10.1021/jp310732f`. URL: `https://doi.org/10.1021/jp310732f`.

[292] I. V. Stiopkin et al. “Hydrogen bonding at the water surface revealed by isotopic dilution spectroscopy”. In: *Nature* 474 (2011), p. 192. DOI: `10.1038/nature10173`. URL: `https://www.nature.com/articles/nature10173`.

[293] T. Steinel et al. “Watching hydrogen bonds break: A transient absorption study of water”. In: *J. Phys. Chem. A* 108 (2004), pp. 10957–10964. DOI: `10.1021/jp046711r`. URL: `https://pubs.acs.org/doi/abs/10.1021/jp046711r`.

[294] Snehasis Chowdhuri and Amalendu Chandra. “Hydrogen bonds in aqueous electrolyte solutions: statistics and dynamics based on both geometric and energetic criteria”. In: *Phys. Rev. E* 66 (4 2002), p. 041203. DOI: `10.1103/PhysRevE.66.041203`. URL: `https://link.aps.org/doi/10.1103/PhysRevE.66.041203`.

[295] David M. Jonas et al. “Pump-probe polarization anisotropy study of femtosecond energy transfer within the photosynthetic reaction center of rhodobacter sphaeroides R26”. In: *J. Phys. Chem.* 100.20 (1996), pp. 12660–12673. DOI: `10.1021/jp960708t`. URL: `https://doi.org/10.1021/jp960708t`.

[296] Darcie A Farrow et al. “Polarized pump-probe measurements of electronic motion via a conical intersection”. In: *J. Chem. Phys.* 128 (2006), pp. 144510–144531. DOI: 10.1063/1.2837471. URL: https://doi.org/10.1063/1.2837471.

[297] Attila Szabo. “Theory of fluorescence depolarization in macromolecules and membranes”. In: *The Journal of Chemical Physics* 81.1 (1984), pp. 150–167. DOI: 10.1063/1.447378. URL: https://doi.org/10.1063/1.447378.

[298] G. R. Fleming. *Chemical applications of ultrafast spectroscopy.* Oxford University Press, New York, 1986.

[299] T. C. L. Jansen et al. “Two-dimensional infrared spectroscopy and ultrafast anisotropy decay of water”. In: *J. Chem. Phys.* 132 (2010), p. 224503. DOI: 10.1063/1.3454733. URL: https://aip.scitation.org/doi/abs/10.1063/1.3454733.

[300] T. C. L. Jansen and J. Knoester. “Nonadiabatic effects in the two-dimensional infrared spectra of peptides: Application to alanine dipeptide”. In: *J. Phys. Chem. B* 110 (2006), pp. 22910–22916. DOI: 10.1021/jp064795t. URL: https://pubs.acs.org/doi/abs/10.1021/jp064795t.

[301] J. R. Schmidt, S. A. Corcelli, and J. L. Skinner. “Pronounced non-Condon effects in the ultrafast infrared spectroscopy of water”. In: *J. Chem. Phys.* 123 (2005), p. 044513. DOI: 10.1063/1.1961472. URL: https://aip.scitation.org/doi/abs/10.1063/1.1961472.

[302] A. Tokmakoff. “Orientational correlation functions and polarization selectivity for nonlinear spectroscopy of isotropic media. I. Third order”. In: *The Journal of Chemical Physics* 105.1 (1996), pp. 1–12. DOI: 10.1063/1.471856. URL: https://doi.org/10.1063/1.471856.

[303] Y. L. A. Rezus and H. J. Bakker. “Orientational dynamics of isotopically diluted H_2O and D_2O”. In: *The Journal of Chemical Physics* 125.14 (2006), p. 144512. DOI: 10.1063/1.2353831. URL: https://doi.org/10.1063/1.2353831.

[304] Takuma Yagasaki, Junichi Ono, and Shinji Saito. “Ultrafast energy relaxation and anisotropy decay of the librational motion in liquid water: A molecular dynamics study”. In: *J. Chem. Phys.* 131.16 (2009), p. 164511. DOI: 10.1063/1.3254518. URL: https://doi.org/10.1063/1.3254518.

[305] H. Bakker and J. L. Skinner. “Vibrational spectroscopy as a probe of structure and dynamics in liquid water”. In: *Chem. Rev.* 110 (2010). DOI: 10.1021/cr9001879. URL: https://doi.org/10.1021/cr9001879.

[306] Y. S. Lin et al. “On the calculation of rotational anisotropy decay, as measured by ultrafast polarization-resolved vibrational pump-probe experiments”. In: *J. Chem. Phys* 132 (2010), p. 174505. DOI: 10.1063/1.3409561. URL: https://aip.scitation.org/doi/abs/10.1063/1.3409561.

[307] L. Zhu et al. “Surface self-diffusion of an organic glass”. In: *Phys. Rev. Lett.* 106.25 (2011), p. 256103. DOI: 10.1103/PhysRevLett.106.256103. URL: https://doi.org/10.1103/PhysRevLett.106.256103.

[308] Wei Zhang and Lian Yu. “Surface diffusion of polymer glasses”. In: *Macromolecules* 49 (2016), p. 731. DOI: 10.1021/acs.macromol.5b02294. URL: https://doi.org/10.1021/acs.macromol.5b02294.

[309] Xiaohu Hu et al. “The dynamics of single protein molecules is non-equilibrium and self-similar over thirteen decades in time”. In: *Nature Phys.* 12 (2016), p. 171. DOI: 10.1038/nphys3553. URL: https://doi.org/10.1038/nphys3553.

[310] P. Norvig and S. J. Russell. *Artificial intelligence: A modern approach.* 3rd ed. USA: Pearson Education, 2010. Chap. 19–22, pp. 651–822.

[311] J. Behler and M. Parrinello. “Generalized neural-network representation of high-dimensional potential-energy surfaces”. In: *Phys. Rev. Lett.* 98 (2007), p. 146401. DOI: 10.1103/PhysRevLett.98.146401. URL: https://journals.aps.org/prl/abstract/10.1103/PhysRevLett.98.146401.

[312] J. Behler. “Neural network potential-energy surfaces in chemistry: a tool for large-scale simulations”. In: *Phys. Chem. Chem. Phys.* 13 (2011), pp. 17930–17955. DOI: 10.1039/c1cp21668f. URL: https://pubs.rsc.org/en/content/articlelanding/2011/cp/c1cp21668f.

[313] J. Behler. “Representing potential energy surfaces by high-dimensional neural network potentials”. In: *J. Phys.* 26 (2014), p. 183001. DOI: 10.1088/0953-8984/26/18/183001. URL: https://iopscience.iop.org/article/10.1088/0953-8984/26/18/183001.

[314] B. Kolb, L.C. Lentz, and A.M. Kolpak. “Discovering charge density functionals and structure-property relationships with PROPhet: A general framework for coupling machine learning and first-principles methods”. In: *Sci. Rep.* 7 (2017), p. 1192. DOI: 10.1038/s41598-017-01251-z. URL: https://doi.org/10.1038/s41598-017-01251-z.

[315] Donald H. Kobe. “Gauge transformations and the electric dipole approximation”. In: *Am. J. Phys.* 50.2 (1982), p. 128. DOI: 10.1119/1.13029. URL: https://doi.org/10.1119/1.13029.

[316] P. L. Silvestrelli and M. Parrinello. “Water molecule dipole in the gas and in the liquid phase”. In: *Phys. Rev. Lett.* 82.16 (1999), pp. 3308–3311. DOI: 10.1103/PhysRevLett.82.3308. URL: https://journals.aps.org/prl/abstract/10.1103/PhysRevLett.82.3308.

[317] E. B. Wilson. *Molecular vibrations.* New York: McGraw-Hill Book Company, Inc., 1955.

[318] S. Goedecker, M. Teter, and J. Hutter. “Separable Dual-Space Gaussian Pseudopotentials”. In: *Phys. Rev. B* 54 (3 1996), pp. 1703–1710. DOI: 10.1103/PhysRevB.54.1703. URL: https://link.aps.org/doi/10.1103/PhysRevB.54.1703.

[319] M. Krack. “Pseudopotentials for H to Kr optimized for gradient-corrected exchange-correlation functionals”. In: *Theor. Chem. Acc.* 114 (2005), p. 145. DOI: 10.1007/s00214-005-0655-y. URL: https://doi.org/10.1007/s00214-005-0655-y.

[320] J. VandeVondele and J. Hutte. “Gaussian basis sets for accurate calculations on molecular systems in gas and condensed phases”. In: *J. Chem. Phys.* 127 (2007), p. 114105. DOI: 10.1063/1.2770708. URL: https://doi.org/10.1063/1.2770708.

[321] Hee-Seung Lee and Mark E. Tuckerman. “Dynamical properties of liquid water from ab initio molecular dynamics performed in the complete basis set limit”. In: *J. Chem. Phys.* 126.16 (2007), p. 164501. DOI: 10.1063/1.2718521. URL: https://doi.org/10.1063/1.2718521.

[322] H. Ishikita and K. Saito. “Proton transfer reactions and hydrogen-bond networks in protein environments”. In: *J. R. Soc. Interface* 11.91 (2013), p. 20130518. DOI: `10.1098/rsif.2013.0518`. URL: `https://www.ncbi.nlm.nih.gov/pmc/articles/PMC3869154/`.

[323] H. Tanaka, K. Nakanishi, and N. Watanabe. “Constant temperature molecular dynamics calculation on Lennard-Jones fluid and its application to water”. In: *J. Chem. Phys.* 78.5 (1983), pp. 2622–2634. DOI: `10.1063/1.445020`. URL: `https://aip.scitation.org/doi/10.1063/1.445020`.

[324] Yu. I. Naberukhin and V. P. Voloshin. “Distributions of hydrogen bond lifetimes in instantaneous and inherent structures of water”. In: *Z. Phys. Chem.* 223 (2009), pp. 999–1011. DOI: `10.1524/zpch.2009.6062`. URL: `https://doi.org/10.1524/zpch.2009.6062`.

[325] L. D. Landau and E. M. Lifshitz. *Statistical physics: Part 1*. Elsevier Ltd, 3rd ed, 1980.

[326] T. E. Dirama, G. A. Carri, and A. P. Sokolov. “Role of hydrogen bonds in the fast dynamics of binary glasses of trehalose and glycerol: A molecular dynamics simulation study”. In: *J. Chem. Phys.* 122 (2005), p. 114505. DOI: `10.1063/1.1870872`. URL: `https://aip.scitation.org/doi/abs/10.1063/1.1870872`.

[327] R. Rey, K. B. Møller, and J. T. Hynes. “Hydrogen bond dynamics in water and ultrafast infrared spectroscopy”. In: *J. Phys. Chem. A* 106.50 (2002), pp. 11993–11996. DOI: `10.1021/jp026419o`. URL: `https://doi.org/10.1021/jp026419o`.

[328] K. B. Møller, R. Rey, and J. T. Hynes. “Hydrogen bond dynamics in water and ultrafast infrared spectroscopy: A theoretical study”. In: *J. Phys. Chem. A* 108.7 (2004), pp. 1275–1289. DOI: `10.1021/jp035935r`. URL: `https://pubs.acs.org/doi/abs/10.1021/jp035935r`.

[329] H.-S. Tan et al. “Dynamics of water confined on a nanometer length scale in reverse micelles: Ultrafast infrared vibrational echo spectroscopy ”. In: *Phy. Rev. Lett.* 94 (2005), pp. 057405.1–057405.4. DOI: `10.1103/PhysRevLett.94.057405`. URL: `http://europepmc.org/article/MED/15783696`.

[330] K. Hashimoto and K. Morokuma. “Ab initio molecular orbital study of Na(H_2O)n (n = 1-6) clusters and their ions. Comparison of electronic structure of the "surface" and "interior" complexes”. In: *J. Am. Chem. Soc.* 116.25 (1994), pp. 11436–11443. DOI: `10.1021/ja00104a024`.

[331] Lavanya M. Ramaniah, Marco Bernasconi, and Michele Parrinello. “Density-functional study of hydration of sodium in water clusters”. In: *J. Chem. Phys.* 109.16 (1998), pp. 6839–6843. DOI: `10.1063/1.477250`. URL: `https://doi.org/10.1063/1.477250`.

[332] A. W. Omta et al. “Negligible effect of ions on the hydrogen-bond structure in liquid water”. In: *Science* 301 (2003), p. 347. DOI: `10.1126/science.1084801`. URL: `https://science.sciencemag.org/content/301/5631/347`.

[333] Y. Zhang and P. S Cremer. “Interactions between macromolecules and ions: The Hofmeister series”. In: *Curr. Opin. in Chem. Bio.* 10 (2006), p. 658. DOI: `10.1016/j.cbpa.2006.09.020`. URL: `https://doi.org/10.1016/j.cbpa.2006.09.020`.

[334] I. Ohmine. “Liquid water dynamics: Collective motions, fluctuation, and relaxation”. In: *J. Phys. Chem* 99.18 (1995), pp. 6767–6776. DOI: `10.1021/j100018a004`. URL: `https://pubs.acs.org/doi/abs/10.1021/j100018a004`.

[335] M. Ferrario, M. Haughney, and R. McDonald M. L. Klein. “Molecular-dynamics simulation of aqueous mixtures: Methanol acetone, and ammonia”. In: *J. Chem. Phys.* 93 (1990), p. 5156. DOI: `10.1063/1.458652`. URL: `https://aip.scitation.org/doi/abs/10.1063/1.458652`.

[336] Raymond D. Mountain. “Comparison of a fixed-charge and a polarizable water model”. In: *J. Chem. Phys.* 103.8 (1995), pp. 3084–3090. DOI: `10.1063/1.470497`. URL: `https://doi.org/10.1063/1.470497`.

[337] L. J. Root and B. J. Berne. “Effect of pressure on hydrogen bonding in glycerol: A molecular dynamics investigation”. In: *J. Chem. Phys.* 107 (1997), pp. 4350–4357. DOI: `10.1063/1.474776`. URL: `https://doi.org/10.1063/1.474776`.